Understanding the impact of millennial to sub-decadal climate and limnological change on the stability of arsenic in lacustrine sediments

by

Braden Ross Buchanan Gregory

A thesis submitted to the Faculty of Graduate and Postdoctoral Affairs in partial fulfillment of the requirements for the degree of

Doctor of Philosophy

in

Earth Sciences

Carleton University

Ottawa, Ontario

Abstract

Metal(loid)s are expected to respond to 21st century warming as their stability in lacustrine systems is indirectly influenced by regional temperature and precipitation. In the Northwest Territories (NT), arsenic (As) is a metal(loid) of environmental concern due to elevated concentrations in bedrock and widespread mining-related contamination. To characterize the response of As to long- and short-term climate variability, we developed techniques that enable high temporal resolution analyses of sediment freeze cores, and applied them to a sediment cores (CON01, CON02) recovered from Control Lake, NT. New equipment was designed to enable Itrax X-ray fluorescence (Itrax-XRF) analysis of discrete sediment samples (Chapter 2). This equipment was used to test calibration methods that convert semi-quantitative Itrax-XRF results to near-total geochemical concentrations (Chapter 3). We found that the multi-variate log-ratio calibration provided the best approximation of actual geochemical concentrations. Subsequently, equipment was designed to permit scanning of freeze-cores using Itrax-XRF (Chapter 4). To characterize millennial-scale shifts in sedimentary As concentration in response to climate change, Arcellinida and ICP-MS analysis were conducted on core CON01 that recorded 4000 yr of sedimentation (Chapter 5). Arsenic concentrations the in core were related to shifts in the proportion of organic matter and shifts in minerogenic content (Rb, K). Comparison to regional records suggests changes in temperature impacted autochtonous productivity, which is hypothesized to have influenced sedimentary As concentrations. To characterize the response of As to quasi-periodic climate oscillations, CON02 was analyzed using Itrax-XRF. Itrax-XRF data were calibrated to paired ICP-MS data, and geochemical proxies for particle size (log(Zr/Ti)), in-lake productivity (log(Ca/Ti)), and As preservation (log(As/Ti)) were examined for cyclities using spectral and wavelet analyses. Periods of 8–15, 30–60, 90–130, and 180–300 yr were observed in all proxies. These periods are temporally related to the North Atlantic Oscillation/El niño/Schwabe sunspot cycles, the Pacific Decadal Oscillation, the Gleissberg cycle, and the Suess cycle, respectively. Cross-wavelet analysis of the paleo-proxies vs. published total solar irradiance reconstructions demonstrate significant relationships, suggesting a solar influence on climate and lake sediment geochemistry in the NT. These results suggest that As sequestration is impacted by short-period climate perturbations.

Acknowledgments

First and foremost, thank you to my co-supervisors Dr. Jennifer Galloway and Dr. Timothy Patterson, whose passion for science and support helped make this dissertation a reality. Thank you for pushing me to publish and present. Thank you to Dr. Eduard Reinhardt. You took me on as an undergraduate student and put me on the path to academia. Without your guidance I would not be into science, coffee or baking as I much as I am today.

Thank you to my colleagues in the Earth Science Department. Thank you (soon to be) Dr. Nasser. We (finally) made it! Thank you Dr. Macumber, the first person to call me a scientist. To Michel Haché, my best bud in Ottawa, thank you for helping me through my early days at Carleton. Thank you, Mike Thompson for hosting DnD, for getting me back to the gym, and for being my gardening buddy. Thank you Arjan for joining me on my quest to become a master swordsman.

To my family who supported me throughout my PhD, thank you for your patience, your kind words, and your support. A special thanks to Kevin MacKay for always being there, and for all the free cocktails. I cannot thank Holleh Rahmati enough. Thank you for always believing in me, and for being there through the good times and the rough patches.

Thank you to the Natural Sciences and Engineering Research Council of Canada, Polar Knowledge Canada, the Canadian Foundation for Innovation, the Geological Survey of Canada, the Geological Society of America, the Jeletzky Memorial Foundation, The Journal of Foraminiferal Research, and the Northern Scientific Training Program for providing funding for this research. Thank you also to TerraX Minerals Inc., and Seabridge Gold Inc. who provided in-kind support, field assistants and field assistance, and helped out however they could. Thank you to Indigenous and Northern Affairs Canada for supporting access to the Tundra-Salmita Mine site, and for First Nations and Inuit communities of northern Canada that provided additional context to our research through Traditional Knowledge reports and shared some of their traditions with us out on the land.

Table of Contents

List of Tables

List of Figures

List of Appendices

Chapter 1: Introduction

Environmental systems in high northern latitudes are disproportionately affected by climate change relative to lower latitudes (Serreze et al. 2000; Weller et al. 2005; SWIPA 2017; AMAP 2019). Recent climate warming in northern latitudes over the past several decades has caused a series of cascading changes to environmental systems, including shifts in the location of the tundra to boreal-forest transition zone (Elmendorf et al. 2012; Zhang et al. 2013; Martin et al. 2017), a reduction in permafrost extent (Payette et al. 2004; Smith et al. 2005; Coleman et al. 2015; Lund et al. 2014; Box et al. 2019), an extended ice-free season (Michelutti et al. 2003; Duguay et al. 2006; Arp et al. 2010; Šmejkalová et al. 2016), changes to the hydrological cycle (Jacques and Sauchyn 2009), shifts in the carbon cycle that impact type and availability of organic carbon (Streigl et al. 2005; Guo et al. 2007) and alterations to forest fire regimes (Hu et al. 2010; Chipman and Hu 2017). These environmental changes are likely to impact the mobility, transportation and sequestration of metal(loid) contaminants within environmental systems (Macdonald et al. 2005; Spence et al. 2014; Carlsson et al., 2016). With twice the global rate of temperature change projected for the Arctic (IPCC 2013; SWIPA 2017), understanding controls on metal(loid) sequestration in environmental systems is critical for identification of future risks to anthropogenic, ecological and environmental systems.

Arsenic (As) is a metal(loid) of environmental concern worldwide (Smedley and Kinniburgh 2000; Bowell et al. 2014; Chung et al. 2014). Elevated concentrations of As in the environment may be caused by weathering of mineralized bedrock and derived surficial materials, through anthropogenic activities, such as wood treatment (Stilwell and Gorny 1997; Townsend et al. 2003), pesticide use (Handson 1984; Wolz et al. 2003), or due to mineral extraction and processing (Camm et al. 2004; Jamieson 2014; Cott et al. 2016; Galloway et al. 2018). Lacustrine systems serve as a semi-permanent storage for metal(loid) contaminants, including As (Becker et al. 2001; Keimowitz et al. 2005; Bai et al. 2010; Bing et al. 2011; Bowell et al. 2014). In lacustrine systems, redox state and pH act as the dominant controls on the cycling of As between sediment and overlying waters, ultimately controlling the long-term storage of As in lake sediments (Smedley and Kinniburgh 2000; Campbell and Nordstrom 2014; Palmer et al. 2019). Under oxidizing

conditions, As will sorb to metal-oxides and remain in sediment (Torres et al. 2015; Guénet et al. 2016; Lock et al. 2018). Under reducing conditions, dissolution of metal oxides and reduction of As releases As into porewaters, resulting in the possible efflux of As into overlying waters from sediment; if conditions are euxinic, As can be sequestered by authigenic minerals including framboidal pyrites, arsenopyrite, or arseno-sulfides (Benning et al. 2000; Butler and Rickard 2000;Bostick and Fendorf 2003; Xu et al. 2011; Burton et al. 2013; Torres et al. 2015; Thiel et al. 2019). Temperature and precipitation can also affect sedimentary As concentrations through modification of the rate of weathering and transport of As in lake catchments, or through controlling second-order processes, such as in-lake productivity or lake stratification regimes that affect the redox state of bottom waters and shallow sediments. The mobility and sequestration of As is therefore expected to respond to long- and short-term climate change (MacDonald et al. 2005; Galloway et al. 2018).

Quasi-periodic oscillations in the coupled oceanic-atmosphere system impact worldwide precipitation and temperatures. Regional climate has been related to periodic shifts in equatorial winds and corresponding sea-surface temperatures (ENSO - El niño/Southern Oscillation; McCabe and Dettinger 1999; Mann et al. 2000; Torbenson et al. 2019); anomalies in sea surface temperatures in the North Pacific and associated re-organization of the predominant low-pressure systems (PDO – Pacific Decadal Oscillation; Zhang et al. 2010; Galloway et al. 2013; Patterson et al. 2013; Sankaran 2017); and sea surface temperature changes in the Atlantic (Atlantic Multi-decadal Oscillation – AMO; Birkel et al. 2018) among others (North Atlantic Oscillation – NAO, Trigo et al. 2002; Iles and Hegerl 2017; Montaldo and Sarigu 2017; Arctic Oscillation - AO; Dai and Tan 2017; Sezen and Partal 2019). Regional shifts in temperature and precipitation driven by ocean-atmosphere events and their teleconnections are expected to impact the stability of As in environmental systems through their impact on regional climate. This topic has rarely been addressed, in part due to past technological restrictions and the high costs associated with analyzing the high volume of samples required to reliably capture decadal climate cycles, but also because only recently have climate oscillations been observed to have a substantial impact on regional climate.

In the last decade, high-resolution core-scanning devices have been increasingly deployed for paleoenvironmental and paleoclimate reconstructions (Rothwell and Croudace 2015, and references therein). The newest versions of core scanners are capable of providing high-resolution imagery, X-radiography, X-ray fluorescence (XRF), and magnetic susceptibility data at 0.1 mm resolution on sediment or rock cores (Croudace et al. 2006; Richter et al. 2006; Hascke 2006; Sakamoto et al. 2006). Of primary interest to paleolimnologists are the XRF capabilities of XRF core scanners that enable determination of sediment geochemistry, which can be used as a proxy for a wide variety of in-lake and catchment processes (Davies et al. 2015; Croudace and Rothwell 2015). An unfortunate drawback of analyzing un-prepared material at this high resolution is the semi-quantitative nature of the data. Traditional energy- or wavelength-dispersive XRF requires sediment be dried and ground to homogenous particle size to eliminate specimen and matrix effects, allowing for the quantification of absolute geochemical concentrations based on the energy of the emitted X-radiation. When analyzing unprepared sediment using core-scanning XRF, variations in particle size, sediment geochemistry, and proportion of non-detectable material (*e.g.* organic matter, water) preclude reliable determination of absolute elemental concentrations. In spite of the semi-quantitative nature of XRF core scanners, the high resolution allows for interpretation of climate signals at resolutions not previously possible. Moreover, the high-resolution and non-destructive analysis can allow for better quantification of the inherent geochemical variability of samples as many replicate measurements of the same material can be recorded. Itrax-XRF can also offer advantages in detection of select elements of other traditional geochemical techniques. For example, estimating whole-rock As concentrations in sediment is difficult with ICP-MS as the multi-acid digestion required prior to analysis can volatilize As (Parsons et al. 2010). Itrax-XRF may thus better estimate actual geochemical variability of As than ICP-MS as no prior digestion is required. This technology could allow examination of the response of As to short-term climate perturbations over long stretches of time, closing an important gap in our knowledge of how climate impacts chemical mobility.

Lake sediments, surface waters, and soils around Yellowknife, the Northwest Territories (NT), exhibit elevated concentrations of As. Pre-mining background levels of

As in sediments of lakes in the Yellowknife region are ~20-30 ppm, higher concentrations than the CCME guidelines of 5.9 ppm (Interim Sediment Quality Guideline) and 17 ppm (Probable Effect Level; CCME 2002) (Galloway et al. 2010, 2015, 2018; Palmer et al. 2015; 2019; Houben et al. 2016). Concentrations of As in lake sediment above CCME guidelines and above the global average for igneous/metamorphosed rocks may be the result of the natural weathering of greenstone bedrock and related surface materials that exhibit elevated As concentration near heavily-mineralized shear zones. High natural concentrations of As in the region are further exacerbated by extraction of gold ores from the shear zones of the greenstone belts. Gold mines have operated in the region from its earliest establishment until nearly modern day, including Con Mine (1938–2003) and Giant Mine (1948–2002) that collectively produced > 12 million ounces of gold (Silke 2009). The refractory nature of gold recovered in Yellowknife necessitated roasting of arsenopyrite ores before cyanidation, which caused the volatilization of As (Jamieson et al. 2014) and subsequent aerial deposition of arsenic as arsenic trioxide across the region (Galloway et al. 2010, 2015, 2018; Palmer et al. 2015, 2018; Nasser et al. 2016). Over the lifetime of the mine, it is estimated that >20,000 tonnes of arsenic trioxide where released into the environment (Wrye 2008). The remediation of this former mine site is the most expensive project ever untaken in Canada, with an estimated cost of 904 million dollars CAD (AANDC 2012). Recent increases in gold prices have renewed interest in gold extraction in the region. Information on the effect of long- and short-term climate variations on As concentrations in sediment can help create realistic and reliable remediation plans for the region to minimize future contamination of environmental systems.

The purpose of this dissertation is to examine long- and short-term variations in metal(loid) concentration in lake sediments that may be related to climate change. To accomplish this, we developed new equipment and methodologies to analyze sediment using Itrax-XRF (Chapter 2 and 4), tested recently proposed methods of calibration to provide an estimate of actual geochemical variability in sediment based on the measure of relative geochemical change provided by Itrax-XRF (Chapter 3) and characterized the impact of millennial-scale (Chapter 5) and sub-centennial scale (Chapter 6) climate variability on As stability in lake sediment during the late Holocene. To accomplish these

goals, freeze cores were recovered from Control Lake, a small lake ~240 km NE of Yellowknife adjacent to Tundra Mine, NT. Unlike the gold ores processed in Giant and Con Mines near Yellowknife, gold ores at Tundra mine did not require roasting before cyanidation. As such, nearby lakes were not impacted by aerial deposition of As minerals. Monitoring in the region showed that Control Lake has been unimpacted by mining activities, including the storage of tailings onsite. It has therefore been selected as a site to examine the impact of climate on natural variations in As concentration during the Late Holocene. Chapters within this dissertation have been prepared for publication in academic journals, with Chapters 2, 3, and 4 already published, and Chapters 5 and 6 in preparation for publication. To demonstrate the work of the first author, PhD candidate Braden R.B. Gregory, the contributions from the relevant authors are stated before each chapter.

1.1 References

Aboriginal Affairs and Northern Development Canada (2013) Water Balance Monitoring at the Tundra Mine Site: 2012 Update. 101 p.

AMAP (2019) Arctic Climate Change Update 2-19 – An assessment by the Arctic Monitoring and Assessment Programme.12 p.

Arp CD, Jones BM, Whitman M, Larsen A, Urban FE (2010) Lake temperature and ice cover regimes in the Alaskan Subarctic and Arctic: Integrated monitoring, remote sensing, and modeling. J Am Water Resour Assoc 46:777–791.

Bai J, Yang Z, Cui B, Gao H, Ding Q (2010) Some heavy metals distribution in wetland soils under different land use types along a typical plateau lake, China. Soil Tillage Res 106:344–348.

Becker A, Klöck W, Friese K, Schreck P, Treutler H-C, Spettel B, Duff, MC (2001) Lake Süber See as a natural sink for heavy metals Lake Su from copper mining. J Geochemical Explor 74:205–217

Benning LG, Wilkin RT, Barnes HL (2000) Reaction pathways in the Fe-S system below 100°C. Chem Geol 167:25–51.

Bing H, Wu Y, Sun Z, Yao S (2011) Historical trends of heavy metal contamination and their sources in lacustrine sediment from Xijiu Lake, Taihu Lake Catchment, China. J Environ Sci 23:1671–1678.

Birkel SD, Mayewski PA, Maasch KA, Kurbatov AV Lyan B (2018) Evidence for a volcanic underpinning of the Atlantic multidecadal oscillation. npj Clim Atmos Sci 1:1–7.

Biswas B, Qi F, Biswas J, Wijayawardena A, Khan MAI, Naidu R (2018) The Fate of Chemical Pollutants with Soil Properties and Processes in the Climate Change Paradigm—A Review. Soil Syst 2:51.

Bostick BC, Fendorf S (2003) Arsenite sorption on troilite (FeS) and pyrite (FeS2). Geochim Cosmochim Acta 67:909–921.

Bowell RJ, Alpers CN, Jamieson HE, Nordstrom DK, Majzlan J (2014) The Environmental Geochemistry of Arsenic: An Overview. In: Arsenic: Environmental geochemistry, mineralogy and microbiology. pp 1–16

Box JE, Colgan WT, Christensen TR, Schmidt NM Lund M, Parmentier F-J, Brown R,

Bhatt US, Euskirchen ES, Romanocsky VE, Walsh JE, Overland JE, Wang M, Corell RW, Meier WN, Wouters B, Mernild S, Märd J, Pawlak J, Olsen MS (2019) Key indicators of Arctic climate change: 1971–2017. Environ Res Lett 14:045010.

Burton ED, Johnston SG, Planer-Friedrich B (2013) Coupling of arsenic mobility to sulfur transformations during microbial sulfate reduction in the presence and absence of humic acid. Chem Geol 343:12–24.

Butler IB, Rickard D (2000) Framboidal pyrite formation via the oxidation of iron (II) monosulfide by hydrogen sulphide. Geochim Cosmochim Acta 64:2665–2672.

Camm GS, Glass HJ, Bryce DW, Butcher AR (2004) Characterisation of a mining-related arsenic-contaminated site, Cornwall, UK. J Geochemical Explor 82:1–15.

Campbell KM, Nordstrom DK (2014) Arsenic Speciation and Sorption in Natural Environments. In: Arsenic: Environmental geochemistry, mineralogy and microbiology. pp 170–201

Canadian Council of Ministers of the Environment (CCME) (2002) Canadian Soil Quality Guidelines for the Protection of Environmental and Human Health - Arsenic (Inorganic)

Carlsson P, Christensen JH, Borgå K, Kallenborn R, Pfaffhuber KA, Odland JØ, Reiersen L-O, Pawlak JG (2016) Influence of Climate Change on Transport, Levels, and Effects of Contaminants in Northern Areas - Part 2. Arctic Monitoring and Assessment Programme (AMAP), Oslo. 52 p.

Chipman ML, Hu FS (2017) Linkages Among Climate, Fire, and Thermoerosion in Alaskan Tundra Over the Past Three Millennia. J Geophys Res Biogeosciences 122:3362–3377.

Chung JY, Yu S Do, Hong YS (2014) Environmental source of arsenic exposure. J Prev Med Public Heal 47:253–257.

Coleman KA, Palmer MJ, Korosi JB, Kokelj SV, Jackson K, Hargan KE, Mustaphi CJC, Theinpont JR, Kimpe LE, Blais JM, Pisaric MFJ, Smol JP (2015) Tracking the impacts of recent warming and thaw of permafrost peatlands on aquatic ecosystems: A multi-proxy approach using remote sensing and lake sediments. Boreal Environ Res 20:363–377

Cott PA, Zajdlik BA, Palmer MJ, McPherson MD (2016) Arsenic and mercury in lake

whitefish and burbot near the abandoned Giant Mine on Great Slave Lake. J Great Lakes Res 42:223–232.

Croudace IW, Rindby A, Rothwell RG (2006) ITRAX: description and evaluation of a new multi-function X-ray core scanner. Geol Soc London, Spec Publ 267:51–63.

Dai P, Tan B (2017) The nature of the Arctic oscillation and diversity of the extreme surface weather anomalies it generates. J Clim 30:5563–5584.

Davies SJ, Lamb HF, Roberts SJ (2015) Micro-XRF Core Scanning in Palaeolimnology: Recent Developments. In: Micro-XRF Studies of Sediment Cores: Applications of a Non-Destructive tool for Environmental Sciences. pp 189–226

Duguay CR, Prowse TD, Bonsal BR, Brown RD, Lacroix MP, Ménard P (2006) Recent trends in Canadian lake ice cover. Hydrol Process 20:781–801.

Elmendorf SC, Henry GHR, Hollister RD (2012) Plot-scale evidence of tundra vegetation change and links to recent summer warming. Nat Clim Chang 2:453–457.

Galloway JK, Macumber AL, Patterson RT, Falck H, Hadlari T, Madsen E (2010) Paleoclimatological assessment of the southern Northwest Territories and implications for the long-term viability of the Tibbitt to Contwoyto winter road, Part 1: Core collection. Northwest Territories Geoscience Office, NWT Open Report. 21 p.

Galloway JM, Palmer M, Jamieson HE, Patterson RT, Nasser NA, Falck H, Macumber AL, Goldsmith SA, Sanei H, Normandeau P, Hadlari T, Roe HM, Neville LA, Lemay D (2015) Geochemistry of lakes across ecozones in the Northwest Territories and implications for the distribution of arsenic in the Yellowknife region. Part 1 Sediments Open File. 50 p.

Galloway JM, Swindles GT, Jamieson HE, Palmer M, Parsons MB, Sanei H, Macumber AL, Patterson RT, Falck H (2018) Organic matter control on the distribution of arsenic in lake sediments impacted by ~ 65 years of gold ore processing in subarctic Canada. Sci Total Environ 622–623:1668–1679.

Galloway JM, Wigston A, Patterson RT, Swindles GT, Reinhard E, Roe HM (2013)

Climate change and decadal to centennial-scale periodicities recorded in a late Holocene NE Pacific marine record: Examining the role of solar forcing. Palaeogeogr Palaeoclimatol Palaeoecol 386:669–689.

Guénet H, Davranche M, Vantelon D, Pedrot M, Al-Sid-Cheikh M, Dia A, Jestin J (2016) Evidence of organic matter control on As oxidation by iron oxides in riparian wetlands. Chem Geol 439:161–172.

Guo L, Ping CL, Macdonald RW (2007) Mobilization pathways of organic carbon from permafrost to arctic rivers in a changing climate. Geophys Res Lett 34:1–5.

Handson PD (1984) Lead and arsenic levels in wines produced from vineyards where lead arsenate sprays are used for caterpillar control. J Sci Food Agric 35:215–218.

Hascke M (2006) The Eagle III BKA system, a novel sediment core X-ray fluorescence analyser with very high spatial resolution. In: Rotherwell RG (ed) New techniques in sediment core analysis, Geological Society of London Special Publications, 267:31–37.

Houben AJ, D'Onofrio R, Kokelj SV, Blais JM (2016) Factors affecting elevated arsenic and methyl mercury concentrations in small shield lakes surrounding gold mines near the Yellowknife, NT, (Canada) region. PLoS One 11:1–16.

Hu FS, Higuera PE, Walsh JE, Chapman WL, Duffy PA, Burbaker LB, Chipman ML (2010) Tundra burning in Alaska: Linkages to climatic change and sea ice retreat. J Geophys Res Biogeosciences 115:1–8.

Iles C, Hegerl G (2017) Role of the North Atlantic Oscillation in Decadal Temperature Trends. Environ Res Lett 12:

IPCC (2013) Climate Change 2013: The Physical Science Basis. In: Climate Change 2013. p 1535

Jacques JMS, Sauchyn DJ (2009) Increasing winter baseflow and mean annual streamflow from possible permafrost thawing in the Northwest Territories, Canada. Geophys Res Lett 36:1–6.

Jamieson HE (2014) The Legacy of Arsenic Contamination from Mining and Processing Refractory Gold Ore at Giant Mine, Yellowknife, Northwest Territories, Canada. pp 533–551

Keimowitz AR, Zheng Y, Chillrud SN, Mailloix B, Jung HB, Stute M, Simpson HJ (2005)

Arsenic redistribution between sediments and water near a highly contaminated source. Environ Sci Technol 39:8606–8613.

Lock A, Wallschläger D, Belzile N, Spiers G, Gueguen C (2018) Rates and processes affecting As speciation and mobility in lake sediments during aging. J Environ Sci (China) 66:338–347.

Lund M, Hansen BU, Pedersen SH, Stiegler C, Tamstorf MP (2014) Characteristics of summer-time energy exchange in a high Arctic tundra heath 2000-2010. Tellus, Ser B Chem Phys Meteorol 66:1–14.

Macdonald RW, Harner T, Fyfe J (2005) Recent climate change in the Arctic and its impact on contaminant pathways and interpretation of temporal trend data. Sci Total Environ 342:5–86. doi: 10.1016/j.scitotenv.2004.12.059

Mann M, Bradley R, Hughes M (2000) Long-term variability in the El Niño/Southern Oscillation and associated teleconnections. El Nino and the Southern Oscillation: Multiscale Variability and its Impacts on Natural Ecosystems and Society (2000): 357–412.

Martin AC, Jeffers ES, Petrokofsky G, Myers-Smith I, Macias-Fauria M (2017) Shrub growth and expansion in the Arctic tundra: An assessment of controlling factors using an evidence-based approach. Environ Res Lett 12:085007.

McCabe GJ, Dettinger MD (1999) Decadal variations in the strength of ENSO teleconnections with precipitation in the western United States. Int J Climatol 19:1399–1410.

Michelutti N, Douglas MSV, Smol JP (2003) Diatom response to recent climatic change in a high arctic lake (Char Lake, Cornwallis Island, Nunavut). Glob Planet Change 38:257–271. 6

Montaldo N, Sarigu A (2017) Potential links between the North Atlantic Oscillation and decreasing precipitation and runoff on a Mediterranean area. J Hydrol 553:419–437.

Nasser NA, Patterson RT, Roe HM, Galloway JM, Falck H, Palmer MJ, Spence C, Sanei H, Macumber AL, Neville LA (2016) Lacustrine Arcellinina (Testate Amoebae) as Bioindicators of Arsenic Contamination. Environ Microbiol.

Palmer MJ, Chételat J, Richardson M, Jamieson HE, Galloway JM (2019) Seasonal

variation of arsenic and antimony in surface waters of small subarctic lakes impacted by legacy mining pollution near Yellowknife, NT, Canada. Sci Total Environ 684:326–339.

Palmer MJ, Galloway JM, Jamieson HE, Patterson RT, Falck H, Kokelj SV (2015) The concentration of arsenic in lake waters of the Yellowknife area. NWT Open File 2015-06 29

Parsons MB, LeBlanc KWG, Hall GEM, Sangster AL, Vaive JE, Pelchat P (2012) Environmental geochemistry of tailings, sediments and surface waters collected from 14 historical gold mining districts in Nova Scotia. Geological Survey of Canada Open File 7150, pp. 1–312.

Patterson RT, Chang AS, Prokoph A, Roe HM, Swindles GT (2013) Influence of the Pacific Decadal Oscillation, El Niño-Southern Oscillation and solar forcing on climate and primary productivity changes in the northeast Pacific. Quat Int 310:124–139.

Payette S, Delwaide A, Caccianiga M, Beauchemin M (2004) Accelerated thawing of subarctic peatland permafrost over the last 50 years. Geophys Res Lett 31:1–4.

Richter TO, Van der Gaast S, Koster B, Vaars A, Gieles R, de Stiger HC, de Haas H, van Weering TCE (2006) The Avaatech XRF core scanner: technical description and application to NE Atlantic sediments. In: Rotherwell RG (ed) New techniques in sediment core analysis, Geological Society Special Publication, 267:39–55.

Rothwell RG, Croudace IW (2015) Micro-XRF Studies of Sediment Cores: A Perspective on Capability and Application in the Environmental Sciences. In: Croudace IW, Rothwell RG (eds) Micro-XRF studies of sediiment cores. Springer, Dordrecht Heidelberg New York London, pp 1–21

Sakamoto T, Kuroki K, Sugawara T, Aoike K, Iijima K, Sugisaki S (2006) Non-destructive X-ray fluorescence (XRF0 core-imaging scanner, TATSCAN-F2. Scientific Drilling, 2:37–39

Sankaran A (2017) Unveiling the multiscale teleconnection between Pacific Decadal Oscillation and global surface temperature using time-dependent intrinsic correlation analysis. Int J Climatol 37:548–558.

Serreze MC, Walsh JE, Chapin FS, Osterkamp T, Dyurgerov M, Romanovsky V,

Oechel WC, Morison J, Zhang T, Barry RG (2000) Observational Evidence of Recent Change in the Northern High-Latitude Environment. Clim Change 46:159–207

Sezen C, Partal T (2019) The impacts of Arctic oscillation and the North Sea Caspian pattern on the temperature and precipitation regime in Turkey. Meteorol Atmos Phys 2019:1–20.

Smedley PL, Kinniburgh DG (2000) Source and behaviour of arsenic in natural waters. United Nations Synth Rep Arsen Drink 1–61

Šmejkalová T, Edwards ME, Dash J (2016) Arctic lakes show strong decadal trend in earlier spring ice-out. Sci Rep 6:1–8.

Smith SL, Burgess MM, Riseborough D, Nixon FM (2005) Recent trends from Canadian permafrost thermal monitoring network sites. Permafr Periglac Process 16:19–30.

Spence C, Kokelj SV, McCluskie M, Hedstrom N (2014) Evidence of a change in water chemistry in Canada's subarctic associated with enhanced winter streamflow. J Geophys Res Biogeosciences 119:487–507.

Stilwell DE, Gorny KD (1997) Contamination of soil with copper, chromium, and arsenic under decks built from pressure treated wood. Bull Environ Contam Toxicol 58:22–29.

Striegl RG, Aiken GR, Dornblaser MM, Raymond PA, Wickland KP (2005) A decrease in discharge-normalized DOC export by the Yukon River during summer through autumn. Geophys Res Lett 32:1–4.

SWIPA (2017) Snow, Water, Ice and Permafrost in the Arctic. Oslo, Norway, 269 pp.

Thiel J, Byrne JM, Kappler A, Schink B, Pester M (2019) Pyrite formation from FeS and H_2S is mediated through microbial redox activity. Proc Natl Acad Sci 201814412.

Torbenson MCA, Stahle DW, Howard IM, Burnette DJ, Villanueva-Diaz J, Cook ER, Griffin D (2019) Multidecadal modulation of the ENSO teleconnection to precipitation and tree growth over subtropical North America. Paleoceanogr Paleoclimatology 886–900.

Torres E, Couture RM, Shafei B, Nardi A, Ayora C, Van Cappellen P (2015) Reactive

transport modeling of early diagenesis in a reservoir lake affected by acid mine drainage: Trace metals, lake overturn, benthic fluxes and remediation. Chem Geol 419:75–91.

Townsend T, Solo-Gabriele H, Tolaymat T, Stook K, Hosein N (2003) Chromium, Copper, and Arsenic Concentrations in Soil Underneath CCA-Treated Wood Structures. Soil Sediment Contam An Int J 12:779–798.

Trigo RM, Osborn TJ, Corte-Real JM (2002) The North Atlantic Oscillation influence on Europe: Climate impacts and associated physical mechanisms. Clim Res 20:9–17.

Wolz S, Fenske RA, Simcox NJ, Palcisko G, Kissel JC (2003) Residential arsenic and lead levels in an agricultural community with a history of lead arsenate use. Environ Res 93:293–300.

Wrye LA (2008) Distinguishing between natural and anthropogenic sources of arsenic in soils from the Giant Mine, Northwest Territories and the North Brookfield Mine, Nova Scotia. Unpublished M.Sc. thesis. Queen's University, Kingston, ON, Canada. 241 p.

Xu W, Wang H, Liu R, Zhao X, Qu J (2011) Arsenic release from arsenic-bearing Fe-Mn binary oxide: Effects of E_h condition. Chemosphere 83:1020–1027.

Zhang W, Miller PA, Smith B, Wania R, Koenigk T, Döscher R (2013) Tundra shrubification and tree-line advance amplify arctic climate warming: Results from an individual-based dynamic vegetation model. Environ Res Lett 8:1–10

Zhang X, Wang J, Zwiers FW, Groisman PY (2010) The influence of large-scale climate variability on winter maximum daily precipitation over North America. J Clim 23:2902–2915.

Chapter 2: Sequential sample reservoirs for Itrax-XRF analysis of discrete samples

2.1 Authors and Addresses

Gregory BRB[1], Reinhardt EG[2], Macumber AL[1], Nasser NA[1], Patterson RT[1], Kovacs SE[2], Galloway JM[1,3,4]

[1]Ottawa-Carleton Geoscience Centre, Carleton University, 1125 Colonel By Drive, Ottawa, ON, Canada, K1S 5B6

[2]School of Geography and Earth Sciences, McMaster University, Hamilton L8S 4K1, Ontario, Canada

[3]Aarhus Institute of Advanced Studies, Aarhus University, 8000 Aarhus C., Denmark

[4]Geological Survey of Canada/National Resources Canada (Commission géologique du Canada/Ressources naturelles Canada), 3303 33 St. N.W., Calgary AB, Canada, T2L 2A7

2.2 Foreword

This was the first publication produced from the Canadian High Arctic Research grant to Dr. J.M. Galloway and Dr. R.T. Patterson. Before attempting Itrax-XRF analysis using freeze cores, and subsequent calibration of geochemical data from these freeze cores, we wanted to review present calibration methods to determine an ideal methodology. Scanning discrete, homogenized surface sediments would provide a more accurate test of calibration as there would not be the variability in sample caused by temporal changes in sedimentary environments, or possible issues associated with scanning freeze cores. Prior to assessing the relative merit of different calibration methods, we developed equipment and adapted methodologies to scan discrete sediments samples. The methodologies and equipment described in this chapter were published as a short note in The Journal of Paleolimnology. The manuscript has been modified slightly to accommodate the formatting requirements for Carleton University dissertations.

Dr. E.G. Reinhardt and Dr. S.E. Kovacs developed initial designs for the equipment. Prototypes were constructed by P & A Plastics, Hamilton, ON. Dr. R.T. Patterson collected sample material from Harvey Lake. I was responsible for preparing samples, testing the equipment, and developing methodologies for subsequent data extraction. I wrote the manuscript and drafted the figures with assistance from Dr. Macumber and Nawaf Nasser. This work was funded by a Polar Knowledge Canada grant to Dr. Patterson and Dr. Galloway, as well as a Canadian Foundation for Innovation grant to Dr. Reinhardt. All co-authors provided feedback and helped to revise the manuscript. It should be cited as follows:

Gregory BRB, Reinhardt EG, Macumber AL, Nasser NA, Patterson RT, Kovacs SE, Galloway JM (2017) Sequential sample reservoirs for Itrax-XRF analysis of discrete sediment samples. *Journal of Paleolimnology, 57*(3):287–293.

2.3 Abstract

Geochemical analysis of sediment samples can be used to characterize between- and within-lake variability and provide insights into lake chemistry, depositional processes and contamination sources. The number of samples for geochemical studies is restricted by cost, sample volume required, and the destructive nature of inductively coupled plasma mass spectrometry, instrumental neutron activation analysis, or wavelength dispersive x-ray fluorescence. Core scanners that incorporate energy dispersive x-ray fluorescence spectrometry, such as the Cox Itrax-XRF core scanner, have high throughput and can be used to produce high-quality geochemical datasets at low cost without destroying sample material. Here we describe a new analysis vessel that enables rapid, non-destructive Itrax-XRF analysis of discrete sediment samples.

2.4 Introduction

Synoptic limnological studies can be used to characterize the range of lake environmental variability on regional and local scales. These studies provide background information essential for interpretation of paleolimnological records (Pienitz et al. 1997; Rühland and Smol 1998; Rühland et al. 2003) and characterization of water quality and other parameters (Patterson et al. 2012; Roe et al. 2010). Multi-station, intra-lake studies have proven that no single site can fully represent conditions throughout a lake (Engstrom and Rose 2013). Understanding the mechanisms that underlie within-lake spatial environmental heterogeneity can shed light on depositional processes (Dietze et al. 2012) and point-source contamination (Li et al. 2013). The primary limitations to carrying out detailed multi-station, intra-lake studies are cost, sample volume requirements and the destructive nature of conventional techniques, such as inductively coupled plasma mass spectrometry (ICP-MS), wavelength dispersive x-ray fluorescence (WD-XRF), and instrumental neutron activation analysis (INAA).

Core scanners that incorporate energy-dispersive x-ray fluorescence spectrometry (ED-XRF), such as the Cox Itrax-XRF core scanner, are being used increasingly in the environmental sciences. Core scanners have improved the ability of researchers to carry out rapid, inexpensive, and non-destructive assessment of environmental variables in cores. The 0.1-mm scanning resolution that can be obtained with Itrax-XRF core analysis means that sub-annual-scale temporal resolution is possible in many cases (Rothwell and Croudace 2015). Adapting the Itrax-XRF instrument for geochemical analysis of discrete sediment samples has the potential to increase the capacity to analyze samples non-destructively and inexpensively by at least an order of magnitude, *e.g.* from tens to hundreds. This new tool can thus dramatically increase spatial coverage in studies that use discrete sediment samples, such as lacustrine sediment-water interface samples, soils in archaeological contexts, or even subsamples from previously sampled or degraded sediment cores that are no longer suitable for conventional core scanning. Here we: 1) describe a vessel that enables Itrax-XRF analysis of discrete sediment samples, 2) discuss pre-analysis and post-analysis protocols required for analysis carried out using the vessel, and 3) provide an example of its use.

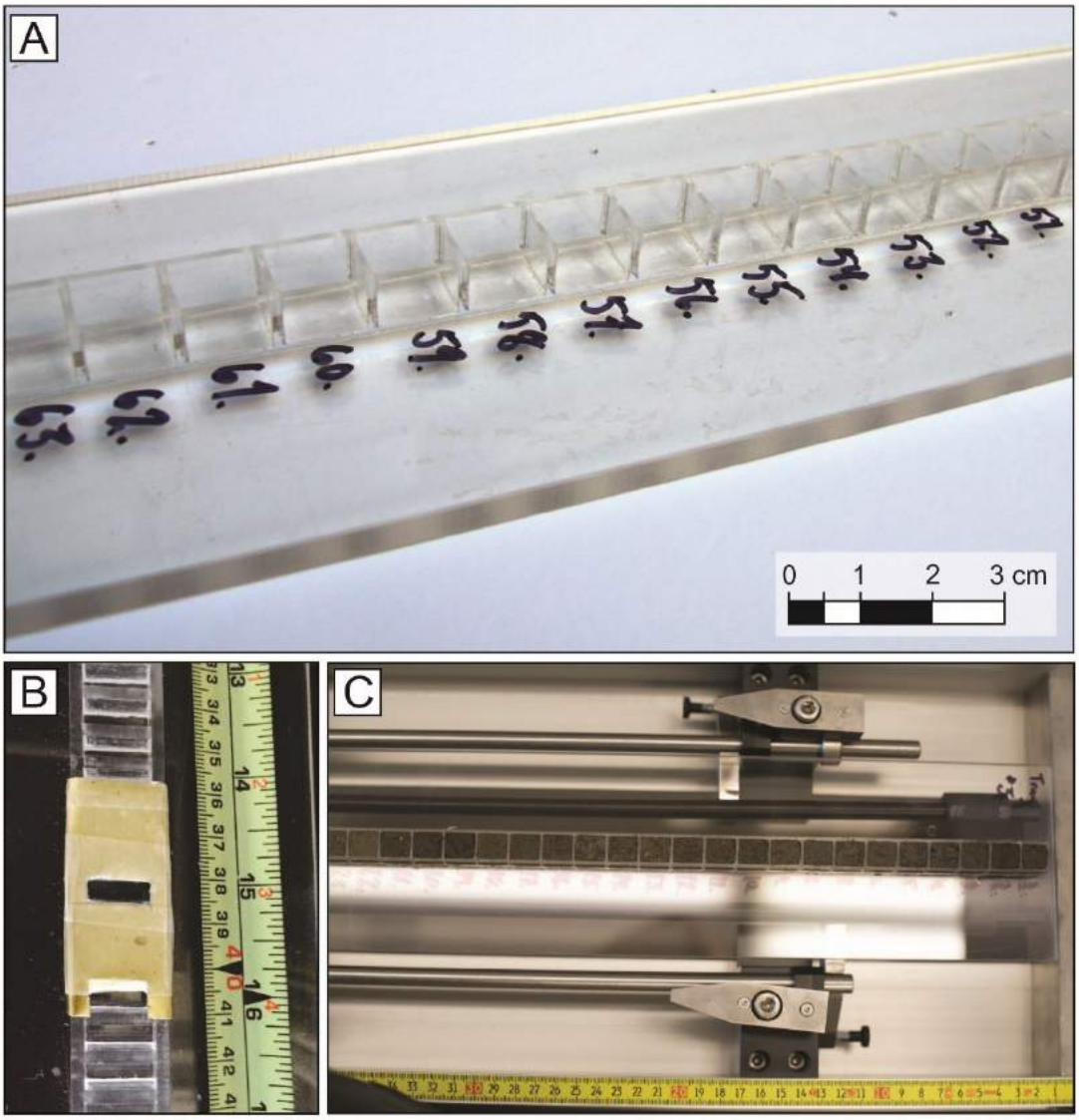

Figure 2.1: (A) Oblique view of the SSR showing detailed 3D structure. (B) SSR with shorter reservoirs, used when sample material is limited. Pictured also is the brass cover to minimize cross-contamination and streamline loading. (C) Close-up of SSR showing sediment in compartments, forming a continuous "core" for analysis.

2.5 Analysis of sediment with the Itrax-XRF

The Itrax-XRF core scanner is designed to record continuous geochemical changes throughout the length of a dewatered sediment core, which can even have been left in the original, split core barrel. In order to enable analysis of discrete sediment samples

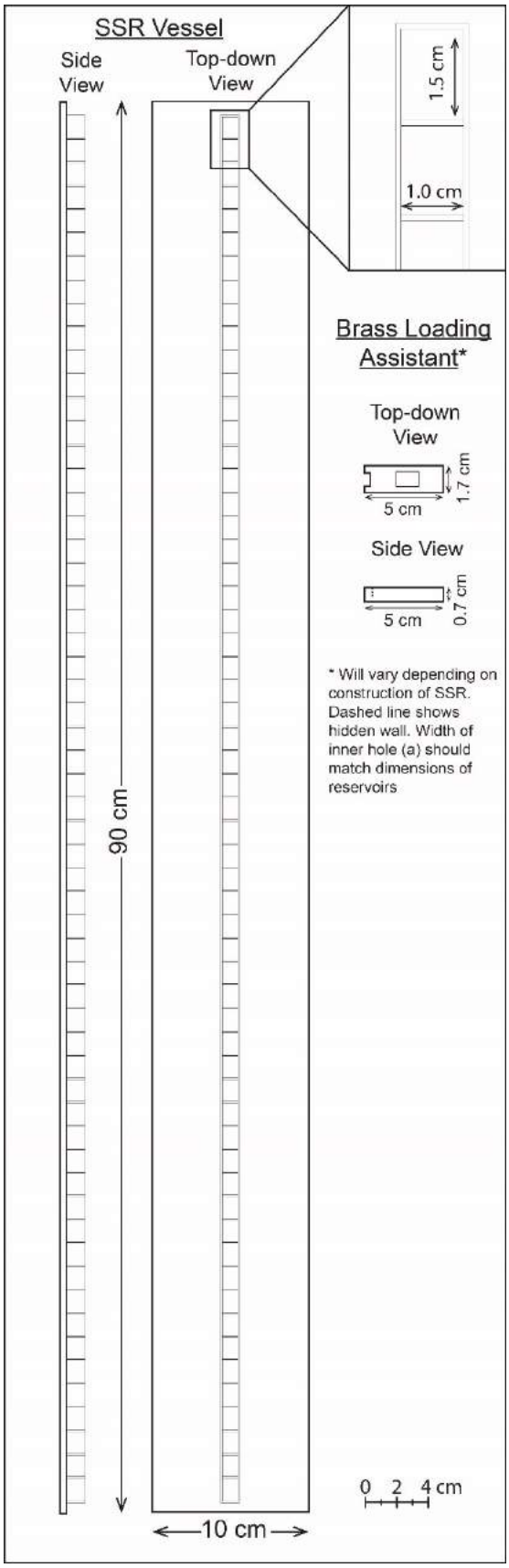

with the Itrax-XRF, sediment samples must be arranged to form a “continuous” record in a de-watered form, thus simulating a conventional sediment core.

2.6 Description of the Itrax Sequential Sample Reservoir (SSR) vessel

The Itrax Sequential Sample Reservoir (SSR) described here is comprised of connected acrylic compartments, 1.5 x 1 x 1 cm, aligned down the center of a clear acrylic base, 10 cm wide by 90 cm long (Figures 2.1A and 2.2). This length allows two full vessels to be loaded sequentially into the Itrax for analysis. If sample volume is restricted, smaller wells can be used (1.5 x 0.5 x 1 cm; Figure 2.1B). The SSR accommodates 59 compartments in a configuration that mimics a conventional sediment core. Acrylic was selected for construction material because of its low cost, durability, and ease of assembly.

Figure 2.2: Schematic diagram of the SSR with larger wells and the brass loader assistant used to minimize cross-contamination and facilitate rapid loading of the SSR. Device is 90 cm long by 10 cm wide. Inset shows magnified reservoirs with dimensions 1.0 cm wide by 1.5 cm long by 1.0 cm deep. Brass loader is 5 cm long be 1.7 cm wide, with the inner hole having the same dimensions as the reservoirs (1.5 x 1.0 cm). The brass loader assistant has folded sides to hold it in place and a small fold on the front to hook the device in place on a subsequent reservoir (dashed line on side view). The brass loader assistant should be long enough to cover at least one previous and subsequent reservoir

Acrylic was used instead of commonly available white PVC, which during prototype testing was found to contain high amounts of Ti and Zn that are used to color the plastic and can potentially contaminate analytical results.

2.7 Operation of the SSR vessel

Water content in sediment-water interface samples is often very high, in some cases >90%. High water content in samples could potentially increase attenuation of the XRF signal (Tjallingii et al. 2007). Sediment that is too wet may also bleed over into adjacent compartments during loading of the vessel and result in cross-contamination. To minimize this problem, we recommend that samples be centrifuged, the supernatant discarded, and sediment plugs dried at room temperature until they reach the consistency of moist paste. Alternatively, supernatant can be retained and samples dried at room temperature if there is concern about the loss of soluble elements in the water. The sediment, however, should not be too dry, as there is risk of airborne cross-contamination between samples, and oxidation of sensitive materials that may be subsequently analyzed (*e.g.* microfossils). By drying to a moist paste, samples will be more comparable to the sediment consistency and content of conventional cores.

Before loading samples into the SSR, material should be homogenized with a spatula. When loading samples into the SSR, it is necessary to pack the sediment using a spatula, to ensure there are no air pockets at the bottom of the reservoir. Air pockets can result in the settling of sediment during analysis, creating uneven surface topography. Abrupt changes in surface topography can cause "data shadows" in areas where depressions or protrusions exist because the Itrax-XRF detector automatically adjusts its position to ensure it does not make contact with the sediment surface. Sediment should be allowed to settle overnight and more should be added, if necessary, to ensure the sample surface is flush with the top of the SSR. A brass cover coated with cellophane tape, which has an opening the same dimensions as one reservoir, can be used to block previously loaded and subsequent reservoirs to prevent cross-contamination and speed the loading process (Figures 2.1B and 2.2). Before analysis, the surface of sediment samples loaded into the SSR should be smooth and flat, as the Itrax-XRF detector must remain at a constant distance from the sample

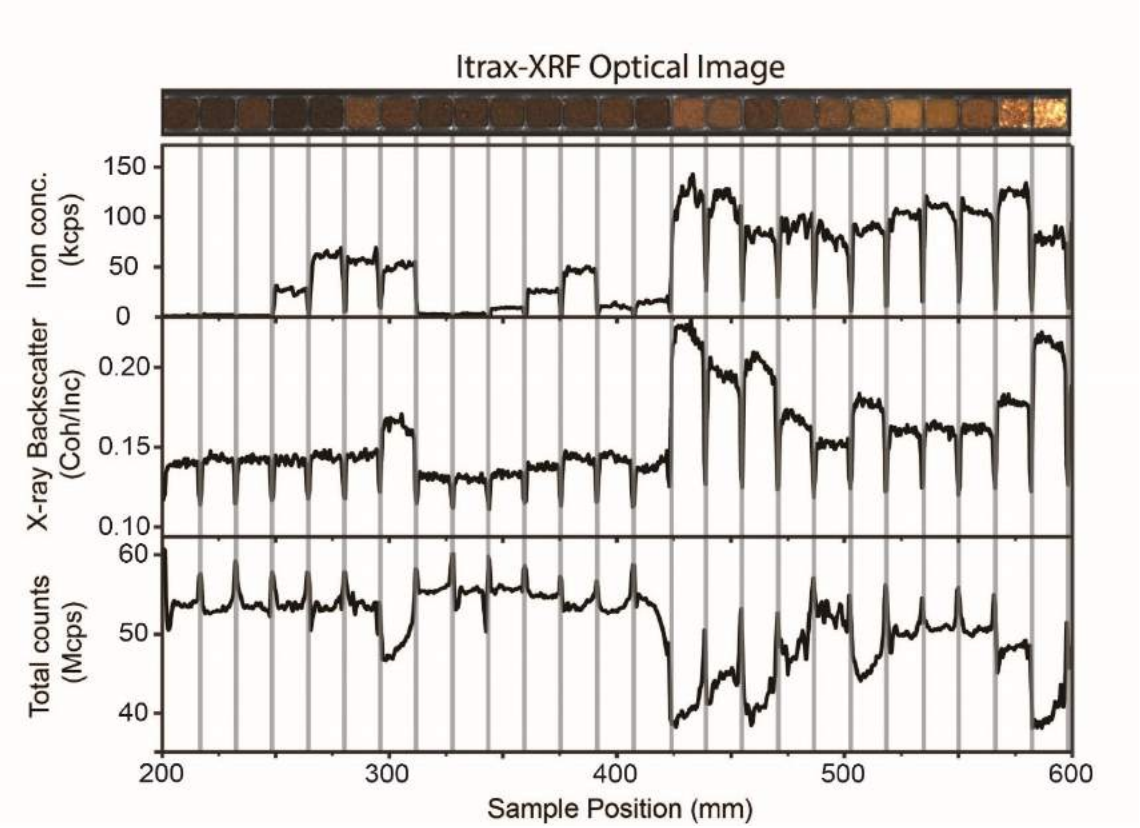

Figure 2.3: Line graphs of changing iron content in thousands of counts per second (kcps; top graph), the ratio of coherent to incoherent x-ray backscatter (middle graph), and total counts in millions of counts per second (Mcps; lower graph) with increase in sample position being analyzed (mm). The photo at the top of the figure shows the optical image of the SSR device loaded with sediment taken by the Itrax core scanner. Abrupt shifts represent analysis of acrylic between compartments of the SSR vessel (indicated in grey). These intervals should be removed before further statistical analysis.

surface and even minor topographic artifacts may induce errors in analysis. To ensure that the plastic dividers between reservoirs are easily identifiable, they should be cleaned before analysis.

Once sediment samples are loaded into the SSR, it is fitted to the rails of the Itrax-XRF (Figure 2.1C). The rails of the Itrax-XRF should be placed at their highest setting and rubber-tubing shims should be added to bring the SSR close to the XRF detector. The compartments must be aligned straight down the center of the rails and taped in place as the XRF beam follows a 2-mm-wide path down the center of the track during analysis. During the surface scan prior to analysis, centering of the sampler can be checked and corrected, if necessary. Once properly centered, analysis can proceed using

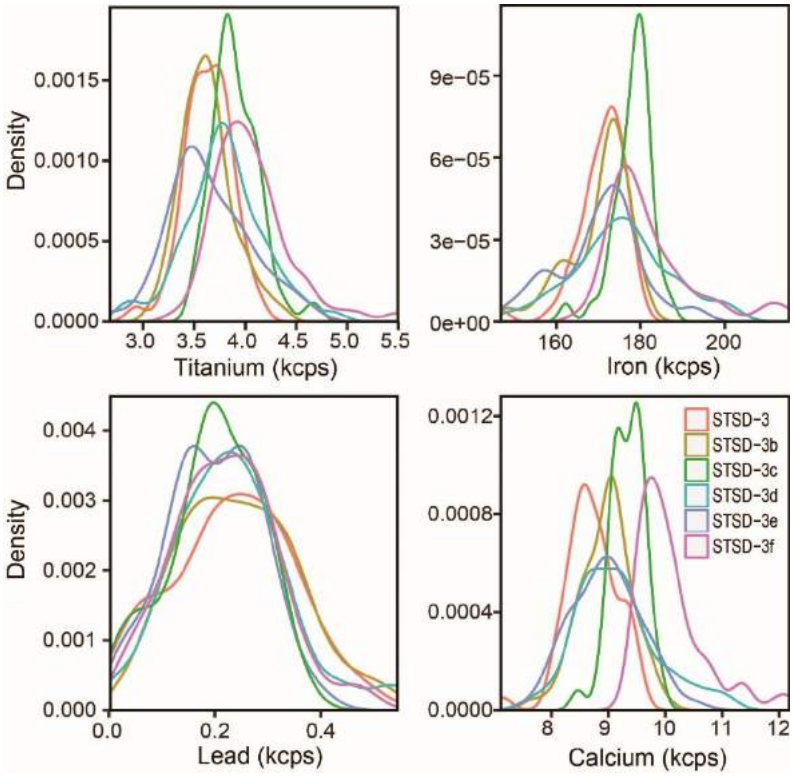

Figure 2.4: Density plots for replicate scans of powdered Geological Survey of Canada Stream Sediment Standard-3 (STSD-3) for calcium, lead, titanium and iron measured in thousands of counts per second (kcps). STSD-3 was added at the start and end of the SSR device when analyzing Harvey Lake surface samples. Elements displayed span lighter elements (Ca, Ti) that have poor detection relative to heavier elements that have better detection (Fe, Pb) by the Itrax-XRF, using a Mo-anode.

standard Itrax operating procedures (Croudace et al. 2006).

2.8 Post analysis data interpretation

Prior to interpreting results, sample measurements must be distinguished from measurements of the acrylic borders that separate the reservoirs. Simple line graphs plotted from the Itrax-XRF results will reveal analytical results associated with the acrylic. The acrylic comprising the SSR compartment walls can be identified readily on the basis of: 1) a significant shift in the total number of counts for a given interval, as the acrylic generally has a density different from sediment and may increase x-ray scatter because of the abundance of lighter elements in acrylic; 2) a major decrease in abundant element concentrations (Fe has proven to be a useful marker in our research); 3) a considerable decrease in the ratio of coherent/incoherent backscatter, which is a proxy for mean atomic

number (Boyle et al. 2015); and 4) knowledge of the length of each compartment (Figure 2.3). Once identified, the SSR compartment-wall data can be removed from the results. We also recommend removing analysis results collected within 1 mm of the acrylic edge, to minimize possible boundary effects. The mean square error (MSE) of measurements made by the Itrax-XRF core scanner can be used to assess whether data were influenced by air pockets close to the compartment walls, caused by settling of sediment, and data points identified as outliers can be removed accordingly. At a sampling resolution of 0.2 mm, a scan of each sample compartment will provide 75 data points in 18.75 minutes at an exposure time of 15 s. Itrax-XRF core scanners allow the user to adjust count time and resolution to increase the speed or accuracy and precision of geochemical results. Summary statistics (*e.g.* mean, median, standard deviation, coefficient of variation, *etc.*) can be calculated for each sample, allowing users to characterize heterogeneity of the surface sample (Figure 2.4). Although samples are partially homogenized by mixing with a spatula after centrifugation and prior to analysis, multiple measurements provide an opportunity to assess intra-sample variation that would be prohibitively expensive with other analytical techniques, and thus offer an advantage over techniques that assume a single measurement is representative of the analyzed sample (ICP-MS, benchtop XRF, WD-XRF).

2.9 Application of the SSR

In summer 2015, 71 sediment-water interface samples were taken from Harvey Lake, York County, New Brunswick, Canada (N45.745°, W67.03°), and analyzed using the SSR at the Itrax-XRF core-scanning facility at McMaster University, Hamilton, Ontario. Samples were analyzed at 0.2-mm resolution for 15 seconds/point at 15 mA and 30 kV, using a Mo-anode x-ray tube in three separate runs. Geological Survey of Canada Stream Sediment Standard 3 (STSD-3) was rehydrated from powdered form, using de-ionized water to achieve a consistency similar to surface sediment samples, and was loaded in SSR compartments at the start and end of each run of Harvey Lake samples. Preparing samples and loading them into the SSR took ~6 hours of active time. Analysis with the Itrax-XRF took ~25 hours and generated >3000 data points after post-processing. Density plots for replicate analysis of STSD-3 show good agreement between peaks, suggesting

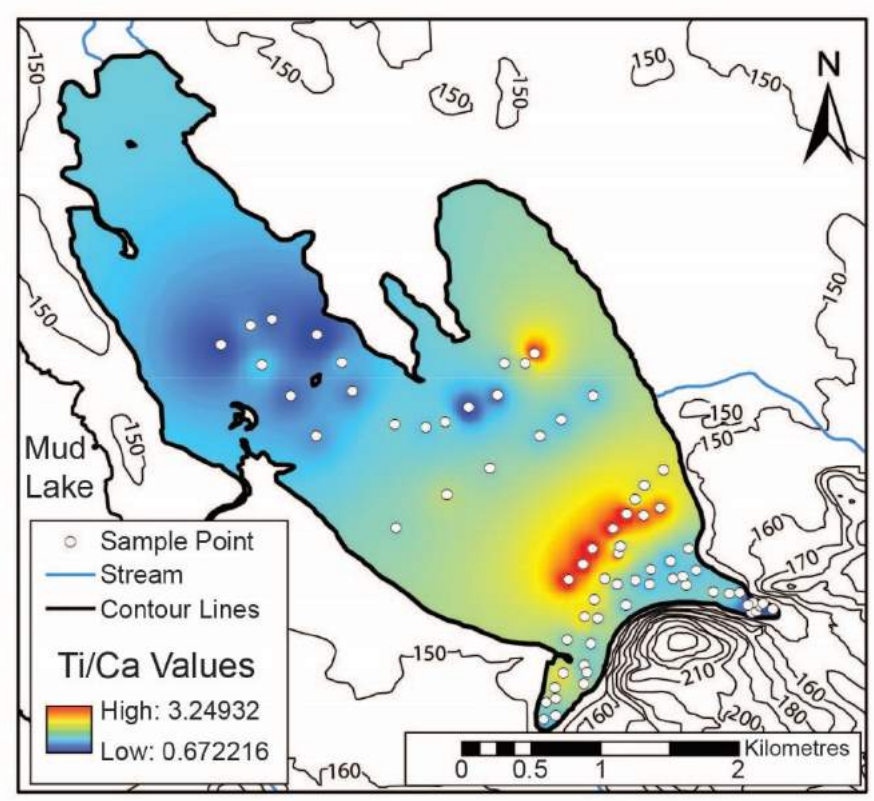

Figure 2.5: Ti/Ca values for Harvey Lake, NB, Canada. Seventy-one surface samples were analyzed using the Itrax-XRF at McMaster University. Values were interpolated using the IDW tool in ArcGIS. Lighter shades of grey represent higher Ti/Ca values, which indicate proportionally higher allochthonous sediment input.

good reproducibility between scans, *i.e.* within expected variations caused by changes in bulk density and water content that may have occurred during rehydration and subsequent drying during analysis (Figure 2.4). Density plots also show near normal distribution, implying that mixing samples with a spatula adequately homogenizes the sediment. Reducing the scan resolution would significantly reduce the required scan time, and based on the results obtained for Harvey Lake, would yield a similar outcome. Figure 2.5 shows Ti values normalized to Ca. Values between sample points were interpolated using inverse distance weighting (IDW). Ti/Ca is a proxy for relative change in allochthonous input as variations Ti can be caused by changes weathering or sediment transport within a given catchment area (Davies et al. 2015). High Ti/Ca values, however, may be a result of variations in Ca content caused by productivity changes across the lake basin (Wetzel 2001; Davies et al. 2015). Elevated Ti/Ca values occur in the southern

basin where a nearby stream and steep hill result in high deposition rates. This may be an ideal site for future paleoenvironmental studies using conventional sediment cores.

2.10 Conclusions

The SSR enables researchers to carry out inexpensive geochemical studies through analysis of discrete sediment samples using the Itrax-XRF core scanner. The use of this durable, easy-to-assemble sample vessel can maximize the spatial resolution of analyzed sediment samples in between- and within-lake studies that seek to characterize the range of lake environmental variability, and allow for more direct comparisons with conventional core analyses that employ the Itrax.

2.11 References

Croudace IW, Rindby A, Rothwell RG (2006) Itrax: description and evaluation of a new multi-function X-ray core scanner. In: Rothwell RG, Rack FR (eds), New techniques in sediment core analysis, Geological Society London Special Publications 267: 51-63

Davies SJ, Lamb HF, Roberts SJ (2015) Micro-XRF Core Scanning in Palaeolimnology: Recent developments. In: Croudace IW, and Rothwell RG, Micro-XRF Studies of Sediment Cores. Springer Science, New York, pp 189-226

Dietze E, Hartmann K, Diekmann B, IJmker J, Lehmkuhl F, Opitz S, Stauch G, Wünnemann B, Borchers A (2012) An end-member algorithm for deciphering modern detrital processes from lake sediments of Lake Donggi Cona, NE Tibetan Plateau, China. Sediment Geol 243:169–180.

Engstrom DR, Rose NL (2013) A whole-basin, mass-balance approach to paleolimnology. J Paleolimnol 49:333-347

Li F, Huang J, Zeng G, Yuan X, Li X, Liang J, Wang X, Tang X, Bai B (2013) Spatial risk assessment and sources identification of heavy metals in surface sediments from the Dongting Lake, Middle China. J Geochem Explor 132:75–83.

Patterson RT, Roe HM, Swindles GT (2012) Development of a thecamoebian (testate amoebae) based transfer function for sedimentary Phosphorous in lakes. Palaeogeogr Palaeoclimatol Palaeoecol 348: 32–44

Pienitz R, Smol JP, Lean DR (1997) Physical and chemical limnology of 59 lakes located between the southern Yukon and the Tuktoyaktuk Peninsula, Northwest Territories (Canada). Can J Fish Aquat Sci 54:330–346

Roe HM, Patterson RT, Swindles GT (2010) Controls on the contemporary distribution of lake thecamoebians (testate amoebae) within the Greater Toronto Area and their potential as water quality indicators. J Paleolimnol 43:955–975.

Rothwell RG, Croudace IW (2015) Micro-XRF studies of sediment cores: a perspective on capability and application in the environmental sciences. In: Croudace IW, Rothwell RG (eds) Micro-XRF studies of sediment cores. Springer Science, New York, pp 1–24

Rühland KM, Smol JP (1998) Limnological characteristics of 70 lakes spanning Arctic

treeline from Coronation Gulf to Great Slave Lake in the Central Northwest Territories, Canada. Int Rev Hydrobiol 83:183–203

Rühland KM, Smol JP, Wang X, Muir DCG (2003) Limnological characteristics of 56 lakes in the Central Canadian Arctic Treeline Region. J Limnol 62:9–27

Tjallingii R, Röhl U, Kölling M, Bickert T (2007) Influence of the water content on X-ray fluorescence core-scanning measurements in soft marine sediments. Geochem Geophys Geosyst 8:1-12

Wetzel R (2001) Limnology: Lake and river ecosystems, 3rd edition. Gulf professional Publishing.

Chapter 3: An evaluation of methodologies for calibrating Itrax X-ray fluorescence counts with ICP-MS concentration data for discrete sediment samples

3.1 Authors and Addresses

Gregory BRB[1], Patterson RT[1], Reinhardt EG[2], Galloway JM[1,3,4], Roe HM[5]

[1]Ottawa-Carleton Geoscience Center and Department of Earth Sciences, Carleton University, 1125 Colonel By Dr., Ottawa, Ontario, Canada, K1S 5B6

[2]School of Geography and Earth Sciences, McMaster University, 1280 Main St. W., Hamilton, Ontario, Canada, K1S 5B6

[3]Geological Survey of Canada/National Resources Canada (Commission géologique du Canada/Ressources naturelles Canada), 3303 33 St. N.W., Calgary AB, Canada, T2L 2A7

[4]Aarhus Institute of Advanced Studies, Aarhus University, 8000 Aarhus C., Denmark

[5]School of Natural and Built Environment, Queen's University Belfast, Belfast, United Kingdom, BT7 1NN

3.2 Foreword

After designing the SSR (Chapter 2), we used the device to analyze discrete sediment samples and test different recommended methodologies of calibration. Although Itrax-XRF offers significant advancements in analytical resolution, the drawbacks of analyzing unprepared sediments have many researchers skeptical of the applicability of the instrument to understand relative and absolute geochemical change in sediment. Calibration of Itrax-XRF data services two purposes: 1) to provide actual values to the semi-quantitative geochemical variations observed in core; and 2) to "ground-truth" geochemical variations to be sure that the observed changes represent actual geochemical changes and are not due to variations in specimen or matrix effects down core. Several researchers have previously attempted calibration of data with varying success. Although direct linear calibration showed some success, recent work has shown applying a correction for shifts in water content or using log-ratios that account for closed-sum effects in the geochemical dataset could improve relationships between Itrax-XRF results and quantitative methods of determining sediment geochemistry. In this paper, we compare different calibrations methods to determine which methods are able to best represent actual geochemical changes in sediment cores. This manuscript, originally published in Chemical Geology, has been modified slightly to meet the formatting requirements of Carleton University, but is otherwise unchanged.

Dr. R.T. Patterson and Dr. H.M. Roe conducted the field work for this study. Dr. E.G. Reinhardt provided technical support and instrumentation for analysis. I prepared and analyzed samples, conducted statistical analyses for comparison of different calibration methods, wrote the manuscript and designed the figures. All co-authors provided feedback and helped to revise the manuscript. This research was funded by a Polar Knowledge Canada grant to Dr. Patterson and Dr. Galloway and a Canadian Foundation for Innovation grant to Dr. Reinhart. It should be cited as follows:

Gregory BRB, Patterson RT, Reinhardt EG, Galloway JM, Roe HM. (2019). AN evaluation of methodologies for calibrating Itrax X-ray fluorescence counts with ICP-MS concentration data for discrete sediment samples. *Chemical Geology*.

3.3 Abstract

Core-scanning X-ray Fluorescence (XRF-CS) is a well-established technique for rapid (< 30 s/interval) analysis of sediment core geochemistry at sub-mm resolution with substantially less analytical cost compared to methods that rely on physical sub-sampling. Due to issues inherent in analyzing wet sediment of heterogeneous particle size and composition with irregular surface topography using XRF, XRF-CS results are generally considered semi-quantitative. The result of early efforts to calibrate XRF-CS data with conventional geochemical results (*e.g.* WD- or ED-XRF, ICP-AES, ICP-MS) showed weak correlations for less abundant or poorly detectable elements, however, more recent methods have been proposed to improve accuracy. These methods include: 1) converting XRF-CS results to dry mass concentration; 2) normalizing XRF-CS data to conservative elements (Si, Ca), total counts/second, or X-ray scatter (CIR); and 3) calibration of data using multivariate analysis of elemental log-ratios (MLC). These approaches are not yet widely employed, and require additional testing on a variety of sediment compositions. Recently developed equipment enables analysis of discrete sediment samples, providing >30 replicate analyses for up to 180 samples in a single XRF-CS run. These replicate measurements allow for rigorous testing of precision and accuracy of XRF-CS data. To determine the ideal method of data transformation to improve XRF-CS calibration to quantitative geochemical concentration, 100 lake sediment-surface samples collected from Harvey Lake, New Brunswick, Canada, were analyzed using Itrax-XRF-CS, and then with ICP-MS analysis after multi-acid digestion. Normalization using the CIR and correction for water content showed strong correlation coefficients (Kendall's τ) for elements with atomic number >18 and high concentrations in the sediment. Results for lighter elements and those with lower concentrations did not perform well using these calibration methods. The MLC provided the most accurate reproduction of observed ICP-MS trends and strong correlations (R) between predicted and actual geochemical concentrations. Based on these results, CIR-normalized or wet-corrected calibrations are ideal for studies where absolute geochemical values are of lesser importance, and the MLC method is appropriate for studies with large numbers of sediment samples (n > 100), or those where absolute concentrations of elements are of greater importance.

3.4 Introduction

The use of high-resolution, non-destructive, X-ray fluorescence core scanners (XRF-CS) has become commonplace in the study of paleoenvironments and paleoclimate (Turner et al. 2010; Giralt et al. 2011; Gregory et al. 2015; Profe et al. 2016; Peros et al. 2017), sediment provenance (Kujau et al. 2010; Hunt et al. 2015; Zielhofer et al. 2017) and soil and sediment contamination (Guyard et al. 2007; Miller et al. 2015; Rodríguez-Germade et al. 2015; Lintern et al. 2016; Schillereff et al. 2016). X-ray fluorescence core scanners are capable of analyzing sediment cores at up to 0.1 mm resolution at < 30 s per interval, offering a major advantage in speed, cost, and resolution over conventional geochemical analysis (ED- or WD-XRF, ICP-MS, INAA). A consequence of this rapid, high-resolution analysis is loss of geochemical accuracy and precision (Tjallingii et al. 2007; Hennekam and de Lange 2012; Maclachlan et al. 2015). Traditional XRF analysis uses sediment which is ground to homogenous particle size and either fused to glass beads or compressed into a puck with a smooth surface to minimize matrix and specimen effects (International Atomic Energy Agency 1997; Weltje and Tjallingii 2008). XRF-CS measurements can be influenced by heterogeneities in the sample surface, such as an uneven topography or variation in particle size (specimen effects), or by reabsorption, re-emission and scattering of primary X-radiation by some component of the sediment being analyzed, such as interstitial water content, sediment porosity, or the sediment itself (matrix effects; Croudace et al. 2006; Tjallingii et al. 2007; Maclachlan et al. 2015). Additional issues arise due to matrix effects influencing different elements to different degrees, with lighter elements commonly experiencing more pronounced deviations from actual geochemical values compared to heavier elements (Tjallingii et al. 2007). XRF-CS data are thus considered semi-quantitative, particularly for light elements.

Analysis of sediment using ICP-MS is relatively expensive and often requires large sample volumes for standard commercial analysis, which can restrict the resolution of temporal or spatial studies, and it is time consuming in terms of sampling. Many researchers therefore use XRF-CS data to examine relative changes in elemental concentrations at high resolution in core samples while using conventional geochemical analysis of select samples to accurately determine absolute geochemical values. In environmental studies, XRF-CS is used to identify the timing of impacts, or the spatial

and temporal extent of contaminated horizons, which are then verified using conventional geochemical results (Guyard et al. 2007; Miller et al. 2015; Rodríguez-Germade et al. 2015; Lintern et al. 2016; Schillereff et al. 2016). If it were possible to obtain more reliable geochemical values using XRF-CS, it would represent an enormous advancement in the ability of researchers to study environmental systems, contamination, and high-resolution climate events in terms of rapidity and cost-effectiveness.

Since the introduction of the first XRF-CS in 1998, researchers have attempted to calibrate XRF-CS data to total elemental concentrations derived from conventional geochemical analytical methods (Jansen et al. 1998). Early attempts that used linear regression to convert XRF-CS data to absolute concentrations showed substantial scatter about regression lines. These variations in data distribution were likely due to matrix and specimen effects that impacted elemental detection by XRF in a non-linear fashion, making it difficult to correct for their influence (Kido et al. 2006). Several methods for reducing the influence of matrix and specimen effects before calibration or interpretation have been developed. These methods can be broadly categorized into three groups: 1) correction for a variable that cannot be measured directly by XRF-CS, typically water or organic content (Tjallingii et al. 2007; Boyle et al. 2015; Chen et al. 2016); 2) normalization of data to a variable measured by the XRF-CS device, such as a conservative element, X-ray scatter, or total counts per second (Wei et al. 2004; Guyard et al. 2007; Turner et al. 2010; Bouchard et al. 2011; Cuven et al. 2011; Kylander et al. 2011; Löwemark et al. 2011; Berntsson et al. 2014; Chawchai et al. 2016); and 3) data transformation aimed at normalizing or scaling data, such as log-normalized (Weltje and Tjallingii 2008; Hennekam and de Lange 2012; Weltje et al. 2015) or median-normalized calibration methods (Lyle and Backman 2013; Lyle et al. 2014; Shackford et al. 2014). Application of these methods has generally resulted in stronger correlations and reduced scatter in linear regressions, yet they have not yet been widely adopted, and still need to be tested on a variety of substrate types.

Although XRF-CS is designed for analysis of split cores, recent studies have begun to adapt core scanners for other purposes including the analysis of discrete samples. A study by Huang et al., (2016) analyzed discrete sediment standards to determine optimal

count times for XRF-CS. Profe et al. (2017) analyzed discrete sub-samples of a 20-m loess-paleosol sequence from Hungary to characterize climatic changes in the region. Gregory et al. (2017) developed the design specifications and recommendations for use of a discrete sample holding device that could accommodate up to 180 sediment samples for analysis using the Itrax-XRF-CS (Sequential Sample Reservoirs - SSR). Analyzing discrete sediment samples using XRF-CS has the potential to enable rapid characterization of sediment geochemistry. The resultant reduced analytical costs can increase both the scale and resolutions of research projects. Discrete sediment samples are ideal for testing calibration methods as they do not exhibit geochemical variations inherent to sediment cores caused by temporal changes in sedimentation and allow for multiple measurements of each sample. This permits for a more direct comparison to the larger, homogenous samples analyzed using conventional geochemical techniques, and enables evaluation of analytical precision that is difficult to quantify when attempting XRF-CS calibration using core samples.

To compare the accuracy of various existing calibration methodologies on XRF-CS data using discrete sediment samples, we obtained 100 sediment-water interface samples from Harvey Lake, New Brunswick, Canada. Representatives from the Harvey Lake Association, the New Brunswick Alliance of Lake Associations, and the adjacent Village of Harvey Station are interested in assessing the current and past health of Harvey Lake to elucidate how any contamination risks may hinder the lakes' recreation use by locals and tourists visiting the region due to the occurrence of a major cyanobacterial bloom in Harvey Lake during the summer of 2016. The ability to quantify the spatial variability in metal concentrations in lacustrine environments would be of considerable utility in identifying contaminants that pose a health risk, and facilitates detection of contaminations sources. Harvey Lake is a typical lake found in developed regions: a relatively small water body, irregular in shape, with moderate depth (~ 11 m),

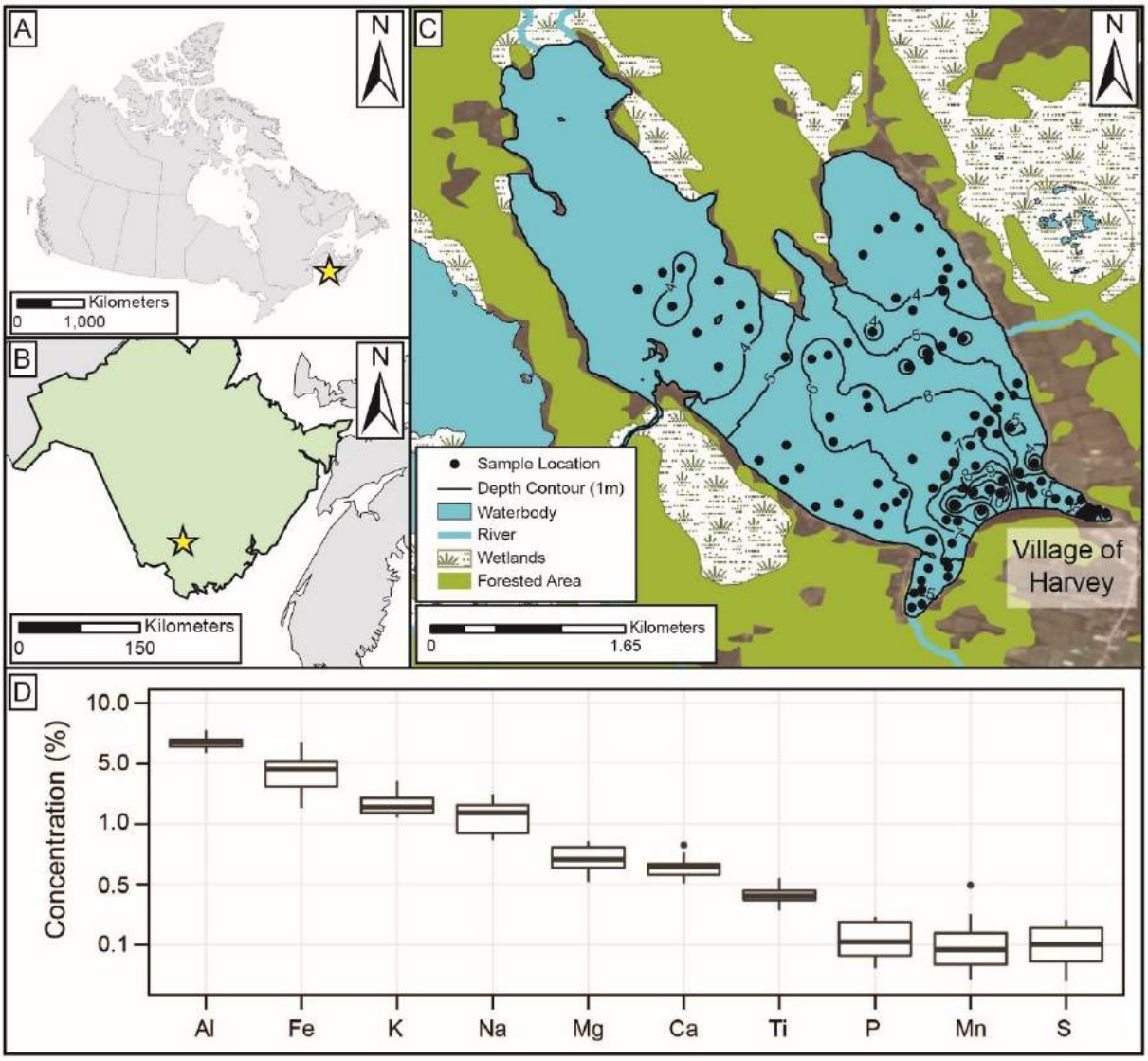

Figure 3.1: The location of Harvey Lake within Canada (A), and within New Brunswick (B). (C) Shows the location of surface sediment samples within Harvey Lake as well as important locations around Harvey Lake. Bathymetry contours at 1-m depth intervals interpolated using depths of sediment samples are shown with black lines. (D) Boxplot of elemental concentration of 10 most abundant elements in sediment determined through ICP-MS.

and varied land use around the periphery (natural, recreational, residential and formerly industrial). It is thus an ideal site for testing calibration methods.

3.5 Methods

3.5.1 Study Area and Sample Collection

Harvey Lake (45°43′45″ N, 67°00′25″ W) is irregularly shaped, has a surface area of 6.9 km^2, was non-thermally stratified during late summer sample collection, and has a maximum depth of 11 m (Figure 3.1). Water flows into this lake from one stream in the south-western cove of the lake, and from another stream in the middle of the eastern shore. There is a small outflow on the middle of the western shore where water flows to the adjacent Mud Lake (Figure 3.1). Harvey lake is surrounding by wetlands and forest on the western, northern and eastern shores, with a strip of cottages running the length of the eastern shore. The Village of Harvey Station is just south of the lake adjacent to Cherry Mountain, a ~100 m topographic high at the southern end of the lake. The northern portion of Harvey Lake is underlain by Silurian- to Devonian-aged sedimentary rocks including red sandstones, conglomerates and shales (Bottomley1984; Payette and Martin 1986). The southern end of the lake is underlain by Mississippian volcanic rocks including rhyolitic lava flows, and ash-fall/ash-flow tuffs that outcrop on Cherry Mountain (Bottomley 1984; Payette and Martin 1986). One hundred samples (HV-01 too HV-100) were collected from the sediment-water interface using an Ekman grab sampler in September, 2016. Sample locations were recorded using a Garmin GPSMAP 76CSx GPS. The upper 0.5 cm of sediment collected was sampled into plastic bags using a plastic spoon. Sediment samples were stored in coolers for transport to Carleton University for subsequent analysis.

3.5.2 Laboratory methods

The Harvey Lake samples were divided into sub-samples for laboratory analysis. For ICP-MS analysis, sediment was homogenized with a spatula, then ~10 mL of sediment were subsampled into 50 mL falcon centrifuge tubes and sent to Bureau Veritas, Vancouver, BC, where the sediment was dried, ground to a homogenous powder and digested using a multi-acid wash before analysis (DYAIR, PULCB, and MA250 packages). Bureau Veritas measured 10 % of samples in triplicate as well as two quality control standards

OREAS45E and OREAS25A-4A, to ensure accurate analysis. All elements studied were within two standard deviations of certified elemental concentrations. The use of multi-acid wash ensured that the results of this analysis best represent whole rock geochemistry measured by XRF-CS (Parsons et al. 2012). A total of 48 samples were analyzed using ICP-MS, of which 28 were unique sediment samples, with 10 being analyzed as blind triplicates for statistical control purposes. Sub-samples selected for ICP-MS evenly covered the area sampled, and included all sediment lithologies observed in samples. Sediment was typically dark-brown, organic-rich gyttja, with only a few samples collected nearer the periphery and the south-east corner of the lake showing slight increases in silt and sand content. Full results from ICP-MS analysis are available in Gregory et al. (2018a).

Preparation of subsamples for XRF-CS followed Gregory et al. (2017). Sediment was stirred using a spatula to homogenize material, then approximately 20 mL of wet sediment (more for watery samples) was subsampled into 50 mL falcon tubes, centrifuged at 4000 rpm for 4 minutes and the supernatant decanted; if time allows, samples can be dried at room temperature to the required consistency to ensure no material is lost during decanting of samples. Each sample was covered to minimize the possibility of contamination, and then left at room temperature to dry until sediment samples reached a paste-like consistency that enables easy loading and reduces the risk of cross contamination (Gregory et al. 2017). The dried samples were transported to the McMaster University Core Scanning Facility, homogenized by stirring with a spatula, loaded into an acrylic SSR (1 x 1 x 1.5 cm = 1.5 cc), and analyzed using a Cox Analytics Itrax core scanning X-ray fluorescence (Itrax-XRF-CS) device. Some sediment samples did not completely fill sediment reservoirs in the SSR. In these cases, the excess lateral volume was filled with phenolic plastic foam (Oasis Floral Foam) to ensure that the sediment surface did not subside during scanning as this can cause inaccuracies in the XRF-CS analysis. Samples were analyzed using a Mo-anode X-ray tube at 30 kV and 19 mA at 0.2 mm resolution for 15 seconds per interval. These parameters were selected as they represent the typical settings for Itrax-XRF-CS analysis of lacustrine material. Although count time, scanning resolution, or XRF voltage/amperage may be modified if experimental design has a specific goal (*e.g.* detection of rare earth elements [Hennekam

et al. 2018]), the results presented here are meant to inform typical XRF-CS researchers as to the best methods for calibration under normal conditions. Subsequent to analysis, the Itrax-XRF-CS results were batch analyzed using RediCore software created by Cox Analytical Solutions. The ICP-MS analysis results in conjunction with known XRF-CS elemental detection limits were used to inform the selection of elements for batch analysis using RediCore. Processed XRF-CS results are available in Gregory et al. (2018b).

Once the non-destructive XRF-CS analysis was complete, sample water content was measured. Material was extracted from the SSR, placed into pre-weighed crucibles, and the wet weight of sediment was measured using a Sartorius BP 121 S scale. Material was placed in a 110 °C oven for 24 hours then weighed again to determine the dry weight. The difference between wet and dry weight was considered to be the weight % water content of the sample (Heiri et al. 2001). The organic matter content in each sample was derived using loss on ignition (LOI; after Heiri et al. 2001). Approximately 5 cm3 of sediment was placed into a weighed crucible, dried in an oven at 110 °C, and then combusted at 550 °C for four hours, with the sample being weighed between each step. The difference between dry weight and weight after combustion was considered to be the weight % of organic matter in the sample. Data regarding water and organic content in sediment are available in Gregory et al. (2018c).

3.5.3 Analytical methods

XRF-CS sediment data were isolated from the extraneous measurements of the SSR acrylic reservoir dividers and floral foam before calibration attempts. Gregory et al. (2017) were able to easily discriminate acrylic dividers from sediment on the basis of the abrupt shifts in the ratio of coherent to incoherent X-ray scatter (CIR), known width of the acrylic compartment walls, total counts per second (kcps), and abundance of the elements (Fe and Ca) in sediment. Subsequent to removal of the non-sediment XRF-CS data points, at least 15 and up to 67 discrete sample measurements remained for each sample depending on whether or not floral foam had been required to fill excess space in sample reservoirs. The median XRF elemental values obtained for each sample were taken as a measure of central tendency because several elements, notably those nearer instrument detection limits, showed non-normal distributions. The relative standard deviation (RSD),

expressed as percent relative to them mean value of an elements, was calculated after the formula:

$$(1)\ \%\ \mathrm{RSD}_{jn} = \frac{\sigma_j}{\mu_j} \times 100$$

Where σ is the standard deviation of element *j* for sample *n*, and μ is the mean of element *j* for sample *n*. To express the relative standard deviation of elements in the XRF-CS dataset, the mean of the relative standard deviation across all samples was used.

The standard deviation for triplicate measurements of elemental concentration using ICP-MS was calculated using the following equation (Mccurdy and Garrett 2016):

$$(2) \qquad \sigma_j = \sqrt{\left(\frac{\sum_{i=1}^{3}\left(x_{ijn} - \mu_{jn}\right)^2}{3N}\right)}$$

where *x* represents replicate measurement *i* for element *j* in triplicate set *n*, μ represents the mean concentration of element *j* in a triplicate set *n*, and N equals the total number of triplicate sets measured. The RSD of elements for ICP-MS data was calculated following equation (1); μ_j was considered the mean of all triplicate measurements for element *j*.

3.5.3.1 Simple Linear Calibration

All 28 unique ICP-MS sample measurements were compared to Itrax-XRF values and a linear equation was derived on an element-by-element basis after the formula:

$$(3) \qquad \mathrm{W}_{ij} = a_j + \mathrm{I}_{ij} B_j$$

where W_{ij} represent the weight proportion of element *j* at interval *i*, I_{ij} represents the XRF-CS-measured concentration of element *i* at interval *j*, a_j represents the y intercept of element *j*, and B_j the slope of the regression line for element *j*. Correlation between ICP-MS and XRF-CS data was examined using Kendall's Tau (τ) as data were non-normally distributed.

3.5.3.2 Cox Analytics Q-Spec Calibration

Cox Analytics Qspec software was used for the batch evaluation of XRF-CS results and to calculate absolute concentrations (ppm or weight %) of analyzed XRF-CS data based

on results of previous XRF-CS analysis of geological standards. To test the accuracy of this automated calibration in comparison to other recommended methods, the XRF-CS data from the Harvey Lake samples were calibrated using Qspec software. Whereas typical calibration methods (*e.g.* Jansen et al. 1998; Boyle et al. 2015; Weltje et al. 2015; Chen et al. 2016) require analysis of sediment using conventional geochemical techniques as well as XRF-CS, calibration using Qspec software requires no additional analysis for conversion of XRF-CS results to absolute concentrations as it bases calibration equations on elemental standards previously measured using XRF-CS. The XRF-CS results were converted to absolute concentrations using the Green River Shale standard (USGS SGR-1). The median value of each element in each sample was taken as a measure of central tendency. The results were then compared to the ICP-MS values using linear regression and Kendall's τ; no calibration equation was derived. Qspec-calibrated XRF-CS results are available in Gregory et al. (2018d).

3.5.3.3 Normalized Calibrations

It is common practice to normalize XRF core-scanner data to a conservative element (Wei et al. 2004; Guyard et al. 2007; Turner et al. 2010; Löwemark et al. 2011; Chawchai et al. 2016), or other variables measured by Itrax-XRF-CS, such as total counts per second (kcps; Turner et al. 2010; Bouchard et al. 2011; Cuven et al. 2011; Haenssler et al. 2013), or X-ray scatter (Kylander et al. 2011; Marshall et al. 2011; Berntsson et al. 2014). In theory, such normalization procedures should minimize the influence of matrix and specimen effects that are known to affect XRF-CS measurements, as both the element of interest and the normalization variable should be subject to similar matrix/specimen effects at every measured point. Thus, normalized XRF-CS data should better approximate actual sediment geochemical concentrations measured by conventional geochemical analysis than raw XRF-CS data. Itrax-XRF-CS data were normalized to variables commonly used in XRF-CS research (Si, Ca, kcps and CIR). Silicon and Ca were selected for calibration over other elemental denominators as they are relatively insensitive to redox changes, are abundant in most lacustrine settings, and have been shown in other studies to be ideal denominators for calibration (Weltje and Tjallingii 2008). Normalized XRF-CS results were compared to ICP-MS data to derive linear equations using a formula similar to (3) above:

$$W_{ij} = a_j + (I_{ij}/I_{ki})B_j \quad (4)$$

where I_{kj} represents the value of normalization factor *k* at interval *i*. Correlation coefficients between normalized XRF-CS data and ICP-MS were calculated using Kendall's τ.

3.5.3.4 Water Content Correction

Several authors have recognized the problem of water content in a sample resulting in the attenuation of the XRF signal, both due to interstitial water, and a thin film of water that occurs between the sediment surface and the thin mylar film placed on the core before scanning (Kido et al. 2006; Tjallingii et al. 2007; Boyle et al. 2015). Studies have shown that accounting for water content improves the relationship between the XRF-CS and conventional geochemical data (Kido et al. 2006; Tjallingii et al. 2007; Hennekam and de Lange 2012; Boyle et al. 2015; Chen et al. 2016). Following Boyle et al. (2015), we derived an equation for determining the water content observed at each point by comparing the water content of the surface samples post XRF-CS-analysis to median values of CIR for all samples. Although Boyle et al. (2015) converted geochemical values to wet percent and then compared these wet values to XRF-CS data to derive calibration equations, we alternatively converted the XRF-CS values to dry mass concentrations for comparison to dry mass ICP-MS data. The procedure was carried out using the equation provided by Boyle et al. (2015)

$$D_{ji} = I_{ji}(100/100 - \omega_i) \quad (5)$$

where D_{ji} represents the dry mass concentration of a given element *j* at interval *i* as measured by XRF-CS, and ω_i represents the percent dry mass at interval *i*. At each interval measured by XRF-CS, ω was calculated based on linear regression between median values of CIR for each surface sample and the weight % water content as measured in the lab following the formula:

$$\omega = a_{ij} + (CIR_i)B_{ij} \quad (6)$$

where CIR is the ratio of coherent to incoherent X-ray scatter measured by the Itrax-XRF-CS at interval *i*. After raw XRF-CS data was corrected for water content using formula (5), median values of sediment were taken from the wet-corrected XRF-CS data and

compared to ICP-MS data to create elemental calibration equations using formula (3) above. Kendall's τ was used to exam correlation the two datasets.

3.5.3.5 Multivariate Log-ratio Calibration

Wetlje et al. (2015) developed a multivariate method of calibrating XRF-CS data based on the use of log ratios. Alongside recommendations on how to best approach this new multivariate log-ratio calibration (MLC) method, Weltje et al. (2015) created the program ItraXelerate to automatically perform the calibration. The ItraXelerate software uses data from replicate measurements of sediment analyzed using XRF-CS and conventional geochemical methods to calculate absolute geochemical concentrations of select elements. As the XRF-CS data from the Harvey Lake samples represents multiple measurements of the same sample, and as Weltje et al. (2015) recommend at least triplicate scans of several intervals throughout the core, three new XRF-CS datasets were created based on the original XRF-CS data. Three measurements were randomly sampled (with replacement) from each sediment sample output and placed into a new XRF-CS dataset. This process was repeated three times to create triplicate datasets for each discrete sample. As ItraXelerate was designed for use with XRF-CS core data and not discrete samples, each data point within the triplicate datasets was by necessity assigned an arbitrary depth starting at 0 mm for the first point in the dataset and increasing by an interval of 10 mm for each subsequent data point. For example, the triplicate data from HV-01 were assigned the depths 0, 10, and 20 mm, and data from HV-02 were assigned depths of 30, 40 and 50 mm. These three XRF-CS datasets were compared to the ICP-MS dataset containing triplicate analysis of roughly 30 % of samples. Each ICP-MS sample was assigned a depth corresponding to the centroid of the depths for the same sediment sample in the XRF-CS datasets (*i.e.* the ICP-MS depth of HV-02 would be 40 mm). An additional alteration to ICP-MS data was necessitated prior to loading the Harvey Lake ICP-MS data into the ItraXelerate software. The ItraXelerate software will not load geochemical data that are missing elements always observed in conventional XRF analysis as it was originally designed for comparison of ED or WD-XRF to XRF-CS. As ICP-MS does not detect silicon, and because this element is so ubiquitous as to almost always be found in XRF analysis of sediment, ItraXelerate would not load the ICP-MS dataset from Harvey Lake with zero values for SiO_2. Therefore, an arbitrary value of

0.00001 ppm SiO_2 was substituted into our ICP-MS dataset for all sediment samples analyzed.

ItraXelerate measures the accuracy of calibrations using a goodness-of-fit measurement (R) that uses the mean squared Euclidean distance between predicted and measured compositions (*i.e.* distance of a given point from the regression line; Weltje et al. 2015). Based on the recommendations of Weltje et al. (2015) the number of elements calibrated should equal roughly one third the number of ICP-MS samples analyzed, rounded down. Nine elements can therefore be calibrated from our 28 ICP-MS samples. As this study is meant to act as a foundation for future paleolimnological work, common elements used as paleolimnological proxies were select for calibration (Al, Ca, Ti, Mn, Fe, Zn, K) alongside an element of interest for Harvey Lake (As). Copper was also added as, in spite of the fact that it occurred in concentrations much higher than the detection limit of Itrax-XRF-CS, it performed poorly in initial experimental calibrations using the MLC method. ItraXelerate automatically calculated elemental concentrations in proportions that summed to unity. The actual proportion of sediment that the nine selected elements comprised was near to 9.8 % on average. As such, XRF-CS concentrations output by ItraXelerate where multiplied by the mean proportion of sediment samples comprised by the nine selected elements (0.098) to facilitate comparison with ICP-MS data.

3.6 Results

Analysis of sediment using ICP-MS detected 44 elements representing a median value of 11.6 weight percentage of sediment (Gregory et al. 2018a). Of this ~11 %, Al, Fe, K, Na, Mg, Ca, Ti, P, Mn, and S comprised a median proportion of 99.1 % of the measured distribution of elements. Samples were consistently co-dominated by Al (median = 4.75 %) and Fe (median = 2.86 %), followed by K (median = 1.38 %), Na (median = 1.23 %), Mg (median = 0.51 %), Ca (median = 0.44 %), Ti (median = 0.25 %), P (median = 0.11 %), Mn (median = 0.09 %) and S (median = 0.06 %; Figure 3.1D). Elemental composition of samples remained relatively stable, with similar elemental dominance structure observed in all samples across the basin. The relative standard deviation of elemental concentrations within samples showed a median of 21. 9 %, although S and Al were notable exceptions with a relative standard deviation of 91.3 % and 4.92 %, respectively.

Based on comparison of Itrax-XRF-CS detection limits and ICP-MS results, as well as working to maximize the fit between observed and predicted XRF spectra, 28 elements were detected in Harvey Lake sediment using XRF-CS, including Al, Si, P, Cl, Ar, K, Ca, Ti, V, Cr, Mn, Fe, Ni, Cu, Zn, Ga, As, Rb, Sr, Y, Zr, Ce, Sm, Tm, Yb, Ta, W, and Pb (Gregory et al. 2018b). The parameters set in preliminary analysis of the sum spectra where applied to each interval analyzed and re-evaluated using QSpec software, which automatically determined ideal XRF parameters for each interval through 10 iterations of a pre-programmed wiggle-fitting procedure. The MSE value for the resultant dataset after plastic sections were removed ranged from 0.92 to 2.42 (median = 1.12, n = 4270). Of the 28 elements detected in the sum spectra, 12 were selected for discussion to represent elements with low detectability and high abundance (Al), moderate- to high-detectability and high abundance (K, Ca, Ti, Fe, Mn, Zn), and moderate- to high-detectability and low abundance (Cu, Ni, Zr, As, Ce; Table 3.1).

3.6.1 Raw XRF-CS

Comparison of raw-XRF-CS data to ICP-MS values (n = 28) showed weak to moderate positive Kendall's τ ($0.3 < \tau < 0.6$) for most elements (Table 3.2). Copper and Ce were the only two elements that showed negative correlations. Arsenic showed the strongest correlation observed ($\tau = 0.69$), followed by K, Ca, and Fe ($\tau_K = 0.59$, $\tau_{Ca} = 0.55$, $\tau_{Fe} = 0.52$; n = 28). Aluminum had a weak positive correlation ($\tau = 0.26$). Despite moderate correlations, several elements showed considerable deviation from inferred linear relationships (Figure 3.2, A1.1).

3.6.2 Qspec Calibration

In comparison to the raw-XRF-CS data, Qspec-corrected data show slightly weaker correlations to ICP-MS results (n = 28), although the observed decrease in correlation was often minor (Table 3.2, Figure 3.2, A1.2; Gregory et al. 2018d). For example, Ca decreased from $\tau = 0.55$ to 0.51 and Al from $\tau = 0.26$ to 0.24 from the raw-XRF-CS data to Qspec-Calibrated data, respectively. Kendall's τ for a select few of the elements (As, Ni, and K) did increase, but this change was minor. Almost one third of all the elements analyzed, including Cu, Ti, and Ce, showed negative correlations.

Table 3.1: Depiction of the ability of Itrax-XRF-CS to detect elements versus their concentration in sediment based on median ICP-MS concentrations for all elements included in XRF-CS analysis. Elements included for the comparison of different calibration methods are shown in bold. Argon, Si and Cl are excluded from the table as they were not included in the suite of elements analyzed using ICP-MS

		Itrax-XRF-CS Detection Limit		
		High (<10 ppm)	Moderate (<100 ppm)	Low (>100 ppm)
Concentration in Sediment	High (>1 %)	**Fe**	**K**	**Al**,
	Moderate (100 ppm	**Mn**	**Ca**, **Ti**	P
	Low (<100 ppm)	**Ni**, **Cu**, **Zn**, Ga, **As**, Rb, Sr,	V, Cr, Y, **Zr**, **Ce**, Sm, Tm, Yb, Ta, W, Pb	

3.6.3 Water Content Correction

Comparison of the coherent/incoherent X-ray scatter ratio (CIR) to percent dry mass measured immediately after XRF-CS analysis showed a strong, positive correlation (τ = 0.79, n = 66), with little scatter about the regression line (Figure 3.3). Although Boyle et al. (2015) used X-ray scatter as a proxy for water content, several authors have suggested that X-ray scatter can be used as a proxy for organic content (Brown et al. 2007; Sáez et al. 2009; Burnett et al. 2011; Giralt et al. 2011). Comparison of LOI-derived organic content to CIR (the inverse of more commonly used Incoherent/Coherent ratio) showed a moderate strength negative correlation (τ = - 0.43, n = 61), suggesting a weaker influence of organic matter on X-ray scatter in samples (Figure 3.3; Gregory et al. 2018d). Organic matter comprises a much smaller proportion of sediment than water content. Based on the a_j and B_j values derived from comparison of percent dry mass to CIR, the raw Itrax-XRF-CS data were adjusted at each measured interval to account for variations in water content. After correction for changes in water content within samples, Kendall's τ correlations for all elements became much stronger, with half of the samples showing

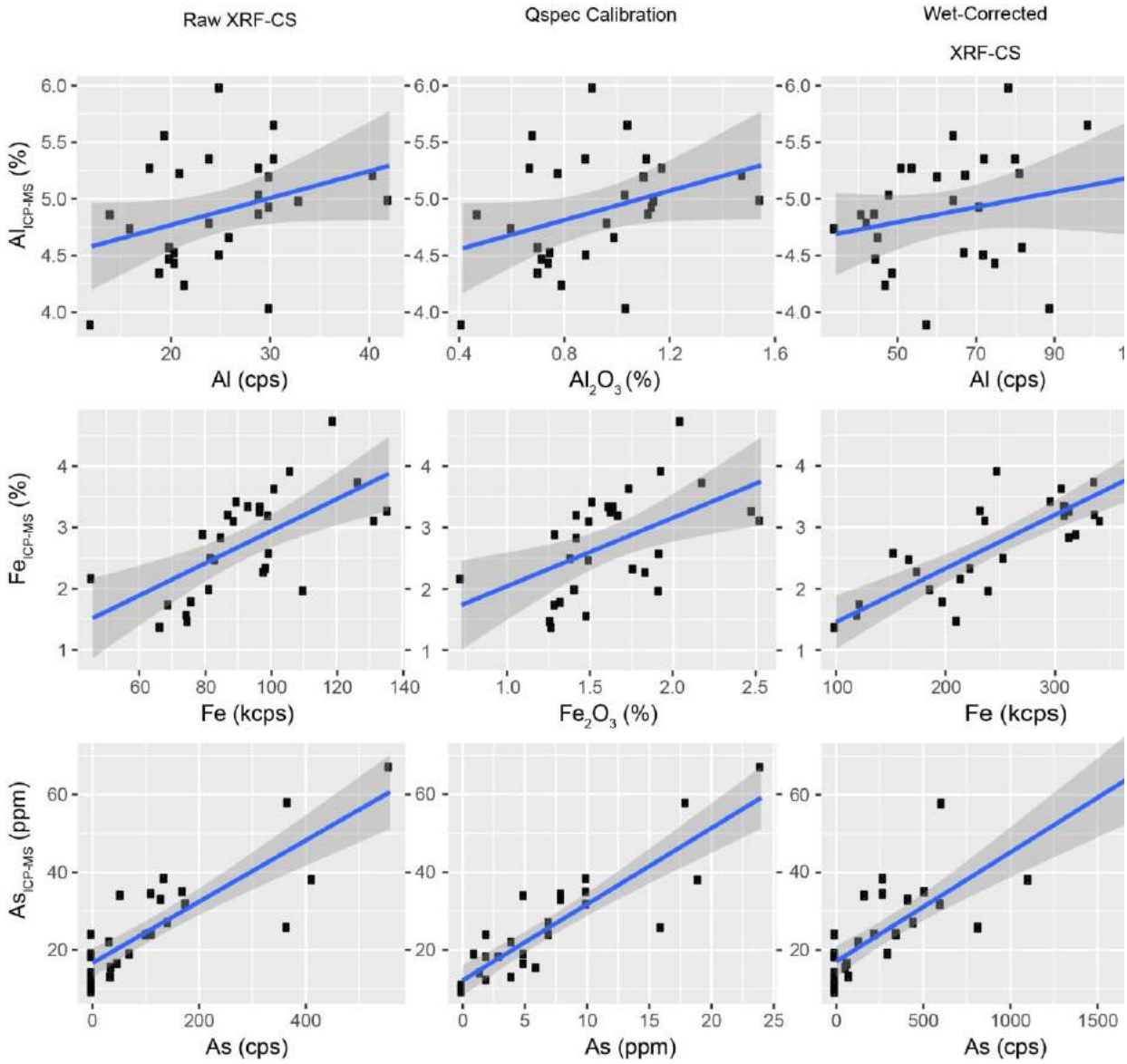

Figure 3.2: Linear regressions comparing raw XRF-CS data (left column), data calibrated using Qspec software (middle column) and data corrected for water content after Boyle et al., (2015; right column) to ICP-MS-derived elemental concentrations. Regression lines are represented by blue lines surrounded by darker grey shaded area indicating 95 % confidence interval of regression. Only select elements (Al, Fe, As) are compared here, see Supplementary Figures A1.1–1.3 for regression of all elements included in XRF-CS analysis.

Table 3.2: Kendall's τ correlations between raw, Q-spec calibrated, and wet-corrected XRF-CS data and ICP-MS results. Mean elemental abundances were calculated using ICP-MS data. Blue values indicate an increase in Kendall's τ value from raw-XRF-CS data, red values indicate a decrease in Kendall's τ value. Detection limits shown are based on analysis of USGS standard SGR-1.

Element	Detection Limit (ppm)	Mean Elemental Abundance	Atomic Number	Raw XRF-CS	Qspec XRF-CS	Wet-Corrected XRF-CS
Al	7704	4.8 %	13	0.26	0.24	0.25
K	43	1.5 %	19	0.59	0.64	-0.15
Ca	27	0.43 %	20	0.55	0.51	0.39
Ti	13	0.26 %	22	0.06	-0.03	0.44
Mn	7	940 ppm	25	0.35	0.29	0.82
Fe	6	2.7 %	26	0.52	0.44	0.80
Ni	5	26 ppm	28	0.49	0.53	0.62
Cu	5	14 ppm	29	-0.04	-0.50	0.78
Zn	5	110 ppm	30	0.27	0.19	0.86
As	5	25 ppm	33	0.69	0.72	0.81
Zr	27	80 ppm	40	0.31	0.27	0.54
Ce	28	51 ppm	58	-0.40	-0.41	0.04

correlations above τ = 0.60 (*n* = 28; Table 3.2, Figure 3.2, A1.3). Only Al, K, and Ce had correlation coefficients below τ = 0.3. Potassium exhibited the only negative correlation of all elements analyzed.

3.6.4 Normalization of Itrax-XRF data

Normalization of XRF-CS data to Ca proved moderately successful (Table 3.3, Figure 3.4, A1.4). On average, Kendall's τ for comparison of Ca-normalized XRF-CS data to ICP-MS data (*n* = 28) increased by 0.06 points compared to raw XRF-CS data, with Cu and Zn showing an increase of at least 0.25 points and only two elements (As, and K) showing decreased correlations. Only Ce showed a negative correlation. Normalization of data to Ca also reduced the spread about the regression line for many elements (*e.g.* Fe; Figure 4).

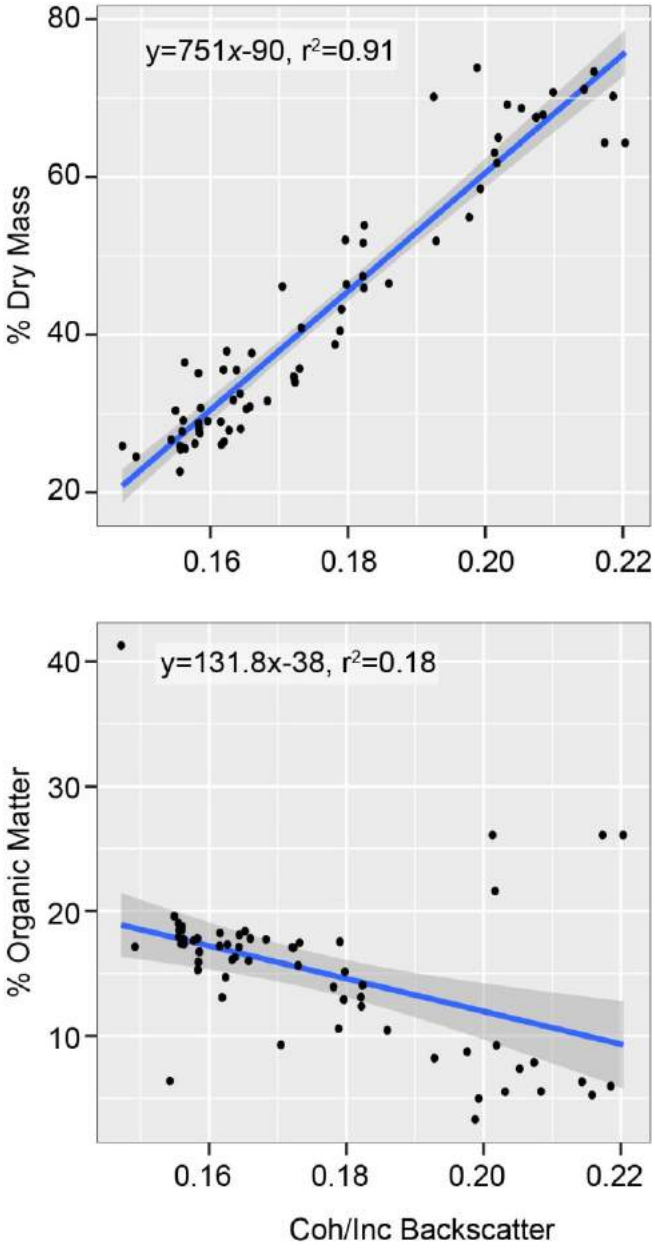

Figure 3.3: Comparison of wt % dry mass and wt % organic material measured using LOI to coherent/incoherent X-ray scatter. The median value of the CIR was used for comparison of x-ray scatter in a sample to water and organic content. Regression lines are shown in blue bordered by 95 % confidence interval indicated by darker grey area.

Normalization of XRF-CS data to Si showed similar improvements as were observed for normalization to Ca (Table 3.3, Figure 3.4, A1.5). Only two elements had negative correlations in the Si-normalized data, K and Ca. Many elements showed large improvements in Kendall's τ, including improvements of over 0.5 points for Cu, and Ce. Kendall's τ for Si-normalized data was, on average, 0.04 points greater than the raw XRF-CS correlations. Six of the elements in the Si-normalized data did not show improved correlations in comparison to raw-XRF-CS data.

In comparison to the raw-XRF-CS data, normalization of data to the total counts per second (kcps) showed an overall decrease in correlation to the observed ICP-MS data (n = 28; Table 3.3, Figure 3.4, A1.6). Cerium, and K showed minor increases in Kendall's τ, while all other elements showed a decrease in τ by an average of 0.05. Titanium, Cu, and Ce had negative correlations.

Table 3.3: Kendall's τ correlations for comparison of ICP-MS data to Ca-, Si-, kcps- and CIR-normalized XRF-CS data. Mean elemental abundances are based on ICP-MS results. Blue values indicate an increase in Kendall's τ values from raw-XRF-CS data, red values indicate a decrease in Kendall's τ values. Detection limits shown are based on analysis of USGS standard SGR-1.

Element	Detection Limit (ppm)	Mean Elemental Abundance	Atomic Number	Raw XRF-CS	Ca-norm	Si-norm	kcps-norm	CIR-norm
Al	7704	4.8 %	13	0.26	0.27	0.21	0.18	0.35
K	43	1.5 %	19	0.59	0.32	-0.18	0.62	0.65
Ca	27	0.43 %	20	0.55	-	-0.11	0.54	0.65
Ti	13	0.26 %	22	0.06	0.16	0.30	-0.04	0.25
Mn	7	940 ppm	25	0.35	0.51	0.54	0.25	0.70
Fe	6	2.7 %	26	0.52	0.70	0.48	0.37	0.82
Ni	5	26 ppm	28	0.49	0.52	0.51	0.36	0.70
Cu	5	14 ppm	29	-0.04	0.49	0.61	-0.21	0.43
Zn	5	110 ppm	30	0.27	0.57	0.63	0.14	0.69
As	5	25 ppm	33	0.69	0.65	0.64	0.69	0.83
Zr	27	80 ppm	40	0.31	0.32	0.30	0.29	0.53
Ce	28	51 ppm	58	-0.40	-0.19	0.23	-0.38	-0.42

Several elements showed spread far from regression lines with little discernable trend (Figure 3.4, A1.6).

Normalization of elements to the CIR showed improvement in Kendall's τ values in comparison to raw XRF-CS (Table 3.3, Figure 3.4, and A1.7). Some elements showed as much as 0.47-point increase in Kendall's τ (mean 0.219-point increase, n = 28). All elements showed positive correlations except for Ce (τ = -0.42, n = 28). Seven of 13 elements considered had correlation coefficients greater than τ = 0.5, with As (τ = 0.83) and Fe (τ = 0.82) showing the highest correlations. There was a reduced spread

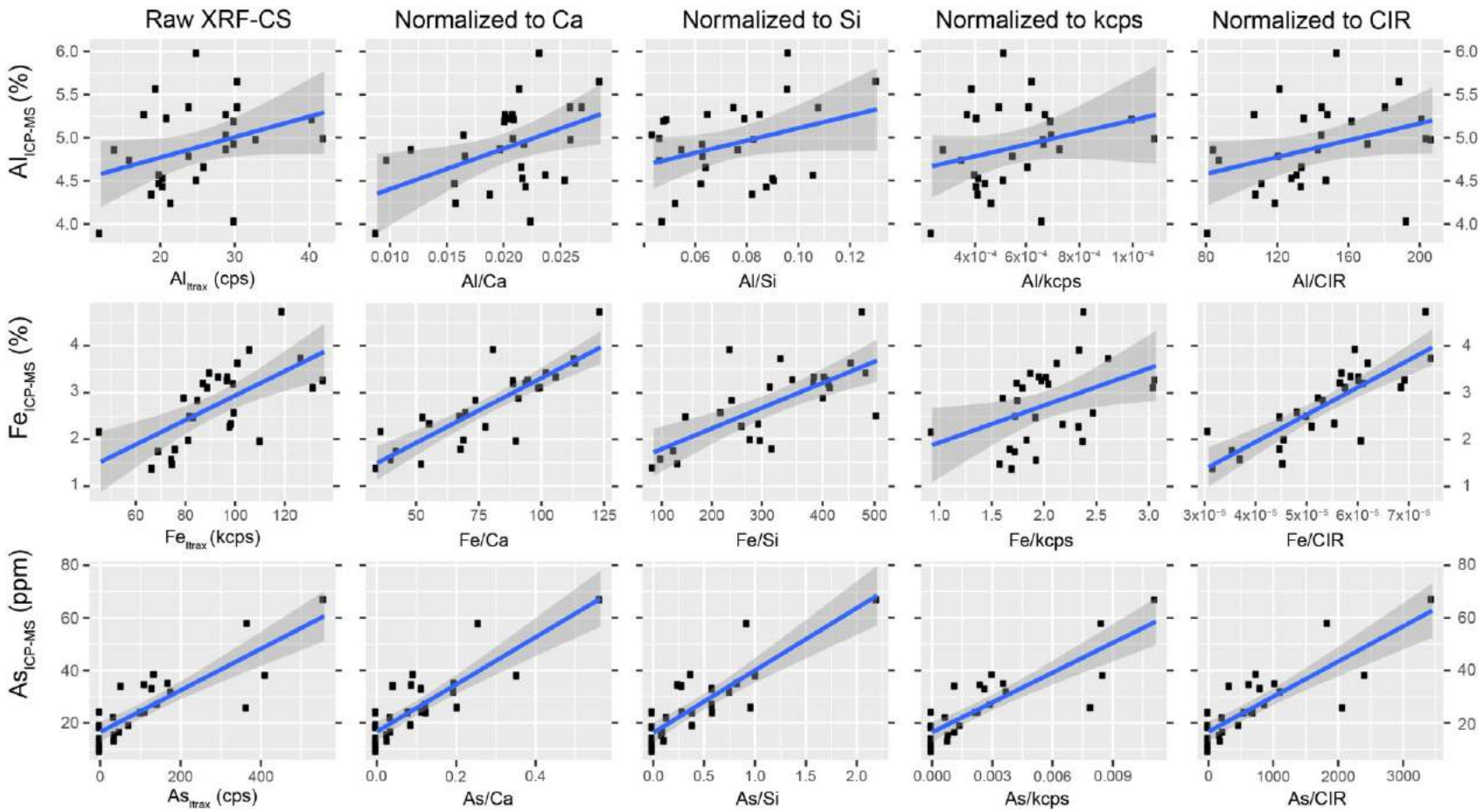

Figure 3.4: From left to right, graphs represent comparison of the ICP-MS data to raw-XRF-CS data, XRF-CS data normalized to Ca, XRF-CS data normalized to Si, XRF-CS data normalized to the total counts per second (kcps) and XRF-CS data normalized to Coherent/Incoherent X-ray scatter (CIR). Regression lines are shown in blue. The dark-grey shaded areas represent the 95 % confidence interval of the regression. Only select elements (Al, Fe, As) are compared here, see Figures A1.1 and A1.4–A1.7 for regression of all elements included in XRF-CS analysis.

of data points about the regression line for abundant, well detectable elements and moderate improvement in poorly detectable, yet abundant Al (Figure 3.4).

3.6.5 Multivariate Log-ratio Calibration

Correlations for eight out of nine elements using MLC showed moderate to strong positive R values ($R > 0.6$, $n = 28$; Figure 3.5). Aluminum, As, Mn, Ti and Zr had moderate R values > 0.64, and Fe, Ca, and K showed strong correlations with $R > 0.8$. Copper showed a weaker correlation with an $R = 0.47$. Most values plotted near the regression line for all elements, and all regression lines passed through the origin. There were no negative correlations.

3.6.6 Comparison of Calibrated XRF-CS to ICP-MS data

To assess the accuracy of each method, the ICP-MS-derived elemental concentrations were compared to the elemental concentrations for all samples predicted by the three XRF-CS calibration methods with that showed strong, positive correlations. The selected methods were: conversion of XRF-CS data to dry mass concentrations after Boyle et al. (2015); CIR-Normalization of XRF-CS data; and the MLC after Weltje et al. (2015). The raw XRF-CS data were included as a baseline for comparison to other methods of calibration. The precision values of the three best Itrax-XRF-CS methods were compared to values observed in a multi-laboratory study by the United States Environmental Protection Agency (USEPA) of the accuracy and precision of ICP-MS analysis of sediment (USEPA 1998), as well as a more recent analysis of the precision and accuracy of handheld-XRF geochemical analysis of sediment (USEPA 2007; Table 3.4).

The raw XRF-CS data showed a moderate degree of overlap with the ICP-MS concentrations of sediment samples (Figure 3.6, A1.8). The concentration of Ni, As, Al and Zr were the only elements of the 12 examined that showed ICP-MS concentrations within 1 SD of the median XRF-CS data for 75 % of samples compared. Potassium, Ca, Mn and Ce showed overlap between ICP-MS and XRF-CS in 50% of sediment samples compared, whereas the remaining 4 elements examined (Cu, Zn, Ti and Fe) showed agreement in less than 50% of samples. For some elements, notably Al, the variations

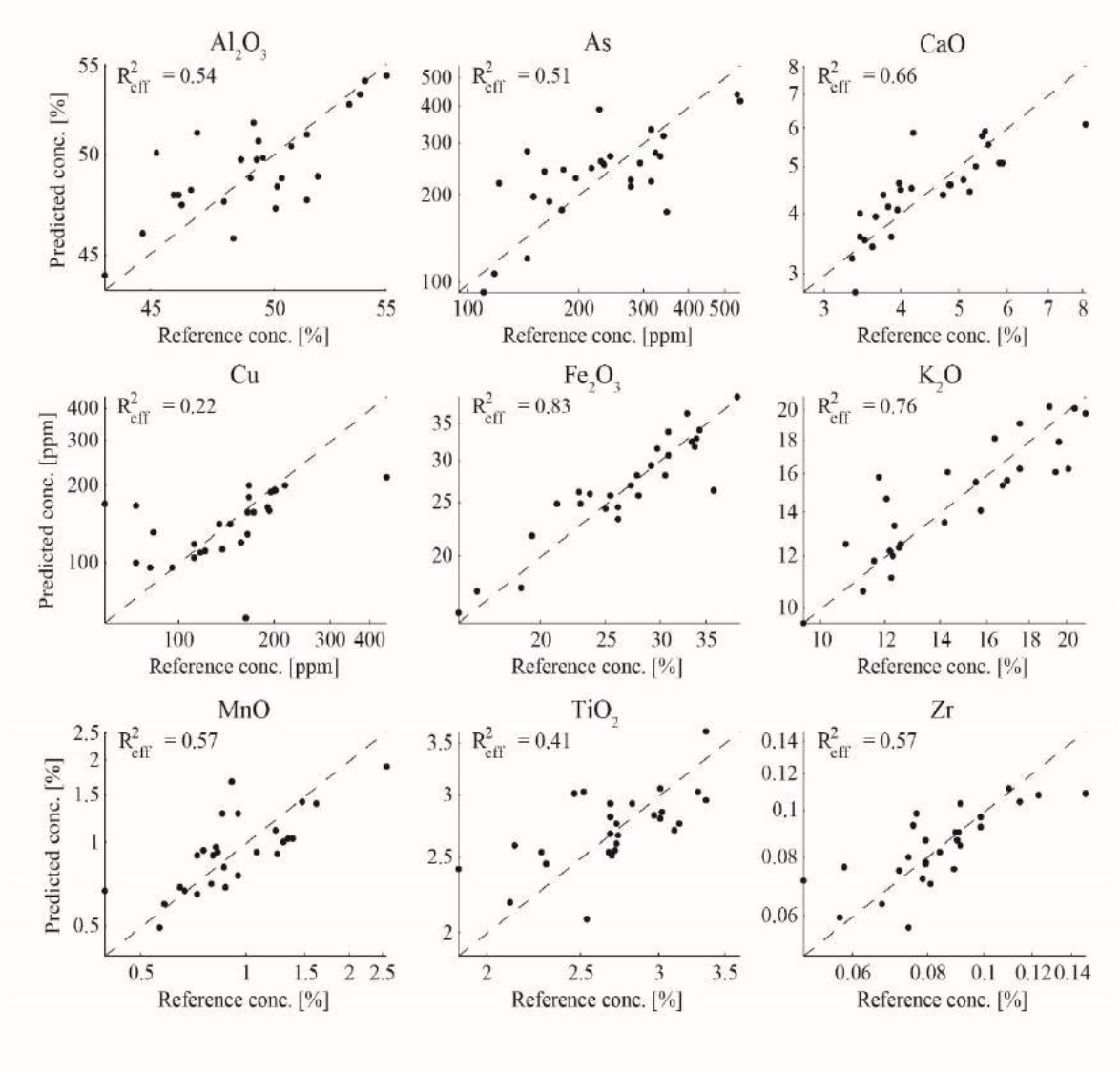

Figure 3.5: Comparison of MLC-XRF-CS (predicted) and ICP-MS derived (actual) geochemical concentrations of nine elements selected for the multivariate log-ratio calibration (MLC) using logarithmic graphs. The dashed lines represent linear regression of the data. This plot was generated using ItraXelerate software.

in ICP-MS results barely exceeded the observed XRF-CS standard deviation. For Cu and Ti, the XRF-CS results greatly underestimated the variability of ICP-MS results.

Normalization of the raw XRF-CS data to CIR showed good agreement between the transformed XRF-CS and ICP-MS data. Aluminum, Fe, Cu, Zr and As concentrations showed overlap between ICP-MS and CIR-normalized XRF-CS in 75 % of samples compared. Only Zn showed agreement between the two geochemical methods in less than 50% of samples; K, Ca, Ti, Mn and Ce all showed agreement between ICP-MS and CIR-normalized XRF-CS within 1 SD in over 50 % of samples (Figure 3.6, A1.9). The variability of ICP-MS-measured Al and Cu was lower than standard deviation of CIR-normalized XRF-CS results (*e.g.* CIR-normalized Cu concentrations in Figure 3.6). In the case of several elements where extreme highs in elemental concentrations occurred in ICP-MS results, notably Mn, Fe and Ca concentrations in sample HV-46, the high values were underestimated by CIR-normalized XRF-CS data. However, there did not appear to be a systematic over- or underestimation of values in this dataset. The RSD of CIR-normalized XRF-CS results was generally slightly higher than the relative standard deviation of Harvey Lake ICP-MS results, and comparable to ICP-MS and handheld-XRF measures of precision as determined by the USEPA (Table 3.4)

Correction of the XRF-CS data for water content (hereafter termed wet-corrected data) also showed good agreement between ICP-MS and XRF-CS data (Figure 3.6, A3.10). Aluminum, Mn, Cu and As showed agreement between CIR-normalized XRF-CS and ICP-MS data in over 75 % of samples compared; Fe, Ti and Zn showed similar concentrations in both datasets for more than 50 % of samples compared, whereas K, Ni, Ca, and Ce showed agreement below this threshold (Figure 3.6, A1.9). Copper concentrations for wet-corrected XRF-CS data show low precision, with almost the entire range of ICP-MS-measured Cu concentrations falling within 1 SD of XRF-CS results. For some elements, notably Ce, K and to a lesser degree Al, the CIR-normalized XRF-CS data underestimated the variability of ICP-MS results. However, the wet-corrected data successfully approximated most extreme highs in elemental concentrations. The relative standard deviation of wet-corrected XRF-CS data generally remained below 10 % with the except of Cu (56 %) and As (36 %). The precision of the wet-corrected data within the

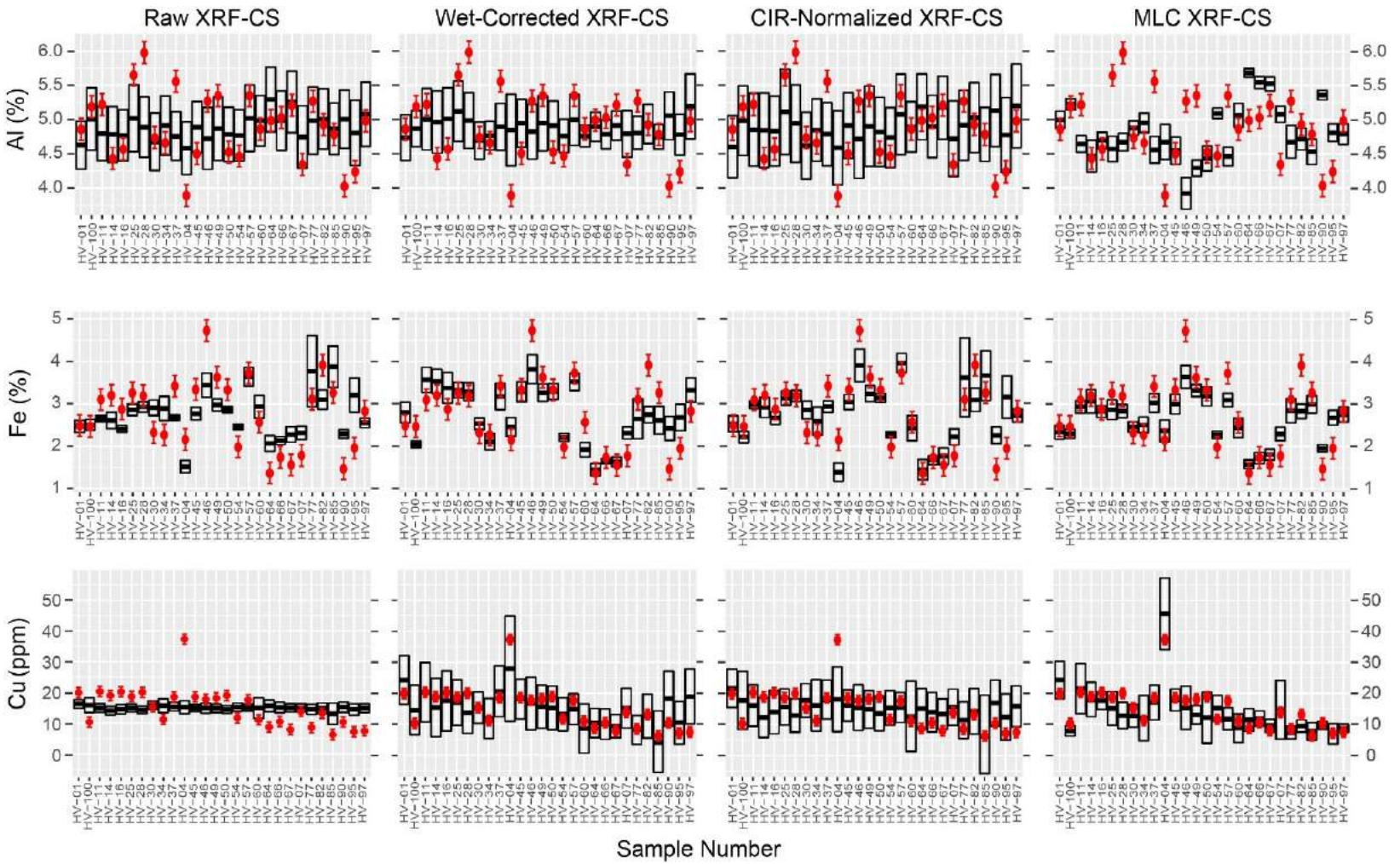

Figure 3.6: Comparison of median elemental concentrations predicted by calibrated XRF-CS data +/- the standard deviation of data (black boxes) and ICP-MS concentrations (red dots). Red crossbars show two relative standard deviations for elements calculated based on triplicate ICP-MS measurements. From left to right, graphs show comparison of ICP-MS data to raw-XRF-CS data, wet-corrected XRF-CS data after Boyle et al. (2015), CIR-normalized XRF-CS data, and data corrected using the MLC method after Weltje et al. (2015). Only select elements (Al, Fe, Cu) are shown here, see Figures A1.8–A1.11 for all the elements included in the calibration.

the range of observed precision values for handheld-XRF and ICP-MS, and were similar to the precision of ICP-MS replicate samples from Harvey Lake with the exception of As and Cu (Table 3.4).

The MLC-XRF-CS data showed good agreement with ICP-MS results, with Mn, Fe, Cu, As and Zr showing overlapping concentrations in 75 % of samples compared between the two methods. K, Ca, Ti showed good agreement between MLC-XRF-CS data in more than 50 % of samples compared, with Al being the only element that did not show a high degree of overlap between ICP-MS and MLC-XRF-CS data (Figure 3.6). The MLC-XRF-CS data has a low relative standard deviation, with values lower than the relative standard deviation measured using ICP-MS for all elements except for potassium and copper; precision tended to be greater than the ranges provided by the USEPA for handheld XRF and ICP-MS (Table 3.4).

3.7 Discussion

The 2nd generation Itrax is capable of analyzing a range of elements with moderate atomic weight ranging from Al to Rb, although the detection limit for Al is generally only reliable at concentrations of > 22,000 ppm (2.2 %; Croudace et al. 2016). Attempts to calibrate lighter elements have been met with success when they are present in higher concentrations (Chéron et al. 2016; Huang et al. 2016; Theden-Ringl and Gadd 2017). It is expected that a successful calibration should have strong positive correlations for most elements with moderate to high atomic weight that are present in higher concentrations, and that those with lower concentration, lower atomic weight, or both, may show weaker positive correlations due to "noise" induced by various matrix and specimen effects interfering with elemental detection. In addition to strong correlations across a range of values, an ideal linear regression of XRF-CS data and conventional geochemical data should have a regression line that passes through the origin, or else through the minimum detection limit of both techniques. Below, the merits of each calibration method are discussed further in light of the aforementioned criteria regarding optimal characteristics of calibrated data.

Table 3.4: Comparison of relative standard deviation for the best calibration methods and an inter-laboratory study on ICP-MS conducted by the USEPA (USEPA, 1998), and results from a study of handheld-XRF results (USEPA, 2007). The range of data for handheld-XRF results represent the range RSD calculated for analysis of dried, ground sediments (lower range) and unprocessed samples (higher range). Detection limits shown are based on analysis of USGS standard SGR-1.

Element	Detection Limit (ppm)	Itrax Relative Standard Deviation			Harvey Lake ICP-MS (%)	USEPA ICP-MS (%)	USEPA handheld-XRF (%)
		Wet-corrected XRF-CS (%)	CIR-normalized XRF-CS (%)	MLC XRF-CS (%)			
Al	7704	6.7	10	1.6	3.6	11 - 39	-
K	43	2.4	5.8	5.6	5.4	11 - 62	2.6 - 18.6
Ca	27	3.4	6.3	5.4	4.2	4.1 - 27	1.2 - 17.5
Ti	13	3.1	2.1	5.4	7.5	-	3.74 - 13.3
Mn	7	12	8.3	12	17.0	11- 40	12.3 - 40.5
Fe	6	8.1	8.8	4.5	9.4	6.7 - 21	1.6 - 10.3
Ni	5	7.9	16	-	3.2	9.2 - 29	18.2 - 29.8
Cu	5	56	51	12	12.5	9.0 - 25	7.9 - 26.4
Zn	5	11	10	-	5.0	14 - 42	11.1 - 26.6
Zr	27	8.6	8.5	9.0	15.3	-	5.18 - 20.2
As	5	36	36	9.8	19.3	12 - 23	3.8 - 22.5
Ce	28	1.7	14	-	11.9	-	-

3.7.1 XRF-CS Calibration

3.7.1.1 Raw XRF-CS Calibration

The raw XRF-CS analyses showed a moderate degree of success. There were moderate-strength positive correlations ($\tau > 0.35$) for most elements considered to be well detectable with Itrax XRF-CS using a Mo-tube. Lighter elements, such as Al, had weak positive correlations as expected. Several heavier elements showed weak negative or weak positive correlations in this calibration method in spite of their atomic weight and the moderate abundance, notably Zn, Cu and Ce. ICP-MS showed that Ce had a mean concentration of 51 ppm, Cu a mean concentration of 14 ppm and Zn a mean concentration of 100 ppm. The mean concentrations of Cu and Ce are close to the lower detection limits of Itrax-XRF-CS for Cu and Ce, which are 6 ppm and 36 ppm, respectively

(Table 3.2). It is possible that the poor correlations are a result of poor elemental detection by Itrax-XRF-CS as the elemental detection limits for Itrax XRF-CS were tested on ideal samples for exposures times much greater than the average XRF-CS runs (100 second exposure time). The lower count time and composition of sediment may have resulted in higher than expected minimum detection limit for several elements. However, Cu and Ce were still fairly well detected by Itrax XRF-CS, with average count rates of 184 cps and 72 cps (n = 4270), respectively, and < 5 % non-detect values (4.1 % for Cu and 0.81 % for Ce). These values are comparable to As, which had a mean count rate of 129 cps (n =4270), a higher proportion of non-detect values (36 %), a low mean concentration (25 ppm) that approached the detection limit of Itrax-XRF-CS (5 ppm), and the highest correlation observed in this dataset (τ = 0.68). Furthermore, Zn had a weak correlation, but a mean concentration much higher than the stated detection limit. It is therefore unlikely that the weak correlations are the result of either imprecise or inaccurate detection of elements due to elemental concentrations near detection limits as similar effects would be observed in As, but not in Zn. The weak correlations could be the result of sampling issues. ICP-MS was measured on larger sample volumes, nearer to 3 cm3, whereas even the multiple measurements of XRF-CS likely constituted less than 1 cm3 (0.2 mm x 0.2 mm x critical depth of a given element). However, we would expect that the same sampling bias effect would similarly be present in As, Cu and Ce due to similarly low concentrations in the ICP-MS dataset, which was not observed. Another possible explanation for the lower τ correlations in heavier elements is that overlapping X-ray escape lines may have interfered with accurate detection of select elemental concentrations. We reject this hypothesis as both As and Pb are known to have overlapping X-ray escape lines (Bearden 1967) and the inclusion of lead in our data did not reduce the correlation for As. It is also possible that absorption of the XRF signal by water could produce spurious correlations, but water should affect lighter elements to a greater degree than heavier elements (Kido et al. 2006; Tjallingii et al. 2007), which is not observed in the Harvey Lake data XRF-CS data. In all likelihood, an unpredictable combination of matrix and specimen effects, dilution effects, variations in actual elemental concentration, and limitations of Itrax-XRF-CS itself combined to create unexpected results that deviated from actual geochemical concentrations in difficult to predict ways.

Better correlation co-efficient for these select elements may have possible with experimental variation of Itrax-XRF settings during analysis or if a greater emphasis was placed on these energies during signal processing.

3.7.1.2 Qspec XRF-CS Calibration

Weaker and more often negative correlations were observed in the Qspec-calibrated XRF-CS data in comparison to raw-XRF-CS, although these decreases were often minor. The calibrated standards the Qspec software uses for calibration are based on analysis of solid materials, which would reduce errors associated with matrix/specimen effects. Analysis of wet sediment from Harvey Lake inherently showed deviations from actual geochemistry because of these effects, possibly resulting in negative or weak correlations. The Green River Shale standard selected for calibration may also not have had a similar enough sedimentary composition to that of the Harvey Lake sediment samples to allow for adequate comparison. Improvements may have been possible if additional standards were added based on analysis of powdered sediment, or if sediment standards were analyzed alongside sediment samples and these results use for calibration. It is also possible that variations in exposure time between analysis of standards (100 s) and the Harvey Lake samples (15 s) may also have contributed to the generation of less precise data, negatively influencing correlations. However, Huang et al. (2016) found that there was no appreciable improvement in correlations between actual and XRF-CS-derived elemental concentrations for most elements of moderate to high atomic number when exposure time was increased from 15 seconds to 100 seconds, and decreases where observed in the dataset even for well detectable, abundant elements, such as Fe, Mn, and Ca. Ultimately, the similarity in correlations observed in both the Qspec-XRF-CS and raw-XRF-CS results is likely due to lack of any transformation of the data. All matrix, or specimen present in the raw-XRF-CS dataset where still present in the Qspec-XRF-CS as the data was not transformed before calibration attempted. This suggests that data transformation or normalization, either before or after calibration, is required for XRF-CS results to accurately reproduce geochemical trends in sediment.

3.7.1.3 Wet-corrected XRF-CS calibration

Boyle et al. (2015) showed that water content is well approximated by the CIR if water content is the most significant influence on mean atomic number in the sediment. Considering that the dominant elements in sediment that comprised ~91 % of the element composition remained fairly stable, varying by only ~20 % of their median values, it is likely that variations in the proportion of water or organic content would exert greater control on the CIR. Comparison of dry mass percentage to CIR showed strong positive correlation, with a $\tau = 0.79$ ($n = 66$), indicating that the CIR approximated variations in water content within the Harvey Lake sediment samples analyzed (Figure 3). Elsewhere, researchers have used X-ray scatter as a proxy for organic content since organic material comprises predominantly lighter elements (C, H, O and N) not detected by XRF-CS methods that would decrease the mean atomic number and thus alter the X-ray scatter (Brown et al. 2007; Sáez et al. 2009; Burnett et al. 2011; Giralt et al. 2011). Comparison of wt % organic matter to Coh/Inc scatter from the Harvey Lake samples did not show a strong correlation ($\tau = -0.43$, $n = 61$; Figure 3.3). Other researchers have shown that there is negligible impact on the XRF-CS signal if water content or large sediment grains constitute < 25 wt % of a sample (Maclachlan et al. 2015). It is possible that a similar relationship is true for organic content, although this was not quantified by Maclachlan et al. (2015). However, recent research has shown that a ratio of Inc/Coh X-ray scatter poorly approximates variations in organic content in sediment with higher organic content, but provides a good approximation organic content when present in lower proportions (Chawchai et al. 2016). The substantially larger proportion (mean = 52 wt %, $n = 66$) and the greater variability (range 22.7–73.8 %) of water than organic content (mean = 15 wt %, $n = 61$) in samples analyzed in this study likely resulted in water having a greater impact on X-ray scatter than organic matter. More organic-rich sediment needs to be tested to fully understand how well X-ray scatter approximates water or organic content for a variety of sedimentary compositions, or how various types of organic matter may alter sediment porosity and thus both interstitial water and organic content.

Using the CIR to convert raw XRF-CS data to dry weight concentrations (wet-corrected dataset) improved the observed correlations between ICP-MS and XRF-CS results. The wet-corrected data performed poorly for some lighter elements, including a

significant decrease in the correlations in the values for K and Ca relative to raw XRF-CS data. The decrease in K and Ca correlations was unexpected as both these elements would be expected to suffer to a greater degree than heavier elements from bias induced by high water content, and thus correction of water content should better improve the accuracy of lighter elements. After correction for water content by Tjalingii et al. (2007) and Boyle et al. (2015) both observed minor increases in Pearson's R value between XRF-CS and ED-XRF of Ca, whereas in Maclachlan et al. (2015) and this study, Ca correlation coefficients decreased slightly after water content correction. Carbonate content in cores examined by Tjalingii et al. (2007) was high at 30–65 wt %, whereas cores examined by Boyle et al. (2015) and Maclachlan et al. (2015) generally ranged from about 5–15 wt % and carbonate content in Harvey Lake was < 1 wt %. Standards analyzed by Bureau Veritas showed that ICP-MS-measured Ca concentrations are accurate to actual concentrations within the 90% confidence interval, indicating ICP-MS accurately reproduced Ca trends in sediment. There are apparent issues with accurately recreating Ca values when correcting XRF-CS for water content when Ca is present in lower proportions. It is unclear why this relationship exists; some research has shown a negative correlation between Ca and water content (R^2 = 0.85; Maclachlan et al. 2017). It is possible that water content influences Ca detection by XRF-CS to such a degree that, below a certain concentration of Ca, a simple shift in absolute concentrations to account for water content does not properly account for the issues induced by changes in sediment water content.

The low K correlation may have been the result of variations in Mg, as Mg can absorb XRF emitted from K (Kido et al. 2006), thus inducing noise in the XRF-CS signal not reproduced by ICP-MS. However, it is unclear whether this would have had a substantial effect as ICP-MS results show Mg is not particularly abundant in sediment (mean = 0.52 %, *n* = 28), even in comparison to K (mean = 1.47 %, *n* = 28). Potassium may also be carried to the surface of the material undergoing analysis by the movement of interstitial water towards the sediment surface where the water forms a thin film between the sediment and the mylar covering used to protect the sediment from desiccation during analysis (Tjallingii et al. 2007). This may result in the XRF-CS

instrument providing an over-estimation of K concentrations, as well as altering actual variations in K in an unpredictable fashion, resulting in spurious correlations.

Tjallingii et al. (2007) observed that only elements lighter than Si are significantly influenced by dilution of water content, yet in this study and elsewhere (Hennekam and de Lange 2012; Chen et al. 2016), correction for water content was shown to improve the relationship between the heavier elements analyzed with XRF-CS. In this study, elements heavier than Ca showed substantial improvements in τ in comparison to raw XRF-CS data. It is apparent that, although water content may not substantially impact the detection of these heavier elements, correction for water content is still able to improve the correspondence between XRF-CS and results from conventional geochemical analyses.

3.7.1.4 Normalized XRF-CS Calibration

Normalization of data to Si or Ca showed an overall increase in τ correlations by 0.04 and 0.06 for Si and Ca, respectively. Decreases in Kendall's τ in comparison to raw XRF-CS data were more frequent Si-normalized dataset than were seen in the Ca-normalized XRF-CS data. Although elemental normalization did increase observed correlations, in most cases the increases were minor, with only Cu and Zn showing an increase in $\tau > 0.2$. Both normalization techniques reduced the spread of data points about the regression lines of multiple elements, although this influence was clearly more prevalent for heavier elements, like Fe, than lighter elements, like Al (Figure 3.4). Weltje and Tjallingii (2008) found that lighter elements, or those with low abundance, were not suitable as elemental denominators during calibration. In their study, elements lighter than Si were suggested to be unsuitable for elemental denominators in log-ratio calibrations, with Ca being considered the ideal denominator. For the Harvey Lake sediments, Ca barely performed better than Si. This result emphasizes the need for consideration of multiple possible elemental denominators before any calibration attempts are made.

In XRF-CS, normalization to an element can help to reduce the influence of matrix/specimen effects under the assumption that both elements will be affected by said effects to the same degree. Although it is expected that correction for these effects would substantially increase correlations for all elements, the minor improvements observed for the normalization of XRF-CS data to Si and Ca may have been caused by subtle

variations in how elements respond to matrix and specimen effects. Absorption of emitted X-radiation occurs predominantly at lower energies, and energy emitted by atoms increases with atomic number (Potts 1987), thus resulting in a greater influence of absorption effects on lighter elements. Furthermore, lighter elements have a smaller critical depth and should be more strongly influenced by a small water film forming between mylar covering samples and the sediment surfaces being analyzed (Kido et al. 2006; Tjallingii et al. 2007). Therefore, using a lighter element as the denominator in elemental ratios may induce larger errors into heavy element concentrations. The samples from Harvey Lake show a slight decrease in correlations for As, and Zr. Similar results were observed in Hennekam and de Lange (2012), where only log ratios of elements with similar atomic number (Ca/K and Ca/Ti ratio) showed a strong correlation between XRF-CS data and weak correlation to water content proxies. We observed a smaller increase in the correlation coefficients for XRF-CS data normalized to Si than to Ca. This may be caused by Si suffering from greater water-induced error. Normalization issues may also arise because elemental denominators respond not just to variations in matrix and specimen effects, but to environmental parameters that change over time and across a study area. Normalization to conservative elements, especially lighter elements susceptible to water content variations, is not ideal for calibration of heavier elements. Furthermore, use of elemental ratios with disparate atomic numbers may induce water-related errors, influencing paleoenvironmental interpretations using elemental ratios even in datasets where calibration is not attempted. Finally, application of elemental ratios to calibration attempts may suffer from comparison of normalized elements to un-normalized elements. Elemental ratios may remove some of the variability associated with matrix/specimen effects, but inherently introduces variability associated with environmental parameters influencing the denominator element, creating unpredictable and possibly incorrect calibrations. The success of the calibrations in this paper indicates calibration using elemental ratios may be possible when sediment geochemistry remains stable. However, in samples where major changes in sediment geochemistry occur (*e.g.* a shift from carbonate to silicate dominated system), calibration attempts using elemental ratios may not be as successful.

Several researchers have normalized XRF-CS data to the total counts per second (kcps) measured by Itrax-XRF-CS (Turner et al. 2010; Bouchard et al. 2011; Cuven et al. 2011) under the assumption that the kcps approximates the overall density of sediment. This effect is regularly observed, and was used here and previously (Gregory et al. 2017) in the analysis of discrete sediment samples to distinguish lighter acrylic-reservoir walls from denser sediment. By normalizing XRF-CS data to variations in density, density-related matrix effects should be minimized and XRF-CS data should better approximate dry-mass concentrations recorded in the ICP-MS data. This is especially true if components of the sample that cannot be measured by XRF-CS, like water and organic content, have a significant impact on overall sediment density. Correlations between kcps-normalized XRF-CS data and ICP-MS for the Harvey Lake samples decreased for almost all elements, and more negative correlations occurred. This may suggest that kcps poorly approximates major changes in sediment density in sediment samples from Harvey Lake. The low variability of kcps (RSD of only 8 %) may have resulted from relatively minor variations in the elemental composition of sediment across samples. Iron comprised ~85 % of the signal recorded by XRF-CS, and did not substantially change between samples (SD = 2 %). The method of densely packing the sediment into reservoirs prior to analysis may have contributed to relatively uniform kcps readings observed. If sediment density and packing remained relatively uniform, kcps may have been approximating variations in other variables, such as minute variations in the distance between the XRF detector and the sediment surface (Croudace and Rothwell 2015), or sample heterogeneity. If sediment density is not approximated by kcps, then normalization to this variable likely induced additional noise into the dataset independent of geochemical variability, resulting in the decrease in correlations observed for this method.

Boyle et al. (2015) used a ratio of Compton (incoherent) to Rayleigh (coherent) X-ray scatter to correct for water content in sediment as this ratio is proportional to the mean atomic mass of material analyzed (Duvauchelle et al. 1999). Assuming that use of elemental ratios eliminates matrix effects for a given sample, and that matrix effects are predominantly caused by variations in water content, sediment density, elemental composition of sediment, or other variables controlled by the mean atomic mass of

sediment, normalizing elemental ratios to CIR values should improve the observed relation between XRF-CS data and dry-mass ICP-MS concentrations. Normalization to X-ray scatter proved to be one of the best methods to approximate quantitative geochemical results. All elements showed positive correlations, commonly with correlation coefficients > 0.5. However, Ce had moderate-strength negative correlation (τ = -0.42). Cerium was an element that commonly had weak correlations between XRF-CS and ICP-MS data across all calibration methods, suggesting possible issues associated with detection of the element rather than issues with the calibration methods. ICP-MS showed a mean Ce concentration of 51 ppm, higher than the stated detection limit of Itrax-XRF-CS of 36 ppm. Although similar issues are not uniformly observed in elements with concentrations that approach the detection limits of XRF-CS, it seems that lower concentration elements are more susceptible to inconsistencies at lower concentrations. It may be possible to better replicate actual Ce concentrations in sediment by refining XRF-CS parameters during scanning or post processing (*e.g.* longer exposure times, a different combination of elements or further refining XRF-CS parameters during batch evaluation) or possibly performing additional sample preparation, such as freeze-drying samples or embedding them in epoxy. As this study is meant to test ability of XRF-CS to be calibrated under typical conditions, additional preparations or optimization of XRF peak fitting for lower concentration elements were not undertaken.

Both the CIR-normalized data and the wet-corrected data showed similar increases in the correlations between corrected XRF-CS data and ICP-MS values, however, the CIR-normalized data shows higher correlations for elements from Fe to Zn (Atomic numbers 26–40) as well as Ca and K. The improved τ values of the CIR-normalized data indicates that, for heavier elements where water content may have less of an effect, or where water content may induce detection errors (*e.g.* K), CIR-normalization better approximates actual geochemical values. This may be caused by shifts in sediment composition of a given interval exerting stronger influence on matrix effects than interstitial water content alone, or else from reduced influence of the water film that forms between the sediment surface and the protective mylar film covering the sediment as the critical depth of X-ray increases with increasing atomic number (Tjallingi et al. 2007).

3.7.1.5 Multivariate Log-ratio Calibration (MLC)

The MLC-XRF-CS data was generated from ItraXelerate software. The output from ItraXelerate assumes that the elements used in calibration sum to unity, however, the nine elements use in our calibration constitute an average of 9.8 wt % of sediment (n = 28). To account for this discrepancy, the Harvey Lake geochemical data were adjusted both by the actual proportion of sediment accounted for by the nine elements calibrated, as well as by the mean proportion of sediment accounted for by the nine elements calibrated (Figure 3.7). When adjusting MLC-output by the actual proportion of sediment represented by the nine elements selected for calibration, the XRF-CS results fell within 1 SD of median ICP-MS concentrations most of the time for all elements calibrated. However, as the purpose of these methods is to calibrate larger datasets, the mean proportion of sediment represented by the nine elements used for calibration must be used for application to the entire dataset.

Direct comparison between MLC and other methods of calibration presented in this paper were difficult as only nine elements were calibrated using the MLC. The correlation coefficients observed in MLC-calibrated data were comparable with those in most successful calibration techniques tested, notably wet-corrected data or CIR-normalized data. However, the ItraXelerate using a goodness-of-fit R values as the log-ratios better approximate a normal distribution, while other methods discussed in this paper use Kendall's τ as raw XRF-CS data had non-normal distributions. The lower correlation coefficients in the MLC dataset than observed for wet-corrected and CIR-normalized data for select elements may also have been due to water content remaining an influence on MLC-XRF-CS data. Previous work has shown that correction for water content before MLC can improve correlations in XRF-CS analysis of sediment cores (Chen et al. 2016). In spite of some lower correlation coefficients, graphs of linear regression showed little spread about the regression line. Copper, for example, had a R value of 0.47, yet showed little spread about the regression line. Furthermore, the regression line for all elements calibrated using the MLC passed through origin not observed for any element the other calibration methods. This suggests that the MLC method is the soundest method for calibrating XRF-CS data.

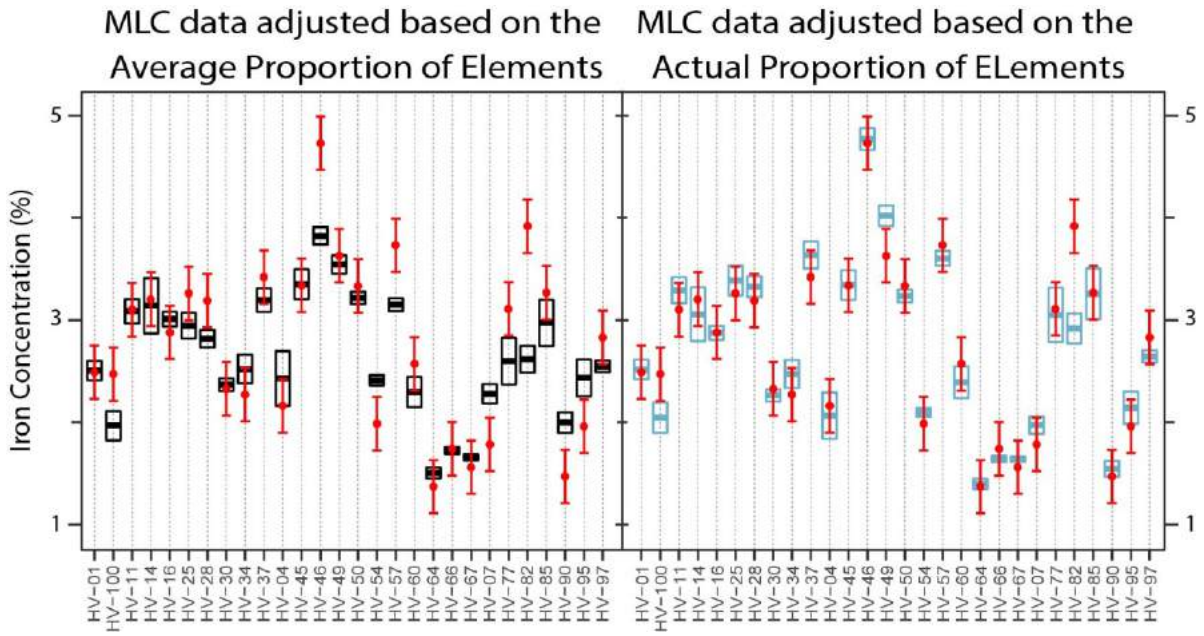

Figure 3.7: Comparison of MLC-derived median elemental concentrations +/- one standard deviation (black and blue boxes) to ICP-MS data (red dots) based on average and actual correction of MLC data. Black boxes represent XRF-CS data transformed to represent the actual proportion of sediment that the nine elements selected for MLC constitute. Blue boxes represent XRF-CS data adjusted to represent the average proportion of the nine elements represented in sediment.

3.7.2 Accuracy and Precision of Calibration Methods

For a calibrated XRF-CS data point to be considered “accurate” the median value of the calibrated dataset had to fall within 1 SD of measured ICP-MS data for a given sediment sample. Comparison of CIR-normalization, wet-corrected data and the MLC elemental concentrations to ICP-MS data showed improved calibration accuracy across all three methods compared to raw XRF-CS data (Figure 3.6). Wet-corrected data was accurate for more elements than the CIR-normalized data, however, the wet-corrected data had a greater tendency to underestimate actual variability of elemental concentrations in sediment. The elements that showed less variability in wet-corrected XRF-CS data than in the ICP-MS data were elements that had moderate detectability and abundance with low correlations (K, Ca), or had high detectability, but had low abundance (Ce). For the CIR-normalized data, elements that underestimated variability were those that were poorly detected or had low abundance and weak correlations across all methods (*e.g.* Ti). Elements with high abundance and poor detectability remained problematic. For example,

calibrated Itrax-XRF results for Al exhibited a higher error than the variability than the ICP-MS data (Figure 3.6). This suggests that in spite of concentration well above the detection limit of Itrax-XRF, Al data may be too noisy to reliably recreate actual geochemical trends. Both the CIR-normalized and the wet-corrected XRF-CS data underestimated some extreme ICP-MS values, although the wet-corrected data was generally closer to extreme values than the CIR-normalized data. For those elements where regressions were observed to be driven by a few anomalously high values, notably As and Mn, ICP-MS trends were still well replicated for both CIR-normalized and wet-corrected data. These results suggested that these were not spurious correlations in spite of being driven by relatively few data points, and that these calibration methods are applicable to contaminated sites that have skewed distributions that are inherently have extremely high values alongside lower background concentrations. Both CIR-normalization and wet-correction before calibration provided reliable results for elements with moderate- to good-detection by the Itrax-XRF-CS using a Mo-tube, although issues may arise when attempting to calibrate elements with lower detection and abundance.

The MLC substantially out-performed both the CIR-normalized and the wet-corrected data when the MLC results were shifted by the average proportion of nine elements used in the calibration. It is clear that the MLC better approximated elemental trends, even for elements with poorer detection, such as Al. In spite of the low R value for Cu (0.47), MLC was able to accurately predict Cu concentrations. For the MLC-XRF-CS, the deviation about the median was substantially smaller, yet MLC-XRF-CS data still showed greater overlap with ICP-MS than other methods. The higher precision of this method may be due to the artificial creation of triplicate datasets wherein there are only nine replicate measurements compared to > 15 measurements for the other calibration methods. In select cases, the MLC-XRF-CS underestimated extreme values. This was likely caused by shifting MLC results by the average proportion of elements in sediment; the samples that strongly deviate from this mean proportion of elements had reduced accuracy. For example, XRF-CS data overestimated the elemental concentrations for most elements for sample HV-54 (Figure 3.6, A1.8-A1.11). The proportion of the nine selected elements in this sample was 8.45 %, lower than the average proportion of 9.8 %. This issue impacted all elements, and correction for the actual proportion of 9-element

concentrations in sediment instead of the average brings these anomalous results into line with ICP-MS concentrations (Figure 3.7). For most elements analyzed and most samples, the influence of this effect is minimal, and ICP-MS results fell within 1 SD of MLC-XRF-CS results.

Comparison of ICP-MS to MLC-XRF-CS data showed that ICP-MS values fell within 1 SD of MLC-XRF-CS data most of the time for all elements, indicating that it was possible to perform MLC on XRF-CS scans of discrete samples by randomly sampling each sample to produce replicate scans attempted for the first time in this paper. Furthermore, it appears that substitution of Si values into our dataset did not substantially alter results, even though Si might have been more abundant than Al, based on XRF-CS results.

The precision of all three XRF-CS calibration methods was comparable to USEPA ICP-MS inter-laboratory comparison (USEPA 1998). The recorded range of the RSD in USEPA-ICP-MS methods is quite outdated, however, and modern ICP-MS provides much higher degrees of precision. This partially explains why the RSD of triplicate ICP-MS measurements of Harvey Lake sediment surpassed the highest precision in the USEPA multi-laboratory study for all elements except Cu, As, Pb and Ca. The more recent review of handheld-XRF by the USEPA (USEPA 2007) showed smaller RSD more comparable to Harvey Lake ICP-MS. Reported RSD in Table 3.4 for USEPA handheld XRF represent the range observed in samples that have undergone no preparation as well as those that had been dried and ground to homogeneous texture. The RSD of Itrax-XRF-CS calibrated data is more often near the upper limit of handheld-XRF RSD commonly associated with analysis of unprepared samples, as is expected, whereas RSD of Harvey Lake ICP-MS results were commonly nearer the lower limit of handheld-XRF RSD measured on prepared sediment samples. The mean RSD of Harvey Lake ICP-MS results was 9.5 % for the 12 elements examined considered in this study, whereas the mean RSD for the three ideal calibration methods were 13 %, 15 % and 7.2 % for the wet-corrected, CIR-normalized and MLC XRF-CS data, respectively. In most cases, XRF-CS RSD was only slightly less precise than the Harvey Lake ICP-MS results. Major issues were present in the As and Cu data, with RSD > 35 % in the CIR-normalized and wet-

corrected datasets. Although both ICP-MS and calibrated XRF-CS data show increase in RSD for these elements, possibly driven by a broader range of concentrations across the lake basin than other elements, the magnitude of the RSD increase is much larger for the calibrated XRF-CS data than the ICP-MS data. The low precision of As and Cu may have been be caused by errors in the XRF quantification of these elements caused by overlapping escape lines. It is unclear as to the cause of high RSD in Cu values. Regardless, the low precision of these low-concentration elements could likely have been improved through refining the XRF spectral fit, or else through longer exposure times. Although increasing exposure has shown little influence on the ability of XRF-CS to accurately recreate the concentration of elements that are readily detected and present in high concentration, minor improvements have been observed for elements present in lower concentrations (Huang et al., 2016). If the goal of a study is to assess rarer elements, in contaminations studies for example, than longer exposure times may help increase the accuracy and precision of data.

3.7.3 Recommended Method for Calibration of Surface Samples

Analysis of sediments using XRF core scanners offers increases in attainable sampling resolution and speed of analysis, as well as a decrease in analytical costs in exchange for providing semi-quantitative data when uncalibrated. An ideal XRF-CS calibration methodology not only preserves the high-resolution, rapid, cost-effective nature of XRF-CS data, but results in accurate and precise measurement of geochemical concentrations from XRF-CS data. In this study, we observed improved relationships between XRF-CS and ICP-MS data using three methods of post-analysis calibration: normalization of XRF-CS data to CIR; transforming data to dry-weight proportions using methods of water content correction modified from Boyle et al. (2015); and using the Multivariate Log-ratio Calibration method with the ItraXelerate software outlined in Weltje et al. (2015). Although all three methods provided precision comparable to USEPA ICP-MS and handheld-XRF, the accuracy of the three calibration methods varied. For our samples, CIR-normalization and correction for water content provided good correlations for most well detectable elements in each analysis that had higher concentrations in sediment. Light elements with higher concentration in sediment (Al) performed poorly for these methods. However, some studies have been able to reliably estimate trends of lighter elements in sediment

using XRF-CS (Chéron et al. 2016; Theden-Ringl and Gadd 2017), suggesting it may be an issue with abundance or possibly XRF-CS parameters. Heavier elements that were less abundant provided mixed results depending on the method used. For example, Ce was heavy, and well above the detection limit for both methods, but was poorly predicted by the wet-corrected method and well approximated by the CIR-normalized data. If either of these methods were used in, for example, analysis of heavy metal pollutants in sediment, relationships between observed and actual values should be examined carefully before undertaking an interpretation of the results. It is likely that additional processing of the data, or modification of analytical procedures (*e.g.* longer count times) may improve the precision or accuracy of said elements.

The MLC method is the method that performed the best of all those tested (Weltje et al. 2015). This method showed the most accurate results after adjusting the ItraXelerate output to account for the average proportion of the calibrated elements in sediment as measured using ICP-MS. However, this accuracy comes with an increased temporal and monetary cost, somewhat diminishing the advantages provided by XRF-CS. This diminished advantage is further emphasized by the inherent issues associated with analysis of discrete samples using XRF-CS that remove the advantage of improved resolution, unless the purpose of a study is to better understand the homogeneity of sediment samples themselves. For analysis of relatively few discrete samples using XRF-CS ($n < 30$), the MLC would thus offer no substantial improvement over conventional geochemical methods as most samples would need to be analyzed to calibrate a reasonable number of elements. However, for projects involving a larger numbers of surface samples ($n > 100$), the MLC offers substantial advantages over conventional geochemical analysis. Furthermore, if a study requires more reliable results for analysis of pollutants in a system, the MLC method offers clear advantages over the other XRF-CS calibration methods considered here. If a research project is investigatory in nature, or is interested in sedimentary processes or trends vs measuring pollutants, XRF-CS with CIR-normalization or wet-correction methods allow sufficient data correction to profit from the time/resolution/cost advantages of the instrumentation.

3.8 Conclusions

In this study, 100 surface sediment samples were analyzed with XRF-CS and ICP-MS, and multiple methods of calibrating XRF-CS data were tested to determine which would provide the highest accuracy, highest precision and most cost-effective results. Linear regression of raw-XRF-CS results showed moderate strength correlations for heavier elements with good detection. Calibration using Qspec software designed by Cox Analytics resulted in decreased correlations, possibly due to disparities between geochemical composition of standards and sediment analyzed, or the material analyzed (pressed pellet vs wet sediment). Normalization of XRF-CS data to Si and Ca showed slight improvement in correlation coefficients for most elements, but was out-performed by normalization to the CIR. Of the normalization methods, only normalization to kcps did not show substantial improvement in correlation coefficients. Correction of XRF-CS data for water content based on the ratio of coherent to incoherent X-ray scatter showed substantial improvement on a similar scale as CIR-normalized data, likely due to the correction being based on the same parameter. Of the simple linear calibration methods, CIR-normalization and water-content correction performed best, recreating trends in elements with good detection. These two methods, however, had minor issues when used to recreate observed geochemical trends in elements that were well detected by XRF-CS but had low concentration in sediment, or those that were poorly detected by XRF-CS. The multivariate log-ratio calibration method performed the best of all tested methods after results were adjusted to account for the proportion of elements in a sample. The MLC reliably recreated trends for elements with lower detection or low concentration, such as Al and Cu. Calibration of XRF-CS data after normalization to CIR or conversion to dry mass concentrations took full advantage of the speed and cost advantages XRF-CS offers, and are ideal for preliminary investigation of study areas, or studies that do not require rigorous quantification of absolute values. Although the MLC method reduced the advantages of XRF-CS by increasing cost and time required for analysis, it greatly out-performed the other methods of calibration in terms of accurately recreating observed ICP-MS trends. Itrax-XRF-CS of discrete samples enables rapid characterization and comparison within or between environmental systems. Although the calibration of data in this study showed precision comparable to other commonly used methods of

geochemical determination used by the USEPA, calibration does not yet show the accuracy that may be required in some contamination studies that have to withstand legal or regulatory scrutiny. The results of the calibration experiments presented here indicate that properly calibrated XRF-CS analyses can be used even in cases where regulatory or planning policy is under consideration to provide high resolution and inexpensive reconnaissance or pilot results to inform subsequent sampling protocols, or to provide approximate elemental concentrations that can later be verified with quantitative analysis.

3.9 References

Bearden JA (1967) X-ray Wavelengths. Rev. Mod. Phys. 39:78–124.

Berntsson A, Rosqvist GC, Velle G (2014) Late-Holocene temperature and precipitation changes in Vindelfjällen, mid-western Swedish Lapland, inferred from chironomid and geochemical data. The Holocene 24:78–92.

Bottomley DJ (1984) Origins of some arseniferous groundwaters in Nova Scotia and New Brunswick, Canada. Journal of Hydrology. 69:223-257.

Bouchard F, Francus P, Pienitz R, Laurion I (2011) Sedimentology and geochemistry of thermokarst ponds in discontinuous permafrost, subarctic Quebec, Canada. J. Geophys. Res. Biogeosciences 116:1–14.

Boyle JF, Chiverrell RC, Schillereff D (2015) Approaches to water content correction and calibration for uXRF Core Scanning: Comparing X-ray Scattering with Simple Regression of Elemental Concentrations. In Micro-XRF Studies of Sediment Cores: Applications of a Non-Destructive tool for Environmental Sciences (eds. Croudace IW, Rothwell RG). Springer Dordrecht, NL. pp. 373–390.

Brown E, Johnson T, Scholz C, Cohen A, King J (2007) Abrupt change in tropical African climate linked to the bipolar seesaw over the past 55 000 years. Geophys. Res. Lett. 34:1–5.

Burnett AP, Soreghan MJ, Scholz CA, Brown ET (2011) Tropical East African climate change and its relation to global climate: A record from Lake Tanganyika, Tropical East Africa, over the past 90+kyr. Palaeogeogr. Palaeoclimatol. Palaeoecol. 303:155–167.

Chawchai S, Kylander ME, Chabangborn A, Löwemark L, Wohlfarth B (2016) Testing commonly used X-ray fluorescence core scanning-based proxies for organic-rich lake sediments and peat. Boreas 45:180–189.

Chen Q, Kissel C, Govin A, Liu Z, Xie X (2016) Correction of interstitial water changes in calibration methods applied to XRF core-scanning major elements in long sediment cores: Case study from the South China Sea. Geochemistry, Geophys. Geosystems 17:1–10.

Chéron S, Etoubleau J, Bayon G, Garziglia S, Boissier A (2016) Focus on sulfur

count rates along marine sediment cores acquired by XRF Core Scanner. X-Ray Spectrom. 45:288–298.

Croudace IW, Rindby A, Rothwell RG (2006) ITRAX: description and evaluation of a new multi-function X-ray core scanner. Geol. Soc. London 267:51–63.

Cuven S, Francus P, Lamoureux S (2011) Mid to Late Holocene hydroclimatic and geochemical records from the varved sediments of East Lake, Cape Bounty, Canadian High Arctic. Quat. Sci. Rev. 30:2651–2665.

Duvauchelle P, Peix G, Babot D (1999) Effective atomic number in the Rayleigh to Compton scattering ratio. Nucl. Instruments Methods Phys. Res. Sect. B Beam Interact. with Mater. Atoms 155:221–228.

Giralt S, Rico-Herrero MT, Vega JC, Valero-Garcés BL (2011) Quantitative climate reconstruction linking meteorological, limnological and XRF core scanner datasets: The Lake Sanabria case study, NW Spain. J. Paleolimnol. 46:487–502.

Gregory BRB, Peros M, Reinhardt EG, Donnelly JP (2015) Middle-late Holocene Caribbean aridity inferred from foraminifera and elemental data in sediment cores from two Cuban lagoons. Palaeogeogr. Palaeoclimatol. Palaeoecol. 426:229-241.

Gregory BRB, Reinhardt EG, Macumber AL, Nasser NA, Patterson RT, Kovacs SE, Galloway JM (2017) Sequential sample reservoirs for Itrax-XRF analysis of discrete samples. J. Paleolimnol. 57:287-293.

[dataset] Gregory BRB, Patterson RT, Reinhardt EG, Galloway JM, Roe HM (2018a) Harvey Lake ICP-MS. Mendeley Data, Version 1.0. DOI: 10.17632/2yj6kpcrpg.1

[dataset] Gregory BRB, Patterson RT, Reinhardt EG, Galloway JM, Roe HM (2018b) Harvey Lake Itrax XRF-CS. Mendeley Data, Version 1.0. DOI: 10.17632/3fpdwcgtcj.1

[dataset] Gregory BRB, Patterson RT, Reinhardt EG, Galloway JM, Roe HM (2018c) Harvey Lake Loss on Ignition. Mendeley Data, Version 1.0. DOI: 10.17632/bshvrjgxfz.1

[dataset] Gregory BRB, Patterson RT, Reinhardt EG, Galloway JM, Roe HM

(2018d) Harvey Lake QSpec Calibration. Mendeley Data, Version 1.0. DOI: 10.17632/pf7f77tzr4.1

Guyard H, Chapron E, St-Onge G, Anselmetti FS, Arnaud F, Magand O, Francus P, Mélières MA (2007) High-altitude varve records of abrupt environmental changes and mining activity over the last 4000 years in the Western French Alps (Lake Bramant, Grandes Rousses Massif). Quat. Sci. Rev. 26:2644–2660.

Haenssler E, Nadeau MJ, Vött A, Unkel I (2013) Natural and human induced environmental changes preserved in a Holocene sediment sequence from the Etoliko Lagoon, Greece: New evidence from geochemical proxies. Quat. Int. 308:89–104.

Hennekam R, de Lange G (2012) X-ray fluorescence core scanning of wet marine sediments: methods to improve quality and reproducibility of high-resolution paleoenvironmental records. Limnol. Oceanogr. Methods 10:991–1003.

Hennekam R, Sweere T, Tjallingii R, de Lange GJ, Reichart G-J (2018) Trace metal analysis of sediment cores using novel X-ray fluorescence core scanning method. Quaternary International, In Press.

Huang J, Löwemark L, Chang Q, Lin T-Y, Chen H-F, Song S, Wei K (2016) Choosing optimal exposure times for XRF core-scanning: Suggestions based on the analysis of geological reference materials. Geochemistry Geophys. Geosystems, 17.

Hunt JE, Croudace IW, Maclachlan SE (2015) Use of Calibrated Itrax-XRF data in determining turbidite Geochemistry and provenance in Agadir Basin, Northwest African Passive Margin. In Micro-XRF Studies of Sediment Cores: Applications of a Non-Destructive tool for Environmental Sciences (eds. Croudace IW, Rothwell RG). Springer Dordrecht, NL. pp. 127–146.

International Atomic Energy Association (1997) Sampling, storage and sample preparation procedures for X ray fluorescence analysis of environmental materials. Vienna, 1997.

Jansen JHF, Van Der Gaast SJ, Koster B, Vaars AJ (1998) CORTEX, a shipboard XRF-scanner for element analyses in split sediment cores. Mar. Geol. 151:143–153.

Kido Y, Koshikawa T, Tada R (2006) Rapid and quantitative major element analysis method for wet fine-grained sediments using an XRF microscanner. 229:209–225.

Kujau A, Nürnberg D, Zielhofer C, Bahr A, Rohl U (2010) Mississippi River discharge over the last~ 560,000 years—Indications from X-ray fluorescence core-scanning. Palaeogeogr. Palaeoclimatol. Palaeoecol. 298:311–318.

Kylander ME, Ampel L, Wohlfarth B, Veres D (2011) High-resolution X-ray fluorescence core scanning analysis of Les Echets (France) sedimentary sequence: New insights from chemical proxies. J. Quat. Sci. 26:109–117.

Lintern A, Leahy PJ, Heijnis H, Zawadzki A, Gadd P, Jacobsen G, Deletic A, Mccarthy DT (2016) Identifying heavy metal levels in historical flood water deposits using sediment cores. Water Res. 105:34–46.

Löwemark L, Chen H-F, Yang T-N (2011) Normalizing XRF-scanner data: A cautionary note on the interpretation of high-resolution records from organic-rich lakes. J. Asian Earth Sci. 40:1250–1256.

Lyle M, Backman J (2013) Data Report: Calibration of XRF-estimated $CaCO_3$ along the Site U1338 splice. Proc. Integr. Ocean Drill. Progr. 320:1–16.

Lyle M, Lyle AO, Gorgas T, Holbourn A, Westerhold T, Hathorn E, Kimoto K, Yamamoto S (2014) Data report: raw and normalized elemental data along the Site U1335, U1336, and U1337 splices from X-ray fluorescence scanning. Proc. Integr. Ocean Drill. Progr. 320.

Maclachlan SE, Hunt JE, Croudace IW (2015a) An Empirical Assessment of Variable Water Content and Grain-Size on X-Ray Fluorescence Core-Scanning Measurements of Deep Sea Sediments. In Micro-XRF Studies of Sediment Cores: Applications of a Non-Destructive tool for Environmental Sciences (eds. Croudace IW, Rothwell RG). Springer Dordrecht, NL. pp. 173–185.

Marshall MH, Lamb HF, Huws D, Davies SJ, Bates R, Bloemendal J, Boyle J, Leng MJ, Umer M, Bryant C (2011) Late Pleistocene and Holocene drought events at Lake Tana, the source of the Blue Nile. Glob. Planet. Change 78:147–161.

Miller H, Croudace IW, Bull JM, Cotterill CJ, Dix JK, Taylor RN (2015) Modern pollution

signals in sediments from Windermere, NW England, determined by micro-XRF and lead isotope analysis. In Micro-XRF Studies of Sediment Cores: Applications of a Non-Destructive tool for Environmental Sciences (eds. Croudace IW, Rothwell RG). Springer, Dordrecht, NL. pp. 1–18.

Parsons MB, LeBlanc KWG, Hall GEM, Sangster AL, Vaive JE, Pelchat P (2012) Environmental geochemistry of tailings, sediments and surface waters collected from 14 historical gold mining districts in Nova Scotia. Geological Survey of Canada Open File 7150, pp. 1–312.

Payette C, Martin RF (1986) The Harvey volcanic suite, New Brunswick. II. Postmagmatic adjustments in the mineralogy and bulk composition of a high-fluorine Rhyolite. Canadian Mineralogist. 24:571-584.

Peros M, Collins S, G'Meiner AA, Reinhardt EG, Pupo FM (2017) Multistage 8.2 kyr event revealed through high-resolution XRF core scanning of Cuban sinkhole sediments. Geophys. Res. Lett., 7374–7381.

Profe J, Zolitschka B, Schirmer W, Frechen M, Ohlendorf C (2016) Geochemistry unravels MIS 3/2 paleoenvironmental dynamics at the loess–paleosol sequence Schwalbenberg II, Germany. Palaeogeogr. Palaeoclimatol. Palaeoecol. 459:537–551.

Profe J, Neumann L, Zolitschka B, Frechen M, Rolf C, Barta G (2017) Geochemical record of the loess-paleosol sequence Süttő (Hungary) derived from X-ray fluorescence scanning of discrete samples. Geophysical Reasearch Abstracts, 19:9085.

Rodríguez-Germade I, Rubio B, Rey D, Borrego J (2015) Detection and monitoring of REEs and related trace elements with an itrax core scanner in the Ria de huelva (SW Spain). Water. Air. Soil Pollut. 226.

Sáez A, Valero-Garcés B, Giralt S (2009) Glacial to Holocene climate changes in the SE Pacific. The Raraku lake sedimentary record (Easter Island, 27 S). Quat. Sci. Rev. 28:2743–2759.

Schillereff DN, Chiverrell RC, Macdonald N, Hooke JM, Welsh KE (2016) Quantifying system disturbance and recovery from historical mining-derived metal contamination at Brotherswater, northwest England. J. Paleolimnol. 56:205–221.

Shackford JK, Lyle M, Wilkens R, Tian J (2014) Data report: raw and normalized elemental data along the Site U1335, U1336, and U1337 splices from X-ray fluorescence scanning.

Theden-Ringl F, Gadd P (2017) The application of X-ray fluorescence core scanning in multi-element analyses of a stratified archaeological cave deposit at Wee Jasper, Australia. J. Archaeol. Sci. Reports 14:241–251.

Tjallingii R, Röhl U, Kölling M, Bickert T (2007) Influence of the water content on X-ray fluorescence core-scanning measurements in soft marine sediments. Geochemistry, Geophys. Geosystems 8(2):1–12.

Turner J, Davis S, Langdon C, Scaife R, Holmes N, Leng M, Mulrooney G, Cummins T (2010) A multiproxy (pollen, stable isotope, chironomid and μXRF) record for the Late Glacial to Holocene transition from Thomastown Bog, Ireland. Journal of Quaternary Science, 6:514-528.

US Environmental Protection Agency (1998) Method 6020A: Inductively Coupled Plasma-Mass Spectrometry. Revision 1 - US Environmental Protection Agency, pp. 1-23.

US Environmental Protection Agency (2007) Method 6200: Field portable X-ray fluorescence spectrometry for the determination of elemental concentrations in soil and sediment. Revision 0 - US Environmental Protection Agency, pp. 1-32.

Wei G, Liu Y, Li X, Shao L, Fang D (2004) Major and trace element variations of the sediments at ODP Site 1144, South China Sea, during the last 230 ka and their paleoclimate implications. Palaeogeogr. Palaeoclimatol. Palaeoecol. 212:331–342.

Weltje GJ, Tjallingii R (2008) Calibration of XRF core scanners for quantitative geochemical logging of sediment cores: Theory and application. Earth Planet. Sci. Lett., 423–438.

Weltje GJ, Bloemsma MR, Tjallingii R, Heslop D, Rohl U, Croudace IW (2015) Prediction of Geochemical Composition from XRF Core Scanner Data: A New Multivariate Approach Including Automatic Selection of Calibration Samples and Quantification of Uncertainties. In Micro-XRF Studies of Sediment Cores:

Applications of a Non-Destructive tool for Environmental Sciences (eds. Croudace IW, Rothwell RG). Springer, Dordrecht, NL. pp. 507–534.

Zielhofer C, von Suchodoletz H, Fletcher WJ, Schneider B, Dietze E, Schlegel M, Schepanski K, Weninger B, Mischke S, Mikdad A (2017) Millennial-scale fluctuations in Saharan dust supply across the decline of the African Humid Period. Quat. Sci. Rev. 171:119–135.

Chapter 4: The iBox-FC: a new containment vessel for Itrax X-ray fluorescence core-scanning of freeze cores

4.1 Authors and Addresses

Gregory BRB[1], Patterson RT[1], Reinhardt EG[2], Galloway JM[1,3,4]

[1]Ottawa-Carleton Geoscience Center and Department of Earth Sciences, Carleton University, 1125 Colonel By Dr., Ottawa, Ontario, Canada, K1S 5B6

[2]School of Geography and Earth Sciences, McMaster University, 1280 Main St. W., Hamilton, Ontario, Canada, K1S 5B6

[3]Geological Survey of Canada/National Resources Canada (Commission géologique du Canada/Ressources naturelles Canada), 3303 33 St. N.W., Calgary AB, Canada, T2L 2A7

[4]Aarhus Institute of Advanced Studies, Aarhus University, 8000 Aarhus C., Denmark

4.2 Foreword

This contribution details the equipment and methodologies employed to all analysis of freeze core sediment with Itrax-XRF. Freeze cores can reliably capture recent sediments that may be too soupy to be captured by traditional gravity coring without risk of homogenizing climate signals. In environments where sedimentation rate is low, freeze coring and high-resolution analysis can be used to understand near-modern geochemical variations and possible recent anthropogenic impact from the past 100s of years. Using easy-to-assemble Styrofoam boxes, were we able to scan sections of freeze core up to 13-cm-long using Itrax-XRF analysis. This contribution represents the first attempts of scanning freeze cores using Itrax-XRF. This manuscript was originally published in Quaternary International in a core-scanning special issue of the journal. The manuscript has been modified slightly to meet the formatting requirements of Carleton University, but is otherwise unchanged.

Dr. R.T. Patterson, Dr. *E.G.* Reinhardt, and I designed the freeze core boxes. Dr. Reinhardt provided equipment for analysis and provided free analysis time during testing of freeze core boxes. I tested the iBoxes, wrote the manuscript, and prepared figures. All co-authors provided feedback on the manuscript to help refine it. This research was funded by a Polar Knowledge Canada grant to Dr. Patterson and Dr. Galloway and a Canadian Foundation for Innovation grant to Dr. Reinhart. It should be cited as follows:

Gregory BRB, Patterson RT, Reinhardt EG, Galloway JM. (2018). The iBox-FC: A new containment vessel for Itrax X-ray fluorescence core-scanning of freeze cores. *Quaternary International.*

4.3 Abstract

High-resolution paleoclimate records are vital for understanding high-frequency climate events and recent anthropogenic alteration to environmental systems. A combination of Itrax x-ray fluorescence core scanning (XRF-CS) and freeze coring can facilitate the development of high-resolution (*e.g.* sub-decadal) paleoclimate records in lacustrine systems where low sedimentation rates and poorly consolidated “colloidal soup” at the sediment/water interface precludes coring and Itrax-XRF-CS using conventional gravity corers. The iBox-FC containment vessel described here delays thawing of highly perishable frozen sediments obtained using a freeze corer for up to two hours, adequate time to carry out high-resolution Itrax-XRF-CS analysis. The iBox-FC is comprised of an open-topped Styrofoam box divided into chambers using high-density polyethylene (HDPE) that are filled with freeze pack gel. When the vessel is frozen, core slabs up to 13 cm long may be positioned into a central chamber and then scanned following normal XRF-CS methodology. To test the reliability of XRF-CS analysis obtained from frozen sediments, a freeze core recovered from Control Lake, Northwest Territories, Canada, was sub-sectioned and analyzed using Itrax-XRF-CS. Subsequent to XRF-CS analysis, the freeze core slabs were subsampled and analyzed by ICP-MS following near-total acid digestion. Comparison of XRF-CS and ICP-MS results showed strong correlations (R^2>0.8) for six of nine elements calibrated, and moderate correlations (R^2>0.3) for the remaining three. Minor edge effects consistently observed through the last ~5 mm of each core slab did not significantly influence analytical reliability, resulting in the loss of only ~4% of normalized data.

4.4 Introduction

Developing robust high-resolution paleo-climate records is important for understanding climate trends and cycles (*e.g.* El Niño/Southern Oscillation, Pacific Decadal Oscillation, North Atlantic Oscillation). The weather patterns associated with these climate drivers impact global economies by influencing agricultural productivity (D'arrigo and Wilson 2008; Deng et al. 2010; Iizumi et al. 2014), alter the frequency and prevailing regional occurrence of natural disasters (Donnelly and Woodruff 2007; Ezer and Atkinson 2014; Kitzberger et al. 2001) and impact terrestrial and oceanic ecosystems (Holmgren et al. 2001; Kilduff et al. 2015; Stenseth et al. 2003). Furthermore, high-resolution paleoclimate and paleoenvironmental reconstructions can be used to discriminate signals of anthropogenic impacts or contamination from the baseline natural variability, which characterizes lacustrine environmental systems (Andrade et al. 2010; Cobelo-Garcia and Prego 2003; Roulet et al. 2000). In regions with poorly developed ground cover, such as the Canadian Arctic or the Yucatan Peninsula, low sedimentation rates preclude high-resolution paleoclimate or anthropogenic impact studies in many lacustrine systems due to difficulty attaining minimum sample weights required for conventional geochemical analysis. Recent advances in analytical techniques, notably the development of high-resolution x-ray fluorescence core-scanners (XRF-CS), has drastically reduced the cost, volume of material, and time required for analysis of sediment. Geochemical data can be generated for sediment cores at sub-mm scale through the use of XRF-CS, and thus permits study of paleoclimate and anthropogenic impacts in these extreme environments at a temporal resolution relevant to land use decision makers and planners.

Sediment near the surface-water interface is poorly consolidated in many lacustrine environments. When using conventional gravity coring, material in the upper few centimetres of the core may be homogenized due to its soupy nature if the core is not kept perfectly still during transport and subsequent sub-sampling. Furthermore, this poorly consolidated material may not be cohesive enough for XRF-CS, creating difficulty when attempting to analyze the environmentally critical uppermost part of gravity cores. Freeze coring freezes sediments in situ to the outside of a hollow metal rectangular prism filled with a slurry of dry ice and ethanol (Figure 4.1A, B). Freeze coring offers the advantages of preserving the stratigraphy of the sediment-water interface without risk of

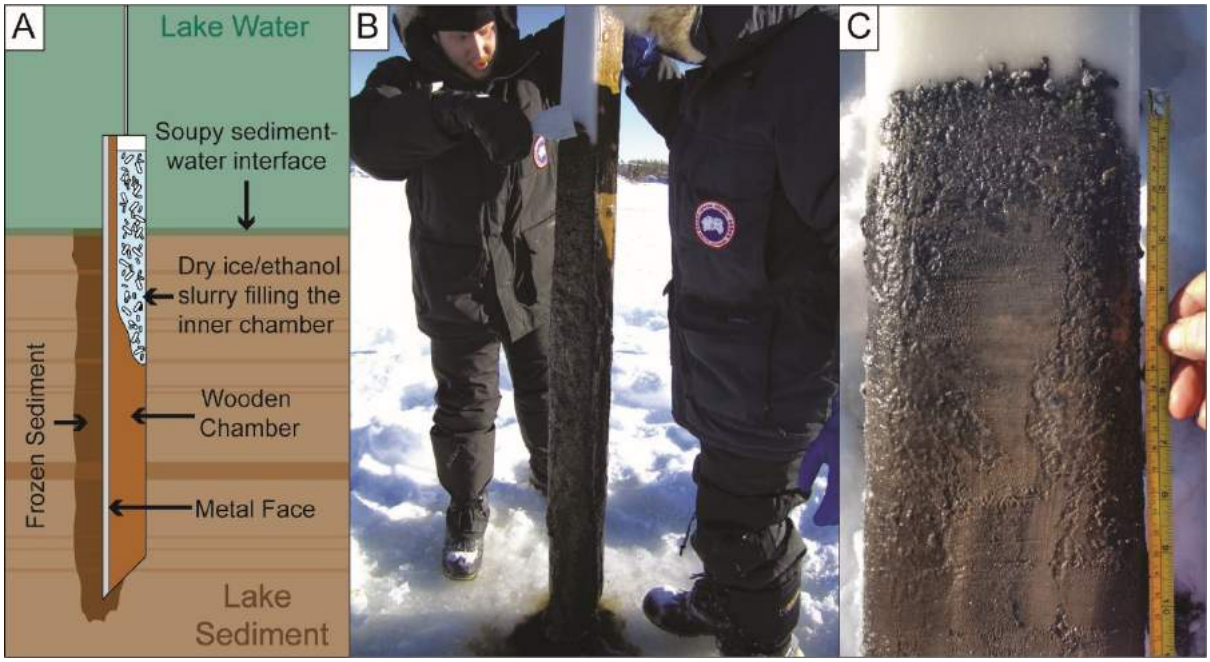

Figure 4.1: (A) Cross section of freeze core in sediment. (B) Freeze core recovered from Control Lake, NWT, Canada, and (C) the preserved sediment-water interface of a freeze core retrieved from Control Lake

homogenization (Figure 4.1C). Because of this, freeze coring is ideal for examining sedimentary records where material near the sediment-water interface is of particular interest.

Combining XRF-CS with freeze-coring methods can provide high-resolution data within sedimentary records, enabling researchers to better examine recent anthropogenic influences on lacustrine systems, study Holocene climate cycles, and bridge the gap between the observed and inferred paleoclimate records. As of yet, analyzing freeze cores with XRF-CS has not been attempted due to the logistical difficulties in maintaining freeze core integrity during analysis, which takes place at room temperature for up to 7 hours per metre, assuming 0.1 mm resolution and 25 second exposure time per measured interval. This paper describes the construction and application of methods for analyzing freeze cores using the Itrax-XRF-CS, and provides an example of the analysis and successful calibration of freeze core data using a freeze core recovered from Control Lake, the Northwest Territories (NWT), Canada.

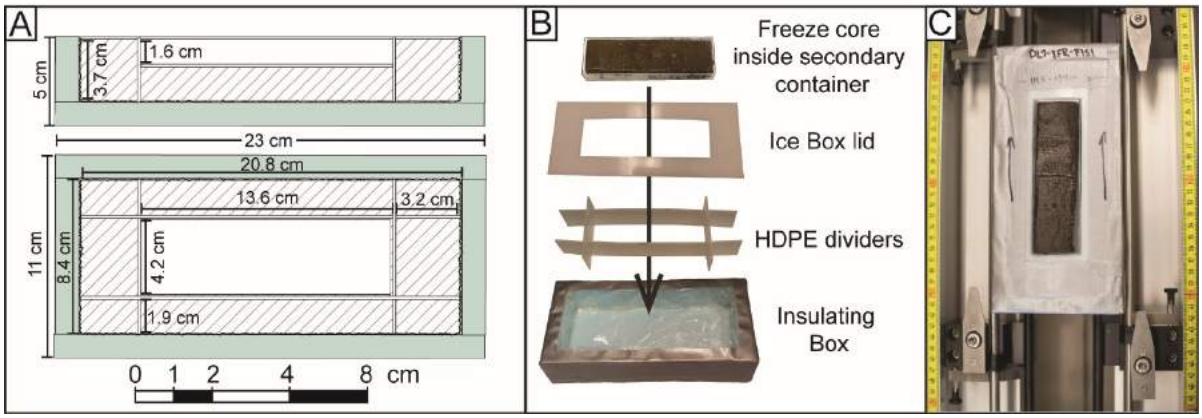

Figure 4.2:(A) Cross section (top) and aerial view (bottom) of iBox-FC. Blue fill represents Styrofoam insulation, hatched areas indicate areas filled with freeze pack gel. (B) Exploded view of different pieces of the iBox-FC including the insulating box, the HDPE sheets used to divide the insulating box into 9 chambers, the lid enclosing the freeze pack gel, and the polystyrene box holding a freeze core slab. (C) A fully assembled iBox-FC loaded into the Itrax-XRF-CS and ready for analysis

4.5 Construction of the Ice-box

In order to maintain the integrity of freeze core slabs during Itrax-XRF-CS scanning, the sediment must remain frozen. To this end, a small ice box freeze core holder, henceforth the iBox-FC, was designed to keep cores cold for the duration of analysis (Figure 4.2). The iBox-FC consists of an open-topped Styrofoam box separated into chambers by high-density polyethylene (HDPE) sheets that are filled with freeze pack gel (*e.g.* hydroxyethyl cellulose (Cellusize), sodium polyacrylate, or vinyl-coated silica gel). Freeze core slabs placed within the central chamber of the iBox-FC show minimal melting (~1 mm of surface melted) after two hours at room temperature, enough time to scan a 12.5 cm core at 1 mm resolution using a 25 second exposure time per measured interval. Detailed dimensions and instructions for construction of the iBox-FC follow. Water can cause significant damage to the x-ray detector located below where cores are analyzed. Care should be taken at all steps during construction of the iBox-FC to minimize any possibility of leaks in the unlikely event that the Itrax-XRF-CS malfunctions and the iBox-FC becomes trapped inside of the central analysis chamber.

The open-topped insulating box is made using 1.3 cm (1/2") thick Styrofoam wall insulation. Two longitudinal Styrofoam walls 23 cm long by 3.7 cm high, and two lateral Styrofoam walls 8.4 cm long by 3.7 cm high are affixed to a Styrofoam base 11 cm wide,

23 cm long, and 1.3 cm thick using gorilla glue (Figure 4.2A, B). These vessel dimensions place the core surface at an ideal height for the Itrax XRF detector when the box is placed on the tracks of an Itrax-XRF-CS at the lowest setting (Figure 4.2C). To ensure no liquid leaks out of the box, the joints of the insulating box are sealed with silicon, and a cling film lining adhered to the inside of the box, again using silicon. Once the glue holding together the insulating box dries, the outside of the box is wrapped in duct tape to further minimize the risk of leaks.

Once assembled, the insulating box is divided into chambers using thin HDPE sheets that will be filled subsequently with freeze-pack gel (Figure 4.2). Although HDPE is not a good conductor of heat, use of other materials can risk contamination (metals), or are difficult to work with and prohibitively expensive (glass, other plastics). To increase transfer of cold directly to the core, thin HDPE are used. Two-mm-thick HDPE is a good compromise between facilitating heat transfer and remaining robust enough to maintain its shape when the freeze pack gel expands. Four rectangles of HDPE, two longitudinal rectangles 20.4 cm long by 3.5 cm high and two latitudinal rectangles 8.4 cm wide by 3.5 cm high, divide the inner chamber of the insulating box into 9 chambers. Slots the same width of the HDPE (2 mm) are cut halfway down the height of the HDPE rectangles centered 3.2 cm from the end of longitudinal rectangles, and centered 2 cm from the latitudinal rectangles; these allow the rectangles to be connected using halved cross lap slot joints. Once the joints are cut, the pieces can be slotted together as illustrated in Figure 4.2B. Once pieced together this frame is placed in the insulating box, which is now divided into nine separate chambers. The outer chambers are then filled with freeze pack gel. Effort should be made to ensure that the gel reaches as close as possible to level with the top of the internal chambers without going over. The central chamber should be approximately half filled with enough freeze pack gel so that when a freeze core slab is eventually placed in it, the slab surface will be level, or just emerging above the surface of the insulating box.

A HDPE lid is then fabricated to cover all chambers except the central opening to minimize possibility of freeze pack gel falling out of the iBox-FC. The lid is shaped like a rectangular donut, 20.4 cm long by 8.4 cm wide with the cut out centre of the lid being

13.7 cm long by 4.4 cm wide (Figure 4.2B). The central cut-out from the HDPE is saved and later placed in the central chamber above the freeze pack gel to separate freeze core material from the freeze pack gel.

It is recommended that the freeze core subsample to be scanned be placed in a separate container sized to fit within the central chamber of the iBox-FC (Figure 4.2B). This facilitates easy removal of freeze core material from the iBox-FC after scanning and protects the subsample from possible contamination associated with coming into contact with freeze pack gel or the HDPE walls of the inner chamber. The dimensions of the iBox-FC as described above was designed to fit polypropylene boxes purchased from US Plastics Corp. (20 dram flextop box, product #201214) with outer dimensions of 13.4 cm long, 4.1 cm wide and 1.8 cm tall.

4.6 Preparing freeze cores for Analysis

Freeze corers used in our field work collect sediment cores 13 cm wide with a maximum length of 2 m. To obtain subsample slabs correctly sized for use with the iBox-FC, freeze cores must be longitudinally and latitudinally sub-sectioned. After an initial cleaning of the freeze core surface, freeze cores are sectioned into small slabs using typical freeze core cleaning implements (chisels, hacksaws, *etc.*). Hacksaws are ideal for making latitudinal core cuts as they minimize material lost during sectioning. A saw with larger teeth, such as a rip saw, should be used for longitudinal cuts as it is much more efficient at slicing through the frozen mud. The utmost care should be taken during sectioning of freeze cores as any cracks during the sectioning process may result in production of invalid data during XRF scanning. If the original freeze core was sectioned in the field for transportation, it is best to use these breaks when preparing subsections for iBox-FC scanning. Alternative equipment, such as ceramic knives, may be used if the purpose of the research is trace element analysis. Between cuts, slicing implements need to be thoroughly cleaned to minimize possible contamination issues.

Once sectioned, freeze core slabs cannot be trimmed in the longitudinal orientation if they are too long without losing data. It is thus recommended that the freeze core slabs be cut slightly shorter than the dimensions of the central chamber. For the iBox-FC vessel described here core slabs are generally cut to 12.5 cm long and 3.6 cm wide, slightly

smaller than the internal dimensions of the inset box. It is vital to keep a thorough record of all slicing procedures, including notes of relative slab lengths and absolute position of slabs within the greater core. It is also useful to manufacture several iBoxes that can be loaded at the same time to increase analysis throughput. Before freeze core material is placed in the iBox-FC, the iBox-FC should be completely frozen. Adding Freeze core material to the iBox-FC before it is completely frozen will cause freeze core section to melt.

As metal implements are used during sub-sectioning of freeze cores, freeze cores should always be cleaned again before analysis with Itrax-XRF-CS. For Itrax-XRF-CS analysis, core slab surfaces need to be made as level as possible to minimize issues caused by surface roughness or analysis of uneven surfaces. If the core surface is uneven due to, for example, an increase in freeze core thickness downcore, HDPE shims can be used to level the core. It is preferable to level the core without the use of shims, however, as the shims reduce the contact of the freeze core slab to the iBox-FC, reducing the ability of the iBox-FC to keep the core cold. A cleaned glass microscope slide can be used to scrape the surface of the core smooth. When cleaning it is important that cleaning be only carried out laterally across the face of the slab to be scanned, to avoid smearing, which may result in false geochemical signals.

4.7 Recommended procedures during analysis

In preparation for analysis, the iBox-FC with contained freeze core slab is removed from the freezer and following standard XRF-CS procedure, a thin mylar sheet is affixed to the surface to ensure that no water is lost due to evaporation during scanning, and to protect the X-ray detector from possible contamination. This film will not adhere to ice, or any core with water content lower than 35% without difficulty (Kido et al., 2006). To ensure the film adheres to the core, the surface of the freeze core slab must be slightly melted. This is accomplished by either leaving the freeze core slab at room temperature for roughly half an hour, or by applying heat to the surface of the core using a heat source for a short period of time. Initial testing and development of the Ice Box took place during humid summer months in southern Ontario. As the room housing the Itrax-XRF-CS at McMaster University does not have humidity control, days with high humidity encouraged

the formation of small water droplets on the core surface. When freeze cores were re-analyzed during the subsequent winter in low-humidity conditions, little condensation was observed on the core surface. As condensation on the surface of the mylar can impact the quality of results, it is recommended that freeze core analysis with Itrax-XRF-CS be conducted under low humidity conditions.

The iBox-FC is then slotted into the Itrax-XRF-CS with the rails lowered to the lowest setting (Figure 4.2C). Afterwards, analysis proceeds following standard Itrax analytical procedures (Croudace et al. 2006). Although X-ray imaging of the freeze core sediments can be performed, however, the iBox-FC may interfere with proper detection of the X-ray signal. Although not performed during initial development of the iBox-FC, X-ray imaging of cores is likely possible. If X-ray imaging is to be carried out in addition to XRF analysis, it is recommended that the analyses are carried out in two separate runs, with freeze core slabs returned to the freezer in between to avoid possible melting of sediments.

Depending on the thickness of the freeze core slab and the ambient temperature, freeze core slabs will remain cohesive for at least 2 hours. The Itrax settings can be altered to accommodate this timing, as well as desired resolution of analysis. As such, higher resolutions necessitate shorter exposure times, or alternatively analysis of shorter core slabs. For a 12.5 cm core, it is possible at room temperature to scan a core segment in an iBox-FC at 1 mm resolution for 25 seconds per interval without sediment melting occurring. To ensure the entire core is scanned, it is sometimes advisable to "over-scan" the core by scanning an additional few mm on either end of the core. This ensures no information is lost at either end of the freeze-core record. Analysis of freeze cores using the Ice-Box generally requires analysis of multiple subsampled slabs. In order to maintain optimal XRF-CS counts between scans, researchers can choose to either adjust XRF parameters to maintain approximately 50 kcps between sections, the recommended value by Cox Analytical Systems, or else keep XRF parameters the same across all core sections. In studies of long sediment cores (100s of metres), it is recommended to adjust XRF parameters before scanning to maintain approximately 50 kcps due to gradual degradation of the x-ray source resulting in decreasing total counts per second over time

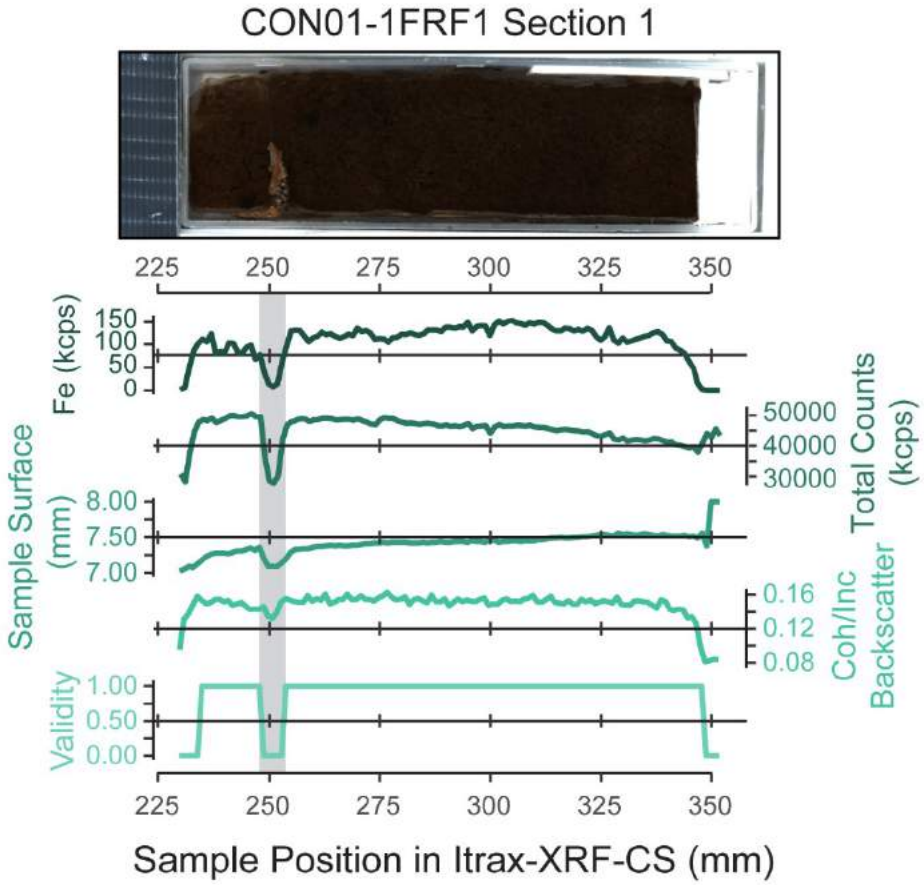

Figure 4.3: Comparison of CON01-1FRF1 Section 1 core image to various parameters of practical use to determine start and end point of a core section. The light grey area denotes a cracked portion of the core that resulted in unusable data.

(Ohlendorf et al. 2015). As most freeze cores do not exceed 2 m, this issue is of less concern for subsamples to be analyzed with the iBox-FC. However, subtle differences in freeze core slab height relative to the X-ray source between difference iBox-FC runs may influence absolute elemental counts, resulting in shifts in the absolute elemental counts between core sections. In any case normalization is almost certainly necessary to account for possible amplitude changes before interpretation of results.

4.8 Post-Analysis Data Processing

Once core scanning and batch re-evaluation is complete, core data must be extracted from the dataset for subsequent analysis. To ensure that no geochemical measurements of non-core material are present in the data, the dataset should be examined for abrupt changes in major elements, total counts per second, sample position, sample validity and using the known total length of core slabs recorded during freeze core sectioning (Figure 4.3). However, when taking these variables into consideration, it can be difficult to discern the absolute edge of a core. Reviewing core data using the Redicore software provided by Cox Analytics helps better discriminate core edges from non-core material as it overlays results directly on an image of the core. When the iBox-FC is used for XRF-CS analysis, the geochemical records begin at roughly 220 mm if using the dimensions for the vessel presented here. Two columns in the XRF-CS dataset for absolute and relative depths help combine all core sections into one record, as well as the subsequent data analysis and interpretation. Assigning absolute and relative core depths is best performed before removal of invalid samples or those with high mean square error (MSE) as poor data for the first and last few mm of XRF-CS results can cause erroneous assignment of depth if removed beforehand.

Analysis of our iBox-FC XRF-CS results show that minor edge effects regularly occur through the lowermost ~5 mm of slabs analyzed (Figure 4.4). These irregularities take the form of an increase in incoherent and coherent x-ray backscatter, which is concurrent with a decrease in total counts per second (kcps) and concentration of abundant elements (Fe in Control Lake core; Figure 4.4B). Although the decrease in incoherent and coherent backscatter may represent an increase in lighter elements (Boyle et al. 2015; Duvauchelle et al. 1999), there was no visible change in sedimentology in our testing to suggest that the results may have been caused by an increase in organic matter or water content in the core slab. The higher x-ray backscatter values may have been due to an increase in the thickness of a layer of water between the core surface and mylar that originated as the core surface slowly melted. If this was the cause, it would be expected that there would have been a gradual increase in x-ray backscatter during scanning, which was not observed (Figure 4.4B). Furthermore, the effect was also observed across multiple cores of varying length, suggesting this phenomenon was not

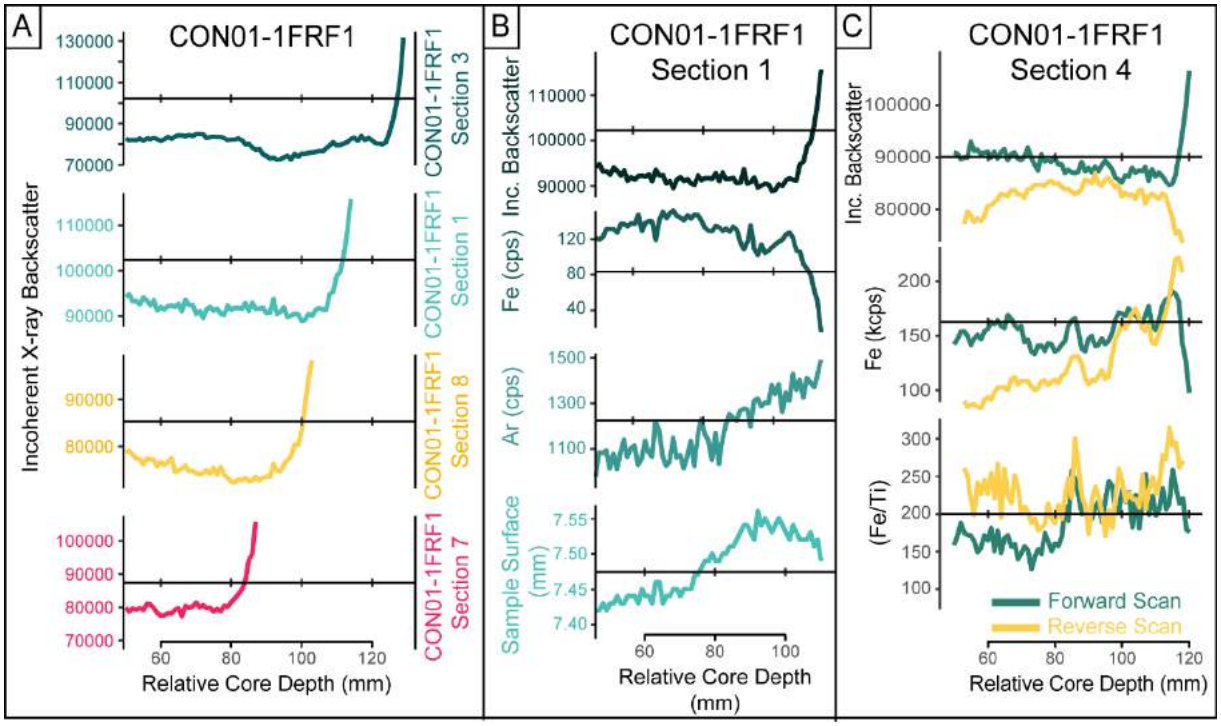

Figure 4.4: (A) Several core sections from CON01-1FRF1 showing an abrupt increase in incoherent x-ray backscatter in the last 5 mm of XRF-CS core scanning. (B) Comparison of the influence of edge effects as indicated by incoherent backscatter to shifts in Fe concentration, Ar concentration, and the surface of the freeze core sample CON01-1FRF1 Section 1. (C) Comparison of Incoherent backscatter, Fe (kcps) and Fe/Ti in cores scanned forwards (turquoise line) and in reverse (yellow line).

due to the melting of core material (Figure 4.4A). An increase in the distance between core surface and detector, possibly due to formation of a fine layer of condensation, is another possible explanation for a decrease in observed kcps. This option was rejected as examination of the Ar record showed no apparent increase coeval with abrupt increase in x-ray backscatter (Figure 4.4B). The most probably explanation for the observed results was that a change in slope through the lowermost few mm of the core slab caused by preferential melting of the edges of the core during slicing, cleaning, and handling, resulted in deflection of X-ray signal. To test this assumption, freeze cores were scanned freeze first forwards (top-down), then in reverse (bottom-up). Incoherent and coherent x-ray back scatter in the reversed core showed that the inverse trend as was observed in freeze core slabs scanned forwards: a sharp decrease in incoherent and coherent x-ray scatter (Figure 4.4C). The inverse trend was not, however, similarly observed in the concentration of major elements, such as Fe, the most abundant element in the tested cores. The impact of this potential

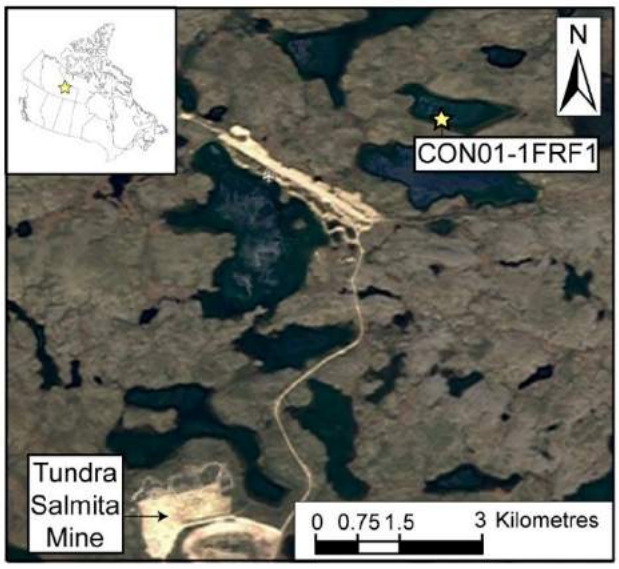

Figure 4.5: Map showing the location of CON01-1FRF1 in Control Lake and nearby Tundra Salmita Mine; Inset shows location of Control Lake in NWT, Canada.

signal degradation on analytical results was tested on a freeze core from a Northwest Territories, Canada. As described in section 6.0 below, these minor edge effects proved to be relatively insignificant, meaning that measured XRF results obtained from these intervals are reliable.

4.9 Application of the equipment

In March, 2016, a 103 cm long freeze core (CON01-1FRF1) was recovered from Control Lake, NWT, Canada (64.07771° N, -111.13493° W; Figure 4.5). Control Lake is a 5 m deep lake with roughly oval shape located ~240 km NW of Yellowknife and just north of the latitudinal treeline in subarctic Canada. Control Lake served as a control lake for an environmental study carried out to evaluate the environmental impact of tailings from the nearby historical Tundra-Salmita gold mine. Control Lake is hydrologically isolated from the flow path that travels from the tailings pond through several small lakes and ponds before connecting to the larger Courageous Lake to the north. In April, 2017, CON01-1FRF1 was sub-sectioned into nine freeze core slabs and transported to McMaster University, Hamilton, ON, Canada, for analysis using Itrax-XRF-CS. CON01-1FRF1 sections one through eight (S1-S8) were analyzed using a Mo-anode at 1 mm resolution, 25 s exposure time, and current and voltage of 22 mA and 25 kV, respectively. Freeze core slabs were analyzed in triplicate, first forwards (top-bottom), then twice in reverse (bottom-top), once at 1 mm resolution and again at 5 mm resolution. The two reverse scans were carried out on only a part of the core to provide triplicate analysis of core material. Freeze core slabs were returned to the freezer and allowed to re-freeze between the first scan and the second/third scan. There was no need to return the iBox-FC to the

freezer between the second and third core scans as the multiple scans took less than 2 hours to analyze collectively.

Results from Itrax-XRF-CS were prepared following the methods described above, and then imported into the ItraXelerate software following the recommendations of Weltje et al. (2015). Following the Itrax-XRF-CS analysis, the freeze core slabs were re-cleaned, and 1 cm long sub-samples were selected for ICP-MS analysis using the results from ItraXelerate calibration analysis as a guideline. Six samples were analyzed in triplicate to provide a measure of absolute geochemical error. Due to the limited material remaining from the freeze core slab, three 1-cm subsamples were combined, allowed to melt, and then homogenized for triplicate analysis of samples. Freeze core subsamples were then submitted to Acme Bureau Veritas, Vancouver, BC, Canada, for ICP-MS analysis. A near total, four-acid digestion was used prior to analysis. Values less than the detection limit in the ICP-MS dataset were converted to 0 values. The standard deviation for elements in the ICP-MS dataset was calculated using the following equation (after Mccurdy and Garrett 2016)

$$\sigma = \sqrt{\left(\frac{\sum_{i=1}^{3}\left(x_{ijn} - \mu_{jn}\right)^2}{3N}\right)}$$

where *x* represents replicate measurement *i* of element *j* in triplicate set *n*, μ represents the mean concentration of element *j* in a replicate set *n*, and N equals the total number of triplicate sets measured. Because data cannot be loaded into ItraXelerate without SiO_2 values, and because MA-ICP-MS cannot detect silicon, a value of 1 ppm Si was added in order to load the ICP-MS dataset.

To test the influence of edge effects on the ability of Itrax-XRF-CS to recreate actual geochemical values, two Itrax-XRF-CS datasets were prepared for calibration. The first, or “original”, dataset represented the entirety of data collect from analysis of freeze core slabs. For the second, or “trimmed”, dataset, analysis results for the lowermost 5 mm from all core scans was removed to eliminate any influence from edge effects. Both datasets were calibrated using the multivariate log-ratio calibration (MLC) method using ItraXelerate software (Weltje et al. 2015). The default sample tolerance in the ItraXelerate

Table 4.1: Comparison of R^2 predicted Itrax-XRF-CS results using a multivariate log-ratio calibration to ICP-MS results using the original dataset and a dataset with values influenced by edge effects removed (trimmed dataset).

Element	Goodness-of-fit R^2	
	Trimmed dataset	Original dataset
As	0.36	0.41
Ca	0.95	0.95
Cu	0.82	0.81
Fe	0.95	0.95
K	0.95	0.94
Mn	0.9	0.91
Ni	0.52	0.53
Ti	0.95	0.94
Zn	0.51	0.53

software is set to 10 mm. As the triplicate ICP-MS values were comprised of 3 cm of sediment, and because the mean sample depth was used to represent depth of geochemical samples, the sample tolerance was increased to 15 mm before calibration was attempted. Nine elements were selected for calibration that spanned a range of poor too excellent detection, and that are of general interest to paleolimnologists as they represent the lithogenic fraction of the sediment, redox-sensitive elements, and variations in carbonate deposition: As, Ca, Cu, Fe, K, Mn, Ni, Ti, and Zn. Relationships between observed and predicted values were measured by a goodness-of-fit R^2 value (Table 4.1). As the calibrated output from ItraXelerate assumed that all calibrated elements sum to unity, and because the nine elements calibrated comprise, on average 8.51 % of the total sample based on ICP-MS results, calibrated results output from the ItraXelerate were converted to proportions of this average percentage.

4.9.1 Comparison of the Original and Trimmed datasets

For both the original and trimmed datasets, R^2 values showed strong relationships between observed and predicted results (R^2 >0.81) for six of the nine elements calibrated (Table 4.1). Arsenic, Ni and Zn exhibit relatively low R^2 values in both original and trimmed datasets. The ^{R2} values for both original and untrimmed dataset were within 0.1 point of each other, with the exception of As that increases from R^2 =0.36 to R^2 =0.41 from the original to the trimmed dataset, respectively. This similarity is expected as removal of the last 5 mm represented a loss of only 4% of the dataset, making both original and trimmed datasets very similar. Comparison of the Itrax-XRF-CS results with ICP-MS results for

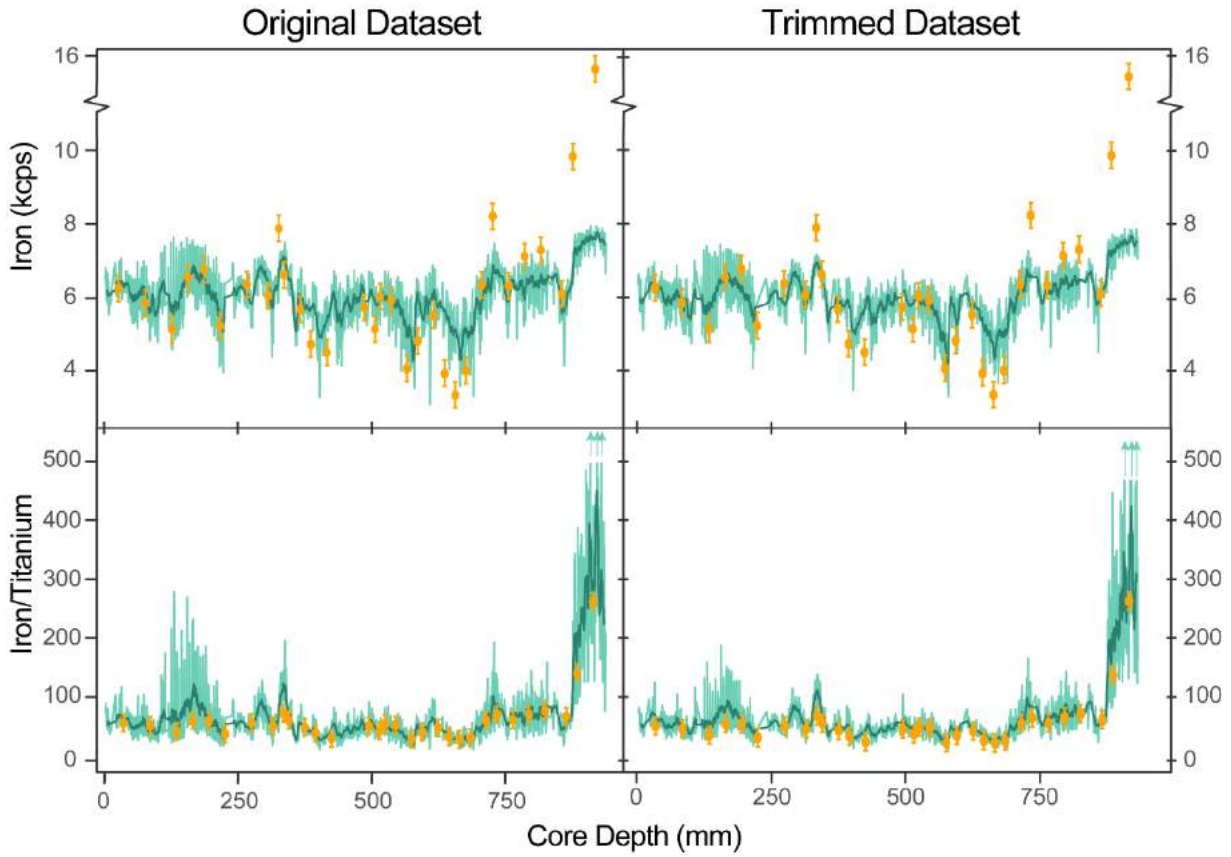

Figure 4.6: Comparison of Itrax-XRF-CS data (light green line) to ICP-MS data (orange circles) for raw Fe and Fe/Ti for CON01-1FRF1-S1 to S9. Graphs in the left column where created using the original dataset and the graphs in the right column where created using a dataset with all points influenced by edge effects removed. The dark green line represents a 10-point moving average of Itrax-XRF-CS data. Orange error bars represent two standard deviations of ICP-MS data.

both the original and trimmed datasets showed little difference, and the agreement between XRF-CS and ICP-MS results were increased in both cases through use of elemental ratios (Figure 4.6). These results suggest that inclusion of data obtained from intervals of core segments subtly influenced by edge effects is accurate, and normalized data can be reliably use for interpretation of XRF-CS results, calibration and critically in applications where elemental ratios are used.

4.9.2 Comparison of Original dataset to ICP-MS data

The Itrax-XRF-CS results show strong correlations for most elements included in the calibration, with the exception of As, Ni, and Zn with R^2 values of 0.36, .0.52 and 0.51 respectively (Table 4.1, Figure 4.7). The poor correlation of As to Itrax-XRF-CS data may have been caused by the tendency of multi-acid digestion to volatilize As (Parsons et al.

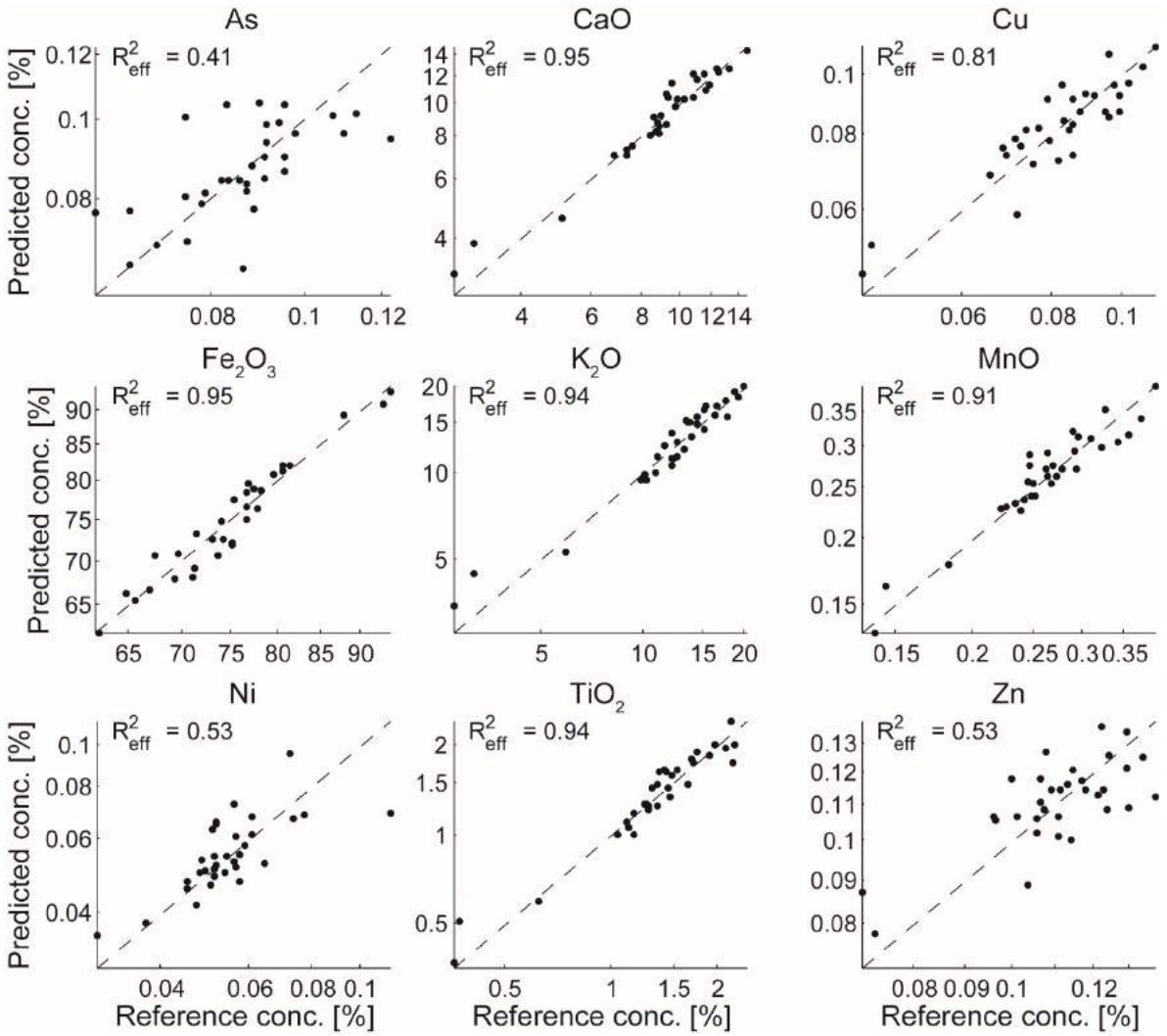

Figure 4.7: Output from Itraxelerate multivariate log-ratio calibration of Itrax-XRF-CS data using ICP-MS data from CON01-1FRF1-S1 to S9. Graphs represent the ability of Itrax-XRF-CS concentrations predicted using MLC (y-axis [%]) to recreate ICP-MS results (x-axis [%])

2012). The combination of geochemical error due to As volatilization in the ICP-MS dataset, and possible attenuation of the XRF-CS signal associated with high water content and organic matter in the freeze core likely resulted in weaker correlations. Nickel and Zn results, however, were comparable to Cu in terms of atomic size, mass, and detection using Itrax-XRF-CS, yet had much lower R^2 values than Cu. Both Ni and Zn had relatively low abundant in the ICP-MS dataset (mean <100 ppm), yet Cu had an average abundance of ~66 ppm and higher R^2 (0.82). Furthermore, Cu, Ni and Zn do not have any apparent overlapping X-ray emission lines with other elements included in this

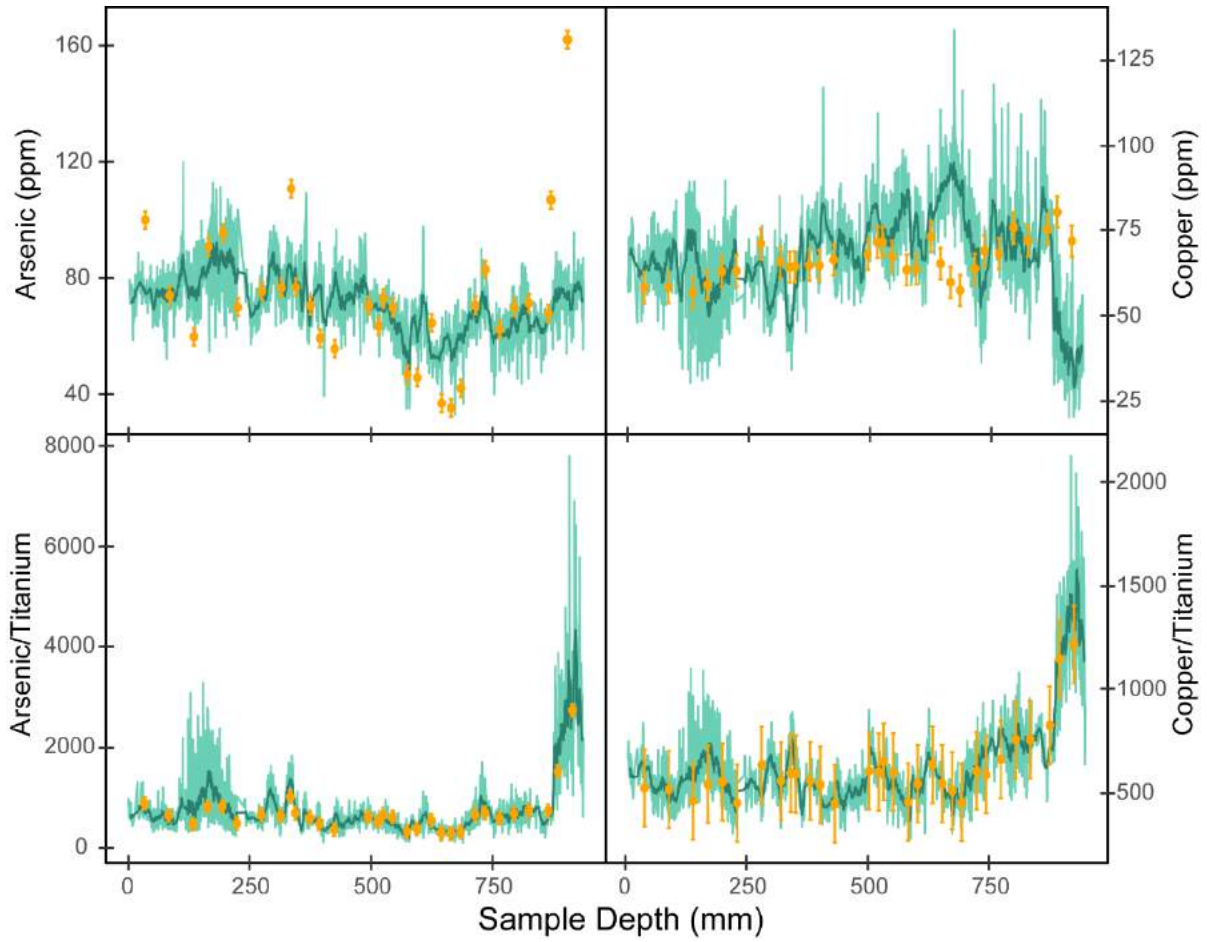

Figure 4.8: Comparison of Itrax-XRF-CS data (light green) to ICP-MS results (orange circles) from CON01-1FRF1-S1 to S9. Two elements, Arsenic (left column) and Cu (right column), and ratios of As and Cu to Ti are shown for comparison. The dark green line represents a 10-point running mean of Itrax-XRF-CS results. Orange error bars represent two standard deviations about ICP-MS results.

Itrax-XRF-CS analysis. Sixteen percent of Zn measurements were below detection, possibly explaining the poor correlations, yet, there are no non-detect values in the Ni data, and less than 1 % non-detect values for Cu Data. Copper data in the ICP-MS dataset has a lower relative standard error (3%) in comparison to Ni (10.5 %) and Zn (~6 %). Nickel and Zn show weak to moderate positive correlations (Pearson's r_{Ni} = 0.41, r_{Zn} = 0.33) to the ratio of incoherent/coherent x-ray backscatter, whereas Cu shows a weak negative correlation (Pearson's r_{Cu} = -0.41). It is possible scatter or absorption effects were influencing XRF-CS detection of Zn and Ni to a greater degree than Cu. However, as signal attenuation preferentially affects elements with weaker fluorescent energies

(Kido et al., 2006), and as fluorescence energies are related to the atomic mass of elements, it is expected that Cu, Zn and Ni should all be affected similarly due to the similarity of their atomic mass. Furthermore, this weak correlation may additionally be related to variations in core composition rather than signal attenuation, as the incoherent/coherent backscatter ratio is commonly used as a proxy for water or organic content (Boyle et al. 2015; Löwemark et al. 2011). It seems likely that the ICP-MS dataset better captured the full variability of Cu in sediment than Ni and Zn, and thus better predicts Cu concentration based on XRF-CS data.

Comparison of predicted absolute elemental concentrations from ICP-MS results to XRF-CS trends showed moderate correspondence for elements with weak or high R^2 values (Figure 4.8). The ICP-MS results followed trends similar to that provided by the XRF-CS data, although in several cases the XRF-CS data did not fall within two standard deviations of the ICP-MS results. In all datasets, there appeared to be a deviation of XRF-CS data from ICP-MS data near the base of the dataset, where ICP-MS data showed a drastic increase in As and Cu concentrations. This suggested that XRF-CS calibration may not be able to fully capture data that exhibit large variability throughout sedimentary cores. Normalizing elemental concentrations to a conservative element, in this case Ti, greatly increased the correspondence between the two disparate geochemical methods, likely because both elements suffered from similar specimen effects during analysis. For the elemental-normalized data, most ICP-MS results fell within the 10-point running mean of the XRF-CS data.

4.10 Conclusions

The iBox-FC containment vessel delays thawing of highly perishable frozen sediments for up to two hours, adequate time to carry out high resolution Itrax-XRF-CS analysis. The iBox-FC is particularly useful for analyzing cores in environments where conventional gravity corers are difficult to deploy (*e.g.* low sedimentation rate environments, lakes where the uppermost sediments are poorly consolidated). Calibration of XRF-CS values to absolute concentrations based on multi-acid ICP-MS results using the MLC method provided accurate results, with most correlations showing $R^2>0.81$. Predicted XRF-CS values showed moderate agreement with ICP-MS results when using raw elemental

counts. Elemental normalization of XRF-CS data greatly improved the concordance between results obtained using the two geochemical methods. Minor edge effects that were observed to occur through the last ~5 mm of freeze core slabs were demonstrated to have an insignificant impact on derived SRF-CS results, at worse resulting in a loss of ~4 % of overall data from the impacted interval when normalization procedures were used on the data.

4.11 References

Andrade CF, Jamieson HE, Kyser TK, Praharaj T, Fortin D (2010) Applied Geochemistry Biogeochemical redox cycling of arsenic in mine-impacted lake sediments and co-existing pore waters near Giant Mine, Yellowknife Bay, Canada. Applied Geochemistry, 25(2):199–211.

Boyle JF, Chiverrell RC, Schillereff D (2015) Approaches to water content correction and calibration for uXRF Core Scanning: Comparing X-ray Scattering with Simple Regression of Elemental Concentrations. In Micro-XRF Studies of Sediment Cores: Applications of a Non-Destructive tool for Environmental Sciences: Part III (Vol. 17, pp. 373–390).

Cobelo-Garcia A, Prego R (2003) Heavy metal sedimentary record in a Galician Ria (NW Spain): background values and recent contamination. Marine Pollution Bulletin, 46:1253–1262.

Croudace IW, Rindby A, Rothwell RG (2006) ITRAX: description and evaluation of a new multi-function X-ray core scanner. In Rothwell RG (eds.) New techniques in sediment core analysis. Geological Society London Special Publications, 267:51-63.

D'arrigo R, Wilson R (2008) El niño and Indian Ocean influences on Indonesian drought: implications for forecasting rainfall and crop productivity. International Journal of Climatology, 28:611–616.

Deng X, Huang J, Qiao F, Naylor RL, Falcon WP, Burke M, Rozelle S, Battisti D (2010) Impacts of El Nino-Southern Oscillation events on China's rice production. Journal of Geographical Sciences, 20(1):3–16.

Donnelly JP, Woodruff JD (2007) Intense hurricane activity over the past 5,000 years controlled by El Niño and the West African monsoon. Nature, 447(7143):465–8.

Duvauchelle P, Peix G, Babot D (1999) Effective atomic number in the Rayleigh to Compton scattering ratio. Nuclear Instruments and Methods in Physics Research, Section B: Beam Interactions with Materials and Atoms, 155(3):221–228.

Ezer T, Atkinson LP (2014) Accelerated flooding along the U.S. East Coast: On the impact of sea-level rise, tides, storms, the Gulf Stream, and the North Atlantic Oscillations. Earth's Future, 2:362–382.

Holmgren M, Scheffer M, Ezcurra E, Gutiérrez JR, Mohren GMJ (2001) El Niño effects on the dynamics of terrestrial ecosystems. Trends in Ecology & Evolution, 16(2):89–94.

Iizumi T, Luo J-J, Challinor AJ, Sakurai G, Yokozawa M, Sakuma H, Brown ME, Yamagata T (2014) Impacts of El Niño Southern Oscillation on the global yields of major crops. Nature Communications, 5:1-7.

Kido Y, Koshikawa T, Tada R (2006) Rapid and quantitative major element analysis method for wet fine-grained sediments using an XRF microscanner. Marine Geology, 229:209–225.

Kilduff DP, Di Lorenzo E, Botsford LW, Teo SLH (2015) Changing central Pacific El Niños reduce stability of North American salmon survival rates. Proceedings of the National Academy of Sciences, 112(35):10962–10966.

Kitzberger T, Swetnam TW, Veblen TT (2001) Inter-Hemispheric Synchrony of Forest Fires and the El Nino-Southern Oscillation. Global Ecology and Biogeography, 10(3):315–326.

Löwemark L, Chen H-F, Yang T-N (2011) Normalizing XRF-scanner data: A cautionary note on the interpretation of high-resolution records from organic-rich lakes. Journal of Asian Earth Sciences, 40(6):1250–1256.

McCurdy MW, Garrett RG (2016) Geochemical Data Quality Control for Soil , Till and Lake and Stream Sediment Samples. Geological Survery of Canada Open File Report 7944. (40 p.)

Ohlendorf C, Wennrich V, Enters D (2015) Experiences with XRF-Scanning of Long Sediment Records. In Micro-XRF Studies of Sediment Cores: Applications of a Non-Destructive tool for Environmental Sciences: Part III (Vol. 13, pp. 351–372).

Parsons MB, LeBlanc KWG, Hall GEM, Sangster AL, Vaive JE, Pelchat P (2012) Environmental geochemistry of tailings, sediments and surface waters collected from 14 historical gold mining districts in Nova Scotia. Geological Survey of Canada Open File Report 7105 (365 p.)

Roulet M, Lucotte M, Canuel R, Farella N, Courcelles M, Guimaraes J-RD, Mergler D,

Amorim M (2000) Increase in mercury contamination recorded in lacustrine sediments following deforestation in the central Amazon. Chemical Geology, 165:243–266.

Stenseth NC, Ottersen G, Hurrell JW, Mysterud A, Lima M, Chan K-S, Yoccoz NG, Adlandsvik B (2003) Studying climate effects on ecology through the use of climate indices: the North Atlantic Oscillation, El Niño Southern Oscillation and beyond. Proceedings. Biological Sciences / The Royal Society, 270(1529):2087–2096.

Weltje GJ, Bloemsma MR, Tjallingii R, Heslop D, Röhl U, Croudace IW (2015) Prediction of Geochemical Composition from XRF Core Scanner Data: A New Multivariate Approach Including Automatic Selection of Calibration Samples and Quantification of Uncertainties. In Micro-XRF Studies of Sediment Cores: Applications of a Non-Destructive tool for Environmental Sciences: Part III (Vol. 17).

Chapter 5: Climate-induced variations in sedimentary arsenic sequestration in Northern Canada during the Mid- to Late-Holocene

5.1 Authors and Addresses

Gregory BRB[1], Patterson RT[1], Galloway JM[1,2,3]

[1]Ottawa-Carleton Geoscience Centre, Carleton University, 1125 Colonel By Drive, Ottawa, ON, Canada, K1S 5B6

[2]Aarhus Institute of Advanced Studies, Aarhus University, 8000 Aarhus C., Denmark

[3]Geological Survey of Canada/National Resources Canada (Commission géologique du Canada/Ressources naturelles Canada), 3303 33 St. N.W., Calgary AB, Canada, T2L 2A7

5.2 Foreword

This contribution represents an examination of the controls on As concentration in lake sediment at coarse temporal resolution (centennial to millennial). Arsenic stability in lake sediment is heavily dependent on the redox state of a lake. Because temperature and precipitation can alter oxygen removal from the water column, As stability is expected to be impacted by climate variability. This relationship has been observed in recent sediments, but has rarely been quantified during the Holocene. Here we examine a freeze core recovered from Control Lake, Northwest Territories, using ICP-MS following *aqua regia* digestion at near-contiguous cm-scale resolution and Arcellinida counts every 5 cm. Together, sediment geochemistry and changes in Arcellinidan communities were used to characterize possible post-depositional mobility of As, and understand the impact of regional climate change on As stability in Control Lake sediment. This manuscript has been prepared for submission to *Science of the Total Environment* pending the addition of Rock Eval pyrolysis results still forthcoming.

I collected core material in the field, sub-sampled cores for radiocarbon, ICP-MS, Rock Eval pyrolysis and Arcellinida analysis, and enumerated Arcellinida in sediment samples. I wrote the manuscript and drafted the figures. I completed statistical analyses with helpful comments and recommendations by N.A. Nasser. Dr. R.T. Patterson and Dr. J.M. Galloway helped to conceptualize this project. All authors provided feedback that helped to refine the manuscript. This research was funded by a Polar Knowledge Canada grant to Dr. Patterson and Dr. Galloway.

5.3 Abstract

High latitudes are projected to experience disproportionate effects from modern climate change relative to lower latitude regions. Characterizing the response of metal(loid) contaminants to climate change is necessary for the management of northern environmental systems. In the Northwest Territories, Canada, arsenic (As) contamination from gold mining and naturally elevated geogenic sources of this metalloid has resulted in As concentration in lake sediments that are above levels recommended by the Canadian Council of Ministers of the Environment. To understand the impact of climate change on sedimentary As concentrations, a 135-cm long freeze core (CON02) was recovered from Control Lake (64.07771°N, -111.13493°W) ~240 km north of Yellowknife at a site considered to be unimpacted by As contamination from gold mining. Sediment geochemistry was analyzed at near contiguous 1-cm resolution by ICP-MS following *aqua regia* digestion. Arcellinida (testate lobose amoeba), micro-organisms that have been shown to respond to As concentration, were enumerated downcore at 5-cm intervals to assess post-depositional movement of As. Radiocarbon dating was used to provide temporal reference to core depth. Arcellinida indicate a generally healthy system, with oligo- to mesotrophic conditions. Redundancy analysis (RDA) comparing Arcellinida and ICP-MS geochemical determinations, and stratigraphic comparison of As and Arcellinida variations suggests stress indicator taxa were not strongly related to As concentrations in the core, possibly indicating post-depositional movement of As. Examination of ICP-MS results using CONISS cluster analysis showed three phases of deposition. Phase 1: ca. 4100–3250 cal. BP contains sediment with relatively low As concentration (50–100 ppm), low concentration of minerogenic indicators (K, Rb), and elevated Ca/Rb indicative of and higher productivity associated with the relatively warm temperatures and more northern-positioned treeline. Phase 2: ca. 3250–2150 cal. BP exhibited the highest concentrations of As (116–258 ppm) associated with a reduced terrestrial organic matter (OM) and a shift in sedimentation towards increased minerogenic input. Arsenic was sequestered in sediment only after major changes in minerogenic content, suggesting reduced OM may have induced sequestration of As in sediment. Phase 3: ca. 2150–0 cal yr. BP corresponded to a shift to tundra vegetation in the catchment and establishment of near-modern climate conditions. Within Phase 3 two major shifts in As concentration occur that

we interpret to be in response to temperature change. Shifts in temperature caused by the MWP and LIA impacted As sequestration through increased autochthonous OM production. This process in turn led to increased As stability in sediments due to prevailing reducing bottom water and sediment porewater conditions. Both temperature and sedimentary processes acted as important controls on As concentration and long-term stability in Control Lake over the late Holocene.

5.4 Introduction

The Arctic is projected to experience greater impacts associated with changing climate than lower latitudes due to unique climate feedback loops (Overpeck et al. 1997; SWIPA, 2017). In response to recent climate change, there has been an observed decrease in permafrost (Payette et al. 2004; Smith et al. 2005; Coleman et al. 2015), longer ice-free seasons (Michelutti et al. 2003; Duguay et al. 2006; Arp et al. 2010; Šmejkalová et al. 2016), reduction of the extent and volume of sea ice (Stroeve et al. 2007; Kwok and Rothrock 2009), changes to the hydrological cycle (Jacques and Sauchyn 2009) and alterations to forest fire regimes (Hu et al. 2010; Chipman and Hu 2017) in subarctic and Arctic environments. These climate-induced environmental changes impact chemical cycling in the environment through alteration of the rate of weathering, movement of chemicals through environmental systems, or mechanisms of chemical sequestration (MacDonald et al. 2005; Spence et al. 2014). The cumulative effects of these mechanisms may cause the release of previously stored chemical contaminants, that may have a deleterious effect on northern ecosystems. It is imperative that the impact of climate change on geochemical cycling be characterized to predict the influence of future climate change on ecosystems in northern environments.

Arsenic (As) is a metal(loid) naturally found in environmental systems. Concentrations of As may be elevated locally due to bedrock geology and derived surficial materials, particularly in association with hydrothermal gold ores, or otherwise through anthropogenic contamination as a by-product of ore extraction, agricultural practices, or treatment of lumber (Smedley and Kinniburgh 2000; Bowell et al., 2014). Arsenic is a major element of concern in the Northwest Territories (NT), Canada due to a legacy of mining and local geogenic sources. Elevated natural background concentrations of As in lake sediments of the Yellowknife area (> 20 ppm As; Galloway et al. 2015) are higher than the CCME Interim Sediment Quality Guideline and the Probable Effect Level for the protection of aquatic life (5.9 ppm and 17 ppm, respectively; CCME 2001). Elevated background As concentrations in the region are partially due to weathering of bedrock that host elevated As concentration. This geogenic source is overprinted by substantial As contamination in the area associated with gold ore processing. The Giant Mine (1948–2002) extracted and processed refractory gold from arsenopyrite through roasting

followed by density separation (Silke 2009). The roasting of ores before density separation volatilized As, and ultimately released ~20,000 tonnes of arsenic trioxide directly into the environment, most of which occurred during the early operation of mines in the region (Galloway et al. 2012, 2015, 2018). Dissemination of this As into the atmosphere resulted in widespread contamination of the landscape along the direction of prevailing winds. As a result of legacy mining activities, median As concentration in lake sediments within an immediate zone of contamination (~20 km) of 600 ppm, with some lakes exhibiting sedimentary As concentrations greater than the analytical detection limit used in previous studies (> 10,000 ppm; Galloway et al. 2012, 2015, 2018; Palmer et al. 2015; Nasser et al. 2016). Continued interest in the extraction of gold from similar deposits in the mineral-rich Yellowknife region raises concerns about additional contamination. Environmental regulations have since been enacted that require remediation of impacted environmental systems to natural conditions after mine closure. A major factor that needs to be considered for reliable remediation of environmental systems and sustainable future resource development is the long-term impact of climate change on As concentrations in lake sediments and the conditions that may induce sequestration or release of As in environmental reservoirs.

Due to the redox-sensitivity of As and post-depositional mobility, reconstructing As concentrations over time using sediment geochemistry alone is difficult. Several studies examining past As contamination in the Yellowknife region document two As peaks; a deep peak associated with initial contamination; and, a secondary peak in shallower sediments caused by post-depositional migration (Andrade et al. 2010; Gavel et al. 2018; Van Den Berghe et al. 2018; Schuh et al. 2019). Although the presence of the double peak in As concentrations observed in the aforementioned studies suggests that variations in As can be preserved over centennial timescales, but that the absolute magnitude may be diluted by subsequent cycling of As in the system, or may be lost all together over extended periods of anoxia present after burial of sediment. Paleo-As signals may be further complicated by variations in the environmental system. Studies have shown that changes in lake productivity, and thus the oxygenation of sediment, can alter the amount of As retained in sediment (Martin and Pedersen 2002; Galloway et al. 2018). Variations in sedimentary As downcore may therefore be associated with changes

in As input into environmental systems, or variations in the long-term stability of As signal as controlled by productivity or sediment compositional changes. Although it is difficult to characterize past controls on absolute As concentrations, it should be possible to understand climate controls on ultimate sequestration of As in environmental systems. Moreover, non-geochemical proxies for As concentration, where available, make it possible to characterize initial increases in As and their subsequent sequestration under unique environmental conditions.

Arcellinida are generally immobile in the sediment column (Patterson and Kumar 2000a) and preserve a snapshot of environmental conditions at the time of sedimentary deposition. Arcellinida (testate lobose amoeba), are a group of protists that agglutinate a test from surrounding minerogenic material or scavenged skeletal material (Patterson and Kumar 2000a). Arcellinida are ubiquitous in freshwater (Patterson and Kumar 2000a; Nasser et al. 2016; Steele et al. 2018) to brackish water environments (Collins et al. 2015; Van Hengstum et al. 2015; Peros et al. 2017), and have been used previously as indicators of lake trophic state (Roe et al. 2010; Patterson and Roe 2012; Drljepan et al. 2014; Prentice et al. 2018), salinization of lake systems (Roe and Patterson 2014; Cockburn et al. in press), land-use change (Patterson et al. 2002), ecosystem health (Neville et al. 2011), and metal contamination (Kauppila et al. 2006; Reinhardt et al. 2006; Kihlman and Kauppila 2009; Nasser et al. 2016; Gavel et al. 2018). Recent work in the Yellowknife area indicates that testate amoeba communities are highly sensitive to variations in sediment As concentrations, with assemblages dominated by stress indicator taxa (*Difflugia elegans, Centropyxis constricta* “constricta”, *C. constricta* “aerophila”) found in lakes with high (>360 ppm) to extreme (>760 ppm) As concentrations (Nasser et al. 2016; Nasser et al. in press). Examination of testate amoeba communities for key As-indicating taxa may thus inform whether an observed change in As concentration in sediment is the result of new deposition of arsenic into the system, or remobilization of As in the sediment column due to shifts in environmental parameters within the lake systems.

To understand the impact of climate on transport and long-term stability of As in lake sediment, two cores were recovered from Control Lake, NT, a site un-impacted by

legacy mining. Elemental geochemistry was determined through inductively coupled plasma mass spectrometry (ICP-MS) following *aqua regia* digestion. Bulk geochemistry was compared to shifts in relatively immobile Arcellinida communities to elucidate whether observed signals in sediment cores were associated with *in situ* increases in As in the environment, or secondary sequestration of As through redox pathways and As-movement through the sediment.

5.5 Background – As mobility in lake sediments

In lacustrine sediments, As is commonly found as inorganic arsenate (As(V)) in oxidizing environments, arsenite (As(III)) in reduced environments, or as organic methylated arsenic species (Campbell and Nordstrom 2019). The mobility of As is dictated by the availability of Fe and Mn oxides and (oxy)hydroxides, sulfides and organic matter to which As readily sorbs to or complexes with (Figure 5.1A; La Force et al. 2000; Du Laing et al. 2009; Guénet et al. 2016; Campbell and Nordstrom 2019). Stability of these phases, as well as the stability of As in the system, is controlled by the pH and redox state of the system (Smedley and Kinniburgh 2000; Campbell and Nordstrom 2019). Under oxygenated conditions in sediment, As is typically present as As(V) sorbed onto Fe and Mn (oxy)hydroxides (Torres et al. 2015; Guénet et al. 2016; Lock et al. 2018). Under reducing conditions, reductive dissolution of metal-(oxy)hydroxides (*e.g.* FeO(OH)) releases As(III) into sediment porewaters or into the overlying water column. If conditions in the shallow sediment become euxinic (no oxygen, high sulfide), precipitation of FeS can occur, typically as amorphous mackinawite, which again acts as a sink for As (Bostick and Fendorf 2003; Xu et al. 2011; Burton et al. 2013; Torres et al. 2015). If reducing conditions persist, and pending the availability of elemental sulfur or sulfide, FeS may be oxidized by sulfur species to framboidal pyrite (FeS_2) (Benning et al. 2000; Butler and Rickard 2000; Burton et al. 2013; Schuh et al. 2019; Thiel et al. 2019). Pyrite is typically assumed to be the stable end-member of the iron-sulphur pathway under reducing conditions with adequate sulfate availability, and acts as a key sink for As that readily sorbs to pyrite or partially replaces S in pyrite and iron mono-sulfides (Burton et al. 2013; Neumann et al. 2013; Torres et al. 2015; Schuh et al. 2019). Although it is possible for other As-sulfides, such as realgar or orpiment, to form, their precipitation typically only

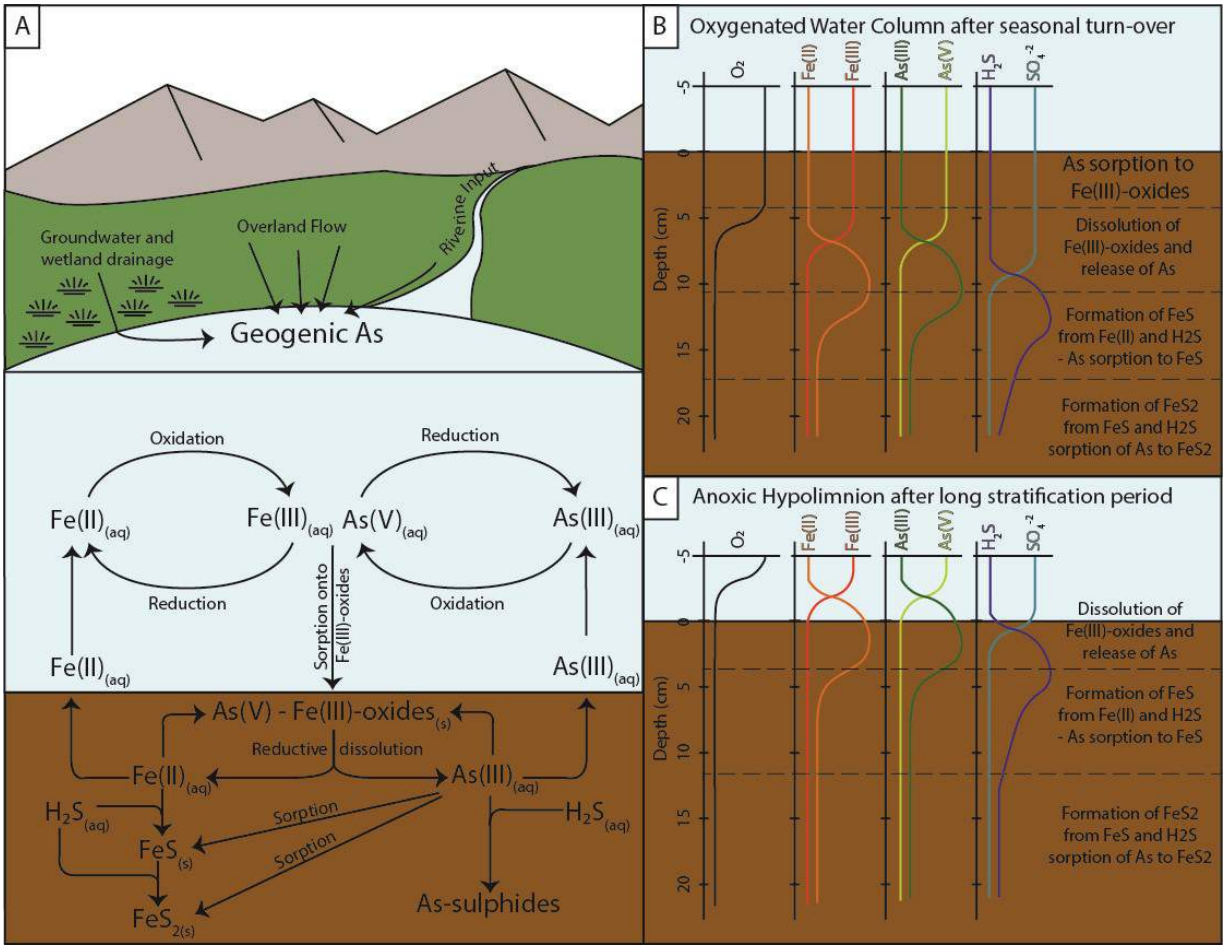

Figure 5.1: The arsenic cycle in lacustrine systems and its relation to Fe and S in sediment porewater of lakes. (1A) General model for As movement in a lake. (1B) Expected As concentrations in porewaters under oxygenated bottom waters. (1C) Expected As concentrations in porewaters under anoxic conditions.

occurs where lower iron concentrations result in greater availability of sulfide in sediment porewater (Wilkin and Ford 2006).

Arsenic movement in sediment is cyclical under typically assumed dimictic lacustrine progression (Figure 5.1). Seasonal turnover of lake waters results in oxygenation of the water column and creates a redoxicline in the sediment column. The depth of redoxiclines in lake sediments can vary drastically depending on the time of year, the organic content in sediment, and the stratification of lakes. Several studies have observed redoxiclines at depths from 0.5 to 10 cm in sediment columns (Spliethoff et al. 1995; Torres et al. 2015; Lock et al. 2018; Van Den Berghe et al. 2018), with an extreme

example of > 45 cm deep in intertidal systems where sediment is exposed to oxygen during low tide (Masuda et al. 2005; Noël et al. 2017). In the sediment column, the consumption of oxygen during the decomposition of (OM) gradually depletes oxygen in the sediment, resulting in reducing conditions at depth. The location of the redoxicline within or above the sediment column is a major control on the sequestration of As in sediment. Arsenic is transferred to porewater at the redoxicline through reductive or oxidative dissolution of minerals, a process that typically occurs in days to weeks (Burton et al. 2006; Polizzotto et al. 2006; Burton et al. 2013; Meng et al. 2016; Choppala et al. 2017). Once dissolved, As diffuses away from its source until it reaches a zone conducive to re-adsorption or re-precipitation of minerals, either under more reducing conditions where sulfide availability promotes precipitation of FeS, or under oxidizing conditions where it will be sorbed to FeO(OH). If the redoxicline is above the sediment-water interface, As diffuses into the overlying waters (Figure 5.1C). A thick oxidized layer within the sediment acts to reduce As release into overlying lake systems by trapping upward diffusing As on FeO(OH) (Figure 5.1B). Arsenic will cycle through sorption onto Fe-O(OH) and FeS until sedimentation results in the sequestration of As into the permanently anoxic zone below the oscillating redoxicline in the lake sediment.

5.6 Study Area

Control Lake is located ~240 km NE of Yellowknife on the former Tundra/Salmita Mine property. The region is within the Courageous Lake Greenstone Belt that is composed of ca. 2.6 Ga metamorphosed volcanic and sedimentary rocks that belong to the Yellowknife Supergroup (Moore, 1956; Padgham 1992; Tetra Tech Wardrop 2012). The landscape consists of hummocks of bedrock outcrops and swales filled with till (McCurdy and Mcneil 2014); lakes dot the landscape filling topographic lows left by glaciated terrain. Geochemical analysis of till in the region showed the <0.002 mm fraction to be dominated by Fe, Na, Mg, and Ca, with minor concentrations of As, Pb, Hg, and other heavy metal(loid)s (Moore, 1986). The study area is ~80 km north of the modern treeline and is characterized by low, shrub-like tundra vegetation (Seabridge Gold Inc. 2010; Aboriginal Affairs and Northern Development Canada 2013). The region exhibits a tundra-desert climate, with an average yearly precipitation of 213 mm) most of which occurs from July

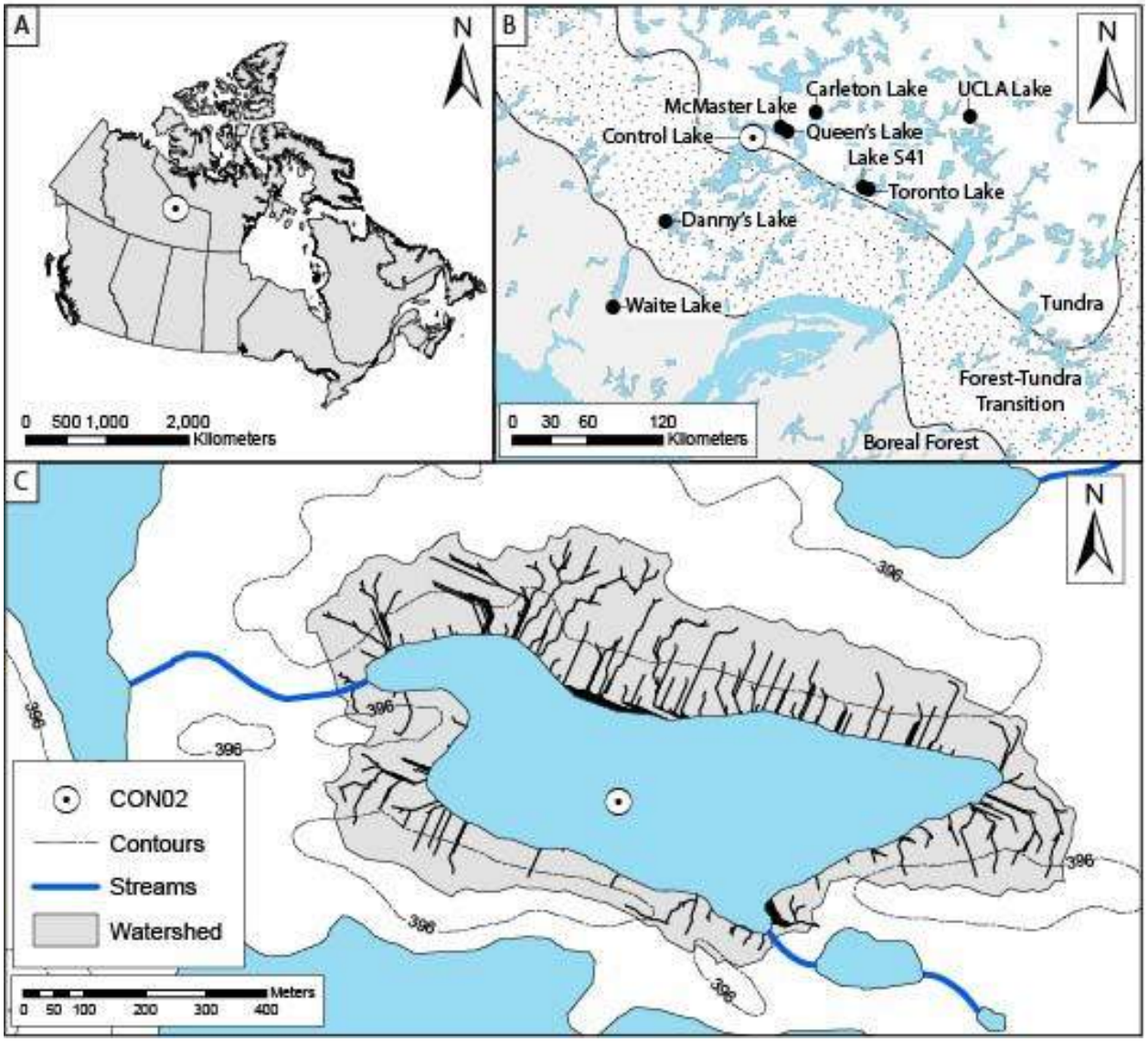

Figure 5.2: Location of Control Lake and core CON02 in the context of (A) Canada, and (B) the Northwest Territories and location of various paleoclimate records discussed in this paper. (C) Control Lake and location of CON02. The grey polygon indicates the watershed delineated for Control Lake based on 2-m DEM of the location; black lines indicate flow paths towards the lake.

to September (125 mm, 2007–2010 data; Seabridge Gold Inc. 2010). The average daily temperature is -9.2 °C with a range from -43.1 to 26 °C (Seabridge Gold Inc. 2010). The region experiences long winters and short summers, with typical freeze-up of lakes occurring in late September and break-up occurring in June (Aboriginal Affairs and Northern Development Canada 2013). Typical ice thickness on lakes can reach up to 2-m-thick (Aboriginal Affairs and Northern Development Canada 2013) and varied from 1.0 to 1.3 m on lakes sampled during field work in March, 2016.

Gold deposits were first recognized near Courageous Lake in 1939. Claims were staked after subsequent exploration in 1946 by Territories Exploration Limited (Moore 1986). Ore extraction and processing on site occurred between 1964-1968 and again from 1983-1986 (Silke 2009; Aboriginal Affairs and Northern Development Canada 2013). After production ceased in 1986, there was concern for seepage of mine tailings from a tailings containment pond through a series of small lakes that ultimately drain into Courageous Lake. Subsequent studies suggest that widespread metal(loid) contamination from the tailings containment pond has resulted in elevated metal(loid) concentrations in several lakes along this flow path from the tailings pond towards Courageous Lake (Miller et al. 2019; Aboriginal Affairs and Northern Development Canada, 2013). Control Lake is upstream of this flow path and was not observed to show anomalously high metal(loid) concentrations during recent water monitoring (Aboriginal Affairs and Northern Development Canada 2013).

Control Lake is a shallow lake with a surface area of 23.4 ha and depth of ~5 m where sediment cores were recovered (Figure 5.2). Water monitoring during the open water season in 2010 showed pH in the lake was circum-neutral ($\bar{x}$ = 7.05), conductivity measurements were low ($\bar{x}$ = 13.34 SpC) and lake temperature was cool during the summer ($\bar{x}$ = 12.09 °C; Aboriginal Affairs and Northern Development Canada 2013). Although no oxygen or temperature profiles have been taken at Control Lake, shallow subarctic lakes rarely stratify during the summer due to cooler temperatures, with only those >7 m depth typically showing summer stratification (Galloway et al. 2015; Palmer et al. 2015, 2019). However, Palmer et al. (2019) found oxygen stratification does occur in subarctic lakes during the winter, particularly in shallower, low-volume lakes. Although Control Lake is north of the treeline, it may be expected to experience similar winter oxygen stratification, but to be well mixed during the open-water season as Arctic lakes are typically associated with reduced productivity and available organic matter (Pienitz 1997). Geological maps of the region indicate Control Lake is underlain by low grade phyllite and slate, with a possible dioritic to granitic intrusive pluton underlying the north-western end of the lake (Thompson and Kerswill 1994). Hydrological modelling based on 2-m-DEM of the region shows Control Lake has a small watershed that collects water via overland or sub-surface flow from the surrounding area (Figure 5.2C). The hydrological

model shows Control Lake has two outflows, one to the west and one to the south-east. The lake is directly underlain by 2–10 m of till with no bedrock outcrops within the delineated watershed (Kremer et al. 2014).

Previous work was conducted on Control Lake on a short (~43 cm) gravity core recovered by Miller et al. (in press). Miller et al. (in press) found that, based on Scanning Electron Microscopy coupled with automated mineralogy and integrated Energy-Dispersive X-ray Spectroscopy, As was predominantly associated with FeO(OH) in sediment, with only a minor fraction (<20%) associated with framboidal pyrites and scorodite. Interpretation of trends in *aqua regia* (AQ)-ICP-MS, particle size data, organic petrography and Rock Eval pyrolysis by Miller et al. (in press) suggested that As may have been post-depositionally mobile, that labile OM (S2) was a dominant control on As concentrations in sediment, and that weathering changes in the system may have altered As input into Control Lake. In this study, we examine microfossil evidence to examine the possibility of post-depositional movement of As in Control Lake sediments and examine an extended record to explore whether the Miller et al. (2019)'s posited controls on As sequestration hold true for earlier in the Holocene when Control Lake was exposed to different environmental stressors.

5.7 Methods

Core CON02 (length = 136 cm) was collected in March, 2016, using a single-faced freeze-corer from Control Lake, NT (64.07771 °N, -111.13493 °W; Figure 5.1C). CON02 was cleaned onsite and wrapped in clingfilm for transport to Carleton University. Upon arrival, approximately 2 mm of material was removed from all faces of the freeze core to minimize risk of on-site contamination, the core was photographed, and the sedimentology was recorded. The core was subsequently sub-sampled for radiocarbon, ICP-MS, and Arcellinida analysis.

5.7.1 Radiocarbon Chronology

Radiocarbon dating was used to provide temporal reference to core depth. As large organic fragments were not observed in the core, approximately 2 mL subsamples of bulk organic material were collected at 6 regular intervals from CON02 for analysis. Material was subsampled using ceramic and stainless-steel instruments that were

Table 5.1: Radiocarbon analysis conducted at the Lalonde AMS laboratory at University of Ottawa, Canada

Lab ID	Depth (cm)	Material	14C yr BP	error	F14C	error	cal. BP
UOC-3564	13	Bulk OM	1525	46	0.8271	0.0047	1529 - 1328 (95.4 %)
UOC-3565	35	Bulk OM	1489	38	0.8308	0.0039	1518 - 1461 (10.7 %)
							1419 - 1303 (85.7 %)
UOC-3566	67	Bulk OM	2206	38	0.7599	0.0036	2328 - 2131 (95.4%)
UOC-3567	92	Bulk OM	2833	38	0.7028	0.0033	3060 - 2855 (95.4 %)
UOC-3568	112	Bulk OM	3909	38	0.6147	0.0029	4438 - 4235 (95.2 %)
UOC-3569	134	Bulk OM	3959	38	0.6109	0.0029	4522 - 4292 (95.4 %)

sterilized with isopropyl alcohol and distilled water between subsamples. Samples were analyzed at the Lalonde AMS facility at University of Ottawa following a triple acid wash (Table 5.1).

The age model for CON02 was created using the **B**ayesian **A**ge **C**alibrati**ON** (BACON) package for R statistical software v. 3.5.1 (R Core Team, 2019; Blaauw and Christen, 2011). Ages were calibrated in BACON before creation of age models using the terrestrial radiocarbon curve IntCal13 after Reimer et al. (2013). Radiocarbon dating of the adjacent core CON01 showed modern dates at 1 cm depth (Supplementary Figure A1.12, Supplementary Table A2.1), suggesting no age-offset should be applied. An additional date of -66 calibrated years before present (cal. BP) was added at 0 cm depth to represent modern sedimentation in calibrated years before present (cal. BP). The model is based on six calibrated radiocarbon ages (Figure 5.3).

5.7.2 Arcellinida analysis

Subsamples of approximately 3 cc were recovered from CON02 at 5 cm intervals for Arcellinida analysis. Material was allowed to melt, then was gently washed for 10 minutes using 297 µm and 37 µm sieves to remove coarse and fine material. Sieved sediment was split into 6 aliquots using a wet splitter modelled after Scott et al. (1993). Arcellinida were enumerated wet on a gridded petri dish under an Olympus SZH10 stereo microscope (70x magnification) until at least 200 specimens were identified following key references that contained illustrated specimens (Supplementary Table A2.2; Medioli and Scott 1988; Reinhardt et al. 2006; Roe et al. 2010; Patterson et al. 2012; Nasser et al.

2016). In two samples at depths 1.5 and 100.5 cm, only 100 and 148 specimens could be counted, respectively. Arcellinida display phenotypic plasticity, with ecophenotypes of identified species representing environmental niches important for paleoenvironmental interpretations (Asioli et al. 1996; Patterson and Kumar 2002; Kauppila et al. 2006; Macumber et al. 2014; Nasser et al. 2016). Specimens were therefore identified to the strain/phenotype level that, although not a formally recognized taxonomic distinction within the International Code of Zoological Nomenclature (ICZN), allows for more detailed ecological characterization of past environments. Standard error was calculated for testate amoeba following Patterson and Fishbein (1989). Identified species whose abundance was less than the standard error in >70% of samples were removed from subsequent statistical analysis. The Shannon-Wiener index was used as a measure of diversity of Arcellinida (Spellerberg and Fedor 2003).

5.7.3 Inductively Coupled Plasma Mass Spectrometry

Bulk sediment samples (*n* =133) were analyzed for major and trace elements by ICP-MS following *aqua regia* digestion at Bureau Veritas Ltd., Vancouver (Gregory et al. 2019). Two subsamples of GSC standard stream mud (GSC-STSD-3) and replicate subsamples from core material were submitted for quality control in addition to analytical replicates run by Acme – Bureau Veritas. GSC standards were within 10% of expected values for partial extraction of elements. Analytical replicates run by Acme – Bureau Veritas showed an average relative standard deviation of 5% of the mean elemental concentration across all elements (max = 25 %, min = 0.42 %, *n* = 41). Sample replicates showed a similar relative standard deviation of 8% of mean elemental concentration.

5.7.4 Statistical analysis

Arcellinidan data were Hellinger transformed in order to minimize the influence of rare taxa on the analysis prior to statistical analyses. To visualize changes in the community of testate amoeba, Hellinger-transformed data were subjected to Q-mode and R-mode cluster analysis using Ward's method (Figure 5.4). Q-mode clusters were separated into four distinct assemblages. Assemblages were also explored using non-metric multi-dimensional scaling (NMDS). Assemblage groups identified using Q-mode cluster

analysis and NMDS were carried forward for stratigraphic interpretation and in subsequent multivariate analysis.

To understand the impact of environmental variables on Arcellinida communities, redundancy analysis (RDA) of Arcellinida data and sediment geochemistry was performed. Prior to multivariate and subsequent statistical analyses, elements with >30 % non-detects in the bulk sediment geochemistry dataset were removed. Values where concentrations were below the minimum detection limit of the instrument were replaced by half the stated minimum detection limit for the purpose of statistical analysis (Lubin et al. 2004; Reimann et al., 2008). For RDA analysis, several samples in the AQ-ICP-MS dataset were missing concentrations at concurrent depths as Arcellinida samples due to limited core material and high proportion of water in sediment samples. Data for missing intervals were interpolated by calculating the mean concentration of elements in samples above and below the missing interval. For RDA, select elements of environmental importance, including minerogenic indicators (Rb), redox sensitive elements (Mn, Fe, As, S) and a proxy for increased authigenic productivity (Ca/Rb) were examined (Figure 5.6). Although AQ-ICP-MS is a partial digestion method that does not dissolve silicate minerals (Chao 1984; Church et al. 1987; Schilling et al. 2014), Rb showed strong correlations between Itrax X-ray fluorescence data ($\rho = 0.59$, $p < 0.001$, $n = 81$) and ICP-MS results following a four acid digestion (HCl, HNO_3, HF, $HClO_4$; $\rho = 0.63$, $p < 0.001$, $n = 45$) analyzed on the adjacent core CON01 (Supplementary Figure A1.13). The strong, statistically significant correlation between XRF, multi-acid ICP-MS and *aqua regia*-ICP-MS suggests Rb trends were reliably identified using AQ-ICP-MS. Calcium normalized to lithogenic input increases with increased precipitation of authigenic carbonate, either due to increasing evaporative pressure, or changes to the partial pressure of CO_2 in the system caused by increased authigenic productivity during the open-water season (Wetzel 2001; Davies et al. 2015). Raw geochemical data were log-transformed to improve normality before multivariate analysis. Shapiro-Wilk tests of log-normalized elements considered for RDA analysis suggested data approach a normal distribution. Variance partition based on ANOVA was used to characterize variance explained by environmental variables and their statistical significance (Figure 5.6). For stratigraphic interpretation of ICP-MS results, constrained incremental sum of squares (CONISS)

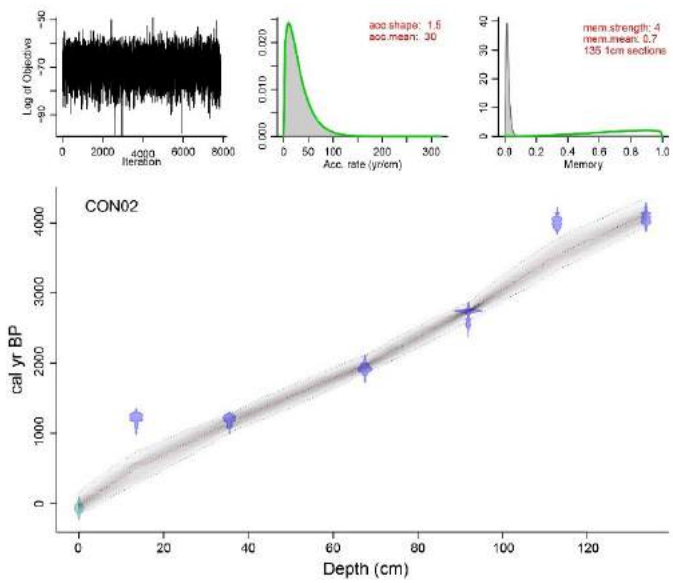

Figure 5.3: Age-depth model for CON02 constructed in BACON based on radiocarbon dates of bulk organic matter. A date at -66 +/- 40 cal. BP was used to represent modern conditions.

cluster analysis was applied to elemental variables of environmental importance (Rb, K, Ca/Rb, As, Mn, Fe, S) to assist in delineation of major geochemical phases (Figure 5.7). Subsets of geochemical variables based on CONISS analysis were used to assist in understanding the impact of variable climate change on Control Lake sediment (Figure 5.8). Although the original data approached normality, subsets of the elemental variables showed non-normal distribution. As such, Spearman's Rho (ρ) was used as a measure of correlation between elements in sediment geochemistry. All statistical analyses and figures were created using R Statistical Software (version 3.5.1) and RStudio including the packages vegan, rioja, MASS, analogue and zoo (Zeileis and Grothendieck, 2005; Juggins, 2017; Simpson and Okansen, 2018; Oksanen et al., 2019).

5.8 Results

5.8.1 Radiometric data

Core CON02 recorded 4100 +/- 200 years of deposition over the 134-cm-long core (Table 5.1, Figure 5.3). Radiocarbon analysis showed 2 minor age reversals: one at 13.5 cm and another at 111.5 cm, owing to anomalously old ages, possibly from re-working of sediment or deposition of old carbon from erosion of the catchment. CON02 was homogenously dark brown, with no apparent stratigraphic variability visible in the core. Bayesian age-depth modelling indicates CON02 had a stable accumulation rate, with a median of 3 mm/yr (max = 3.9 mm/yr, min = 2.5 mm/yr). The mean age error of the age-depth model is 314 years, with maximum errors of 435 and 455 years centered at 15 and 41 cm, respectively; age error remains below median values from 32 to 96 cm with a minimum age range of 236 cal. BP (Figure 5.3).

5.8.2 Testate amoeba

A total of 25 species and strains of arcellinida were identified in CON02, of which 16 were present in statistically significant numbers in >70% of samples, including: *Difflugia oblonga "*oblonga*", D. protaeiformis "*acuminata*", D. acutissima, D. elegans, D. glans "*glans*", D. glans "*distenda*", D. glans "*pulex*", D. globulosa, D. minuta, Centropyxis constricta "*constricta*", C. constricta "*aerophila*", C. constricta "*spinosa*", C. aculeata "*aculeata*", C. aculeata "*discoides*", Cucurbitella tricuspis, Pontigulasia compressa, Lesqueresia spiralis,* and *Lagenodifflugia vas* (Supplementary Table A2.2). Q-mode cluster analysis and NMDS show four distinct arcellinida assemblages (Figure 5.4).

Assemblage 1 (69 cm, 97 cm, 111-130 cm, *n* = 7) exhibited the highest observed concentrations of *D. oblonga* of any assemblage ($\bar{x}$ = 44%, σ = 7.6%; Figure 5.5). *Centropyxis constricta* "aerophila" was moderately abundant ($\bar{x}$ = 10%, σ = 3.1%) with similarly higher proportions of *D. protaeformis* "acuminata" ($\bar{x}$ = 8.7%, σ = 2.3%), *D. glans* "glans" ($\bar{x}$ = 6.0%, σ = 1.75%), *D. elegans* ($\bar{x}$ = 5.8%, σ = 2.2%), and *P. compressa* ($\bar{x}$ = 5.5%, σ = 0.75%). The proportion of *Cucurbitella tricuspis,* a species often used as a proxy for trophic state in lake systems (Roe et al. 2010; Drljepan et al. 2014; Roe and Patterson 2014), exhibited low average abundance of 1.27 % (σ = 0.52%). The SDI was the lowest observed in core (1.97) alongside relatively low tests/cc (142 tests/cc).

In Assemblage 2 (81–86 cm, 91–106 cm, *n* = 5), *D. oblonga* population decreased to the lowest observed of all assemblages ($\bar{x}$ =25% σ = 7.7%), although it remained the dominant taxon in all samples belonging to this assemblage (Figure 5.5). Stress indicating taxa *D. elegans* ($\bar{x}$ = 11%, σ = 2.8%), *C. constricta* "aerophila" ($\bar{x}$ = 19%, σ = 4.3%) and *C. constricta* "constricta" ($\bar{x}$ = 9.1%, σ = 2.9%) reached their highest abundance in core. *Pontigulasia compressa* ($\bar{x}$ = 6.7%, σ = 1.9%), *D. protaeiformis* "acuminata" ($\bar{x}$ = 6.3%, σ = 2.9%) and *D. glans* "glans" ($\bar{x}$ = 4.6%, σ = 2.1%) were present in low proportions. The SDI increased slightly ($\bar{x}$ = 2.21) alongside a decrease in the Arcellinida population ($\bar{x}$ = 136 sp/cc).

Assemblage 3 (40–65, 75 cm, *n* = 5) was dominated by *D. oblonga*, although in slightly lower proportions than were observed in Assemblage 1 ($\bar{x}$ = 30%, σ = 3.8%;

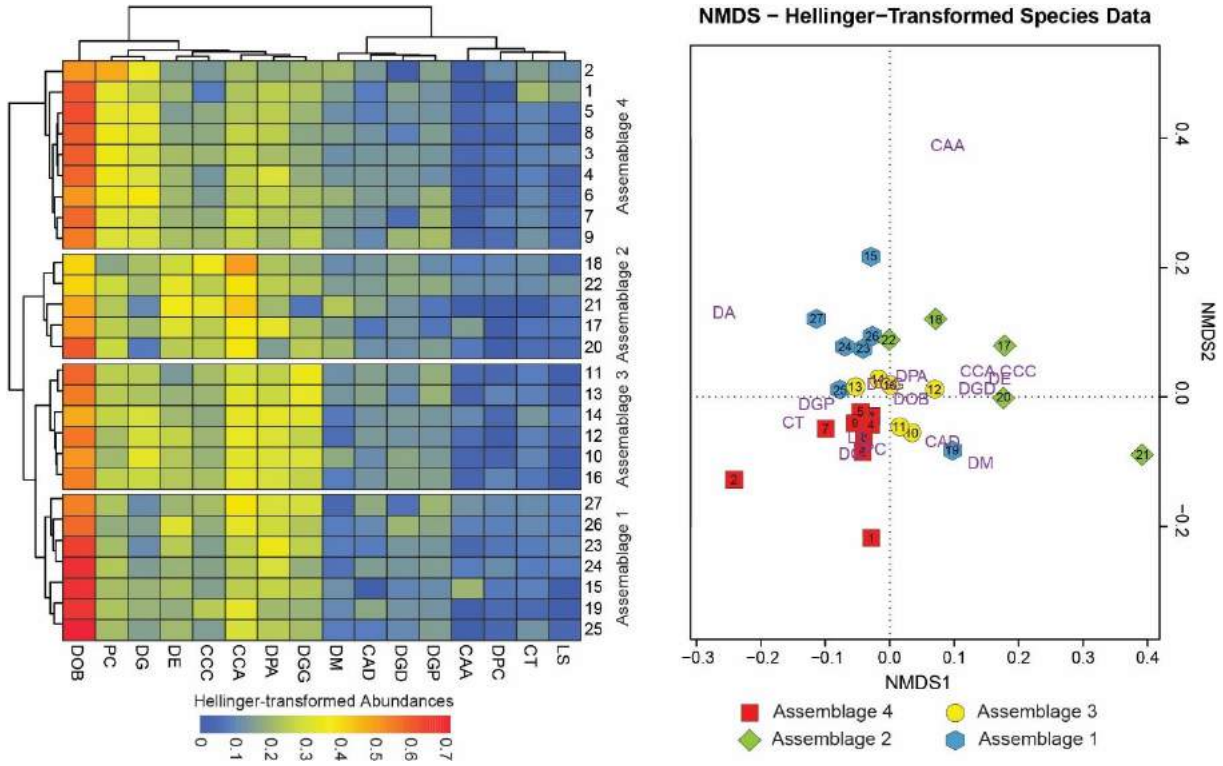

Figure 5.4: Two-way cluster analysis of Hellinger-transformed Arcellinida data using Ward's method. NMDS of Hellinger-transformed data recovers the same groupings as R-mode cluster analysis. For two-way cluster analysis, warm colors represent higher Hellinger-transformed abundances, cooler colors represent lower abundances. For NMDS, colored samples represent distinct A1 (red squares), A2 (yellow circles), A3 (green diamonds), A4 (blue hexagons). DOB = *Difflugia oblonga* "oblonga", DPA = *D. protaeiformis* "acuminata", DA = *D. acutissima*, DE = *D. elegans*, DGG = *D. glans* "glans", DGD = *D. glans* "distenda", DGP = *D. glans* "pulex", DG = *D. globulosa*, DM = *D. minuta*, CCC = *Centropyxis constricta* "constricta", CCA = *C. constricta* "aerophila", CAA = *C. aculeata* "aculeata", CAD = *C. aculeata* "discoides", CT = *Cucurbitella tricuspis*, PC = *Pontigulasia compressa*, LS = *Lesqueresia spiralis*

Figure 5.5). *Centropyxis constricta* "aerophila" ($\bar{x}$ =11%, σ = 0.98%), *D. protaeiformis* "acuminata" ($\bar{x}$ = 9.7%, σ = 1.5%) and *D. glans* "glans" ($\bar{x}$ = 10%, σ = 2.0%) were relatively abundant in samples, followed by *D. globulosa* ($\bar{x}$ = 8.6 %, σ = 2.1%), *P. compressa* ($\bar{x}$ = 6.5 %, σ = 1.1%), *D. elegans* ($\bar{x}$ = 5.2 %, σ = 1.7%) and *C. constricta* "constricta" ($\bar{x}$ = 4.6%, σ = 0.61%). The SDI remained moderate in this assemblage ($\bar{x}$ = 2.21). There was a minor increase Arcellinida population from in this assemblage up to 201 tests/cc.

In Assemblage 4 (0–40 cm, *n* = 9), *D. oblonga* remained the dominant species ($\bar{x}$ = 34.29%), followed by *P. compressa* ($\bar{x}$ = 12%, σ = 4.7%), *D. globulosa* ($\bar{x}$ = 11%, σ = 2.1%), and minor proportions of *Centropyxis constricta* "aerophila" ($\bar{x}$ = 7.1%, , σ = 1.1%), *D. protaeformis* "acuminata" ($\bar{x}$ = 6.54 %, σ = 1.8%), *D. glans* "glans" ($\bar{x}$ = 5.0%, σ = 1.2%),

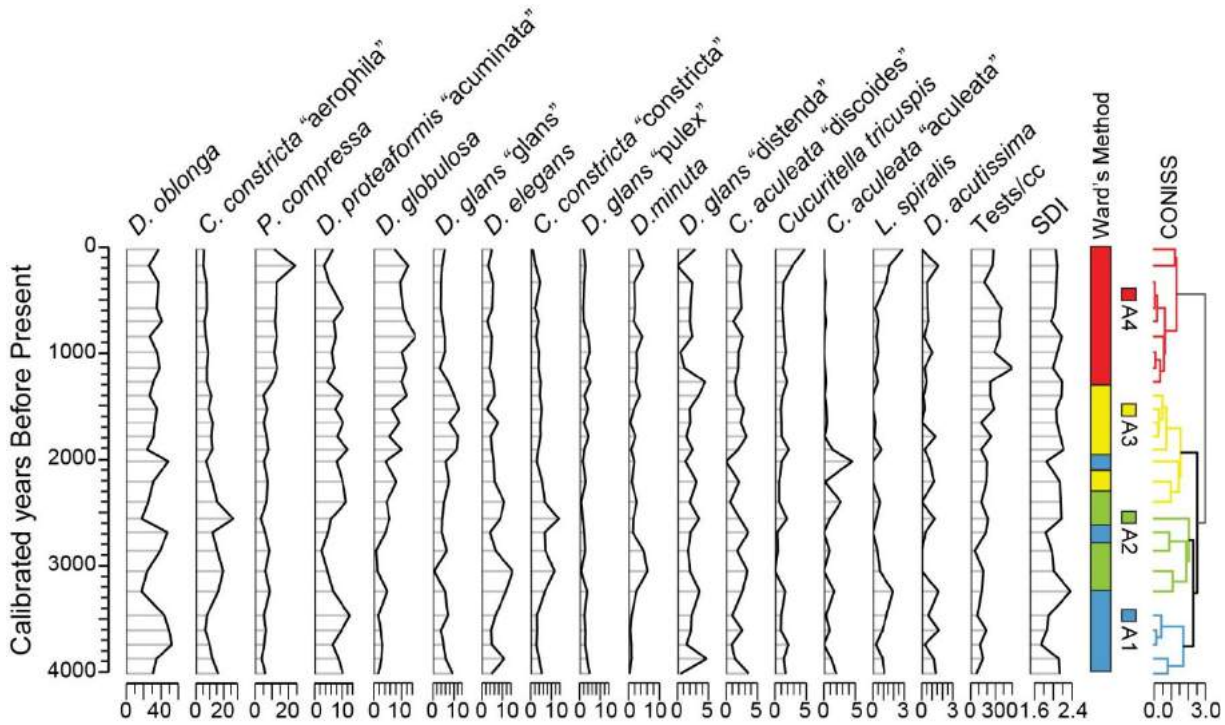

Figure 5.5: Stratigraphic representation of arcellinida relative to age of sediment. Shown on the right are results from Ward's Q-mode cluster analysis alongside CONISS results. Assemblage 4 is shown in red, Assemblage 3 in yellow, Assemblage 2 in green and Assemblage 1 in blue.

and *D. elegans* ($\bar{x}$ = 4.4%, σ = 0.93%; Figure 5.5). *Cucurbitella tricuspis* showed the highest concentrations observed in core ($\bar{x}$ = 1.96 %, σ = 1.1%). In Assemblage 1, the SDI is indicative of transitional to healthy environments ($\bar{x}$ = 2.14) and arcellinida test/cc are the highest observed in core ($\bar{x}$ = 312 tests/cc).

5.8.3 Redundancy analysis

The RDA indicates that Rb, As, Mn, Fe, S and Ca/Rb explained 55 % of the variability in the species dataset (r^2_{adj} = 0.39), with Axis 1 and Axis 2 explaining 27% and 12% of the species variability, respectively (Figure 5.6). ANOVA of RDA results showed that Axis 1, 2 and 3 statistically significant at the 0.95 level. Variance partitioning of RDA results indicates that S, Fe Mn and As explain most of the variability within the species data set (S = 22.1%, Fe = 10.5%, Mn = 8.4%, As = 5.4%), and have p-values <0.05. Manganese, S, and Ca/Rb are strongly positively associated with Axis 1 while K and Rb shows strong negative scores along this axis. Arsenic and Fe show strong positive association to Axis 2, with almost no association to Axis 1.

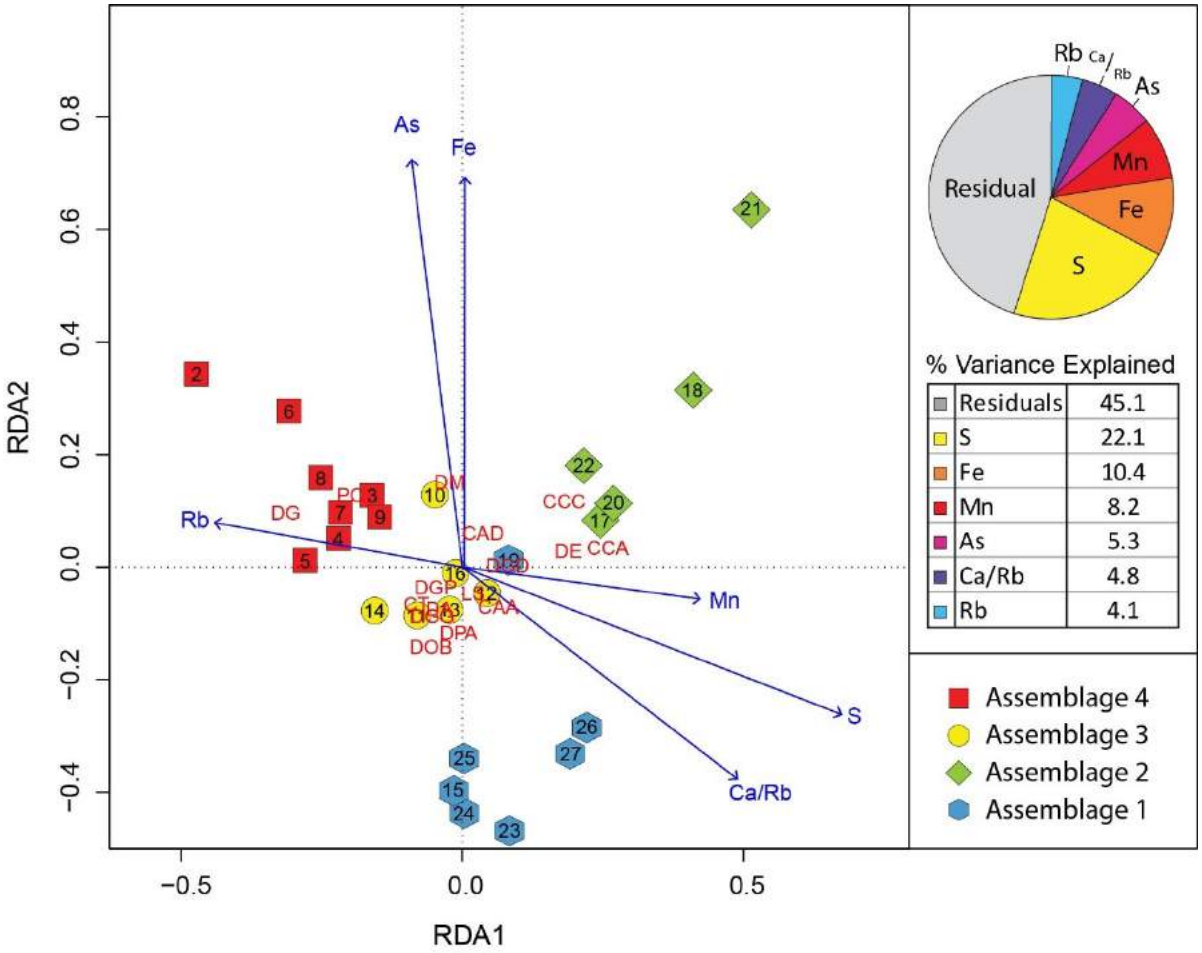

Figure 5.6: Redundancy analysis comparing Arcellinida shifts to changes in key geochemical indicators. Triplot shows first two significant axes. Arcellinida assemablges are indicated on the triplot using red squares (A1), yellow circles (A2), green diamonds (A3) and blue hexagons (A4). Inset shows variance partitioning of environmental variables indicating the proportion of variance explained. DOB = *Difflugia oblonga* "oblonga", DPA = *D. protaeiformis* "acuminata", DA = *D. acutissima*, DE = *D. elegans*, DGG = *D. glans* "glans", DGD = *D. glans* "distenda", DGP = *D. glans* "pulex", DG = *D. globulosa*, DM = *D. minuta*, CCC = *Centropyxis constricta* "constricta", CCA = *C. constricta* "aerophila", CAA = *C. aculeata* "aculeata", CAD = *C. aculeata* "discoides", CT = *Cucurbitella tricuspis*, PC = *Pontigulasia compressa*, LS = *Lesqueresia spiralis.*

Samples from Assemblage 1 (ca. 1250 to -66 cal. BP; Figure 5.6) show strong negative association on Axis 1 and weak positive associated to Axis 2. Assemblage 2 (ca. 2200–1250 cal. BP) clustered around the origin of the triplot, indicating there was little variance in the selected elements during this phase of deposition. Assemblage 3 (ca. 3200–2200 cal. BP) showed strong positive associated with both Axis 1 and 2, whereas Assemblage 4 (ca. 4000–3200 cal. BP) showed weak positive associated with Axis 1 and a stronger negative association with respect to Axis 2. *Centropyxis constricta* "aerophila", *C. constricta* "constricta", and *D. elegans* exhibited strong, positive association with Axis

1, with little variation along Axis 2 (Figure 5.6). *Difflugia minuta* and *C. aculeata* "discoides" were weakly associated with Axis 2 and showed little variation along Axis 1. *Pontigulasia compressa* and *D. globulosa* were negative associated with Axis 1. The remaining species clustered near the origin, with a slight negative association along Axis 2.

5.8.4 Sediment geochemistry

Shifts in elements (K, Rb, Fe, Mn, S, As, Ca/Rb) over the last ca. 4100 cal. BP are shown in Figure 5.7. Cluster analysis using CONISS based on the select elements above was used to delineate three major zones based on major shifts in the concentration of these elements in CON02. The earliest phase of deposition, Phase 1, occurred from ca. 4100 to 3250 cal. BP (n = 21). Sediments of this interval had lower K and Rb concentrations ($\bar{x}_K$ = 719 ppm, σ_K = 87 ppm; $\bar{x}_{Rb}$ = 5.6 ppm, σ_{Rb} = 0.75 ppm) than overlying material. During Phase 1, Ca/Rb, S and Mn were at the highest concentrations observed in sediment ($\bar{x}_S$ = 0.6%, σ_S = 0.005%; $\bar{x}_{Mn}$ = 178 ppm, σ_{Mn} = 12 ppm) relative to younger sediments, whereas Fe and As exhibited the lowest concentrations observed in core ($\bar{x}_{Fe}$ = 3.0%, σ_{Fe} = 0.05%; $\bar{x}_{As}$ = 64 ppm, σ_{As} = 6.6 ppm). Ca/Rb gradually decreased through Phase 1. In this phase, As was strongly positively correlated to Fe (ρ = 0.81, p-value < 0.001), weakly positively correlated to Mn (ρ = 0.51, p-value = 0.02) and weakly negatively correlated to both S and Rb (Table 5. 2; Figure 5.8). Sulfur exhibited a strong negative correlation to both Mn (ρ = -0.72, p-value < 0.001) and Fe (ρ = -0.72, p-value < 0.001). Minerogenic indicators Rb and K did not correlate well with the other elements considered during Phase 1.

Phase 2 occurred from ca. 3250 to 2150 cal. BP (n = 27; Figure 5.7). Minerogenic indicators K and Rb increase sharply during this interval at ca 2700 cal. BP. Arsenic and Fe reach peak concentrations (max_{As} = 258 ppm, max_{Fe} = 12 %, n = 27). Manganese and S show decreasing trends concurrent with the changes in Rb and K. The productivity indicator Ca/Rb continues to decrease throughout this period reaching a minimum by the end of Phase 2. There were strong positive correlations between As and Fe and Mn (ρ > 0.63, p-value < 0.001; Table 5. 2, Figure 5.8) during Phase 2 of deposition. The correlation between As to S becomes positive during this interval (ρ = 0.41, p-value =0.03). Redox

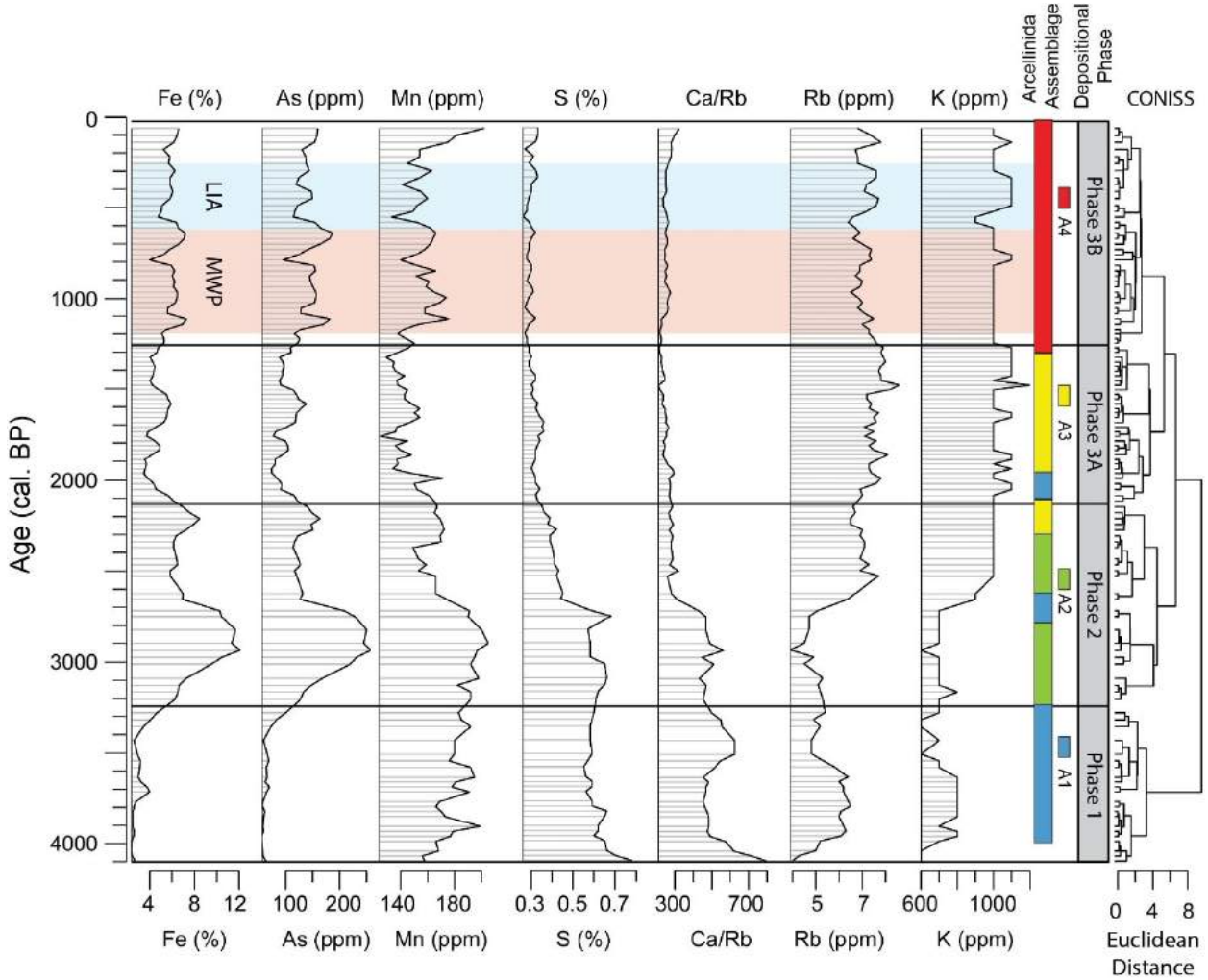

Figure 5.7: Stratigraphic shifts in sediment geochemistry relative to age of sediment. Phases of deposition are based on CONISS cluster analysis using select elements of environmental importance. The Little Ice Age (LIA) and Medieval Warm Period (MWP) are indicated by shaded blue and red intervals, respectively. Shifts in testate amoeba assemblage are indicated by color bars (A4 = red; A3 = yellow; A2 = green; A1 = blue)

sensitive elements (As, Mn, Fe, S) exhibited strong negative relationships to minerogenic indicators Rb and K ($\rho > 0.54$, p-values < 0.01) and moderate to strong positive relationships to Ca/Rb ($0.38 < \rho < 0.77$, p-values <0.05).

During Phase 3 (ca. 2150 to -66 cal. BP, *n* = 32), Control Lake sediment geochemistry remained relatively stable. Phase 3 is broken up into two sub-phases characterized by minor shifts in sediment geochemistry. In Phase 3A (ca. 2150 and 1250 cal. BP) As, and Fe decreased ($\bar{x}_{Fe}$ = 4.6%, σ_{Fe} = 0.76%; $\bar{x}_{As}$ = 100 ppm, σ_{As} = 17 ppm), and Rb and K are slightly higher relative to Phase 3B ($\bar{x}_{K}$ = 1047 ppm, σ_{K} = 57 ppm; $\bar{x}_{Rb}$ = 7.5 ppm, σ_{Rb} = 0.39 ppm; *n* = 32). Manganese and S remained low throughout Phase 3A and Phase 3B. In Phase 3A (ca. 2150 to 1250 cal. BP), As exhibited the strongest correlation to Fe observed in sediment ($\rho = 0.94$, p-value < 0.001; Table 5. 2 Figure 5.8). There is a decrease in the correlation between Mn and Fe as well as Mn and As relative to earlier intervals of sedimentation. Sulfur remains positively correlated to As, Fe, and Mn, albeit with a weaker correlation ($\rho = 0.17$, p-value = 0.34). Rubidium and K were negatively correlated to redox-sensitive elements (Fe, Mn, As, S) but with weaker correlations than observed in Phase 2. There was a moderate positive correlation between S and Ca/Rb ($\rho = 0.47$, p-value = 0.01).

In Phase 3B (ca. 1250 cal. BP until present, *n* = 39), there were increases in As and Fe ($\bar{x}_{Fe}$ = 5.9%, σ_{Fe} = 0.71%; $\bar{x}_{As}$ = 142 ppm, σ_{As} = 21 ppm), and minor decreases in Rb and K concentrations ($\bar{x}_{K}$ = 1017 ppm, σ_{K} = 51 ppm; $\bar{x}_{Rb}$ = 7.1 ppm, σ_{Rb} = 0.31 ppm; *n* = 39). In Phase 3B, all redox sensitive elements exhibited strong, positive ($\rho > 0.59$), statistically significant (p-value < 0.001) correlations with each other (Table 5. 2, Figure 5.8). Ca/Rb is positively correlated with the redox-sensitive elements ($\rho > 0.17$, p-value < 0.1). There are weak negative correlations between redox sensitive elements and indicators of minerogenic indicators (K, Rb).

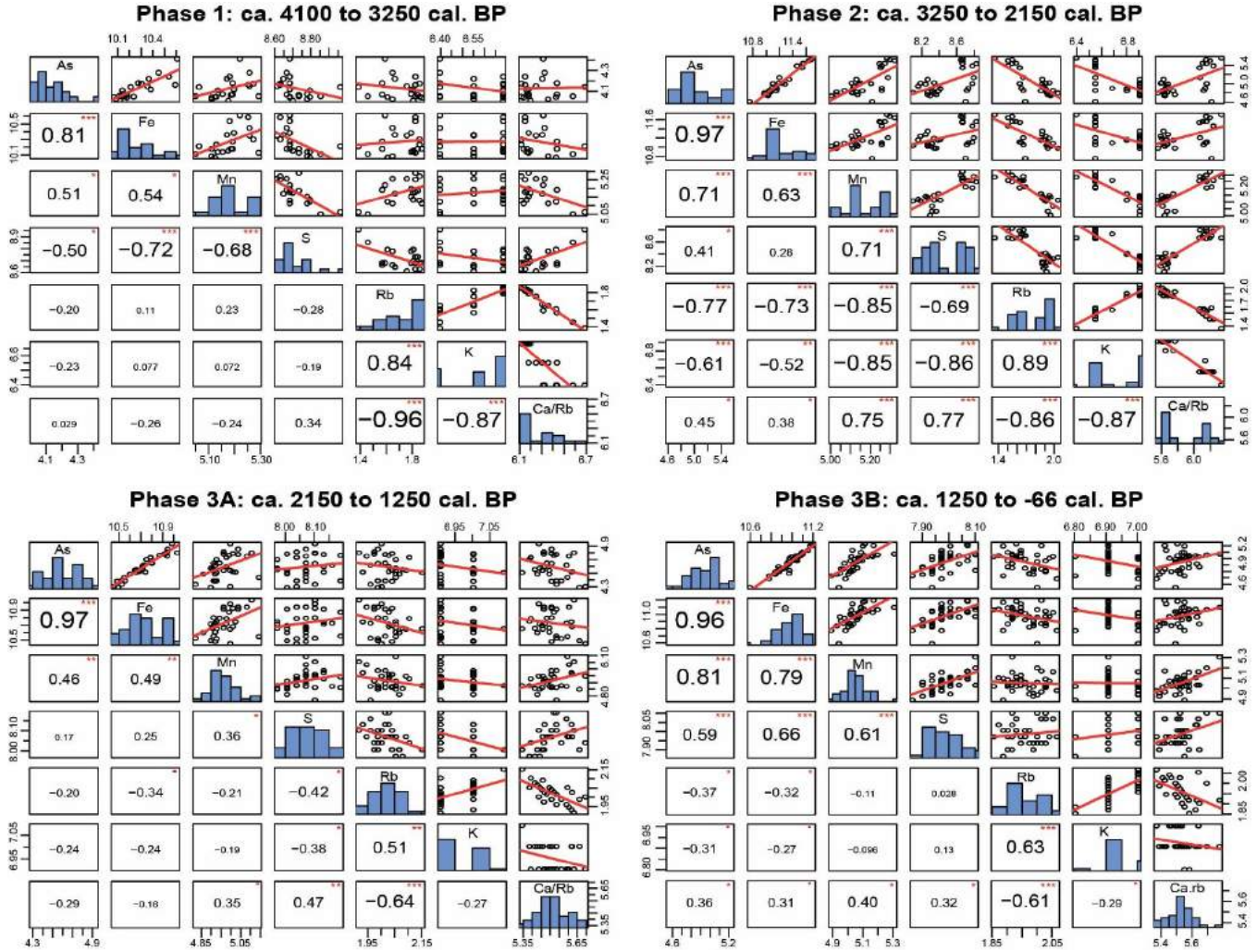

Figure 5.8: Correlations for elements of interest during different phases of deposition. Histograms of data are shown along the diagonal. Below the diagonal, Spearman correlations are shown, with size corresponding to strength of correlation; p-values are indicated using red symbols (p < 0.001 = ***; p < 0.01 = **, p < 0.05 = *, p < 0.1 = ·)

5.9 Discussion

5.9.1 Impact of Arsenic on testate amoeba

Arcellinida assemblages in the CON02 sediment core are typical of those observed in oligo- to mesotrophic systems, with an abundance of *D. oblonga*, *P. compressa*, and *D. glans* "glans" (Figure 5.5) that are commonly observed in lower-trophic state systems (Roe et al. 2010; Drljepan et al. 2014; Roe and Patterson 2014). An oligo- to mesotrophic state is supported by low proportion of other eutrophic indicators, such as *C. tricuspis* that is ubiquitous in lakes with high algal population (Reinhardt et al. 2005; Roe et al. 2010; Drljepan et al. 2014b; Roe and Patterson 2014). Assemblages are either co-dominated by As-tolerant species *C. constricta* "aerophila", *C constricta* "constricta", and *D. elegans*, or these stress indicator taxa are present in relatively high abundances (>5%). Nasser et al., (2016) found *C. constrica* "aerophila", *C. constricta* "constricta", and *D. elegans* dominating the high arsenic samples ($\bar{x}$ > 1400 ppm) in a survey of surface samples from lakes in the Yellowknife region. A subsequent expansion of this dataset and re-analysis to determine tolerance limits of Arcellinida strains showed that most testate amoeba are capable of tolerating As in concentrations up to 360 ppm, and *Conicocassis pontigulasiformis*, *D. bidens*, *D. elegans*, *C. constricta* "constrica", *C. aculeata* "discoides", *C. constricta* "aerophila", and *C. constricta* "spinosa" can tolerate extreme As in concentrations >760 ppm (Nasser et al., in press). Although As concentrations in the sediment core studied are below this lower threshold of 360 ppm, we may expect to see a response of Arcellinida to As variations in As is the primary stressor on the Arcellinida communities, or if possible diagenetic alteration of As concentrations may underestimate environmental As concentrations in the environment during deposition of Arcellinida. The low concentration of As in core does not preclude the application of micro-fossil techniques *a priori,* but may cloud interpretation during paleoclimate reconstructions.

Redundancy analysis on Control Lake Arcellinida showed the S and Fe and Mn explained the largest proportion of Arcellinida variability in the Control Lake record. Stress indicating Arcellinida strains that can withstand the highest levels As are closely associated to Axis 1, which correlates positively with S, Mn, and Ca/Rb, and negatively correlated to Rb and K. Arsenic-indicating taxa do not show much variability along Axis 2 that strongly corresponds to As and Fe concentrations in sediment (Figure 5.6). This

indicates that either As was not the dominant stressor on testate amoeba, or else As has moved post-depositionally. The correspondence between Axis 1 and stress indicator taxa, and the strong relation between Axis 1 and environmental variables associated with reducing conditions (S), higher OM content (Rb), and higher productivity (Ca/Rb), may indicate that redox state and bottom-water oxygenation is inducing greater stress on Arcellinidan communities. Reducing conditions induced by increased productivity (Ca/Rb) would result in greater preservation of S and reductive dissolution of As-Fe/Mn (oxy)hydroxides in the sediments.

There is disagreement between As-indicating testate amoeba and As concentrations in the sediment core, which supports post-depositional mobility of As in the sediment column. The As concentrations preserved in the core during Phase 1 and 3 are lower than suggested lower tolerance limits of <360 ppm As (Nasser et al. 2016; in press). Although this may be caused by post-depositional mobility, arcellinida fauna indicate generally healthy conditions in Phase 1 and Phase 3, supporting the fact that geogenic As levels remained low enough that they did not induce major stress on Arcellinida communities. Stress indicating taxa were most abundant during Phase 2 of deposition where the highest As concentrations are measured (range = 113–258 ppm, $\bar{x}_{As}$ = 161 ppm, n = 25), suggesting an increase in stress on the system during this period of higher overall As concentration (Figure 5.7). However, two prominent increases in As concentration occur from ca. 3100 to 2700 cal BP (258 ppm) and ca. 2300 to 2100 cal. BP (150 ppm), immediately after increases in stress indicators (Centropyxids, *D. elegans*) and coeval with peaks in *D. oblonga*. The assemblage preserved in the CON02 core may have responded to one or some of these other variables. It is possible that stressed taxa are recording initially elevated As concentrations, but these As concentrations were not preserved until later due to changes in OM availability or changes in minerogenic content. Unfortunately, low As concentrations relative to As-tolerance limits (>760 ppm; Nasser et al. 2016; Nasser et al. in press), likely post-depositional movement of As, and additional stressors on the system, such as the major depositional change during this interval based on sharp increases in minerogenic indicators (K, Rb), clouds the relationship between As and Arcellinida down core. Regardless, it is apparent that As has either moved in the sediment of CON02 following its deposition, or that arcellinida communities did not

respond to sedimentary As concentrations because As concentrations may have been too low to elicit a threshold response.

5.9.2 Environmental evolution of Control Lake

5.9.2.1 Phase 1 – Forest or forest-tundra lake

The earliest phase of deposition recorded at Control Lake occurs ca. 4100–3250 cal. BP. Arcellinida during this phase of deposition are indicative of transitional conditions (SDI = 1.97; Patterson and Kumar 2000b), with co-dominance of *D. oblonga* and stress indicating *C. constricta* "aerophila". It is unclear what is inducing this stress; As concentrations are low in core, but it is unclear whether the signal represents *in situ* deposition of As. Productivity appears to be relatively high based on elevated Ca/Rb concentrations in core. However, the lack of *C. tricuspis*, a taxon ubiquitous in eutrophic environments (Reinhardt et al. 1998; Roe et al. 2010; Drljepan et al. 2014), suggests that the lake remained meso- to oligotrophic during this interval.

Phase 1 corresponds to the end of the Holocene hypsithermal in the region (ca. 4300 cal. BP; Kaufman et al. 2004; Upiter et al. 2014). A decrease in regional temperature of 2–3°C occurred from ca. 4000 to 1500 cal. BP, with ~1°C cooling occurring during Phase 1 of deposition at Control Lake (Upiter et al. 2014). This decrease in temperature resulted in treeline retreat across the subarctic. Local records from Toronto, Danny's and Queen's Lake suggest this occurred near the end of Phase 1 between ca. 3500 to 3000 cal. BP (Moser and MacDonald 1990; MacDonald et al. 1993; Pienitz et al. 1999; Sulphur et al. 2016). Sediment geochemistry during this phase may indicate lower minerogenic content based on low concentrations of Rb and K. Alternatively, Rb and K may indicate input of finer sediment as these elements have a strong correspondence to intervals of fine sediment deposition in lakes (Daas and Haake, 2003**;** Guyard et al. 2007; Cuven et al. 2010; Kylander et al. 2011; Davies et al. 2015; Amann et al. 2017). Studies of snowmelt rate across the subarctic have shown that forested areas melt slower than surrounding tundra or shrub-tundra (Rouse et al. 1984; Lundberg and Beringer 2005). Slower snowmelt during spring thaw has been linked to increased particle size and thicker varves as gradual snowmelt results in the pooling of melt water followed by a higher-energy deluge of meltwater pools that carries a greater volume of coarser sediment into the lake

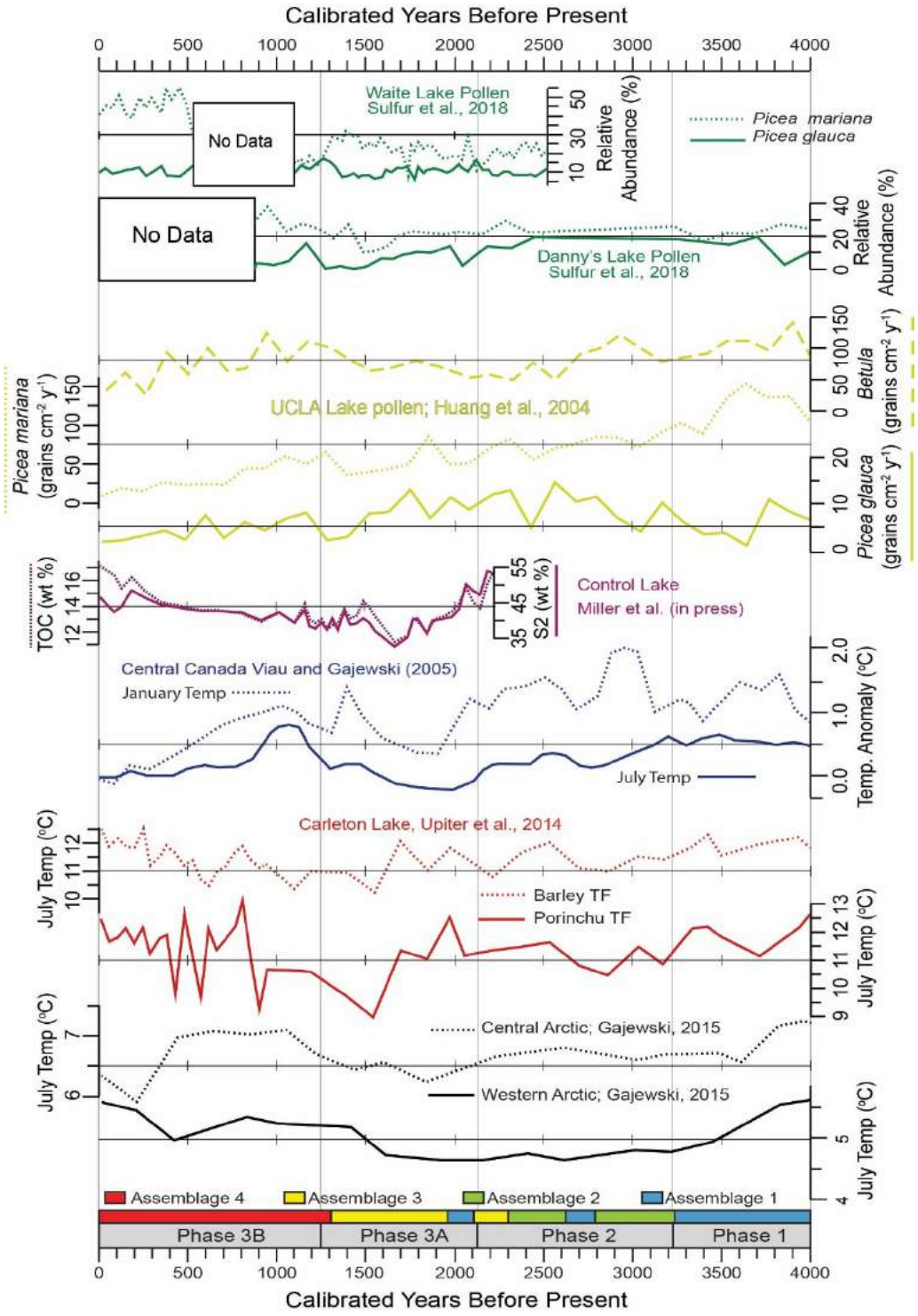

Figure 5.9: Paleoclimate reconstructions for Northern Canada. Temperatures reconstructions are based on chironomid head capsules (Upiter et al. 2014); and palynology (Viao and Gajewski 2004; Gajewski 2015). Paylnology from Waite's Lake, Danny's Lake (Sulphur et al., 2016) and UCLA Lake (Huang et al. 2004) are included to provide information on relative wetness above and below the treeline. Total organic content (TOC) and labile organic fraction (S2) are based on a short core from Control Lake studied by Miller et al. (in press).

basins (Cockburn and Lamoureux 2008a,b; Tomkins et al. 2010; Lapointe et al. 2012**;** Amann et al. 2017). The lower proportion of Rb and K relative to shallower sediments may thus represent a reduced input of fine material (coarser sediment in the system) or reduced minerogenic input into control lake (same particle size, more OM). However, without data on organic content or ICP-MS following total digestion, it is not possible to quantify what degree variations in minerogenic content and coarse particles play in low Rb and K concentrations.

Sediment geochemistry showed relatively high Ca/Rb during Phase 1 (ca. 4100 to 3250 cal. BP), suggesting increased authigenic precipitation of carbonate content, possibly due to increased productivity in the lake system (Davies et al. 2015; Wetzel, 2001). Previous research characterizing differences between tundra and forest lakes in the sub-Arctic have shown that forested lakes have higher DOC, higher ionic concentrations and higher P and N concentrations in lake water (Pienitz et al. 1997, 2011; Ruhland and Smol 1998). These nutrients encourage higher lake productivity. Both S and Mn are higher during this interval in CON02 and show strong negative correlations to one another. Such a relationship is expected as reducing conditions are typically associated with higher S concentrations (Smedley and Kinniburgh 2000; Wetzel, 2001) and oxidizing conditions with higher Mn preservation (Thamdrup et al. 1994; Calvert and Pedersen 1996). Higher S and Mn concentrations may also be caused by increased sedimentary input into Control Lake or by higher proportions of OM in the region at this time, as has been observed at several lakes near the treeline (Moser and MacDonald 1990; MacDonald et al. 1993; Huang et al. 2004), that in turn modified redox conditions in CON02 during winter stratification.

Arsenic concentrations during Phase 1 are low and show little variability (62 +/- 6.7 ppm). There are strong positive correlations between As and Fe, a moderate positive correlation between Mn and As, and moderate negative correlation to S during this interval of deposition, (Figure 5.8, Table 5. 2). These relationships may indicate that most of the As deposited during this phase is still preserved in FeO(OH) and Scorodite (FeAsO). Although under reducing conditions found deep in the sediment column,

reduced iron-sulfides (*e.g.* mackinawite, pyrite, goethite) are expected to be more stable than FeO(OH), Miller et al (in press) found that much of the As in a shallow sediment core collected the Control Lake was preserved predominantly in FeO(OH), with only a subordinate amount of total sedimentary As associated with FeS_2. The moderate negative correlation between As and S suggests that even at maximum core depths (up to 135 cm), As may still be associated with FeO(OH). Mineralogy is needed to explore this hypothesis.

Low concentrations of As during Phase 1 may be associated with As release into shallow sediment during oscillating redox conditions through cyclic reductive dissolution under reducing conditions or sorption of As with Fe/Mn (oxy)hydroxides under oxic conditions. Palmer et al (2019) observed in several shallow Boreal lakes near Yellowknife that during prolonged ice coverage degradation of OM consumed oxygen and resulted in anoxic conditions in bottom waters. These conditions promoted a release of As from Fe/Mn (oxy)hydroxides into lake waters as As(III). Higher autochthonous productivity and delivery of terrigenous OM from a vegetated catchment would increase the likelihood of development of winter under-ice anoxia. Seasonal cycling would result in perpetual enrichment of As in near-surface sediment and would not result in preservation of As in the long-term sediment record. Although As can also sorb to FeS or precipitate as As-sulfides under reducing conditions, poor correlations between Fe and S suggest that precipitation of As-iron-sulfides was not a dominant process in Control Lake.

5.9.2.2 Phase 2 – Transition to tundra environment

A marked change in sediment geochemistry and Arcellinida assemblages mark the initiation Phase 2 of sediment deposition at Control Lake (ca. 3250–2150 cal. BP). Arcellinida during this phase showed the highest proportion of stress indicators in the core, associated with highly elevated sedimentary As concentrations of up to 258 ppm. There are two major peaks in As concentration that occur in sediment, however, peaks in stress indicating taxa predate As peaks by ca. 200–300 years, and peaks in healthy indicator taxa (*i.e. D. oblonga, D. glans* “glans”, *D. protaeformis* “acuminata”) postdate As increases ca. 100 years, with some degree in overlap between decreasing in As and increasing in healthy indicators. As discussed above, it may be that initial peaks in As

concentration resulted in stress to Arcellinida taxa, but As was not preserved in sediment until ideal conditions for sequestration occurred.

During Phase 2 (ca. ~3250 to 2150 cal. BP) S and Ca/Rb decrease in sediment coeval with an increase in Rb, and K (Figure 5.7). This change in sediment geochemistry may corresponds treeline retreat that occurred between ca. 4000 and 3000 cal. BP based on abundance of *Picea* pollen and decreased in sedimentary OM and DOC at McMaster Lake, Queen's Lake, Waterloo Lake, Danny's Lake and UCLA lake (Moser and MacDonald 1990; Larsen and MacDonald 1993; Pienitz et al. 1999; Huang et al. 2004; Sulphur et al. 2016). Minerogenic indicators (Rb, K) increased at ca. 2700 cal. BP indicating either an increase in minerogenic content or an increase in deposition of fine particle in Control Lake. The shift towards Tundra vegetation would have caused a fining of sediment as tundra or shrub-tundra vegetation that typically result in more rapid melting of snow pack (Rouse et al. 1984; Lundberg and Beringer 2005), and thus an increase in the delivery of finer particles to the lake (Forbes and Lamoureux 2005; Cockburn and Lamoureux 2008a). The shift minerogenic indicators from Phase 1 to Phase 2 shows vegetation may be a first order control on sedimentation in subarctic lacustrine systems due to the impact of vegetation on melt rate and snow pack volume.

During Phase 2 of deposition, redox-sensitive elements (As, Mn, S, Fe) exhibited strong positive correlations with one another. A higher correlation between As and S may suggest increased sequestration of As in FeS, FeS_2 or As-sulfides. However, there is a weak correlation between Fe and S ($\rho = 0.28$, p-value = 0.15, $n = 27$), suggesting As may be preserved as As-sulfides, in spite of the fact that As-sulfides generally only form when available Fe is limited compared to As concentrations (Wilkin and Ford 2006). There is a positive correlation between Mn, S and Ca/Rb. This is somewhat unexpected as Mn is commonly assumed to be preserved in oxygenated conditions (Thamdrup et al. 1994; Calvert and Pedersen 1996) and S is more stable as sulfide minerals that form under reducing conditions (Smedley and Kinniburgh 2000; Wetzel, 2001). During this interval, Mn decreases similar to S, but variations on this trend correspond better to variations in As and Fe. It seems likely that shifts in the sedimentary system are creating a first-order

control and Mn and S and redox-related controls impose second-order variations on this decreasing trend.

There is a moderate positive correlation between As and Ca/Rb. A shift towards a tundra setting would result in decreased input of terrestrial OM. Lake-oxygen stratification in a tundra setting would thus be more dependent on in-lake productivity as the digestion of OM drives de-oxygenation of lacustrine systems during winter. The strongest correlation between Ca/Rb and redox-indicating elements during this phase of deposition suggests that in-lake productivity is important to the redox state of the lake. An additional proxy for productivity would be helpful for confirming the impact of in-lake productivity, such as biogenic silica, or Rock Eval pyrolysis (*e.g.*, S2 carbon), on As sequestration during this interval.

The large peaks in As concentration during Phase 2 of deposition (ca. 3250 to 2150 cal. BP) may be associated with gradual increased preservation of As during a major change in sedimentary system. Palmer et al. (2019) found that As in Boreal lakes repeatedly cycled between lake water and lake sediment due to seasonal anoxia. In the winter, extended periods of ice coverage restricted mixing of lake water, which allows the degradation of OM to reduce oxygen near the sediment-water interface, inducing release of As from sediment. During Phase 2 of deposition, lower proportion of OM based on increases in lithogenic indicators during the transition from boreal forest to tundra vegetation may decrease the likelihood of Control Lake experiencing anoxic conditions during winter. Reduced productivity caused by cooler temperatures, and as recorded by Ca/Rb at Control Lake, would further decrease OM availability, decreasing the period of winter anoxia and possibly reduced the As released into the overlying water column.

Changes in minerogenic content in the lake may also be impacted preservation of the As signal. The largest peak of As concentration at ca. 2700 cal. BP occurred before sharp increase in minerogenic indicators (Figure 5.7). There is also a strong, negative, statistically significant correlation between As and minerogenic indicators ($\rho_{As\text{-}Rb}$ = -0.77, p-values <0.001; $\rho_{K\text{-}As}$ =-0.61, p-values <0.001) during this interval. The increased As sequestration may be related to reduced periods of anoxia and increased depth of the

redoxcline in sediment year round due to OM-poor sediment limiting the use of oxygen by bacteria for degradation of OM.

5.9.2.3 Phase 3a – Cool Tundra conditions

Phase 3 (ca. 2150–1250 cal. BP) exhibited relatively stable sediment geochemistry, representing the establishment of near-modern tundra conditions surrounding Control Lake after a sharp decline in temperature following the end of the Holocene hypsithermal. Testate amoeba during this interval are indicative of healthy conditions, with high proportions of *D. oblonga* and lower proportions of Centropyxids than were previously observed. An increase in the proportion of *D. glans* "glans" during this interval from 5% to 10% may indicate deeper lake conditions (Nasser et al., 2016; Reinhardt et al., 1998), possibly associated with widespread cool conditions and reduced evaporative pressure during this phase of deposition. However, Neville et al. (2010) also observed an increase in *D. glans* "glans" during cooler lake temperatures in late winter/early spring, suggesting the earlier observed depth-dependence may be a function of cooler temperatures below the thermocline, and an increase in *D. glans* "glans" during this interval may be the result of overall cooler temperatures observed in chironomid and palynological records (Viau and Gajewski, 2004; Upiter et al., 2014). A higher concentration of Arcellinida tests/cc may be indicative of higher biomass and healthier conditions as the age model does not suggest substantial change in deposition rate during this interval.

During Phase 3A, Rb and K values exhibited the highest concentrations observed in core (7.5 +/- 0.40 ppm and 1047 +/- 57 ppm, respectively), with a gradual increasing trend towards the end of this phase. The gradual increase in proportion of minerogenic material may be indicative of increased winter snow pack. Huang et al (2004) observed an increase in *Betula* and *Alnus* pollen in nearby UCLA lake from ca. 1500–1000 cal. BP. As there is typically thicker snowpack in shrub-tundra environments than in full tundra settings, and because shrub-tundra melts faster than either forested or tundra systems (Lundberg and Beringer 2005; Pomeroy et al. 2006; Charman et al. 2010), the high proportion of fine, minerogenic indicators be a response to subtle shifts in vegetation affecting snowpack.

Phase 3A corresponds to a period of lower concentration in Mn, Fe, and As, and generally low concentrations of S, although not as low as S concentration in subsequent Phase 3B. Miller et al. (in press) observed decreased TOC and labile organic matter in a short gravity core collected from Control Lake during this interval, suggesting a possible association between organic content and Mn, Fe, and As. A decrease in organic content may result in reduced periods of anoxia in sediment and increased sequestration of As in minerals stable under oxidizing conditions (Fe- and Mn-oxyhydroxides). Strong correlations between As, Mn, and Fe and weak negative correlations to S support this interpretation. Alternatively, labile organic matter may have promoted As sequestration through direct sorption (Redman et al. 2002; Meunier et al. 2011), or through providing increased surface area for nucleation/growth of minerals (Sanei et al. 2005), encouraging the precipitation of Fe-oxyhydroxides, As-sulphides, or ferrous-As minerals (Weber et al. 2006; Du Laing et al. 2009; Root et al. 2009; Thiel et al. 2019). Increased labile organic matter acting to increase As sequestration has previously been observed in the Yellowknife region by Galloway et al. (2018), and was posited by Miller et al. (in press) as the method As sequestration in Control Lake during this interval. However, Ca/Rb in our sediment cores shows a weak negative relationship to As during Phase 3A ($\rho = -0.29$, p-value >0.1, $n = 32$). It may be that long-term (multi-centennial) shifts in As are control by overall decreased labile OM, as observed by Miller et al (in. press), but cm-scale (multi-decadal) variations in As are controlled through different mechanisms.

Increases in As concentration from approximately 80 ppm to 120 ppm were observed between ca. 1700 to 1550 cal. BP and ca. 1900 to 1800 cal BP. Both of these intervals are proceeded by abrupt increases in K and Rb concentrations. Similarly, an increase in As concentration from ca. 2300 to 2100 cal BP during the transition from Phase 2 to Phase 3A is proceeded by three abrupt peaks in Rb and K. It is possible that rapid deposition of minerogenic material associated with summer storm activity caused increased preservation of As by depositing relatively thick, labile-OM-poor sediment that pushes the redoxicline deeper into sediment. Confirmation of this hypothesis, however, would require additional grain-size data or quantification of organic content in core.

5.9.2.4 Phase 3B – Tundra high-As concentrations

The final phase of deposition at Control Lake (ca. 1250–0 cal. BP) exhibited Arcellinida community indicative of low stress similar to those observed in Phase 3A. This interval is again dominated by *D. oblonga*, with further decreases in proportion of Centropyxids in sample. Although there is a slight decrease in SDI during this interval, an increase to the highest observed Arcellinida tests/cc indicates generally healthy conditions. A minor increase in *C. tricuspis* suggests a slight increase in productivity as may be expected by generally warmer conditions reconstructed across the arctic during this interval (Viau and Gajewski 2004; Upiter et al., 2014; Gajewski 2015). There is a decrease in the proportion of *D. glans* "glans" suggesting a possible return to lower lake levels, although again this may be increased temperatures as Neville et al. (2010) suggests this relationship may be temperature-dependent. There is an increase in the proportion of *P. compressa* such that it co-dominates the assemblage during this final phase of deposition. Scott and Medioli (1983) found high concentrations of *P. compressa* nearer the shores of Lake Erie up to depths of 50 feet. Research on road-adjacent ponds and lakes in Ontario, Canada, by Roe et al. (2010) found that *P. compressa* and *Lagenodifflugia vas,* another arcellinida species that constructs an internal diaphragm, were tolerant to high levels of phosphorous and high-pH. Murray (1967) found *P. compressa* were able to tolerate low salinity conditions to a similar degree as centropyxids, and thrived in temperatures ranging from 11–20°C. Qin et al., (2013) found elevated concentrations of *P. compressa* alongside *D. oblonga* in higher pH, higher chlorophyll *a*, and higher depth lakes. Neville et al., 2010 observed an increase in *P. compressa* during the late summer and fall in northern Albertan lakes, suggesting a possible preference towards lower oxygen conditions. This increase in *P. compressa* may therefore indicate generally higher pH in the system, or possibly increased late-season anoxia. However, it is still unclear what environments *P. compressa* thrives in or the advantage of the internal diaphragm.

Sediment geochemistry changes slightly during this interval of deposition. There is a minor decrease in Rb and K concentration in CON02 sediments deposited between ca. 1200 and 600 cal. BP followed by a subsequent increase in Rb and K from ca. 600 to 250 cal. BP. There is a minor increase in Fe, and As concentrations, between ca. 1100 and 600 cal. BP. Arsenic, and Fe are slightly lower between ca. 600 and 250 cal. BP. Similar

to Phase 3A, there is strong positive correlations of Fe, As and Mn ($p > 0.89$, p-value < 0.001, $n = 39$) and a notable shift to positive correlations between S and other redox-sensitive elements ($p > 0.59$, p-value < 0.001, $n = 39$). Although the positive correlation between As, Fe and S may indicate an increase in the proportion of Fe and As forming solid phases with sulfides, Miller et al (in press) observed As was predominantly sorbed to FeO(OH) during this interval at Control Lake, with only minor contributions from FeS_2 in similar proportion to those observed in previous intervals

The cause of step-change towards high As concentration (~50 ppm difference in mean) is likely caused by increased labile OM deposition during this interval as was observed in Miller et al. (in press). Increased labile OM may directly increase As sorption in sediment, or indirectly increase the possibility of As sorption by encouraging formation of FeO(OH) (Redman et al. 2002; Weber et al. 2006; Galloway et al., 2018; Miller et al. in press). During Phase 3B, the weak negative correlation between As and minerogenic indicators (Rb, K), and weak, positive, statistically significant correlation to Ca/Rb indicates that productivity may have been more important for As sequestration than processes impacted minerogenic content.

The Little Ice Age (LIA; ca. 500–250 cal. ry BP) and Medieval Warm Period (MWP; ca. 1000–700 cal. BP) are globally documented temperature anomalies. An increase in C:N and $\delta^{13}C$ at Danny's Lake from ca. 1500–1000 cal. BP may suggest increased productivity associated with increased warm temperatures (Sulphur et al. 2016); this is followed by substantial decreases in C:N after 700 cal. BP likely representative of recent climate warming in the subarctic. Macumber et al (2018) observed an increase in coarse sediment end members at Danny's Lake and Waite Lake ca. 1100 cal. BP until 250 cal. BP indicative of possibly cooler summer temperatures. Palynological and microfossil temperature reconstructions suggest generally warmer temperatures from ca. 1100 to 700 cal. BP and cooler temperatures from ca. 500 to 200 cal. BP in the subarctic (Gajewski and Viau, 2009; Upiter et al. 2014; Gajewski 2015).

At Control Lake, a brief period of elevated sedimentary As concentration is preserved between ca. 1200 and 600 cal. BP, alongside minor decreases in Rb and K. A minor decrease in Rb and K occurs between ca. 600 and 250 cal. BP coeval with increase

in the preservation of As in sediment. The increase in the concentration of Rb and K between ca. 600–250 cal. BP may have been caused by cooler conditions encouraging prolonged snowmelt period, increasing transport of minerogenic material into the basin during the LIA (Cockburn and Lamoureux 2008a; Tomkins et al. 2010; Amann et al. 2017). Decrease in Rb and K between ca. 1200-600 cal. BP would have been caused by warmer temperatures that would have induced a rapid snowmelt period during the MWP. Increased temperatures between ca. 1200–600 may have encouraged productivity, increasing As sequestration, as is observed during this period. The opposite is true of the inferred conditions between ca. 600–250 cal. BP, when cooler temperatures prevailed and would have decreased productivity, and thus As sequestration in sediment. It is apparent that during periods of stable environmental conditions, temperature may be affecting Control Lake As sequestration by influencing autochthonous productivity.

5.10 Conclusions

The sedimentary record at Control Lake recorded the last ca. 4100 cal. BP of environmental change in the central NT. Throughout this interval, Arcellinida indicate a generally healthy, oligo- to mesotrophic lake. Control Lake transitioned through 4 phases of deposition corresponding to (1) forested catchment and reduced input of minerogenic material or possibly finer particle size; (2) a transition towards tundra dominated system and sedimentation dominated by increased input of minerogenic material; (3A) a period of increased minerogenic content and low As concentrations driven by cool temperatures and reduced productivity; and (3B), a period of reduced minerogenic input and greater As concentrations driven by warmer temperatures and increased productivity. Subtle changes in sedimentation from ca. 1200–600 and 600–250 cal. BP may record the LIA and MWP at Control Lake. As sequestration during early phases of deposition was nearly non-existent, possibly because of abundant OM and reduced minerogenic input resulting in seasonal anoxia. When the surrounding catchment shifted towards a tundra environment, As concentrations increased possibly due to lower OM content available for digestion, and thus shorter intervals of anoxia. Arsenic peaks occur below major changes in Rb and K, suggesting shift to high-minerogenic sediment may have result in preservation of increase As concentration due to reduced intervals of anoxia. Once tundra vegetation was established, longer-term variations in sedimentary As concentration were

controlled by shifts in regional temperature and resulting changes in productivity. Although minerogenic input may have played some part in transport of As into the system, or altering sequestration through rapid burial during summer storms that can rapidly deposit centimeters of OM-poor sediment (Amann et al. 2017), there were weak correlations between As and Rb, indicating this was a secondary control on As concentrations in sediment. Regional vegetation and temperature, and local sedimentary processes controlled As concentrations in sediment during the studied deposition sequence at Control Lake.

5.11 References

Aboriginal Affairs and Northern Development Canada (2013) Water Balance Monitoring at the Tundra Mine Site: 2012 Update. 101

Amann B, Lamoureux SF, Boreux MP (2017) Winter temperature conditions (1670–2010) reconstructed from varved sediments, western Canadian High Arctic. Quat Sci Rev 172:1–14.

Andrade CF, Jamieson HE, Kyser TK, Praharaj T, Fortin D (2010) Applied Geochemistry Biogeochemical redox cycling of arsenic in mine-impacted lake sediments and co-existing pore waters near Giant Mine , Yellowknife Bay , Canada. Appl Geochemistry 25:199–211.

Arp CD, Jones BM, Whitman M, Larsen A, Urban FE (2010) Lake temperature and ice cover regimes in the Alaskan Subarctic and Arctic: Integrated monitoring, remote sensing, and modeling. J Am Water Resour Assoc 46:777–791.

Asioli A, Medioli FS, Patterson RT (1996) Thecamoebians as a tool for reconstruction of paleoenvironments in some Italian lakes in the foothills of the southern Alps (Orta, Varese and Candia). J Foraminifer Res 26:248–263.

Benning LG, Wilkin RT, Barnes HL (2000) Reaction pathways in the Fe-S system below 100°C. Chem Geol 167:25–51.

Blaauw M, Christen JA (2019) rbacon: Age-depth modelling using bayesian statistics. R Package version 2.3.7.

Bostick BC, Fendorf S (2003) Arsenite sorption on troilite (FeS) and pyrite (FeS2). Geochim Cosmochim Acta 67:909–921.

Bowell RJ, Alpers CN, Jamieson HE, Nordstrom DK, Majzlan J (2014) The environmental geochemistry of arsenic—an overview. Reviews in Mineralogy and Geochemistry, 79(1):1–16.

Burton ED, Bush RT, Sullivan LA (2006) Acid-volatile sulfide oxidation in coastal flood plain drains: Iron-sulfur cycling and effects on water quality. Environ Sci Technol 40:1217–1222.

Burton ED, Johnston SG, Planer-Friedrich B (2013) Coupling of arsenic mobility to sulfur transformations during microbial sulfate reduction in the presence and absence of humic acid. Chem Geol 343:12–24.

Butler IB, Rickard D (2000) Framboidal pyrite formation via the oxidation of iron (II) monosulfide by hydrogen sulphide. Geochim Cosmochim Acta 64:2665–2672.

Calvert SE, Pedersen TF (1996) Sedimentary geochemistry of manganese: Implications for the environment of formation of manganiferous black shales. Econ Geol 91:36–47.

Campbell KM, Nordstrom DK (2019) Arsenic Speciation and Sorption in Natural Environments. In: Arsenic: Environmental geochemistry, mineralogy and microbiology. pp 170–201

Canadian Council of Ministers of the Environment (CCME) (2002) Canadian Soil Quality Guidelines for the Protection of Environmental and Human Health - Arsenic (Inorganic)

Charman DJ, Gehrels WR, Manning C, Sharma C (2010) Reconstruction of recent sea-level change using testate amoebae. Quat Res 73:208–219.

Chao TT (1984) Use of partial dissolution techniques in geochemical exploration. Journal of Geochemical Exploration, 20:101-135.

Chipman ML, Hu FS (2017) Linkages Among Climate, Fire, and Thermoerosion in Alaskan Tundra Over the Past Three Millennia. J Geophys Res Biogeosciences 122:3362–3377.

Choppala G, Bush R, Moon E, Ward N, Wang Z, Bolan N, Sullivan L (2017) Oxidative transformation of iron monosulfides and pyrite in estuarine sediments: Implications for trace metals mobilisation. J Environ Manage 186:158–166.

Church SE, Mosier EL, Motooka JM (1987) Mineralogical basis for the interpretation of multi-element (ICP-AES), oxalic acid, and Aqua Regia partial digestions of stream sediments for reconnaissance exploration geochemistry. Journal of Geochemical exploration, 28:207–233.

Cockburn CF, Gregory BRB, Nasser NA, Patterson RT (in press) Intra-lake arcellinida (testate lobose amoebae) response to winter de-icing contamination in an eastern Canada road-side "Salt Belt" lake. Microbial Ecology. (Man #: MECO-D-19-00183).

Cockburn JMH, Lamoureux SF (2008a) Hydroclimate controls over seasonal sediment yield in two adjacent High Arctic watersheds. Hydrol Process 22:2013–2027.

Cockburn JMH, Lamoureux SF (2008b) Inflow and lake controls on short-term mass

accumulation and sedimentary particle size in a High Arctic lake : implications for interpreting varved lacustrine sedimentary records. J Paleolimnol 40:923–942.

Coleman KA, Palmer MJ, Korosi JB, Kokelj SV, Jackson K, Hargan KE, Courtney-Mustaphi JC, THeinpont JR, Kimpe LE, Blais JM, Pisaric MFJ, Smol JP (2015) Tracking the impacts of recent warming and thaw of permafrost peatlands on aquatic ecosystems: A multi-proxy approach using remote sensing and lake sediments. Boreal Environ Res 20:363–377

Collins S V, Reinhardt EG, Werner C, Le Maillot C, Devos F, Rissolo D (2015) Late Holocene Mangrove Development and Onset of Sedimentation in the Yax Chen Cave System (Ox Bel Ha) Yucatan, Mexico: Implications for Using Cave Sediments as a Sea-Level Indicator. Paleogeography, Paleoclimatology, Paleoecol 438:124–134.

Cuven S, Francus P, Lamoureux SF (2010) Estimation of grain size variability with micro X-ray fluorescence in laminated lacustrine sediments, Cape Bounty, Canadian High Arctic. J Paleolimnol 44:803–817.

Das BK, Haake B-G (2003) Geochemistry of Rewalsar Lake sediment, Lesser Himalaya, India: implications for source-area weathering, provenance and tectonic setting. Geosciences Journal, 7(4):299-312

Davies SJ, Lamb HF, Roberts SJ (2015) Micro-XRF Core Scanning in Palaeolimnology: Recent Developments. In: Micro-XRF Studies of Sediment Cores: Applications of a Non-Destructive tool for Environmental Sciences. pp 189–226

Drljepan M, McCarthy FM, Hubeny JB (2014) Natural and cultural eutrophication of Sluice Pond, Massachusetts, USA, recorded by algal and protozoan microfossils. The Holocene 24:1731–1742.

Du Laing G, Chapagain SK, Dewispelaere M, Meers E, Kazama F, Tack FMG, Rinklebe J, Verloo MG (2009) Presence and mobility of arsenic in estuarine wetland soils of the Scheldt estuary (Belgium). J Environ Monit 11:873–881.

Duguay CR, Prowse TD, Bonsal BR, Bonsal BR, Brown RD, Lacroix MP, Ménard P (2006) Recent trends in Canadian lake ice cover. Hydrol Process 20:781–801.

Forbes AC, Lamoureux SF (2005) Climatic Controls on Streamflow and Suspended Sediment Transport in Three Large Middle Arctic Catchments , Boothia Peninsula ,

Nunavut , Canada. 37:304–315

Gajewski K (2015) Quantitative reconstruction of Holocene temperatures across the Canadian Arctic and Greenland. Glob Planet Change 128:14–23.

Galloway JM, Sanei H, Patterson RT, Mosstajiri T, Hadlari T, Falck H (2012) Total arsenic concentrations of lake sediments near the City of Yellowknife, Northwest Territories. Geological Survey of Canada open file 7037, pp. 1-47.

Galloway JM, Palmer M, Jamieson HE, Patterson RT, Nasser NA, Falck H, Macumber AL, Goldsmith SA, Sanei H, Normandeau P, Hadlari T, Roe HM, Neville LA, Lemay D (2015) Geochemistry of lakes across ecozones in the Northwest Territories and implications for the distribution of arsenic in the Yellowknife region, Part 1: Sediments. Geological Survey of Canada Open File 7908, pp. 1-50.

Galloway JM, Swindles GT, Jamieson HE, Palmer M, Parsons MB, Sanei H, Macumber AL, Patterson RT, Falck H (2018) Organic matter control on the distribution of arsenic in lake sediments impacted by ~65 years of gold ore processing in subarctic Canada. Sci Total Environ 622:1668–1679.

Gavel MJ, Patterson RT, Nasser NA, Galloway JM, Hanna BW, Cott PA, Roe HM, Falck H (2018) What killed Frame Lake? A precautionary tale for urban planners. PeerJ 6:e4850.

[dataset] Gregory BRB, Patterson RT, Nasser NA, Galloway JM (2019) Control Lake aqua regia ICP-MS. Mendeley Data, Version 1.0.

Guénet H, Davranche M, Vantelon D, Vantelon D, Pédrot M, Al-Sid-Cheikh M, Dia A, Jestin J (2016) Evidence of organic matter control on As oxidation by iron oxides in riparian wetlands. Chem Geol 439:161–172.

Guyard H, Chapron E, St-Onge G, Anselmetti FS, Arnaud F, Magand O, Francus P, Mélières M-A (2007) High-altitude varve records of abrupt environmental changes and mining activity over the last 4000 years in the Western French Alps (Lake Bramant, Grandes Rousses Massif). Quat Sci Rev 26:2644–2660.

Van Hengstum, P (2008) Paleoenvironmental analysis using thecamoebians and foraminifera in Mexican anchialine caves: a focus on Aktun Ha (Carwash) Mexico. Unpublished MSc thesis, McMaster University, Hamilton, ON, Canada.

Hu FS, Higuera PE, Walsh JE, Chapman WL, Duffy PA, Brubaker LB, Chipman ML (2010)

Tundra burning in Alaska: Linkages to climatic change and sea ice retreat. J Geophys Res Biogeosciences 115:1–8.

Huang CC, MacDonald G, Cwynar L (2004) Holocene landscape development and climatic change in the low arctic, Northwest Territories, Canada. Palaeogeogr Palaeoclimatol Palaeoecol 205:221–234.

Jacques JMS, Sauchyn DJ (2009) Increasing winter baseflow and mean annual streamflow from possible permafrost thawing in the Northwest Territories, Canada. Geophys Res Lett 36:1–6.

Juggins S (2005) Rioja: Analysis of Quaternary Science Data. R package version (0.9-9). http://cran.r-project.org/package=rioja.

Kaufman DS, Ager TA, Anderson NJ, Anderson PM, Andrews JT, Bartlein PJ, Brubaker LB, Coats LL, Cwynar LC, Duvall ML, Dyke AS, Edwards ME, Eisner WR, Gajewski K, Geirsdóttir A, Hu FS, Jennings AE, Kaplan MR, Kerwin MW, Lazhkin AV, MacDonald GM, Miller GH, Mock CJ, Oswald WW, Otto-Bliesner BL, Porinchu DF, Rühland K, Smol JP, Steig EJ, Wolfe BB (2004) Holocene thermal maximum in the western Arctic (0-180°W). Quat Sci Rev 23:529–560.

Kauppila T, Kihlman S, Mäkinen J (2006) Distribution of arcellaceans (testate amoebae) in the sediments of a mine water impacted bay of lake retunen, Finland. Water Air Soil Pollut 172:337–358.

Kihlman SM, Kauppila ÆT (2009) Mine water-induced gradients in sediment metals and arcellacean assemblages in a boreal freshwater bay (Petkellahti, Finland). J Paleolimnol 42:533–550.

Kremer M, Chan R, Ward BC, Dredge LA, Kerr DE, Eagles S (2014) Surficial Geology, Lac de Gras, Northwest Territories, NTS 76-D. Geological Survey of Canada Geoscience Map 184 (2nd edtition, preliminary, Surficial Data Model v. 2.0 conversion of Map 1870A).

Kwok R, Rothrock DA (2009) Decline in Arctic sea ice thickness from submarine and ICESat records: 1958-2008. Geophys Res Lett 36:1–5.

Kylander ME, Ampel L, Wohlfarth B, Veres D (2011) High-resolution X-ray fluorescence core scanning analysis of Les Echets (France) sedimentary sequence: new insights from chemical proxies. Journal of Quaternary Science, 26(1):109-117

LaForce MJ, Hansel CM, Fendorf S (2000) Arsenic speciation, seasonal transformations and co-distribution with iron in a mine waste-influenced palustrine emergent wetland. Environ Sci Technol 34:3937–3943.

Lapointe F, Francus P, Lamoureux SF, Said M, Cuven S (2012) 1750 years of large rainfall events inferred from particle size at East Lake, Cape Bounty, Melville Island, Canada. Journal of Paleolimnology, 48:149-173.

Larsen CPS, MacDonald GM (1993) Lake morphometry, sediment mixing and the selection of sites for fine resolution palaeoecological studies. Quat Sci Rev 12:781–792.

Lock A, Wallschläger D, Belzile N, Spiers G, Gueguen C (2018) Rates and processes affecting As speciation and mobility in lake sediments during aging. J Environ Sci (China) 66:338–347.

Lubin JH, Colt JS, Camann D, Davis S, Cerhan JR, Severson RK, Bernstein L, Hartge P (2004) Epidemiologic evaluation of measurement data in the presence of detection limits. Environ Health Perspect 112:1691–1696.

Lundberg A, Beringer J (2005) Albedo and snowmelt rates across a tundra to forest transition. 15th Int North Res Basins Symp Work 1–10

MacDonald GM, Edwards TWD, Moser KA, Pienitz R, Smol JP (1993) Rapid response of treeline vegetation and lakes to past climate warming. Nature 361:243–246.

Macdonald RW, Harner T, Fyfe J (2005) Recent climate change in the Arctic and its impact on contaminant pathways and interpretation of temporal trend data. Sci Total Environ 342:5–86.

Macumber AL, Patterson RT, Roe HM, Reinhardt EG, Neville LA, Swindles GT (2014) Autoecological approaches to resolve subjective taxonomic divisions within Arcellacea. Ann Anat 165:305–316.

Martin AJ, Pedersen TF (2002) Seasonal and interannual mobility of arsenic in a lake impacted by metal mining. Environ Sci Technol 36:1516–1523.

Masuda H, Yamatani Y, Okai M (2005) Transformation of arsenic compounds in modern intertidal sediments of Iriomote Island, Japan. J Geochemical Explor 87:73–81.

Mccurdy MW, Mcneil RJ (2014) Geological Survey of Canada Open File 7577,

Geochemical Data from Stream Silts and Surface Waters in the Pine Point Mining District, Northwest Territories (NTS 85-B).

Medioli FS, Scott DB (1988) Lacustrine thecamoebians (mainly arcellaceans) as potential tools for palaeolimnological interpretations. Palaeogeogr Palaeoclimatol Palaeoecol 62:361–386.

Meng X, Dupont RR, Sorensen DL, Jacobson AR, McLean JE (2016) Arsenic solubilization and redistribution under anoxic conditions in three aquifer sediments from a basin-fill aquifer in Northern Utah: The role of natural organic carbon and carbonate minerals. Appl Geochemistry 66:250–263.

Meunier L, Koch I, Reimer KJ (2011) Effects of organic matter and ageing on the bioaccessibility of arsenic. Environmental Pollution 159:2530-2536.

Michelutti N, Douglas MSV, Smol JP (2003) Diatom response to recent climatic change in a high arctic lake (Char Lake, Cornwallis Island, Nunavut). Glob Planet Change 38:257–271.

Miller CB, Parsons MB, Jamieson HE, Swindles GT, Nasser NA, Galloway JM (2019). Lake-specific controls on the long-term stability of mining-related, legacy arsenic contamination and geochemical baselines in a changing northern environment, Tundra Mine, Northwest Territories, Canada. Applied Geochemistry 104403.

Miller CB, Parsons MB, Jamieson HE, Ardakani OH, Gregory BRB, Galloway JM (in press). Influence of late Holocene climate on solid-phase speciation and long-term stability of arsenic in sub-Arctic lake sediments. Science of the Total Environment.

Moore JCG (1986) Courageous-Matthews Lake area, district of MacKenzie, Northwest Territories. Geological Survey of Canada Department of Mines and Technical surveys Report # 2524.

Moser KA, MacDonald GM (1990) Holocene Vegetation Change at Treeline North of Yellowknife, Northwest Territories, Canada. Quat Res 34:227–239.

Nasser NA, Patterson RT, Roe HM, Galloway JM, Falck H, Palmer MJ, Spence C, Sanei H, Macumber AL, Neville LA (2016) Lacustrine Arcellinina (Testate Amoebae) as Bioindicators of Arsenic Contamination. Environ Microbiol 72(1):130–149.

Nasser NA, Patterson RT, Roe HM, Galloway JM, Hendrik F, Sanei HA (in press) Use of Arcellinida-based arsenic tolerance limits as novel tool for biomonitoring As

contamination in lakes. Ecological Indicators.

Neumann T, Scholz F, Kramar U, Ostermaier M, Rausch N, Berner Z (2013) Arsenic in framboidal pyrite from recent sediments of a shallow water lagoon of the Baltic Sea. Sedimentology 60:1389–1404.

Neville LA, McCarthy FMG, MacKinnon MD, Swindles GT, Marlowe P (2011) Thecamoebians (Testate Amoebae) As Proxies of Ecosystem Health and Reclamation Success in Constructed Wetlands in the Oil Sands of Alberta, Canada. J Foraminifer Res 41:230–247.

Noël V, Juillot F, Morin G, Marchand C, Ona-Nguema G, Viollier E, Prévot F, Dublet G, Maillot F, Delbes L, Marakovic G, Bargar JR, Brown Jr. GE (2017) Oxidation of Ni-Rich Mangrove Sediments after Isolation from the Sea (Dumbea Bay, New Caledonia): Fe and Ni Behavior and Environmental Implications. ACS Earth Sp Chem 1:455–464.

Oksanen J, Blanchet FG, Friendly M, Kindt R, Legendre P, McGlinn D, Minchin PR, O'Hara RB, Simpson GL, Solymos P, Stevens MHH, Szoecs E, Wagner H (2019) Vegan: Community ecology package. R. package version 2.5-4. https://cran.r-project.org/package=vegan.

Overpeck J, Hughen K, Hardy D, Bradley R, Case R, Douglas M, Finney B, Gajewski K, Jacoby G, Jennings A, Lamoureux S, Lasca A, MacDonald G, Moore J, Retelle M, Smith S, Wolfe A, Zielinski G (1997) Arctic environmental change of the last four centuries. Science 278:1251–1256

Padgham WA (1992) Mineral deposits in the Archean Slave Structural Province; lithological and tectonic setting. Precambrian Researc 58:1–24

Palmer MJ, Galloway JM, Hamieson HE, Patterson RT, Falck H, Kokelj SV. (2015). The concentration of arsenic in lake waters of the Yellowknife area. Northwest Territories Geological Survey, NT Open File, 6, 25.

Palmer MJ, Chetelat J, Richardson M, Jamieson HE, Galloway JM (2019) Seasonal variation of arsenic and antimony in surface waters of small subarctic lakes impacted by legacy mining pollution near Yellowknife, NT, Canada. Science of the Total Environment, 684, 326-339.

Patterson RT, Baker T, Burbidge SM (1996) Arcellaceans (thecamoebians) as proxies of

arsenic and mercury contamination in northeastern Ontario lakes. J Foraminifer Res 26:172–183.

Patterson RT, Dalby A, Kumar A, Henderson LA, Boudreau REA (2002) Arcellaceans (thecamoebians) as indicators of land-use change : settlement history of the Swan Lake area , Ontario as a case study . J Paleolimnol 28:297–316.

Patterson RT, Fishbein E (1989) Re-examination of the statistical methods used to determine the number of point counts needed for micropaleontological quantitative research. Journal of Paleolimnology 63(2):245–248.

Patterson RT, Kumar A (2002) A review of current testate rhizopod (thecamoebian) research in Canada. Palaeogeogr Palaeoclimatol Palaeoecol 180:225–251.

Patterson RT, Kumar A (2000a) Arcellaceans (thecamoebians): new tools for monitoring long- and short-term changes in lake bottom acidity. Environ Geol 39:689–697

Patterson RT, Kumar A (2000b) Assessment of Arcellacean (Thecamoebian) Assemblages, Species, and Strains As Contaminant Indicators in James Lake, Northeastern Ontario, Canada. J Foraminifer Res 30:310–320.

Patterson RT, Lamoureux EDR, Neville LA, Macumber AL (2013) Arcellacea (Testate Lobose Amoebae) as pH Indicators in a Pyrite Mine-Acidified Lake, Northeastern Ontario, Canada. Microb Ecol 65:541–554.

Patterson RT, Roe HM, Swindles GT (2012) Development of an Arcellacea (testate lobose amoebae) based transfer function for sedimentary Phosphorus in lakes. Palaeogeogr Palaeoclimatol Palaeoecol 348–349:32–44.

Payette S, Delwaide A, Caccianiga M, Beauchemin M (2004) Accelerated thawing of subarctic peatland permafrost over the last 50 years. Geophys Res Lett 31:1–4.

Peros M, Collins S, G'Meiner AA, Reinhardt EG, Pupo FM (2017) Multistage 8.2 kyr event revealed through high-resolution XRF core scanning of Cuban sinkhole sediments. Geophys Res Lett 44:7374–7381.

Pienitz R, Smol JP, Lean DR (1997) Physical and chemical limnology of 59 lakes located between the southern Yukon and the Tuktoyaktuk Peninsula, Northwest Territories (Canada). Can J Fish Aquat Sci 54:330–346.

Pienitz R, Smol JP, Lean DR (2011) Physical and chemical limnology of 24 lakes located between Yellowknife and Contwoyto Lake, Northwest Territories (Canada). Can J

Fish Aquat Sci 54:347–358.

Pienitz R, Smol JP, Macdonaldt GM (1999) Paleolimnological Reconstruction of Holocene Climatic Trends from Two Boreal Treeline Lakes, Northwest Territories, Canada. Arctic, Antarctic, and Alpine Research 31(1):82-93.

Polizzotto ML, Harvey CF, Li G, Badruzzman B, Ali A, Newville M, Sutton S, Fendorf S (2006) Solid-phases and desorption processes of arsenic within Bangladesh sediments. Chem Geol 228:97–111.

Pomeroy JW, Bewley DS, Essery RLH, Hedstrom NR, Link T, Granger RJ, Sicart JE, Ellis CR, Janowicz JR (2006) Shrub tundra snowmelt. Hydrol Process 20:923–941.

Prentice S V., Roe HM, Bennion H, Sayer CD, Salgado J (2018) Refining the palaeoecology of lacustrine testate amoebae: insights from a plant macrofossil record from a eutrophic Scottish lake. J Paleolimnol 60:189–207.

Qin YM, Fournier B, Lara E, Gu Y, Wang H, Cui Y, Zhang X, Mitchel EAD (2013) Relationships between testate amoeba communities and water quality in Lake Donghu, a large alkaline lake in Wuhan, China. Frontiers of Earth Sciences 7(2):182-190

R Core Team (2014) R: A language and environment for statistical computing. R foundation for Statistical Computing, Vienna, Austria.

Redman AD, Macalady DL, Ahmann D (2002) Natural organic matter affects Arsenic speciation and sorption onto hematite. Environ Sci Technol 36:2889–2896.

Reimann C, Filzmoser P, Garrett RG, Dutter R (2008). Statistical data analysis explained. Applied environmental statistics with R. England: Wiley & Sons Ltd.

Reimer PJ, Bard E, Bayliss A, Beck JW, Blackwell PG, Ramsey CB, Buck CE, Cheng H, Edwards RL, Friedrich M, Grootes PM, Guilderson TP, Haflidason H, Hajdas I, Hatte C, Heaton TJ, Hoffman DL, Hogg AG, Hughen KA, Kaiser KF, Kromer B, Manning SW, Niu M, Reimer RW, Richards DA, Scott EM, Southon JR, Staff RA, Turney CSM, ven der Plicht J (2013). IntCal13 and Marine13 Radiocarbon age calibration curves 0-50,000 years cal BP. Radiocarbon 55:1869-1887.

Reinhardt EG, Dalby AP, Kumar A, Patterson RT (2006) Arcellaceans as Pollution Indicators in Mine Tailing Contaminated Lakes near Cobalt, Ontario, Canada. Micropaleontology 44:131.

Reinhardt EG, Dalby AP, Kumar A, Patterson RT (1998) Arcellaceans as Pollution Indicators in Mine Tailing Contaminated Lakes near Cobalt, Ontario, Canada. Micropaleontology 44:131.

Reinhardt EG, Little M, Donato S, Findlay D, Krueger A, Clark C, Boyce J (2005) Arcellacean (thecamoebian) evidence of land-use change and eutrophication in Frenchman's Bay, Pickering, Ontario. Environ Geol 47:729–739.

Roe HM, Patterson RT (2014) Arcellacea (Testate Amoebae) as Bio-indicators of Road Salt Contamination in Lakes. Microb Ecol 68:299–313.

Roe HM, Patterson RT, Swindles GT (2010) Controls on the contemporary distribution of lake thecamoebians (testate amoebae) within the Greater Toronto Area and their potential as water quality indicators. J Paleolimnol 43:955–975.

Root RA, Vlassopoulos D, Rivera NA, Rafferty MT, Andrews C, O'Day PA (2009). Speciation and natural attenuation of arsenic and iron in a tidally influenced shallow aquifer. Geochimica et Cosmochimica Acta 73:5528-5553.

Rouse R, Bay J, Maria H (1984) Microclimate at Arctic Tree Line: Radiation balance of tundra and forest. Water Resources Research 20(1)57-66.

Ruhland K, Smol JP (1998) Limnological Characteristics of 70 Lakes Spanning Arctic Treeline from Coronation Gulf to Great Slave Lake in the Central Northwest Territories, Canada. Int Rev Hydrobiol 1998:183–203

Sanei H, Stasiuk LD, Goodarzi F (2005) Petrological changes occurring in organic matter from Recent lacustrine sediments during thermal alteration by Rock-Eval pyrolysis. Org Geochem 36:1190–1203.

Schilling J, Reimann C, Roberts D (2014) REE potential of the Nordkinn Peninsula, North Norway: A comparison of soil and bedrock composition. Applied Geochemistry 41:95-106.

Schuh CE, Jamieson HE, Palmer MJ, Martin AJ, Blais JM (2019) Controls governing the spatial distribution of sediment arsenic concentrations and solid-phase speciation in a lake impacted by legacy mining pollution. Sci Total Environ 654:563–575.

Scott DB, Medioli FS (1983) Agglutinated Rhizopods in Lake Erie : Modern Distribution and Stratigraphic Implications. J Paleontol 57:809–820

Seabridge Gold Inc. (2010) Courageous Lake Project Description in Support of a Class "

A ” Land Use Permit (Former Permit MV2003C0050)

Silke R (2009) The Operational History of Mines in the Northwest Territories , Canada. Northwest Territories Geological Survey.

Simpson GL, Oksanen K (2018) Analogue: Analogue matching and Modern Analogue Technique transfer function models. R package version 0.17-1. https://cran-r.project.org/package=analogue.

Smedley PL, Kinniburgh DG (2000) Source and behaviour of arsenic in natural waters. United Nations Synth Rep Arsen Drink 1–61

Šmejkalová T, Edwards ME, Dash J (2016) Arctic lakes show strong decadal trend in earlier spring ice-out. Sci Rep 6:1–8.

Smith SL, Burgess MM, Riseborough D, Nixon FM (2005) Recent trends from Canadian permafrost thermal monitoring network sites. Permafr Periglac Process 16:19–30.

Spellerberg I, Fedor PJ (2003). A tribute to Claude Shannon (1916-2001) and a plea for more rigorous use of species richness, species diversity and the “Shannon Wiener” index. Global Ecology and Biogeography, 12, 177-179.

Spence C, Kokelj SV, McCluskie M, Hedstrom N (2014) Evidence of a change in water chemistru in Canada’s subarctic associated with enhanced winter streamflow. J Geophys Res Biogeosciences 119:487–507.

Spliethoff HM, Mason RP, Hemond HF (1995) Interannual Variability in the Speciation and Mobility of Arsenic in a Dimictic Lake. Environ Sci Technol 29:2157–2161.

Steele RE, Nasser NA, Patterson RT, Gregory BRB, Roe HM, Reinhardt EG (2018) An Assessment of Sub-Meter Scale Spatial Variability of Arcellinida (Testate Lobose Amoebae) Assemblages in a Temperate Lake : Implications for Limnological Studies. Microbial Ecology 76(3):680–694.

Stroeve J, Holland MM, Meier W, Scambos T, Serreze M (2007) Arctic sea ice decline: Faster than forecast. Geophys Res Lett 34:1–5.

Sulphur KC, Goldsmith SA, Galloway JM, Macumber AL, Griffith F, Swindles GT, Patterson RT, Falck H, Clark ID (2016) Holocene fire regimes and treeline migration rates in sub-arctic Canada. Glob Planet Change 145:42–56.

Tetra Tech Wardrop (2012) Courageous Lake Prefeasibility Study. 1–450

Thamdrup B, Fossing H, Barker-Jorgensen B (1994) Manganese, iron, and sulfur cycling

in a coastal marine sediment, Aarhus Bay, Denmark. Geochim Cosmochim Acta 58:5115–29

Thiel J, Byrne JM, Kappler A, et al (2019) Pyrite formation from FeS and H_2S is mediated through microbial redox activity. Proc Natl Acad Sci 201814412.

Thompson PH, Kerswill JA (1994) Preliminary Geology of the Winter Lake - Lac de Gras area, District of MacKenzie, Northwest Territories, Open File 2740 (revised), scale 1:250000. 1

Tomkins JD, Lamoureux SF, Antoniades D, Vincent WF (2010) Autumn snowfall and hydroclimatic variability during the past millennium inferred from the varved sediments of meromictic Lake A, northern Ellesmere Island, Canada. Quat Res 74:188–198.

Torres E, Couture RM, Shafei B, Nardi A, Ayora C, van Cappellen P (2015) Reactive transport modeling of early diagenesis in a reservoir lake affected by acid mine drainage: Trace metals, lake overturn, benthic fluxes and remediation. Chem Geol 419:75–91.

Upiter LM, Vermaire JC, Patterson RT, Crann CA, Galloway JM, Macumber AL, Neville LA, Swindles GT, Falck H, Roe HM, Pisaric MFJ (2014) Middle to late Holocene chironomid-inferred July temperatures for the central Northwest Territories , Canada. J Paleolimnol 52:11–26.

Van Den Berghe MD, Jamieson HE, Palmer MJ (2018) Arsenic mobility and characterization in lakes impacted by gold ore roasting, Yellowknife, NT, Canada. Environ Pollut 234:630–641.

Van Hengstum PJ, Donnelly JP, Kingston AW, Williams BE, Scott DB, Reinhardt EG, Little SN, Patterson WP (2015) Low-frequency storminess signal at Bermuda linked to cooling events in the North Atlantic region. Paleoceanography 30:52–76.

Viau AE, Gajewski K (2009) Reconstructing millennial-scale, regional paleoclimates of boreal Canada during the holocene. J Clim 22:316–330.

Weber T, Allard T, Tipping E, Benedetti MF (2006) Modeling iron binding to organic matter. Environ Sci Technol 40:7488–7493.

Wetzel R (2001) Limnology: Lake and river ecosystems, 3rd edition. Gulf professional publishing.

Wilkin RT, Ford RG (2006) Arsenic solid-phase partitioning in reducing sediments of a contaminated wetland. Chem Geol 228:156–174.

Xu L, Zhao Z, Wang S, Pan R, Jia Y (2011) Transformation of arsenic in offshore sediment under the impact of anaerobic microbial activities. Water Res 45:6781–6788.

Zeileis A, Grotherndieck G (2005). Zoo: S3 infrastructure for regular and irregulat time series. Journal of Statistical Software 14(6): 1–27

Chapter 6: Solar-driven Sub- to Multi-decadal climate oscillations impact arsenic sequestration in lacustrine sediments

6.1: Authors and Addresses

Gregory BRB[1]*, Patterson RT[1], Galloway JM[1,2,3], Reinhardt EG[4]

[1]Ottawa-Carleton Geoscience Center and Department of Earth Sciences, Carleton University, 1125 Colonel By Dr., Ottawa, Ontario, Canada, K1S 5B6

[2]Geological Survey of Canada/National Resources Canada (Commission géologique du Canada/Ressources naturelles Canada), 3303 33 St. N.W., Calgary AB, Canada, T2L 2A7

[3]Aarhus Institute of Advanced Studies, Aarhus University, 8000 Aarhus C, Denmark

[4]School of Geography and Earth Sciences, McMaster University, 1280 Main St. W., Hamilton, Ontario, Canada, K1S 5B6

6.2: Foreword

This contribution represents an examination of the response of As and other sediment geochemistry paleo-proxies to quasi-periodic oscillations in ocean-atmosphere system. Shifts in temperature and precipitation in response to quasi-periodic climate phenomena, such as, the Pacific Decadal Oscillation, El niño/Southern Oscillation or the Arctic oscillation, have recently been identified in historical records in northern Canada. As of yet, there is little literature concerning whether these climate oscillations similarly impacted climate during the Holocene, or how these phenomena might impact metal(loid) sequestration. Although oscillations corresponding to the period of cyclic climate phenomena have been observed in other metal(loid) contaminants – Hg for example – As has not yet examined for response to climate oscillations. Here we examine Itrax-XRF results from core CON01 recovered from Control Lake, NT, using spectral and wavelet analyses to explore our data for oscillatory signals. This manuscript has been prepared for submission to *PeerJ*.

I collected core material in the field, sub-sampled cores for radiocarbon analysis, ICP-MS analysis following multi-acid digestion, analyzed cores using Itrax-XRF at the McMaster University Core Scanning Facility, completed post-processing and statistical analysis of the data, drafted the figures and wrote the manuscript. Dr. Reinhardt offered expert assistance during Itrax-XRF analysis. Dr. R.T. Patterson, Dr. J.M. Galloway, and Dr. E.G. Reinhardt helped in conceptualizing the project and provided feedback to help refine the manuscript. This research was funded by a Polar Knowledge Canada grant to Dr. Patterson and Dr. Galloway and a Canadian Foundation for Innovation grant to Dr. Reinhart.

6.3 Abstract

Lacustrine systems can act as both sink and source of metal(loid) contaminants. The transport and fate of metal(loids) with and to the lake system can be influenced by regional climate. Examining paleoclimate-driven changes in elemental contaminants, such as Arsenic (As), increases our understanding of biogeochemical cycling of this element, and its potential response to future climate change. To examine variability in As sequestration in lake sediments in response to decadal- to centennial-scale climate oscillations, a freeze-core was recovered from Control Lake, Northwest Territories, (CON01: 64.07°N, -111.13°W). Freeze core CON01 was analyzed using Itrax X-ray Fluorescence core-scanning (Itrax-XRF). Bulk organic samples (n = 13) analyzed for radiocarbon content provided a basal age of ca. 3300 cal. BP. Sediment subsamples were analyzed for ICP-MS after multi-acid (MA) digestion to provide a measure of accuracy of changes observed in Itrax-XRF results. ItraXelerate software was used to convert Itrax-XRF to quantitative values based on MA-ICP-MS using a multivariate log-ratio calibration. All elements showed R2 values > 0.8 with the exception of As; the weak correlation was likely caused by volatilization of As during MA digestion. Proxies for in-lake productivity [log(Ca/Ti)], sediment particle size [log(Zr/Ti)] and As concentration [log(As/Ti)] were examined for response to quasi-periodic climate oscillations using spectral and wavelet techniques. Significant oscillations were observed with ca. 8–15, 30–60, 90–130, and 170–300 yr periods across all geochemical proxies, corresponding to the North Atlantic Oscillation/11-yr sunspot cycles, the 30–60-yr Pacific Decadal Oscillation, and centennial-scale solar cycles (90-yr Gleissberg; 205-yr Suess cycle). The co-occurrence of these periods observed in the wavelet analysis results suggests that these oscillations only impact Control Lake when oscillations are in-phase with one another. Cross-wavelet analysis of paleo-proxies with TSI revealed good correspondence, but poor coherence with TSI throughout the Holocene. Cross-wavelet analysis of Itrax-XRF proxies showed log(As/Ti) variations may be preserved at sub-cm resolution (ca. 8¬–15 yr period), and that mechanisms of As sequestration may be related to in-lake productivity and temperature. Unaccounted for variations in the relationship between proxies suggest that additional drivers also influence the As signal in lake sediments.

6.4 Introduction

Lacustrine systems serve as a semi-permanent storage for metal(loid) contaminants (Becker et al. 2001; Keimowitz et al. 2005; Bai et al. 2010; Bing et al. 2011; Bowell et al., 2014). Changes in the redox state, pH or availability of adsorbents in these environmental systems can induce the release of previously sequestered contaminants (Martin and Pedersen 2002; Keimowitz et al. 2005; MacDonald et al., 2005; Bai et al. 2010). The redox state of lake bottom waters and near-surface sediments is controlled partially by the presence or absence of lake stratification, which impacts the mobility of oxygen throughout the water column. Degradation of organic matter (OM) consumes oxygen in the system, and in seasonally thermally stratified lakes, sufficient productivity and subsequent degradation of OM will result in dysoxic to anoxic bottom waters over the summer season until fall overturn re-mixes surface and bottom waters (Wetzel, 2001). In high northern latitude lakes where summer temperatures may be insufficiently high for a duration long enough to induce thermal stratification, shallow basins will instead develop anoxia in winter under ice (Palmer et al., 2019). Temperature and precipitation will thus indirectly affect lake redox state by modifying in-lake productivity, and OM consumption of oxygen under ice or in the hypolimnion of a stratified lake (Wetzel, 2001; MacDonald et al. 2009; Kraemer et al. 2017; Sinha et al. 2017), or lake stratification by changing lake depth, morphology, exposure to wind, and duration of ice cover, (Wetzel, 2001; Quesada et al. 2006; Snortheim et al. 2017). Future climate variability will therefore impact the stability, transportation and sequestration of elements (*e.g.*, Macdonald et al. 2005; Galloway et al. 2018; Miller et al. in press). It is thus imperative to better understand the impact of climate on the mobility and fate of contaminants of potential concern to predict their response to future climate change.

Quasi-periodic shifts in sea surface temperature (SST) and sea-level pressure (SLP), and the resulting re-organization of global atmosphere through teleconnections, control regional temperature and precipitation trends worldwide (Bonsal et al. 2006; Skinner et al. 2006; Sheffield and Wood 2008; Deser et al. 2009; Zhang et al. 2010). By altering precipitation and temperature regimes, and the frequency and severity of storms, climate oscillations may directly or indirectly impact contaminant mobility, transport, and

bioavailability. Although the possible changes in chemical contaminants in response to climate oscillations have been posited (see MacDonald et al. 2005 for a review of possible mechanisms), few studies have attempted to quantify this relationship. Most of the literature concerning this topic has focused on the response of mercury to climate oscillations (Gratz et al. 2009; Rydberg et al. 2010; Loseto et al. 2015; Slemr et al. 2016; Outridge et al. 2017), or the response of other non-metalloid contaminants (Eckhardt et al. 2003; Hung et al. 2005; Christoudias et al. 2012; Rigét et al. 2013). These studies are, however, limited by their relatively short records that prevent recognition of multi-decadal climate oscillations. Extended paleoclimate records are thus needed to address an important knowledge gap to understand the response of contaminants to sub-decadal to centennial climate oscillations.

Arsenic (As) is a contaminant of concern in the environmental systems of the Northwest Territories (NT) due to high geogenic concentrations in mineralized bedrock of the Slave Geological Province. Elevated As concentrations are also due to a legacy of contamination associated with historical gold mining. For example, Giant Mine near the City of Yellowknife, produced >13.5 million ounces of gold while releasing >20,000 tonnes of arsenic trioxide into the environment (Palmer et al. 2015; Galloway et al. 2018). Previous work in the region has shown that OM in lake sediments impacts As sequestration (Galloway et al., 2018) and an apparent link between productivity, temperature variations, and As sequestration on centennial to millennial timescales is emerging (Miller et al. in press; Gregory et al. 2019a). It is possible that As would respond to environmental changes induced by climate oscillations as temperature and precipitation in northwestern Canada are impacted by climate oscillations (Bonsal et al. 2006; Fauria and Johnson 2006; Skinner et al. 2006; Pisaric et al. 2009; Bonsal and Shabbar 2011; Prowse et al. 2011; Patterson et al. 2013; Galloway et al. 2013; Dalton et al. 2018).

To evaluate if quasi-periodic climate oscillations can be related to As concentration in lake sediments of the NT, a freeze-core was recovered from Control Lake, NT, a small lake within the Courageous Lake Greenstone Belt (CLGB) near the present boreal-forest-tundra transition. This site was chosen for detailed study because it occurs in a

mineralized region where As concentrations are high relative to most of the country. This site is also ideal for paleoclimate study as it occurs at the transition zone between forest and tundra, and has experienced dramatic environmental change expected to impact OM over the past ca. 8000 years (*e.g.* Sulphur et al. 2016). The freeze core was analyzed for near total geochemical determination using Itrax high-resolution core scanning x-ray fluorescence (Itrax-XRF). Itrax-XRF data were calibrated to near total concentrations of elements determined by ICP-MS following 4-acid digestion to provide quantitative scale to the measure of relative change provided by Itrax-XRF (Gregory et al. 2019b). Spectral and wavelet analysis were used to evaluate cyclicities in geochemical concentrations in the sediment.

6.5 Study Area

Control Lake is located approximately 240 km NE of Yellowknife, NT, within the transition from boreal forest to tundra vegetation. Modern vegetation surrounding Control Lake consists of grasses and low tundra shrubs (Seabridge Gold Inc. 2010; AANDC 2013). The region exhibits gradually undulating topography, with hummocks comprised of glacially-scoured or frost-heaved bedrock outcrops and swales filled with till >30 m thick in some locations (McCurdy and McNeil, 2014). Regional bedrock is composed of 2.6 Ga metamorphosed volcanic and sedimentary rocks of the CLGB, an extension of the Yellowknife Supergroup (Moore 1986; Padgham 1992; Tetra Tech Wardrop 2012). Control Lake is underlain by low-grade phyllite and slate underneath 2–10 m of till (Thompson and Kerswill 1994; Mccurdy and Mcneil 2014). Gold deposits were first recognized near Courageous Lake in 1939, and the Tundra/Salmita mine was established adjacent to Matthews Lake, located west of Control Lake (Figure 6.1B). Extraction and processing of ores occurred on site between 1964–68 and again from 1983–86 (Silke 2009; AANDC 2013). Mine tailings were stored in a tailings pond adjacent to Matthews Lake. Seepage from the containment pond resulted in the contamination of a series of lakes along the flow-path from the tailings pond northward to Courageous Lake (AANDC 2013; Miller et al., in press). Control Lake is upstream of this flow path, and has been used as a Control site for environmental monitoring (AANDC 2013). Control Lake has not been observed to contain anomalously high metal concentrations during recent

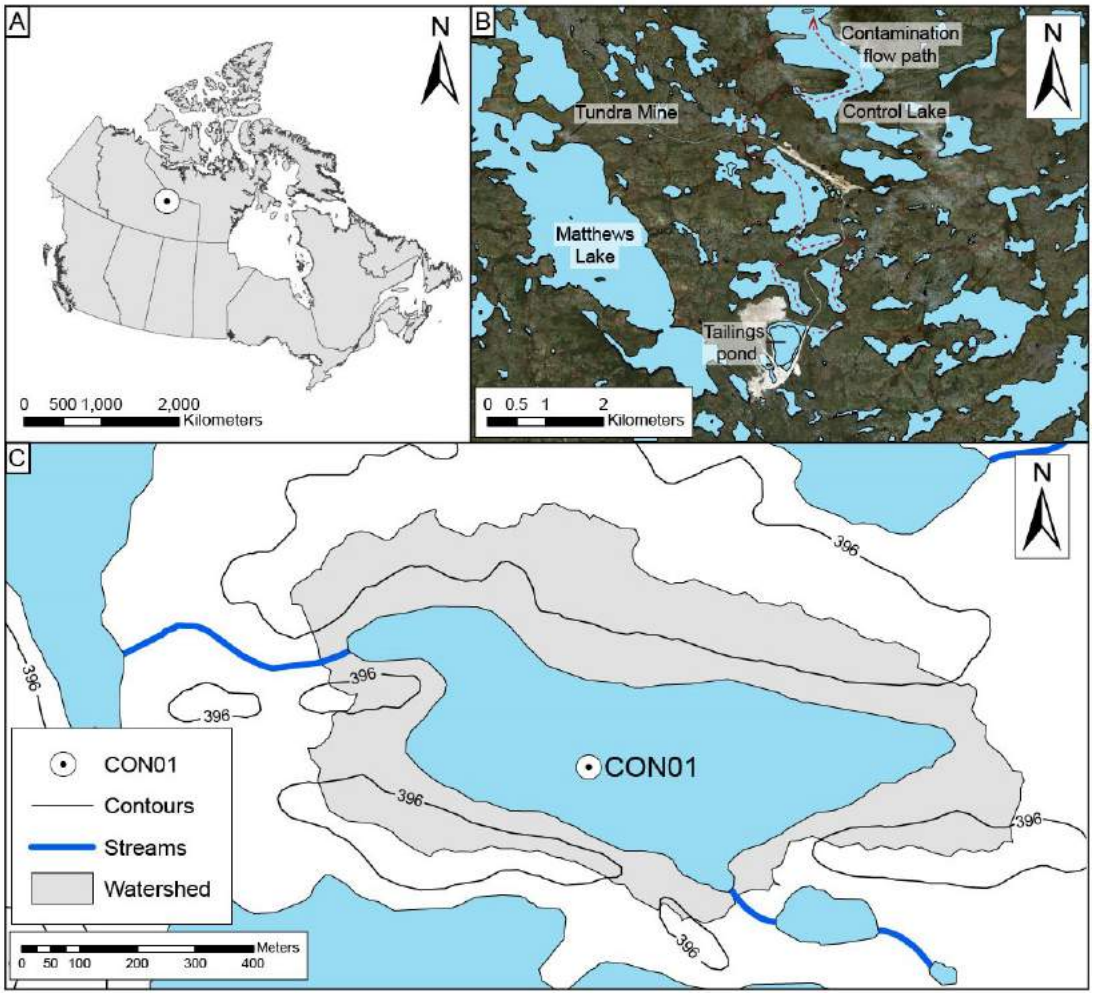

Figure 6.1: Study area showing (A) location of Control Lake in Canada, (B) Control Lake in the context of the Tundra/Salmita Mine and surrounding lake systems, including the suspected flow path of contaminants from the tailings pond north toward Courageous Lake (red dashed line), and (C) the Control Lake watershed and outflows to adjacent lakes.

monitoring of this site (AANDC, 2013; Miller et al., in press). As such, it is a suitable system for assessing the possible impact of natural climate variations on naturally derived As sequestration in an climatically sensitive area and a site of concern for As mobility.

Control Lake is relatively small (surface area = 23.4 Ha) and shallow (depth = 5 m). Water monitoring during summer seasons indicate that Control Lake has a circum-neutral pH ($\bar{x}$ = 7.1), low conductivity ($\bar{x}$ = 13.3 SpC) and cool lake temperature ($\bar{x}$ = 12.1 °C; AANDC, 2013). Hydrological modelling of Control Lake has revealed a small watershed that drains the surrounding glacially-scoured hollow (Figure 6.1C). Although

no dissolved oxygen measurements were taken on site during recovery of core material, Control Lake has similar surface area and depth as lakes in the Yellowknife area that Palmer et al. (2019) found exhibited winter oxygen stratification. There are two stream outflows located on the west and the south-east margins of the lake. No bedrock outcrops occur within the small watershed of Control Lake.

Hydrological monitoring at the Tundra/Salmita mine property indicates that the region receives a relatively low yearly average precipitation (213 mm), most of which occurs between July and September (125 mm) based on data collected from 2007–2010 (Seabridge Gold Inc, 2010). The subarctic tundra experiences short summers and long winters, with typical freeze-up of lakes near Control Lake occurring in late September, and spring break-up of lakes occurring in June (AANDC, 2013). The average daily temperature is -9.2 °C, but can vary between -43 to 6 °C yearly (Seabridge Gold, 2010). The combined North Atlantic Oscillation (NAO), represented by a difference in SLP between the Icelandic Low and the Azores high (van Loon and Rogers 1978), and Arctic Oscillation (AO), defined as persistent SLP anomalies across the entire Arctic (Thompson and Wallace 1998), impact temperature and hydrology in the Canadian Arctic and Northeastern Canada (Buermann et al. 2003; Déry and Wood 2005; Bonsal et al. 2006; Fauria and Johnson 2006; Bonsal and Shabbar 2011; Sarmiento and Palanisami 2011). Because of the strong correspondence between NAO and AO phases, and the possibility that the NAO may be a spatially limited expression of the hemispherical AO (Deser 2000; Dickson et al. 2002), the two oscillations will be discussed together hereafter. Temperature and precipitation patterns in Western and Central Canada show greater influence from Pacific Ocean oscillations including: the El Niño/Southern Oscillation (ENSO), a fluctuation in SLP and SST in equatorial Pacific between Tahiti and South America (Wang and Picaut 2004), and the longer-lived Pacific Decadal Oscillation (PDO; Mantua and Hare 2002), a variation in the position and strength of the Aleutian Low pressure system and corresponding SST anomalies in the NE Pacific (Buermann et al. 2003; Patterson et al. 2004ab; Déry and Wood 2005; Chang et al. 2005; Bonsal et al. 2006; Fauria and Johnson 2006; Patterson et al. 2007; Bonsal and Shabbar 2011; Sarmiento and Palanisami 2011; Galloway et al., 2013; Babalola et al. 2013; Patterson et al. 2013).

The periodicity and strength of these climate oscillations are impacted by internal processes inherent to the ocean-atmosphere system, as well as external forcing from volcanic and solar activity (Gray et al. 2016; Newman et al. 2016). Several authors have observed modulations of AO/NAO, PDO and ENSO in response to short term cycles in total solar irradiance that correspond to 11-yr cycles (Schwabe cycle) in sunspot frequency and longer-term modulations of this trend with 88-yr period (Gleissberg cycle) and 205-yr period (Suess/De Vreis cycle; Christoforou and Hameed 1997; Patterson et al. 2004a, 2005, 2013; Meehl et al. 2008; Van Loon et al. 2012; Galloway et al. 2013; Gray et al. 2013, 2016; Scaife et al. 2013; Ólafsdóttir et al. 2013; Dalton et al. 2018; Veretenenko and Ogurtsov 2019). Although there is controversy regarding the mechanisms that allow relatively minor changes in solar insolation (1–2 Wm^{-2} at the top of the atmosphere in the tropics; Lean et al. 2005) to alter oceanic and atmospheric circulation patterns, modelling efforts suggest that solar insolation nonetheless plays a role in altering oceanic and atmospheric systems (Shen et al. 2006; Velasco and Mendoza 2008; Meehl et al. 2008, 2009; Gray et al. 2010). Moreover, typical SST and SLP anomalies associated with oceanic-atmospheric oscillations are observed to change when examining periods in-phase with peaks in solar variability (*e.g.* Roy and Haigh 2010, 2012; van Loon and Meehl 2016). Variations in temperature and precipitation within the study area may thus be expected to respond to solar forcing, ocean-atmospheric oscillations, or, most likely, a combination of internal and external forcing. These oscillation-induced variations in temperature and precipitation secondarily impact environmental systems, including forest fire frequency, river and lake hydrology, lake productivity, and freeze-up and break-up dates of lakes/rivers (Derry and Wood 2005; Bonsal et al. 2001; Dickson et al. 2002; Buermann et al. 2003; Bonsal et al. 2006; Fauria and Johnson, 2011; Sariemento and Palanisami 2011; Galloway et al. 2013; Patterson et al. 2013; Vincent et al. 2015; Dalton et al. 2019).

6.6 Methods

Core CON01 (length = 103 cm) was collected in March, 2016, through the ice at the approximate z-max of Control Lake using a single-faced freeze corer (64.07771 °N, -111.13493 °W; Figure 6.1). The freeze core was cleaned onsite and wrapped in clingfilm

for transport to Carleton University. To minimize possible risk of geochemical contamination in the field an approximately 2-mm thickness of material was removed from the surface the faces of all the freeze cores by melting the upper surface and removing the melted material using glass slides. This study will focus on analysis of CON01.

6.6.1 Radiocarbon Dating

Radiocarbon dating was used to provide temporal reference to core depth. Bulk sediment samples were collected at even intervals throughout the core length for radiocarbon dating (Table 6.1). Subsamples of approximately 2 mL of material were collected using ceramic and stainless-steel sampling instruments. Samples were analyzed at the A.E. Lalonde AMS facility at the University of Ottawa following a triple acid wash (Table 6.1). An age-depth model was generated using the Bayesian Age Calibration (BACON) package for R statistical software (R Core Team, 2019; Blaauw and Christen, 2011) after calibration of radiocarbon dates using the terrestrial radiocarbon curve IntCal13 (Reimer et al., 2013) (Figure 6.2). As shallow dates (1.5 and 3 cm depth) returned “modern” ages, no freshwater reservoir correction was applied to the core.

6.6.2 Geochemical analysis

The core was prepared for Itrax-XRF analysis following procedures outlined by Gregory et al (2019b). Core CON01 was cut length-wise using a ripsaw into an approximately 3-cm-wide section, then subdivided into nine approximately 12.5-cm-long slabs using a fine-bladed hacksaw so as to minimize loss of information; cores were subsequently re-cleaned to eliminate contamination that may have occurred during slabbing. Core slabs were stored wrapped in clingfilm for transport to McMaster University where they were analyzed at the McMaster Core-Scanning facility using purpose-designed insulated boxes capable of keeping core material frozen for up to 2 hours (Gregory et al. 2019b). Material was analyzed at 1 mm resolution using a Mo-anode for 25 seconds per interval at 25 kV and 22 mA. As scanning small freeze core slabs can induce minor edge effects in the last few mm of cores (Gregory et al. 2019b), cores were scanned once forward (top-to-bottom), then rotated 180 degrees and scanned in reverse (bottom-to-top) twice more, once at high resolution (1 mm), and again at coarse resolution (5 mm) using the same settings as initial scans. These reverse scans, when combined with the initial scan,

Table 6.1: Radiocarbon results for analysis of bulk organic sediment from Control Lake core CON01 showing uncalibrated age (^{14}C yr BP) and the fraction of modern carbon (F^{14}C)

Lab ID	Core Depth (cm)	^{14}C yr BP	Error	F^{14}C	Error
UOC-3555	1 – 2	Modern	38	1.0386	0.0049
UOC-2107	2 – 4	Modern	21	1.0109	0.0026
UOC-3556	10 – 11	1276	38	0.8531	0.0040
UOC-3557	18 – 19	1336	38	0.8468	0.0040
UOC-2108	27 – 27.5	1304	21	0.8505	0.0022
UOC-3558	37 – 38	1868	38	0.7926	0.0038
UOC-3559	47 – 48	1942	38	0.7852	0.0037
UOC-3560	56 – 57	2529	38	0.7299	0.0034
UOC-2109	65 – 65.5	2252	22	0.7561	0.0020
UOC-3561	73.5 – 74.5	2489	38	0.7336	0.0035
UOC-3562	83.5 – 84.5	3020	38	0.6866	0.0032
UOC-3563	91.5 – 92.5	2879	38	0.6988	0.0033
UOC-2110	97 – 97.5	3297	21	0.6640	0.0017

minimize edge effects caused by un-accounted for refraction of the X-ray beam on the semi-curved surface of the core near the core slabs' edge (Gregory et al. 2019b).

6.6.3 Itrax-XRF data processing and Calibration

Scanned core sections were batch evaluated using the RediCore software provided by Cox Analytical Solutions to optimize the fit between observed and predicted elemental concentrations. After batch analysis, datasets from multiple slabs and scans were concatenated and data were screened to remove samples deemed invalid by the Itrax-XRF device. The ItraXelerate software (v.1.0; Weltje et al. 2015) was used to merge the three scans, provide error estimates based on replicate measurements, and replaced all 0 values (non-detects) with half of the lowest observed values for each given element; only elements with <30 % non-detects were considered for subsequent analysis.

In order to assign an estimation of absolute elemental concentrations to the relative changes in elemental concentrations output by the Itrax-XRF, ICP-MS analysis was conducted on the core slabs used for Itrax-XRF analysis. Core slabs were re-cleaned after Itrax analysis and 1-cm long sub-samples were selected for analysis based on recommendations provided by the ItraXelerate software, which has internal protocols designed to suggest sample selection to optimize the variability captured for geochemical

analysis. Six samples were analyzed in triplicate by ICP-MS to provide a measure of absolute geochemical error, which resulted in 3-cm long sub-samples used for the triplicate analysis due to limited material remaining in freeze core slabs. Sub-sampled material was sent to Acme/ Bureau Veritas, Vancouver, for ICP-MS analysis following a near-total multi-acid digestion (MA-ICP-MS; Gregory et al. 2019d). After analysis, MA-ICP-MS results were used to calibrate Itrax-XRF results in the ItraXelerate software using the Multivariate log-ratio Calibration method proposed by Weltje et al. (2015). To account for 3-cm subsamples, tolerance of the MLC calibration in the ItraXelerate software was set to 15 mm before calibration was attempted. Wetlje et al. (2015) recommends that the number of elements calibrated using the MLC be less than one third of the number of geochemical samples analyzed (n = 28 in our study). Based on this recommendation, nine elements of interest were selected from the dataset for calibration, including redox-sensitive elements (As, Fe, Mn, S), indicators of minerogenic input into the system (Zr, Ti, Rb, K), and Ca, which acts a proxy for carbonate precipitation when normalized to sedimentation in the system (Figure 6.3; Gregory et al. 2019c). Because MA digestion can volatilize As during boiling with HF (Parsons et al. 2012), MA-ICP-MS and Itrax-XRF results were compared to ICP-MS results following aqua regia (AQ) analysis of CON01, a core recovered adjacent to CON02 in Control Lake during the same field season (Figure 6.4).

6.6.4 Spectral and Wavelet Analyses

Modern tundra vegetation was established in near Control Lake ca. 2700 calibrated years before present (cal. BP) (82 cm depth in CON01 based on the age model; Gregory et al. 2019a). The transition from forest to tundra can be expected to have resulted in a change in organic and elemental geochemical and sedimentological processes at Control Lake. Spectral and wavelet analyses was therefore restricted to post-2700 cal. BP sediments of the Control Lake core when near modern climate conditions had become established. Following recommendations by Weltje et al. (2015), log-normalized elemental ratios are herein employed to reduce the impact of changes in XRF-scanning environment that can induce spurious elemental variations (matrix and specimen effects; Gregory et al. 2019b), and to negate issues related to analysis of closed datasets. Common lithogenic elements

were examined for possible relation to particle size. Log(Zr/Ti) showed strong correspondence to % sand in the particle size data analyzed on a short core recovered adjacent to CON01 analyzed by Miller et al. in press (Spearman's ρ = 0.43, p-value = 0.006, *n* = 40; Supplementary Figure A1.14). This relationship has been observed extensively in Arctic lakes, with Zr corresponding strongly to sand and coarse silts, and Ti corresponding to fine-silt to clay (Guyard et al. 2007; Cuven et al. 2010; Davies et al. 2015; Amann et al. 2017). Arsenic was normalized to Ti to allow for understanding of As variations in core separate from those caused by changes in minerogenic input into Control Lake (log(As/Ti). Log(Ca/Ti) is used as a proxy for authigenic production of calcium carbonate, which has been linked to increases in productivity (Davies et al. 2015; Wetzel 2001). Comparison to Rock Eval results from a short core recovered adjacent to CON01 shows good correspondence between trends observed in S3 and log(Ca/Ti) and is statistically significant at the 90 % level (Spearman's p = 0.29, p-value = 0.06, *n* = 40; Supplementary Figure A1.14).

Before carrying out wavelet and spectral analyses, data were detrended by subtracting the loess-smoothed trend for the elemental ratios. The uneven spacing of the age model necessitated use of the REDFIT procedure for spectral analysis of data. As outlined by Schulz and Mudelsee (2002), a Lomb-Scargle Fourier Transformation was applied to a series of segments generated from the time series that overlap by 50%, with the penultimate scalogram generated representing the average of the overlapping scalograms (see Figure 6.5). The significance of the scalogram was assessed by comparing data to a null-model generated by Monte Carlo simulations of an AR(1) model. For analysis, the dataset was divided into four overlapping segments and the Monte Carlo null model was generated using 1000 simulations. A Hanning window was used to reduce spectral leakage during Fourier transformation. It is recommended that the confidence interval used to base interpretation of significant peaks vs random correlations be equal to 1 - (1/*n*) x 100 where *n* is the number of datapoints in the overlapping segments (after Thomson, 1990). Four overlapping sections across the dataset yielded 305 datapoints per section, indicating a confidence interval of 99.7 % be used for analysis; we have also included the 95 % confidence interval as background noise does not approach the 95 % confidence interval throughout most of the record.

Wavelet transform of the data was used to examine shifts in periodicity over time (Torrence and Compo 1998). As wavelet analysis requires evenly spaced data, and because most of the age model showed an approximately linear trend, Itrax-XRF results were assumed to represent evenly spaced intervals of 3.32 years, which is the average resolution of the un-smoothed age model (3.32 years/mm). The continuous wavelet transform was computed using the WaveletComp package in R (Roesch and Schmidbauer 2018). The Morlet wavelet was used as it represented a good compromise between frequency and time resolution. Statistical significance of the wavelet power was tested against 1000 Monte Carlo simulations of a red-noise model (AR(1)). Significant periodicities possibly related to solar-activity were observed during exploratory data analysis. For this reason, cross wavelet transformation was also used to compare periodicities observed in the paleo-proxy record of Control Lake to the total solar irradiance (TSI) reconstruction of Steinhilber et al. (2009), which was based on ^{10}Be measurements that represent a 40-year running mean over the past 9300 years. Cross-wavelet analysis was applied using the biwavelet package in R (Gouheir et al. 2017) with the Morlet wavelet being used for the cross-wavelet transform, and the wavelet power tested for significance against a red-noise model. The TSI data was extracted at a resolution of 5-years. To account for differences in step-resolution between TSI and paleo-proxies, the data from TSI were interpolated to 3.32-year resolution using linear interpolation. As no signals were preserved near the Nyquist frequency limit of either sampling resolution (10 years for TSI, 6.65 years for Itrax-XRF data), we do not consider this interpolation an issue for interpretation of the data.

6.7 Results

6.7.1 Age Model

The age-depth model indicates that there was a nearly-linear rate of sedimentation during much of the depositional history of CON01. A slower sedimentation rate of ~0.1 mm/yr prevailed through the upper 10 cm of the core (10 yr/mm), followed by a relatively steady rate of 0.44 mm/yr (2.23 yr/mm) for the remainder of the core (Figure 6.2). The average age-error for the age-depth model was ca. 128 cal. BP. The maximum modelled age-error of ca. 282 cal. BP occurred near the bottom of the core.

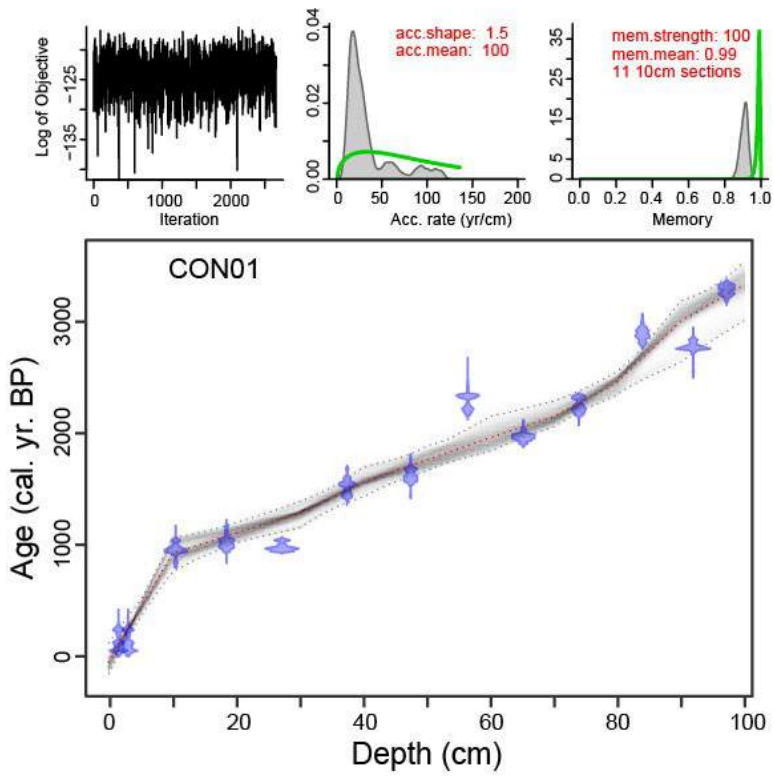

Figure 6.2: Age-depth model for Control Lake sediment core CON01 based on 13 radiocarbon dates created using BACON. Radiocarbon dates are shown in blue, and inferred age in grey – darker areas suggest greater likelihood of age at a given depth.

6.7.2 Itrax-XRF Calibration

Calibration of the Itrax-XRF data based on ICP-MS using a multivariate log-ratio calibration in the ItraXelerate software package showed strong correlations for most elements (Figure 6.3). Calcium, Fe, K, Mn, Rb, Ti, and Zr had Pearson's R^2 values of > 0.9. Manganese and S exhibited slightly weaker R^2 values of 0.89 and 0.76, respectively. Arsenic exhibited a weak correlation between datasets, with R^2 = 0.36. Comparison of the Itrax-XRF results, ICP-MS results carried out after a multi-acid digestion (MA-ICP-MS), and ICP-MS results following an aqua-regia digestion (AQ-ICP-MS) from adjacent core CON02 (Gregory et al. 2019b) indicate that volatilization of As was likely, but Itrax-XRF results exhibit similar trend as AQ-ICP-MS (Spearman's ρ = 0.56, p-value < 0.001, *n* = 75; Figure 6.4). The MA-ICP-MS shows lower As concentrations in sediment than AQ-ICP-MS ($mean_{MA}$ = 75 ppm, *n* = 46; $mean_{AQ}$ = 121, *n* = 117). Calibrated Itrax-XRF results based on MA-ICP-MS show similar trends as AQ-ICP-MS, but exhibit lower concentrations throughout the record. We thus use Log(As/Ti) as a proxy for As concentration to understand periodic oscillations in As concentrations with the caveat that the magnitude of these oscillations may be an under-estimation of actual trends.

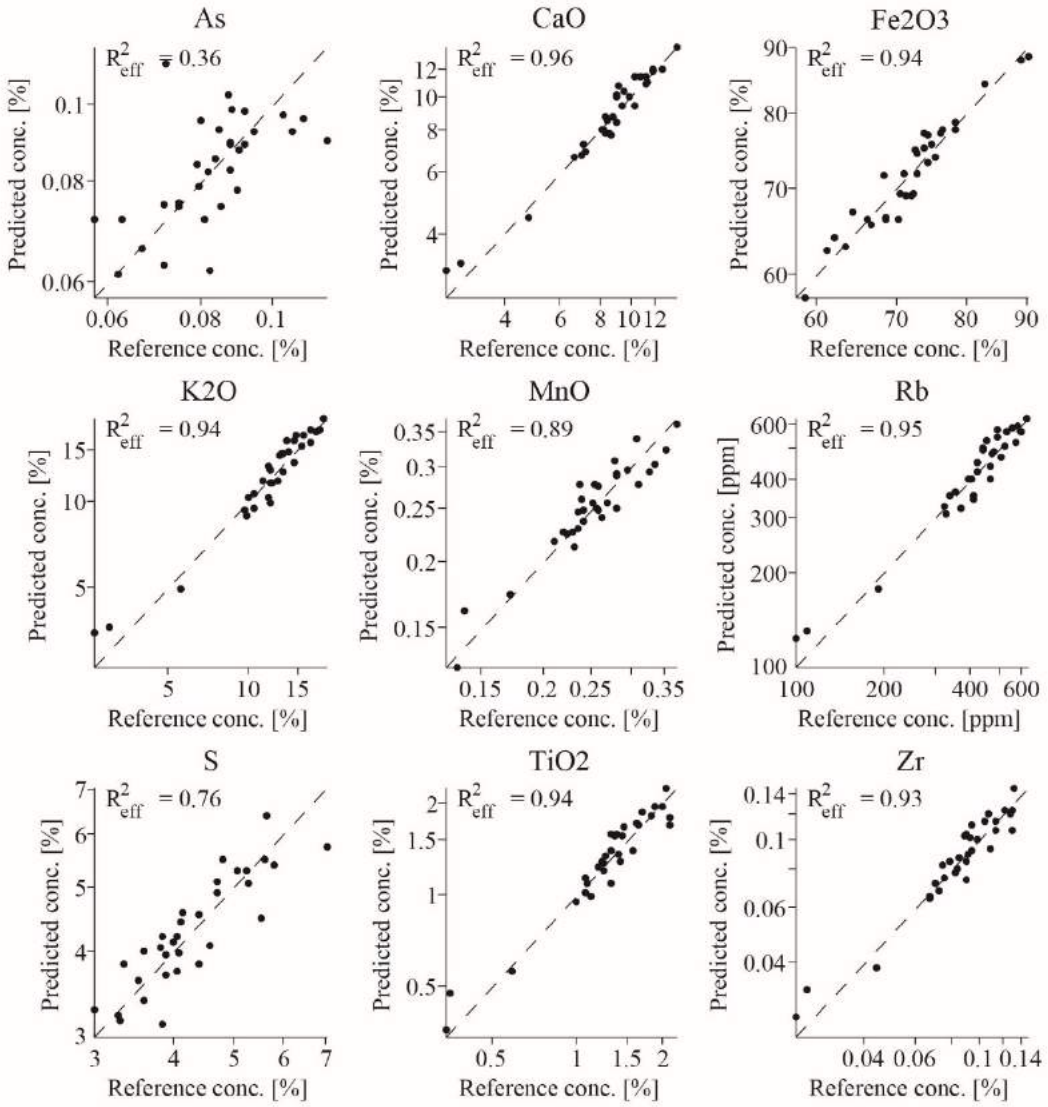

Figure 6.3: Comparison of center log-ratio-calibrated Itrax-XRF results (predicted concentration) to reference MA-ICP-MS results (reference concentration).

6.7.3 Spectral Analysis and Wavelet Analyses

The spectra of elemental log-ratios demonstrate peaks in power above the 95% confidence interval. For log(As/Ti), periods of ca. 6.7, 9.6, 86, 105-120 and 150-300 yr surpassed the 95% confidence interval (Figure 6.5). Spectral analysis of log(Ca/Ti) shows periodicities of ca. 8.8, 9.0, 56, 89–140, and 230–300 yr statistically significant above the 95% confidence interval. The spectrogram for log(Zr/Ti) shows five peaks in power at

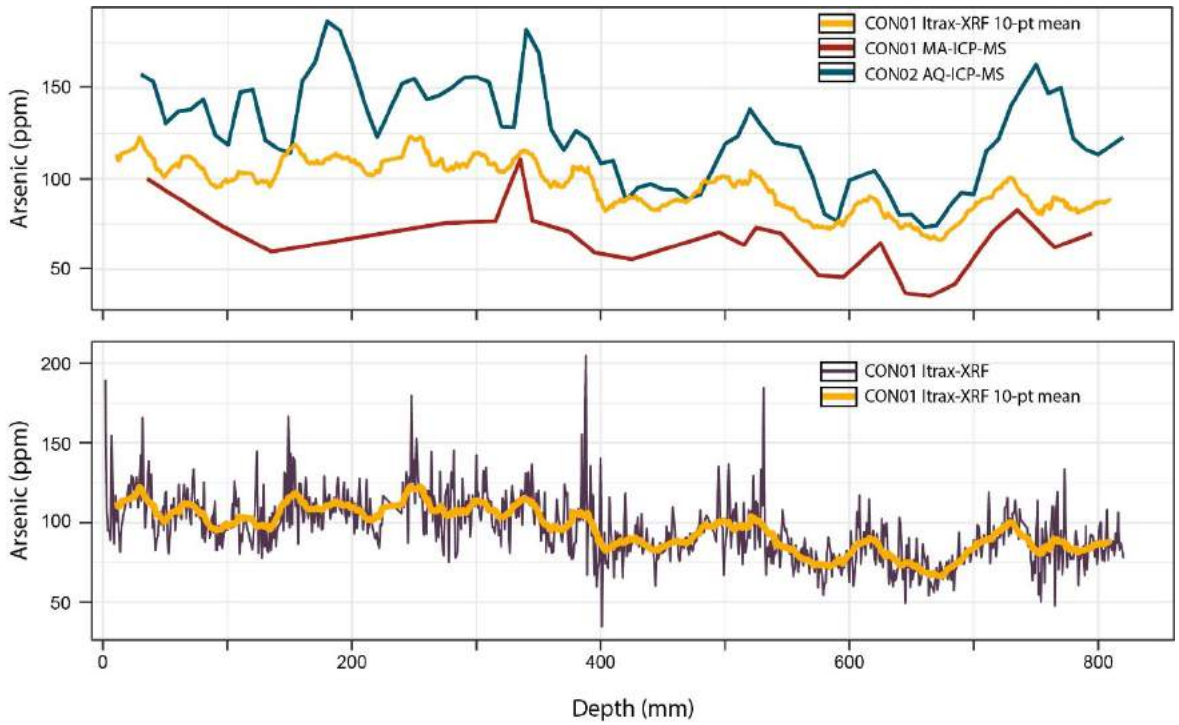

Figure 6.4: Comparison of MA-ICP-MS (red), calibrated Itrax-XRF As concentrations (purple), and a 10-point running mean of calibrated Itrax-XRF-based As (~1 cm resolution; yellow) from core CON01 to AQ-ICP-MS from core CON02 recovered adjacent to CON01.

periods of ca. 8.1, 8.8, 9.0, 95–150, and 215–300 yr that surpass the 95% confidence interval (Figure 6.5).

Wavelet analysis of additive log-ratio data shows that spectral peaks were non-stationary. The log(As/Ti) scalogram shows intermittent peaks with periods ranging from ca. 8–16 yr (Figure 6.6). A broad peak at ca. 100–130 yr was observed from ca. 1250 cal. BP to present day. The low-frequency ca. 200–500-yr period is observed throughout the duration of the record at Control Lake, with greater power and significance from ca. 2600–1200 cal. BP. The wavelet scalogram of log(Zr/Ti) shows similar trends, with spectral peaks of power ca. 8–16 yr and ca. 30–80 yr intermittently through the duration of the core (Figure 6.6). Significant periods of ca. 100–130 yr occur from ca. 2250–250 cal. BP. A ca. 250–500 yr period was observed from throughout the duration of the record. The log(Ca/Ti) results showed significant, but intermittent spectral peaks at periods of ca. 8–16 yr and ca. 30–70 yr throughout the core (Figure 6.6). The log(Ca/Ti) scalogram shows

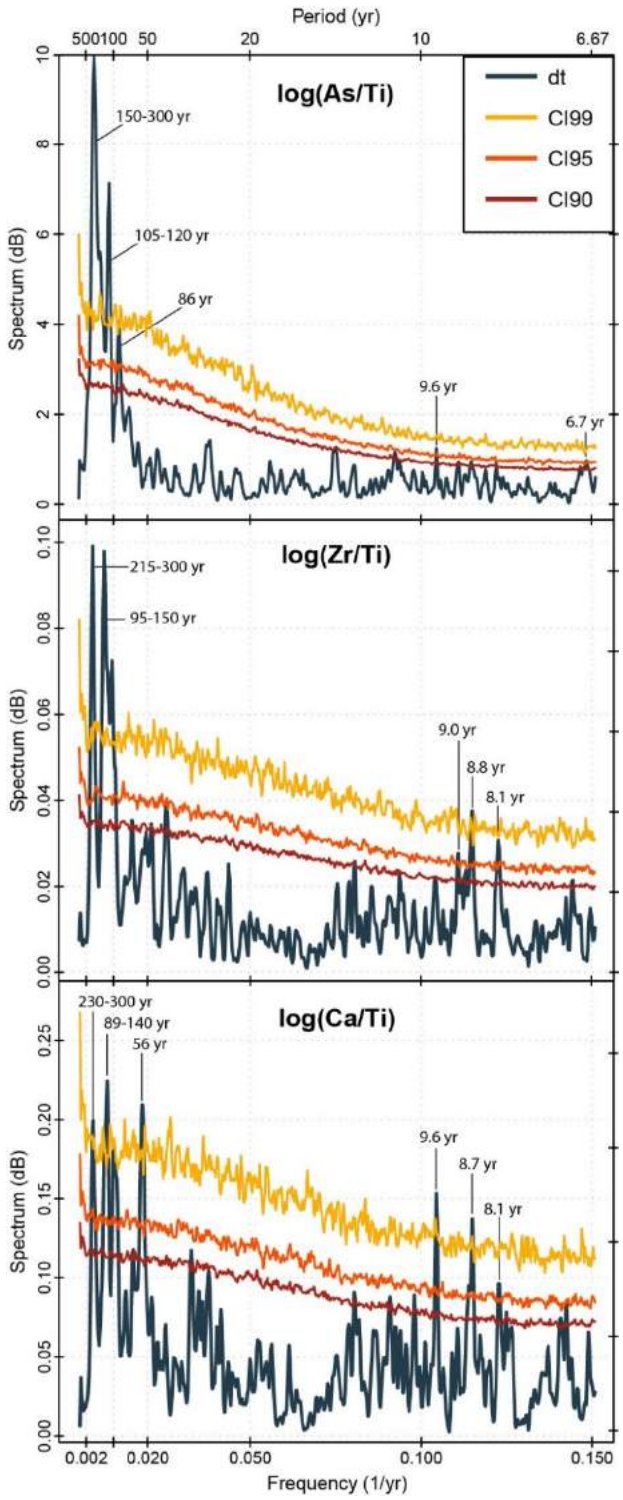

Figure 6.5: Spectral analysis of log(As/Ti), log(Zr/Ti), and log(Ca/Ti) using Redfit. Spectral power is shown in grey and confidence intervals based on red-noise model shown in red (90 %), orange (95 %) and yellow (99 %).

periodicities in the ca. 100-yr band between ca. 500–100 cal. BP, ca. 1500–1000 cal. BP, and ca. 2200–1800 cal. BP. A long period (ca. 200–400 yr) signal is present in the log(Ca/Ti) scalogram from ca. 2600–1500 cal. BP. Across all three records, there was a co-occurrence of periodicities at increasing frequency from 8 up to 130 yr. Intervals of co-occurrence or "stacking" of periodicities occurs for durations of ca. 130 +/- 63 yr with ca. 250 +/- 67 yr in between (length of signal 440 +/- 140 yr).

Cross-wavelet transformation of the TSI versus elemental proxies showed intervals of significance with a period of 30–60 yr throughout the Control Lake record (Figure 6.7). Significant periods were also observed at the ca. 100–130 yr and ca. 200–300 yr frequencies in all proxies, albeit with decreased power and areas of significance in the TSI vs log(Zr/Ti) cross-wavelet scalogram.

Comparison of the log(As/Ti) to log(Zr/Ti) and log(Ca/Ti) results using cross-wavelet analysis

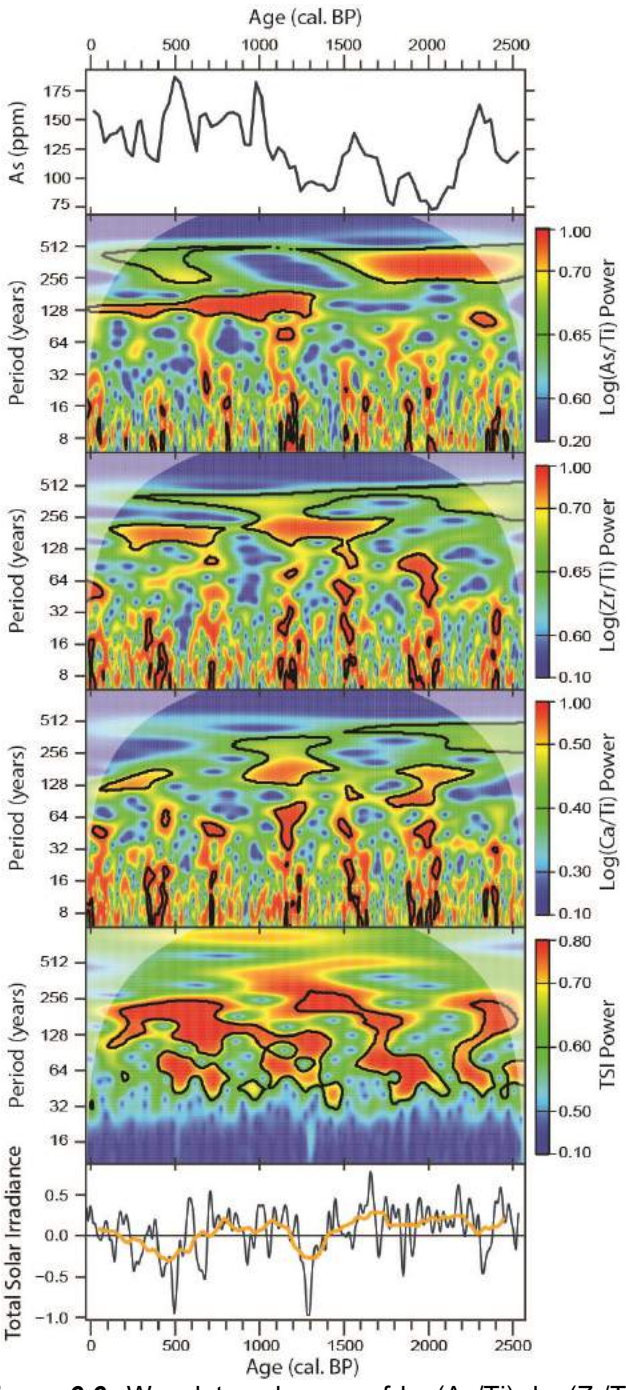

Figure 6.6: Wavelet scalogram of log(As/Ti), log(Zr/Ti), log(Ca/Ti) and total solar irradiance (TSI) using a morlet wavelet. Areas that are significantly different from a red noise model are indicated by black lines. The cone of influence is show by light grey. Warm (cold) colors indicate higher (lower) power of the wavelet transformation. Shown also is As concentrations from core CON02, and TSI deviations from mean TSI concentrations (grey) and a 100-year running mean (yellow)

revealed intervals of significant discontinuous oscillations at a ca. 8–16 yr, ca. 100-130 yr, ca. 200-500 yr and rarely ca. 30-60 year periods. The ca. 100-130 ys periods is more significant from ca. 1500 to -66 cal. BP and ca. 200–500 yr period more significant ca. 2600–1500 cal. BP (Figure 6.8). Oscillations with shorter periods observed in the log(As/Ti) scalogram tend to be in phase with, or lag behind log(Zr/Ti) and log(Ca/Ti).

Significant periods observed in the ca. 200–500 yr band indicate that log(As/Ti) leads geochemical proxies from ca. 1500 to -66 cal. BP, but lags or is out-of-phase with sediment geochemistry from ca. 2600 to 1500 cal. BP. At all periods throughout the record, log(Ca/Ti) and log(Zr/Ti) are in–phase, or deviate slightly from this relationship (<45°).

6.8 Discussion

6.8.1 Periodicities observed in the paleo-proxy records

Variations in temperature and precipitation in Canada are impacted by quasi-periodic climate oscillations and solar variability (Bonsal and Shabbar 2011). Increases in air

temperature impact lake productivity either directly by increasing water temperature (Morin et al. 1999), or indirectly by altering the length of the ice-free season as ice freeze-up and break-up are controlled in large part by air temperature (Livingstone 1999; Patterson and Swindles, 2015). Warmer temperatures also impact the coarseness of sediment transported into Control Lake as the rate of spring melt, driven by spring air temperatures, is a primary driver on particle size in tundra lake systems (Cuven et al. 2011; Amann et al. 2017; Macumber et al. 2018; Gregory et al. 2019a). Changes in precipitation can similarly alter productivity as catchment runoff influences nutrient availability in the lake during the open water growing season (Wetzel 2001). By altering the productivity and the length of the open-water season, temperature and precipitation alter oxygen availability in lake systems (Wetzel 2001; Quesada et al. 2006; MacDonald et al. 2009; Kraemer et al. 2017; Sinha et al. 2017; Snortheim et al. 2017; Palmer et al. 2019). Arsenic mobility in lake sediments is driven primarily through variations in shallow-sediment oxygen availability (Smedley and Kinniburgh 2000; Martin and Pedersen 2002; MacDonald et al. 2005; Palmer et al. 2019). Arsenic mobility is also influenced by the amount and quality of OM in lake sediments (Galloway et al. 2018; Miller et al. in press). Variations in As concentration in sediment can therefore be affected by prevailing climate through processes influencing of the production of labile OM in the system and redox conditions in near-surface sediment.

Spectral analysis of Itrax-XRF geochemical data shows significant frequencies of ca. 8–12 yr in log(As/Ti), log(Ca/Ti), and (Zr/Ti) (Figure 6.5). An oscillation of ca. 8–12 yr is observed in the wavelet scalogram at irregular intervals during the last ca. 2500 cal. BP, although the records for these proxies are also occasionally characterized by oscillations with period approaching ca. 20 yr (Figure 6.6). The ca. 8–12 yr oscillations observed in spectral and wavelet analysis of Control Lake data are broadly consistent with the upper limit of the typically observed range of ENSO quasi-periodicity of 2–7 yr (Wang and Picaut 2004). However, paleo-proxy records of ENSO variability indicate that ENSO period length may have been variable during the Holocene, with periods ranging from 2–12 yr in the proxy record (Moy et al. 2002; McGregor and Gagan 2004). The AO/NAO also tends to exhibit irregular variability over the historical record, with studies documenting an oscillation with a period of 2–10 yr (Hurrel and Loon 1997; Rossi et al.

2011; Massei et al. 2007; Wanner et al. 2002; Olafsdottier. 2013). Most literature that has documented the extent of AO/NAO influence on climate show a strong influence in the high Arctic and in eastern Canada (Bonsal et al. 2001, 2006; Déry and Wood 2005; Bonsal and Shabbar 2011; Vincent et al. 2015). The ENSO and the AO/NAO may both affect the climate of the central NT, and be represented by the high frequency oscillations observed in the geochemical data preserved in the Control Lake core.

The well-known Schwabe sunspot cycle has a periodicity ranging from 8–14 yr in the observational record (Solanki et al. 2004; Brauer et al. 2018) and is well documented in the geological record (see Patterson et al. 2013). Although there is controversy regarding the manifestation of minor changes in solar insolation into changes in large-scale oceanic and atmospheric circulation that affect climate, historical observations demonstrate that solar insolation affects global climate (Meehl et al. 2008, 2009; Gray et al. 2010). Modelling of climate variations has shown that even minor changes in solar insolation at the Earth's surface can impact global climate, either driven by increased shallow-SST in cloud free regions in the tropical Pacific and associated strengthening of the intertropical convergence zone/South Pacific convergence zone (Meehl et al. 2008; Misios et al. 2016, 2019), or by increased solar UV-radiation impacting stratospheric temperature profiles, ozone production, and the strength of Brewer-Dobson circulation that ultimately impacts tropospheric and oceanic temperature/circulation patterns (Kodera and Kuroda 2002; Simpson et al. 2009). Recent examination of climate models controlling for internal ocean variability and volcanic feedback suggested that both of these processes may affect atmospheric circulation (Misios et al. 2019). The ca. 8–12 yr period observed in sediment geochemistry at Control Lake may be caused by a combination of the Schwabe sunspot cycle and the AO/NAO and/or ENSO. Several modelling and observational records have shown that the Schwabe sunspot cycle acts to modulate the AO/NAO such that stronger effects are felt when the oscillation are in phase (Van Loon et al. 2012; Osterberg et al. 2014; Thiéblemont et al. 2015; van Loon and Meehl 2016). Some studies have found AO/NAO shows circum-arctic SLP and SST anomalies only when the oscillation is in phase with sunspot cycles (Kodera 2002; Kodera and Kuroda 2005; Hood and Soukharev 2012). Bonsal and Shabbar (2006) observed changes in the extent of AO/NAO-forced low-pressure excursions into north-central Canada during

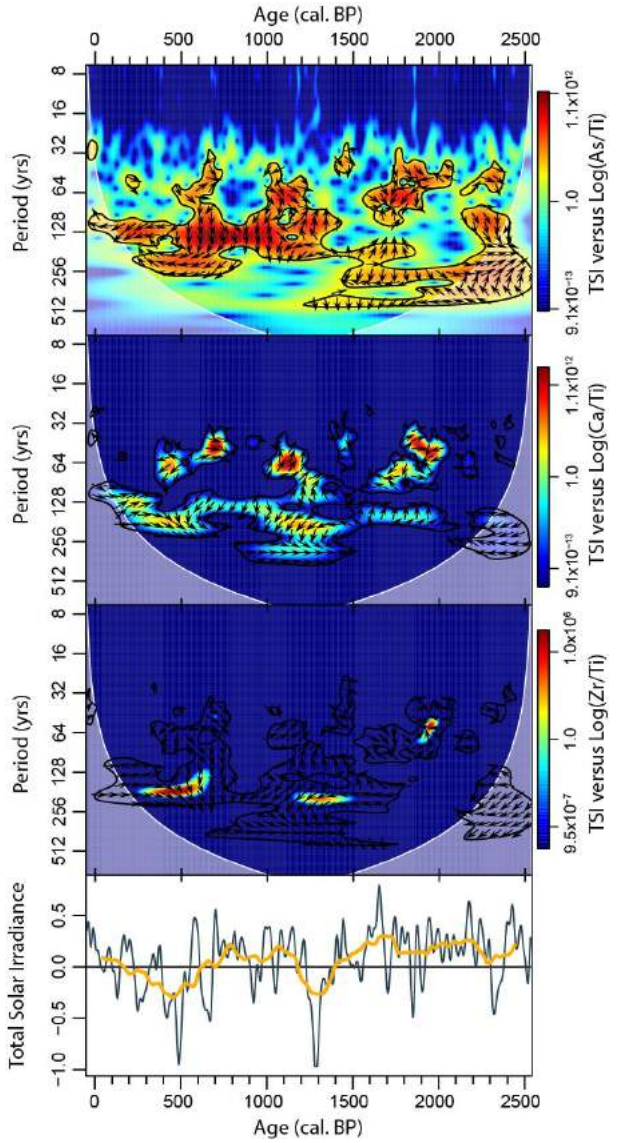

Figure 6.7: Cross-wavelet transformation of total solar irradiance vs log(As/Ti), log(Zr/Ti), log(Ca/Ti) using a morlet wavelet. Areas that are significantly different from a red noise model are indicated by black lines. The cone of influence is show by light grey. Warm (cold) colors indicate higher (lower) power of the wavelet transformation. Arrows indicate phase difference between x (TSI) and y (Itrax-XRF results). Arrows pointing to the right indicate the two signals are in phase, and arrows pointing to the left indicate they are out-of-phase. Arrows pointing up indicate x leads and arrows pointing down shown y leads. The bottom panel shows TSI deviations from mean TSI intensity (blue) and a 100-year running mean of TSI deviations (yellow).

ENSO+ phases, and suggested that ENSO modulates the impact of AO/NAO and Schwabe cycles on the climate of the continental NT. The high frequency oscillations observed in the sediment geochemistry of the Control Lake record thus likely reflect the complex interplay of signal amplification and suppression between AO/NAO and solar forcing altering regional temperature and precipitation, which further impacts in-lake productivity, transport of sediment into the system, and ultimately oxygen stratification and As stability in lake sediment.

Spectral analysis results for both log(Ca/Ti) and log(Zr/Ti) are characterized by 30–60 yr period oscillations (Figure 6.5). Results from the wavelet analysis shows that these periodicities are prominent in log(Zr/Ti), log(Ca/Ti) before ca. 1300 cal. BP, although this signal is weaker from ca. 2600–1300 cal. BP (Figure 6.6). Peaks in spectral power of ca. 30-yr are also observed in the wavelet scalogram of log(As/Ti) (Figure 6.6). The observed ca. 30–60 yr period is interpreted to reflect the influence of the PDO, which has been

demonstrated to have a major impact on temperature in precipitation patterns in northwestern Canada (*e.g.* Bonsal et al. 2001, 2006; Dickson et al. 2002; Dery and Wood 2005; Pisaric et al. 2009; Fauria and Johnson 2011; Bonsal and Shabbar 2011; Galloway et al. 2013; Vincent et al. 2015; Dalton et al. 2018). The positive phase of the PDO is associated with warmer SST in the NE Pacific Ocean, a more intense and south-western positioned Aleutian Low-pressure system, and a more intense high-pressure system over much of the NT (Bonsal et al. 2001; Lapointe et al. 2017; Kren et al. 2016). These pressure cells result in northward displacement of the polar jet, and a weakening of the stratospheric polar vortex, resulting in warmer, drier conditions in the central NT during a +PDO phase (Bonsal et al. 2001; Lapointe et al. 2017; Kren et al. 2016). Warmer temperatures would result in a shorter length of ice coverage during winter, and increasing productivity, which could impact sediment geochemistry by modifying winter oxygen stratification. Warmer temperatures and drier conditions would result more rapid spring-melt and deposition of finer sediment (Cuven et al. 2011; Amann et al. 2017; Macumber et al. 2018), or possibly reduced sediment transport into the system, altering the amount of As transported into Control Lake.

Periodicities are observed in log(As/Ti), log(Zr/Ti) and log(Ca/Ti), with frequencies of ca. 90–120 yr and ca. 150–280 yr (Figure 6.5). Low-frequency oscillations with ca. 90–130 yr and ca. 200–500 yr period are observed in all wavelet scalograms of all proxies examined. The ca. 90–130-yr periodicity observed at Control Lake may be related to the Gleissberg solar cycle, a long-term modulation in the intensity of the Schwabe sunspot cycle (Gleissberg 1971). Ogurtsov et al. (2002) observed a ca. 50–80 yr and ca. 90–140 yr periodicity in this cycle based on an analysis of cosmogenic isotope records, direct observations (sunspots and auroral measurements), and paleoclimate proxies. TSI data also shows this signal (Fig. 5). The ca. 200–300 yr period likely corresponds to the Suess/De Vries cycle, a modulation of solar cycle first observed in records of cosmogenic isotopes (14C, 10Be) and tree-ring thickness with a period of ca. 160–270 yr (Suess 1980, 1986).

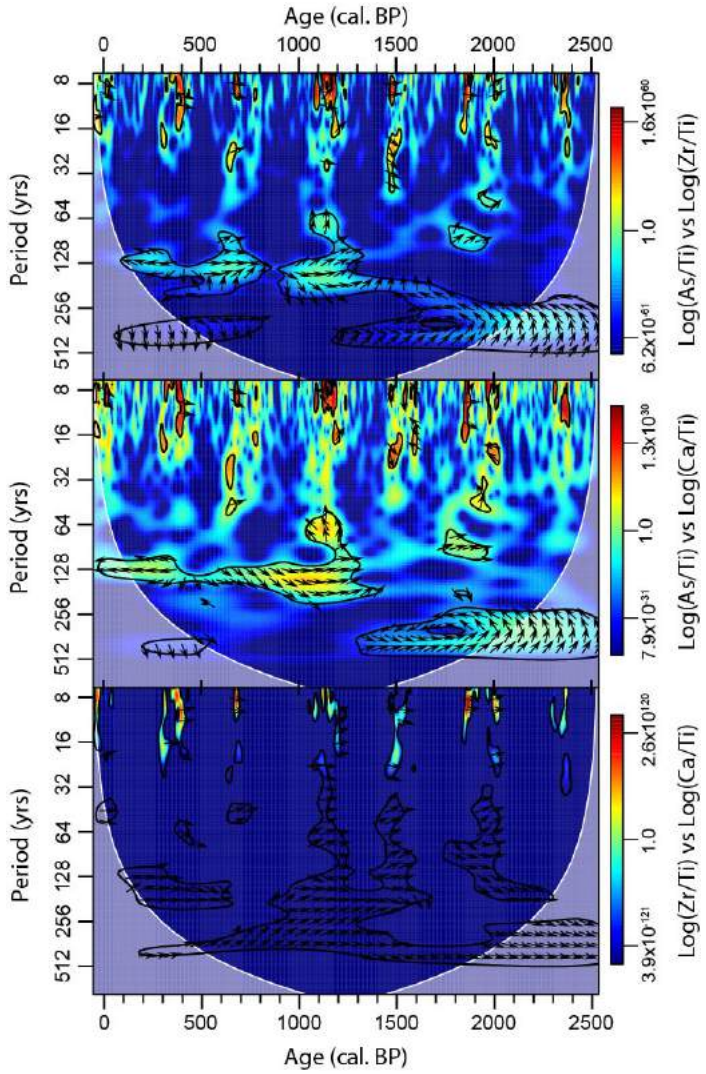

Figure 6.8: Cross-wavelet transformation of log(As/Ti) vs log(Zr/Ti) and log(Ca/Ti) as well as log(Zr/Ti) vs log(Ca/Ti) using a morlet wavelet. Areas that are significantly different from a red noise model are indicated by black lines. The cone of influence is show by light grey. Warm (cold) colors indicate higher(lower) power of the wavelet transformation. Arrows indicate phase difference between x (log(As/Ti) and log(Zr/Ti)) and y (log(Zr/Ti) or log(Ca/Ti)). Arrows pointing to the right indicate the two signals are in phase, and arrows pointing to the left indicate they are out-of-phase. Arrows pointing up indicate x leads and arrows pointing down shown y leads.

Gleissberg and Suess solar cycles have been observed in climate records worldwide (Hodell et al. 2001; Wang et al. 2005; Raspopov et al. 2008; Pena et al. 2015; Liu et al. 2019). Oscillations with similar periodicities as the Gleissberg and Suess cycles have been observed throughout NW North America. For example, the Gleissberg and Suess solar cycles were inferred to have influenced productivity and hydrology in the Seymour Belize Inlet Complex of coastal mainland British Columbia at a frequency of 82–89 and 241–243 yr (Galloway et al. 2013).

Gleissberg and Suess-like oscillations were also observed in the diatom-based productivity records of Danny's Lake, in the central NT, and Arolick Lake, Alaska (Hu et al. 2003; Dalton et al. 2018). Timoney et al. (1997) observed centennial-scale oscillations in the flood-history of the Peace-Athabasca flood plain in Northern Alberta that are attributable to Gleissberg cycles. Wiles et al. (2004) observed shifts in glacial extent corresponding to variations in TSI over centennial timescales.

Gleissberg and Suess cycles may be influencing the climate of the central NT through modulation of AO/NAO and PDO climate oscillations. Recent examination of historical SST and SLP trends provided evidence of modulation of the PDO by Gleissberg cycles (Meehl et al. 2008; van Loon and Meehl 2016). Similarly, Shen et al. (2006) observed an apparent 50–80-yr period in the oscillatory pattern of the PDO index. Several researchers have observed modulation of the PDO associated with 11-yr sunspot cycles within the historical record (Kren et al. 2016) or PDO-like response to solar forcing (van Loon and Meehl 2008, 2011). Hood and Soukharev (2012) observed AO-like response in global climate models in response to 11-yr solar cycles, and several studies have noted an apparent solar modulation of AO/NAO on 11-yr timescales (Boberg and Lundstedt 2002; Van Loon et al. 2012; Scaife et al. 2013; Gray et al. 2016; Smith et al. 2016; van Loon and Meehl 2016). Examination of modern trends in atmospheric response to solar cycles showed statistically significant AO/NAO-like variations only during intervals of increased solar irradiance (Hood et al. 2013). Van Loon et al. (2012) also noted more significant modulation of NAO by the solar cycle depending on the phase of the Gleissberg cycle. It is apparent that lower-frequency oscillations likely corresponding to a 11-yr modulation of PDO, ENSO or AO/NAO are further impacted by amplitude shifts in TSI caused by Gleissberg and Suess cycles.

Intervals that exhibit co-occurrence of oscillations with periods increasing from 8–130 yr ("stacked" periodicities) in the geochemical data at Control Lake have been previously been observed in climate records, including records of diatom productivity in NT (Dalton et al. 2018), in productivity and sedimentation northern British Colombia (Galloway et al. 2013; Patterson et al. 2013), in pollen signals from east Asia (Xu et al. 2015; Park 2017) and precipitation proxies from China (Chu et al. 2014; Zhang et al. 2018). Stacked periodicities were observed in all the examined paleo-proxies with an average return interval of 440 +/- 67 yr. This period likely corresponds to the lower end of an unnamed 400-600 yr cycle preserved in the record of 14C production in the atmosphere (Stuiver and Braziunas 1993). Although originally suggested to be related to ocean circulation (Stuiver and Braziunas 1993), more recent comparison of 10Be and 14C production records suggests that cosmic radiation is a more likely driver of 14C production (Muscheler et al. 2000). This 500-yr cycle has been observed in climate

records in diatom productivity in Lake Arolik, Alaska (Hu et al, 2003), in ostracod abundance and magnetic susceptibility of paleo-lake Pannon in Austria (Kern et al. 2012), pollen from laminated shales of Eocene age associated with a paleo-lake in Germany (Lenz et al. 2016), and pollen data from a Xiaolongwan Lake in China spanning the last ca. 5000 cal. BP (Xu et al. 2015). This 500-year cycle was not observed in the wavelet analysis of the subset of TSI data used herein (Figure 6.5), but was present in analysis of 14C and 10Be datasets that extend throughout the length of the Holocene (Roth and Joos, 2013). The intervals of stacked signal may be partially driven by this 500-yr cycle observed in lake productivity and paleoclimate records worldwide. The apparent stacking of signals throughout the record may suggest that only when several climate cycles are in-phase is there significant enough alteration of temperature and precipitation to alter lake productivity/lake sedimentation and As concentrations in sediment.

Comparison of the TSI reconstruction of Steinhilber et al. (2009) and sediment geochemistry of Control Lake was evaluated using cross-wavelet transformation (Figure 6.6.7). Results show that statistically significant intervals occur in the ca. 30–60, 100–130, and 200–300 yr bands throughout the entire record. The phase relationships between TSI and paleo-proxies is variable, likely reflecting the complex and indirect processes involved in TSI influence on sediment geochemistry.

6.8.2 Climate Oscillations and As

Previous coarse-resolution analysis of Control Lake and the microfossils therein revealed that there likely was post-depositional mobilization of As (Gregory et al. 2019a). In spite of likely post-deposition movement of As, variations in sedimentary As concentrations were observed to broadly correspond to long-term changes in temperature and productivity in the lake. Increased temperature results in higher production of OM. Organic matter may influence biological activity that increases the likelihood of As precipitation either as As-sulphides (realgar, pararealgar, orpiment) or ferrous-As minerals (arsenian pyrite, arsenopyrite) in lake sediments (Du Laing et al. 2009; Root et al. 2009; Galloway et al., 2018; Thiel et al. 2019). Organic matter may further sequester As through acting as an adsorbent (Meunier et al. 2011). This relationship has been observed previously by Galloway et al. (2018) and Miller et al (in press) in subarctic

environments. Here we examine the possibility of these mechanisms acting on finer timescales.

Comparison of log(Zr/Ti) and log(Ca/Ti) are almost always in phase, with only minor deviations across all periods in the paleo-record, suggesting that both proxies are responding to similar forcing throughout the Holocene. Log(As/Ti) is generally in-phase or lags behind both paleo-proxies at 8–16 year periods, indicating, at least during select intervals of particularly strong climate oscillation, log(As/Ti) might preserve some of the original signal of As input into Control Lake before subsequent post-depositional remobilization. Alternatively, post-depositional mobility of As and subsequent authigenic mineralization in sediments with high labile organic content may result in the observed phase relationships. Log(As/Ti) tends to lag both proxies at ca 90–130 yr periods, but leads both proxies at ca. 200–500 yr periods. The ca. 300–500 yr phase relationships may be due to post-depositional movement of As and subsequent sequestration during the next period of oscillatory climate pressure. The observed lag at ca. 90–130 yr periodicities may be induced by increased OM or fine particulate matter trapping As mobile in the sediment column as it migrants upwards. Variations in phase of log(As/Ti) and log(Ca/Ti) suggest that, during select time periods increased OM may act to increase As sequestration by acting as a substrate for mineral formation, although this mechanism is not stable over time. Based on this analysis, centennial to multi-centennial variations in climate were more important controls on As sequestration during the Holocene than lower-period oscillations.

6.9 Conclusions

Sediment cores collected from Control Lake, NT, were analyzed at mm-resolution using Itrax-XRF to understand the impact of quasi-periodic ocean-atmospheric oscillations on lacustrine sediment geochemistry. Spectral and wavelet analyses showed there was a response in geochemical proxies of in-lake productivity and sedimentation to climate oscillations with periods of ca. 8–11, 30–60, 90–130 and 200–300 yr, corresponding to ENSO, AO/NAO, PDO and solar cycles (Schwabe, Gleissberg, Suess). A geochemical response was only observed in Control Lake sediments when several periodicities were in phase. Periods of variability corresponding to solar cycles are apparent in the climate

record. Variations in log(As/Ti) showed decadal- and centennial-scale oscillations. Short-period oscillations may correspond to the original variability in As concentration related to in situ depositional conditions, but could equally represent a tendency of post-depositional mobile As to mineralize in areas of increased labile OM.

6.10 References

Aboriginal Affairs and Northern Development Canada (2013) Water Balance Monitoring at the Tundra Mine Site: 2012 Update. 101

Amann B, Lamoureux SF, Boreux MP (2017) Winter temperature conditions (1670–2010) reconstructed from varved sediments, western Canadian High Arctic. Quat Sci Rev 172:1–14.

Babalola LO, Patterson RT, Prokoph A (2013) Foraminiferal evidence of a late Holocene westward shift of the Aleutian Low. Journal of Foraminiferal Research. 43 (2):127–142.

Bai J, Yang Z, Cui B, Gao H, Ding Q (2010) Some heavy metals distribution in wetland soils under different land use types along a typical plateau lake, China. Soil Tillage Res 106:344–348.

Becker A, Klock W, Friese K, Schreck P, Treutler H-C, Spettel B, Duff MC (2001) Lake Süber See as a natural sink for heavy metals Lake Su from copper mining. J Geochemical Explor 74:205–217.

Bing H, Wu Y, Sun Z, Yao S (2011) Historical trends of heavy metal contamination and their sources in lacustrine sediment from Xijiu Lake, Taihu Lake Catchment, China. J Environ Sci 23:1671–1678.

Blaauw M, Christen JA (2019) rbacon: Age-depth modelling using bayesian statistics. R Package version 2.3.7.

Boberg F, Lundstedt H (2002) Solar Wind Variations Related to Fluctuations of the North Atlantic Oscillation. Geophys Res Lett 29:13-1-13–4.

Bonsal B, Shabbar A (2011) Large-scale climate oscillations influencing Canada, 1900-2008. Canadian biodiversity: Ecosystem status and trends 2010. Technical Thematic Report No. 4. Canadian Councils of Resource Ministers, Ottawa, Canada, pp. 1-15

Bonsal BR, Prowse TD, Duguay CR, Lacroix MP (2006) Impacts of large-scale teleconnections on freshwater-ice break / freeze-up dates over Canada. Journal of Hydrology, 1:340–353.

Bonsal BR, Shabbar A, Higuchi K (2001) Impacts of low frequency variability modes on Canadian winter temperature. Int J Climatol 21:95–108.

Bowell R, Alpers C, Jamieson H, Nordstrom DK, Majzlan J (2014) The environmental geochemistry of Arsenic: An Overview. Reviews in Mineralogy and Geochemistry Volume 79. The Mineralogical Society of America, Virginia, USA.

Buermann W, Anderson B, Tucker CJ, Dickinson RE, Lucht W, Potter CS, Myneni RB (2003) Interannual covariability in Northern Hemisphere air temperatures and greenness associated with El Niño-Southern Oscillation and the Arctic Oscillation. J Geophys Res Atmos 108:1–16.

Chang AS, Patterson RT (2005) Climate shift at 4400 years BP: Evidence from high-resolution diatom stratigraphy, Effingham Inlet, British Columbia, Canada. Palaeogeography, Palaeclimatology, Palaeoecology 226:72-92.

Christoforou P, Hameed S (1997) Solar cycle and the Pacific “centers of action”. Geophysical Research Letters, 24(3):293-296.

Christoudias T, Pozzer A, Lelieveld J (2012) Influence of the North Atlantic Oscillation on air pollution transport. Atmos Chem Phys 12:869–877.

Chu G, Sun Q, Xie M, Lin Y, Shang W, Zhu Q, Shan Y, Xu D, Rioual P, Wang L, Liu J (2014) Holocene cyclic climatic variations and the role of the Pacific Ocean as recorded in varved sediments from northeastern China. Quat Sci Rev 102:85–95.

Cuven S, Francus P, Lamoureux S (2011) Mid to Late Holocene hydroclimatic and geochemical records from the varved sediments of East Lake, Cape Bounty, Canadian High Arctic. Quat Sci Rev 30:2651–2665.

Cuven S, Francus P, Lamoureux SF (2010) Estimation of grain size variability with micro X-ray fluorescence in laminated lacustrine sediments, Cape Bounty, Canadian High Arctic. J Paleolimnol 44:803–817.

Dalton AS, Patterson RT, Roe HM, Macumber AL, Swindles GT, Galloway JM, Vermaire JC, Crann CA, Falck H (2018) Late Holocene climatic variability in Subarctic Canada: Insights from a high-resolution lake record from the central Northwest Territories. PLoS One 13:1–21.

Davies SJ, Lamb HF, Roberts SJ (2015) Micro-XRF Core Scanning in Palaeolimnology: Recent Developments. In: Micro-XRF Studies of Sediment Cores: Applications of a Non-Destructive tool for Environmental Sciences. pp 189–226

Déry SJ, Wood EF (2005) Decreasing river discharge in northern Canada. Geophys

Res Lett 32:1–4.

Deser C (2000) On the teleconnectivity of the "Arctic Oscillation." Geophys Res Lett 27:779–782.

Deser C, Alexander MA, Xie S, Phillips AS (2009) Sea Surface Temperature Variability: Patterns and Mechanisms. Ann Rev Mar Sci 2:115–143.

Dickson RR, Osborn TJ, Hurrell JW, Meincke J, Blindheim J, Adlandsvik B, Vinje T, Alekseev G, Maslowski W (2002) The Arctic Ocean Response to the North Atlantic Oscillation. J Clim 13:2671–2696.

Du Laing G, Chapagain SK, Dewispelaere M, Meers E, Kazama F, Tack FMG, Rinklebe K, Verloo MG (2009) Presence and mobility of arsenic in estuarine wetland soils of the Scheldt estuary (Belgium). J Environ Monit 11:873–881.

Eckhardt S, Stohl A, Beirle S, Spichtinger N, James P, Forster C, Junker C, Wagner T, Platt U, Jennings SG (2003) The North Atlantic Oscillation controls air pollution transport to the Arctic. Atmos Chem Phys 3:1769–1778.

Fauria MM, Johnson EA (2006) Large-scale climatic patterns control large lightning fire occurrence in Canada and Alaska forest regions. J Geophys Res Biogeosciences 111:1–17.

Galloway JM, Palmer M, Jamieson HE, Patterson RT, Nasser N, Falck H, Macumber AL, Goldsmith SA, Sanei H, Normandeau P, Hadlari T, Roe HM, Lemay ND (2015) Geochemistry of lakes across ecozones in the Northwest Territories and implications for the distribution of arsenic in the Yellowknife region. Part 1: Sediments. Geological Survey of Canada Open File 7908:1-49.

Galloway JM, Swindles GT, Jamieson HE, Palmer M, Parsons MB, Sanei H, Macumber AL, Patterson RT, Falck H (2018) Organic matter control on the distribution of arsenic in lake sediments impacted by ~ 65 years of gold ore processing in subarctic Canada. Sci Total Environ 622–623:1668–1679.

Galloway JM, Wigston A, Patterson RT, Swindles GT, Reinhardt E, Roe HM (2013) Climate change and decadal to centennial-scale periodicities recorded in a late Holocene NE Pacific marine record: Examining the role of solar forcing. Palaeogeogr Palaeoclimatol Palaeoecol 386:669–689.

Gleissberg W (1971) The probable behaviour of sunspot cycle 21. Sol Phys 21:240–245

Gouhier TC, Grinsted A, Simko V (2018) R package biwavelet: Conduct univariate and bivariate wavelet analysis version 0.20.17. https://github.com/tgouhier/biwavelet.

Gratz LE, Keeler GJ, Miller EK (2009) Long-term relationships between mercury wet deposition and meteorology. Atmos Environ 43:6218–6229.

Gray LJ, Beer J, Geller M, Haigh JD, Lockwood M, Matthes K, Cubasch U, Fleitmann D, Harrison G, Hood L, Luterbacher J, Meehl GA, Shindell D, van Geel B, White W (2010) Solar influences on climate. Review of Geophysics 48, RG4001.

Gray LJ, Scaife AA, Mitchell DM, Osprey S, Ineson S, Hardiman S, Butchart N, Knight J, Sutton R, Kodera K (2013) A lagged response to the 11-year solar cycle in observed winter Atlantic/European weather patterns. J Geophys Res Atmos 118:13405–13420.

Gray LJ, Woollings TJ, Andrews M, Knight J (2016) Eleven-year solar cycle signal in the NAO and Atlantic/European blocking. Q J R Meteorol Soc 142:1890–1903.

Gregory BRB, Patterson RT, Galloway JM, Nasser NA (2019a) Climate-induced controls on sedimentary arsenic sequestration in Northern Canada during the mid- to late-Holocene. Unpublished PhD dissertation, Carleton University, Ottawa, ON, Canada.

Gregory BRB, Patterson RT, Reinhardt EG, Galloway JM (2019b) The iBox-FC: a new containment vessel for Itrax X-ray fluorescence core-scanning of freeze cores. Quat Int 514:76-84.

[dataset] Gregory BRB, Patterson RT, Galloway JM, Reinhardt EG (2019c) Control Lake calibrated Itrax-XRF dataset. Mendeley Data, Version 1.0.

[dataset] Gregory BRB, Patterson RT, Galloway JM, Reinhardt EG (2019d) Control Lake Multi-Acid ICP-MS dataset. Mendeley Data, Version 1.0.

Guyard H, Chapron E, St-Onge G, Anselmetti FS, Arnaud F, Magand O, Francus P, Mélières M-A (2007) High-altitude varve records of abrupt environmental changes and mining activity over the last 4000 years in the Western French Alps (Lake Bramant, Grandes Rousses Massif). Quat Sci Rev 26:2644–2660.

Hodell DA, Brenner M, Curtis JH, Guilderson T (2001) Solar Forcing of Drought Frequency in the Maya Lowlands. Science (80-) 292:1367–1370

Hood L, Schimanke S, Spangehl T, Bal S, Cubasch U (2013) The surface climate

response to 11-yr solar forcing during northern winter: Observational analyses and comparisons with GCM simulations. J Clim 26:7489–7506.

Hood LL, Soukharev BE (2012) The Lower-Stratospheric Response to 11-Yr Solar Forcing: Coupling to the Troposphere–Ocean Response. J Atmos Sci 69:1841–1864.

Hu FS, Kaufman D, Yoneji S, Nelson D, Shemesh A, Huang Y, Tian J, Bond G, Clegg B, Brown T (2003) Cyclic Variation and Solar Forcing of Holocene Climate inthe Alaskan Subarctic. Science 301:1890–1893.

Hung H, Blanchard P, Halsall CJ, Bidleman TF, Stern GA, Fellin P, Muir DCG, Barrie LA, Jantunen LM, Helm PA, Ma J, Konoplev A (2005) Temporal and spatial variabilities of atmospheric polychlorinated biphenyls (PCBs), organochlorine (OC) pesticides and polycyclic aromatic hydrocarbons (PAHs) in the Canadian Arctic: Results from a decade of monitoring. Sci Total Environ 342:119–144.

Keimowitz AR, Zheng Y, Chillrud SN, Mailloux B, Jung HB, Stute M, Simpson HJ (2005) Arsenic redistribution between sediments and water near a highly contaminated source. Environ Sci Technol 39:8606–8613.

Kern AK, Harzhauser M, Piller WE, Mandic O, Soliman A (2012) Strong evidence for the influence of solar cycles on a Late Miocene lake system revealed by biotic and abiotic proxies. Palaeogeogr Palaeoclimatol Palaeoecol 329–330:124–136.

Kodera K (2002) Solar cycle modulation of the North Atlantic Oscillation: Implication in the spatial structure of the NAO. Geophys Res Lett 29:59-1-59–4.

Kodera K, Kuroda Y (2002) Dynamical response to the solar cycle. J Geophys Res 107:1–12.

Kodera K, Kuroda Y (2005) A possible mechanism of solar modulation of the spatial structure of the North Atlantic Oscillation. J Geophys Res D Atmos 110:1–9.

Kraemer BM, Chandra S, Dell AI, Dix M, Kuusisto E, Livingstone DM, Schladow SG, Silow E, Sitoki LM, Tamatamah R, McIntyre PB (2017) Global patterns in lake ecosystem responses to warming based on the temperature dependence of metabolism. Glob Chang Biol 23:1881–1890.

Kren AC, Marsh DR, Smith AK, Pilewskie P (2016) Wintertime Northern Hemisphere

response in the stratosphere to the Pacific decadal oscillation using the Whole Atmosphere Community Climate Model. J Clim 29:1031–1049.

Lapointe F, Francus P, Lamoureux SF, Vuille M, Jenny J=P, Bradley RS, Massa C (2017) Influence of North Pacific decadal variability on the western Canadian Arctic over the past 700 years. Clim Past 13:411–420.

Lean J, Rottman G, Harder J, Kopp G (2005) SORCE contributions to new understanding of global change and solar variability. Sol Radiat Clim Exp Mission Descr Early Results 27–53.

Lenz OK, Wilde V, Riegel W (2017) ENSO- and solar-driven sub-Milankovitch cyclicity in the Palaeogene greenhouse world; high-resolution pollen records from Eocene Lake Messel, Germany. J Geol Soc London 174:110–128.

Liu X, Rao Z, Shen CC, Liu J, Chen J, Chen S, Wang X, Chen F(2019) Holocene Solar Activity Imprint on Centennial- to Multidecadal-Scale Hydroclimatic Oscillations in Arid Central Asia. J Geophys Res Atmos 124:2562–2573.

Livingstone DM (1999) Ice break-up on southern Lake Baikal and its relationship to local and regional air temperatures in Siberia and to the North Atlantic Oscillation. Limnology 44:1486–1497

Loseto LL, Stern GA, Macdonald RW (2015) Distant drivers or local signals: Where do mercury trends in western Arctic belugas originate? Sci Total Environ 509–510:226–236.

MacDonald GM, Porinchu DF, Rolland N, Kremenetsky KV, Kaufman DS (2009) Paleolimnological evidence of the response of the central Canadian treeline zone to radiative forcing and hemispheric patterns of temperature change over the past 2000 years. J Paleolimnol 41:129–141.

Macdonald RW, Harner T, Fyfe J (2005) Recent climate change in the Arctic and its impact on contaminant pathways and interpretation of temporal trend data. Sci Total Environ 342:5–86.

Macumber AL, Patterson RT, Galloway JM, Falck H, Swindles GT (2018) Reconstruction of Holocene hydroclimatic variability in subarctic treeline lakes using lake sediment grain-size end-members. The Holocene 095968361775283.

Mantua NJ, Hare SR (2002) The Pacific Decadal Oscillation. J Oceanogr 58:35–44

Martin AJ, Pedersen TF (2002) Seasonal and interannual mobility of arsenic in a lake impacted by metal mining. Environ Sci Technol 36:1516–1523.

Massei N, Durand A, Deloffre J, Dupont JP, Valdes D, Laignel B (2007) nvestigating possible links between the north atlantic oscillation and rainfall variability in northwestern France over the past 35 years. Journal of Geophysical Research, 112:1-10.

Mccurdy MW, Mcneil RJ (2014) GEOLOGICAL SURVEY OF CANADA OPEN FILE 7577 Geochemical Data from Stream Silts and Surface Waters in the Pine Point Mining District, Northwest Territories (NTS 85-B).

McGregor H V, Gagan MK (2004) Western Pacific coral $\delta^{18}O$ records of anomalous Holocene variability in the El Niño-Southern Oscillation. Geophys Res Lett 31:1–4.

Meehl GA, Arblaster JM, Branstator G (2008) A coupled air-sea response mechanism to solar forcing in the Pacific region. J Clim 21:2883–2897.

Meehl GA, Arblaster JM, Matthes K, Sassi F, van Loon H (2009) Amplifying the pacific climate system response to a small 11-year solar cycle forcing. Science (80-) 325:1114–1118.

Meunier L, Koch I, Reimer KJ (2011) Effects of organic matter and ageing on the bioaccessibility of arsenic. Environ Pollut 159:2530–2536.

Miller CB, Parsons MB, Jamieson HE, Swindles GT, Nasser NA, Galloway JM (2019). Lake-specific controls on the long-term stability of mining-related, legacy arsenic contamination and geochemical baselines in a changing northern environment, Tundra Mine, Northwest Territories, Canada. Applied Geochemistry 104403.

Miller CB, Parsons MB, Jamieson HE, Ardakani OH, Gregory BRB, Galloway JM (in press). Influence of late Holocene climate on solid-phase speciation and long-term stability of arsenic in sub-Arctic lake sediments. Science of the Total Environment.

Misios S, Gray LJ, Knudsen MF, Karoff C, Schmidt H, Haigh JD (2019) Slowdown of the Walker circulation at solar cycle maximum. Proc Natl Acad Sci 116:7186–7191.

Misios S, Mitchell DM, Gray LJ, Tourpali K, Matthes K, Hood L, Schmidt H, Chiodo G,

Thiéblemont R, Rozanoc E, Krivolutsky A (2016) Solar signals in CMIP-5 simulations: Effects of atmosphere-ocean coupling. Q J R Meteorol Soc 142:928–941.

Moore JCG (1986) Courageous-Matthews Lake area, district of MacKenzie, Northwest Territories. Geological Survey of Canada Department of Mines and Technical surveys Report # 2524.

Morin A, Lamoureux W, Busnarda J (1999) Empirical Models Predicting Primary Productivity from Chlorophyll a and Water Temperature for Stream Periphyton and Lake and Ocean Phytoplankton. J North Am Benthol Soc 18:299–307.

Moy C, Seltzer G, Rodbell D, Anderson D (2002) Variability of El Niño/Southern Oscillation activity at millennial timescales during the Holocene epoch. Nature 420:162–165.

Muscheler AR, Beer J, Wagner G, Finkel RC (2000) Changes in deep-water formation during the Younger Dryas event inferred from ^{10}Be and ^{14}C records. Nature, 408(6812):567–570.

Newman M, Alexander MA, Ault TR, Cobb KM, Deser C, Lorenzo ED, Mantua NJ, Miller AJ, Minobe S, Nakamura H, Schneider N, Vimont DJ, Phillips AS, Scott JD, Smith CA (2016) The Pacific decadal oscillation, revisited. J Clim 29:4399–4427.

Ogurtsov MG, Nagovitsyn YA, Kocharov GE, Jungner H (2002) Long-period cycles of the Sun's activity recorded in direct solar data and proxies. Sol Phys 211:371–394.

Ólafsdóttir KB, Geirsdóttir Á, Miller GH, Larsen DJ (2013) Evolution of NAO and AMO strength and cyclicity derived from a 3-ka varve-thickness record from Iceland. Quat Sci Rev 69:142–154.

Osterberg EC, Mayewski PA, Fischer DA, Kreutz KJ, Maasch KA, Sneed SB, Kelsey E (2014) Mount Logan ice core record of tropical and solar influences on Aluetian Low variability: 500-1998 A.D. J Geophys Res 1–8.

Outridge OM, Sanei H, Stern GA, Hamilton PB, Goodarzi P (2007) Evidence for control of Mercury accumulation rates in Canadian high Arctic lake sediments by variations of aquatic primary productivity. Environmental Science and Technology, 41(15):5259:5265.

Padgham WA (1992) Mineral deposits in the Archean Slave Structural Province;

lithological and tectonic setting. Precambrian Research 58:1–24

Palmer MJ, Galloway JM, Jamieson HE, Patterson RT, Falck H, Kokelj SV (2015) The concentration of arsenic in lake waters of the Yellowknife area. NT Open File 2015-06 29

Palmer MJ, Chetelat J, Richardson M, Jamieson HE, Galloway JM (2019) Seasonal variation of arsenic and antimony in surface waters of small subarctic lakes impacted by legacy mining pollution near Yellowknife, NT, Canada. Science of the Total Environment, 684, 326-339.

Park J (2017) Solar and tropical ocean forcing of late-Holocene climate change in coastal East Asia. Palaeogeogr Palaeoclimatol Palaeoecol 469:74–83.

Parsons MB, LeBlanc KWG, Hall GEM, Sangster AL, Vaive JE, Pelchat P (2012) Environmental geochemistry of tailings, sediments and surface waters collected from 14 historical gold mining districts in Nova Scotia. Geological Survey of Canada Open File Report 7150, 321 p.

Patterson RT, Prokoph A, Chang AS (2004a) Late Holocene sedimentary response to solar and cosmic ray activity influenced climate variability in the NE Pacific. Sedimentary Geology. 172 (1,2): 67-84.

Patterson RT, Prokoph A, Wright C, Chang AS, Thomson RE, Ware DM (2004b) Holocene Solar Variability and Pelagic Fish Productivity in the NE Pacific. Palaeontologia Electronica, 7.1:17 pp.

Patterson RT, Prokoph A, Kumar A, Chang AS, Roe HM (2005) Holocene variability in pelagic fish and phytoplankton productivity along the west coast of Vancouver Island, NE Pacific Ocean. Marine Micropaleontology 55 (3,4): 183-204.

Patterson RT, Prokoph A, Reinhardt A, Roe HM (2007) Climate cyclicity in late Holocene anoxic marine sediments from the Seymour-Belize Inlet Complex, British Columbia. Quaternary Land-Ocean Interactions: Sea-Level Change, Sediments and Tsunami. Marine Geology, 242 (1-3): 123-140.

Patterson RT, Chang AS, Prokoph A, Roe HM, Swindles GT (2013) Influence of the Pacific Decadal Oscillation, El Niño-Southern Oscillation and solar forcing on climate and primary productivity changes in the northeast Pacific. Quaternary International. 310: 124-139.

Patterson RT, Swindles GT (2015) Influence of ocean–atmospheric oscillations on lake ice phenology in eastern North America. Climate Dynamics. 45 (9,10):2293-2308.

Pena JC, Schulte L, Badoux A, Barriendos M, Barrera-Escoda A (2015) Influence of solar forcing, climate variability and modes of low-frequency atmospheric variability on summer floods in Switzerland. Hydrol Earth Syst Sci 19:3807–3827.

Pisaric MFJ, St-Onge SM, Kokelj SV (2009) Tree-ting reconstruction of Early-growing season precipitation from Yellowknife, Northwest Territories, Canada. Arctic, Antarctic, and Alpine Research, 41(4):486-496

Prowse T, Alfredsen K, Beltaos S, Bonsal B, Duguay C, Korhola A, McNamara J, Pienitz R, Vincent WF, Vuglinsky V, Weyhenmeyer GA (2011) Past and future changes in arctic lake and river ice. Ambio 40:53–62.

Quesada A, Vincent WF, Kaup E, Hobbie JE, Laurion I (2006) Landscape control of high latitude lakes in a changing climate. In: Trends in Antarctic Terrestrial and Limnetic Ecosystems: Antarctica as a Global Indicator. pp 221–252

Raspopov OM, Dergachev VA, Esper J, Kozyreva OV, Frank D, Ogurtsov M, Kolstrom T, Shao X (2008) The influence of the de Vries (~ 200-year) solar cycle on climate variations : Results from the Central Asian Mountains and their global link. 259:6–16.

Reimer PJ, Bard E, Bayliss A, Beck JW, Blackwell PG, Ramsey CB, Buck CE, Cheng H, Edwards RL, Friedrich M, Grootes PM, Guilderson TP, Haflidason H, Hajdas I, Hatte C, Heaton TJ, Hoffman DL, Hogg AG, Hughen KA, Kaiser KF, Kromer B, Manning SW, Niu M, Reimer RW, Richards DA, Scott EM, Southon JR, Staff RA, Turney CSM, ven der Plicht J (2013). IntCal13 and Marine13 Radiocarbon age calibration curves 0-50,000 years cal BP. Radiocarbon 55:1869-1887.

Rigét F, Vorkamp K, Hobson KA, Muir DCG, Dietz R (2013) Temporal trends of selected POPs and the potential influence of climate variability in a Greenland ringed seal population. Environ Sci Process Impacts 15:1706–1716.

Roesch A, Schmidbauer H (2018) waveletcomp: Computational Wavelet Analysis. R package version 1.1. https://CRAN.R-project.org/package=WaveletComp

Rossi A, Massei A, Laignel B (2011). A synthesis of the time-scale variability of

commonly used climate indices using continuous wavelet transform. Global and Planetary Change, 78:1-13.

Roth R, Joos F (2013) A reconstruction of radiocarbon production and total solar irradiance from the Holocene 14C and CO2 records: Implications of data and model uncertainties. Clim Past 9:1879–1909.

Root RA, Vlassopoulos D, Rivera NA, Rafferty MT, Andrews C, O'Day PA (2009) Speciation and natural attenuation of arsenic and iron in a tidally influenced shallow aquifer. Geochim Cosmochim Acta 73:5528–5553.

Roy I, Haigh JD (2010) Solar cycle signals in sea level pressure and sea surface temperature. Atmos Chem Phys 10:3147–3153.

Roy I, Haigh JD (2012) Solar Cycle Signals in the Pacific and the Issue of Timings. J Atmos Sci 69:1446–1451.

Rydberg J, Klaminder J, Rosén P, Bindler R (2010) Climate driven release of carbon and mercury from permafrost mires increases mercury loading to sub-arctic lakes. Sci Total Environ 408:4778–4783.

Sarmiento S, Palanisami A (2011) Coherence between atmospheric teleconnections and Mackenzie River Basin lake levels. J Great Lakes Res 37:642–649.

Scaife AA, Ineson S, Knight JR, et al (2013) A mechanism for lagged North Atlantic climate response to solar variability. Geophys Res Lett 40:434–439.

Schulz M, Mudelsee M (2002) REDFIT: Estimating red-noise spectra directly from unevenly spaced paleoclimatic time series. Comput Geosci 28:421–426.

Seabridge Gold Inc. (2010) Courageous Lake Project Description in Support of a Class " A " Land Use Permit (Former Permit MV2003C0050)

Sheffield J, Wood EF (2008) Global trends and variability in soil moisture and drought characteristics, 1950-2000, from observation-driven simulations of the terrestrial hydrologic cycle. J Clim 21:432–458.

Shen C, Wang WC, Gong W, Hao Z (2006) A Pacific Decadal Oscillation record since 1470 AD reconstructed from proxy data of summer rainfall over eastern China. Geophys Res Lett 33:1–4.

Silke R (2009) The Operational History of Mines in the Northwest Territories , Canada

Simpson IR, Blackburn M, Haigh JD (2009) The Role of Eddies in Driving the

Tropospheric Response to Stratospheric Heating Perturbations. J Atmos Sci 66:1347–1365.

Sinha E, Michalak AM, Balaji V (2017) Eutrophication will increase during the 21st century as a result of precipitation changes. Science (80-) 357:1–5.

Skinner WR, Shabbar A, Flannigan MD, Logan K (2006) Large forest fires in Canada and the relationship to global sea surface temperatures. J Geophys Res Atmos 111:1–14.

Slemr F, Brenninkmeijer CA, Rauthe-Schöch A, Weigelt A, Ebinghaus R, Brunke E-G, Martin L, Spain TG, O'Doherty S (2016) El Niño-Southern Oscillation influence on tropospheric mercury concentrations. Geophys Res Lett 43:1766–1771.

Smedley PL, Kinniburgh DG (2000) Source and behaviour of arsenic in natural waters. United Nations Synth Rep Arsen Drink 1–61

Smith DM, Scaife AA, Eade R, Knight JR (2016) Seasonal to decadal prediction of the winter North Atlantic Oscillation: Emerging capability and future prospects. Q J R Meteorol Soc 142:611–617.

Snortheim CA, Hanson PC, McMahon KD, Read JS, Carey CC, Dugan HA (2017) Meteorological drivers of hypolimnetic anoxia in a eutrophic, north temperate lake. Ecol Modell 343:39–53.

Solanki SK, Usoskin IG, Kromer B, Schüssler M, Beer J (2004) Unusual activity of the Sun during recent decades compared to the previous 11,000 years Nature. 431 (7012): 1084–1087.

Steinhilber F, Beer J, Fröhlich C (2009) Total solar irradiance during the Holocene. Geophysical Research Letters, 19:2–5.

Stuiver M, Braziunas TF (1993) Sun, ocean, climate and atmospheric $^{14}CO_2$: an evaluation of causal and spectral relationships. The Holocene 3:289–305

Suess HE (1980) The Radiocarbon Record in Tree Rings of the Last 8000 Years. Radiocarbon 22:200–209.

Suess HE (1986) Secular variations of cosmogenic ^{14}C on Earth: Their discovery and interpretation. Radiocarbon 28:259–265

Sulphur KC, Goldsmith SA, Galloway JM, Macumber A, Griffith F, Swindles GT,

Patterson RT, Falck H, Clark ID (2016) Holocene fire regimes and treeline migration rates in sub-arctic Canada. Glob Planet Change 145:42–56.

Tetra Tech Wardrop (2012) Courageous Lake Prefeasibility Study. 1–450

Thiéblemont R, Matthes K, Omrani NE, Kodera K, Hansen F (2015) Solar forcing synchronizes decadal North Atlantic climate variability. Nat Commun 6:1–8.

Thiel J, Byrne JM, Kappler A, Schink B, Pester M (2019) Pyrite formation from FeS and H_2S is mediated through microbial redox activity. Proc Natl Acad Sci, 201814412, 6 p.

Thompson DWJ, Wallace JM (1998) The Arctic Oscillation signature in the wintertime geopotential height and temperature fields. Geophys Res Lett 25:1297–1300

Thompson PH, Kerswill JA (1994) Preliminary Geology of the Winter Lake - Lac de Gras area, District of MacKenzie, Northwest Territories, Open File 2740 (revised), scale 1:250000. 1

Thomson D (1990) Time Series Analysis of Holocene Climate Data. Philos Trans R Soc London Ser A, Math Phys Sci 330:601–616

Timoney K, Peterson G, Fargey P, Peterson M, McCanny S, Wein R (1997) Spring ice-jam flooding of the Peace-Athabasca Delta: Evidence of a climatic oscillation. Clim Change 35:463–483.

Torrence C, Compo GP (1998) A Practical Guide to Wavelet Analysis. Bull Am Meteorol Soc 79:61–78.

Van Loon H, Brown J, Milliff RF (2012) Trends in sunspots and North Atlantic sea level pressure. J Geophys Res Atmos 117:1–8.

Van Loon H, Meehl GA (2008) The response in the Pacific to the sun's decadal peaks and contrasts to cold events in the southern oscillation. J Atmos Solar-Terrestrial Phys 70:1046–1055.

Van Loon H, Meehl GA (2011) The average influence of decadal solar forcing on the atmosphere in the South Pacific region. Geophys Res Lett 38:1–5.

van Loon H, Meehl GA (2016) Interactions between externally forced climate signals from sunspot peaks and internally generated Pacific Decadal and North Atlantic Oscillations. Geophys Res Lett 161–166.

van Loon H, Rogers JC (1978) The Seesaw in Winter Temperatures between

Greenland and Northern Europe. Part I: General Description. Mon. Weather Rev. 106:296–310

Velasco VM, Mendoza B (2008) Assessing the relationship between solar activity and some large scale climatic phenomena. Advances in Space Research, 42:866-878.

Veretenenko S, Ogurtsov M (2019) Manifestation and possible reasons of ~60-year oscillations in solar-atmospheric links. Adv Sp Res 64:104–116.

Vincent LA, Zhang X, Brown RD, Feng Y, Mekis E, Milewska EJ, Wan H, Wang XL (2015) Observed trends in Canada's climate and influence of low-frequency variability modes. J Clim 28:4545–4560.

Wang C, Picaut J (2004) Understanding ENSO physics—a review. In: Geophysical Monograph Series. pp 21–48

Wang Y, Cheng H, Edwards RL, He Y, Kong X, An Z, Wu J, Kelly MJ, Dykoski CA, Li X (2005) The Holocene Asian monsoon: links to solar changes and North Atlantic climate. Science (80-) 308:854–857.

Wanner H, Bronnimann S, Casty C, Gyalistras D, Luterbacher J, Schmutz C, Stephenson DB, Xoplaki E (2001) North Atlantic Oscillation – Concepts and studies. Surveys in Geophysics, 22:321-382.

Weltje GJ, Bloemsma MR, Tjallingii R, Heslop D, Röhl U, Croudace IW (2015) Prediction of Geochemical Composition from XRF Core Scanner Data: A New Multivariate Approach Including Automatic Selection of Calibration Samples and Quantification of Uncertainties. In: Micro-XRF Studies of Sediment Cores: Applications of a Non-Destructive tool for Environmental Sciences: Part III

Wetzel R (2001) Limnology: Lake and river ecosystems, 3rd edition. Gulf professional publishing.

Wiles GC, D'Arrigo RD, Villalba R, Calkin PE, Barclay DJ (2004) Century-scale solar variability and Alaskan temperature change over the past millennium. 31:2–5.

Xu D, Lu H, Chu G, Wu N, Shen C, Wang C, Mao L (2015) 500-year climate cycles stacking of recent centennial warming documented in an East Asian pollen record. Sci Rep 4:1–7.

Zhang X, Wang J, Zwiers FW, Groisman PY (2010) The influence of large-scale climate

variability on winter maximum daily precipitation over North America. J Clim 23:2902–2915.

Zhang W, Niu J, Ming Q, Shi Z, Lei G, Huang L, Long X, Chang F (2018) Holocene climatic fluctuations and periodic changes in the Asian southwest monsoon region. J Asian Earth Sci 156:90–95.

Chapter 7: Conclusions

To characterize the influence of long-term (millennial) and short-term (sub- to multi-decadal) climate changes on As mobility, transportation and sequestration in lake sediments, we analyzed sediment cores extracted from Control Lake, central NT, using newly developed equipment and examined trends based on optimal calibration methodologies. Development of the Sequential Sample Reservoir (SSR) enabled Itrax-XRF rapid analysis of discrete sediment samples collected from spatial surveys (Chapter 2). The SSR allowed for higher sample numbers to develop rigorous assessment of methodologies to calibrate semi-quantitative Itrax-XRF data to approximate sediment geochemical concentrations through comparison of Itrax-XRF to MA-ICP-MS results (Chapter 3). In an effort to minimize matrix and specimen effects that could impact the accuracy and precision of Itrax-XRF data, several methods of data transformation were conducted before calibration, including normalization to lithogenic indicators, normalization to coherent/incoherent x-ray backscatter, adjustment of samples to account for variations in water content, and multivariate log-ratio calibration using the ItraXelerate software. Based on our results, the multivariate log-ratio approach provided the best approximation of sediment geochemistry. However, adjustment for variations in water content and normalization to x-ray backscatter also performed well and required less post-analytical processes of data. Using these methods, Itrax-XRF can provide a high-resolution estimate of geochemical change in sediment cores that can identify sub-mm response to natural or anthropogenic metal(loid) enrichment.

After testing calibration methods to ensure Itrax-XRF results could be converted to geochemical concentrations results, we also first had to develop technology that would enable analysis of freeze core sediment. The iBox-FC enables analysis of short slabs of frozen sediment using high-resolution Itrax-XRF. During the testing of the iBox-FC, issues relating to edge effects were observed. It is posited that these edge effects are associated with a change in the incident angle that X-radiation strikes the sediment surface, which alters assumed values in the calculation of XRF spectra, and thus Itrax-XRF-inferred sediment geochemistry. To account for this drawback, sediment cores were scanned first top-down (forewords), then again from bottom-up (reverse), and the multiple records

averaged to provide one cohesive record of sediment geochemistry that minimized edge effects. Based on comparison to results of ICP-MS analysis following a multi-acid digestion, this methodology was able to reliably identifies trends in sediment geochemistry in the cores (R^2 >0.81). The iBox-FC enables sub-mm analysis of short cores, and could be particularly useful for identification of recent contamination. Future advancements on the iBox-FC should focus on increasing the length of time a core can remain frozen, possibly through a refrigerated unit that could fit within the Itrax-XRF. This would enable both higher resolution analysis (sub-mm) and the analysis of longer cores, which would minimize issues relating to edge effects.

Following development of equipment and testing of methodologies, paleo-environmental analysis of freeze cores recovered from Control Lake, NT, Canada was conducted. Control Lake is an un-impacted lake that should preserve variations in As concentration responding to primarily to environmental forcing. Its location in the central NT near treeline makes it highly sensitive to climate change. This site is also of interest to the Federal Government of Canada, who own and are remediating the former Tundra Mine site, in which Control Lake is situation, and to Seabridge Gold, who own an adjacent property (Courageous Lake). Analysis of arcellinida counts and sediment geochemistry using redundancy analysis and comparison of stratigraphic trends suggested that As had been post-depositionally mobile in Control Lake sediments. Sediment geochemical results showed major changes in catchment weathering, in-lake productivity and overland hydrology in response to the treeline retreat from the region ca. 2700 cal. BP. Sedimentary As concentrations were lower before treeline retreat (ca. 4300–2700 cal. BP), likely related to cycling of As in shallow sediment due to annual winter anoxia that would be promoted by OM delivery from the vegetated landscape and autochthonous production under warmer temperatures. Peaks in As concentration occurred during the transition from boreal forest to tundra vegetation, possibly related to changes in the type or availability of OM. After treeline retreat, sedimentary As concentrations exhibited millennial-scale variations of up to ~50 ppm that corresponded to changes in regional temperature. This is substantially higher than the probable effect limit of As in lake sediments of 17 ppm (CCME 2002). Contemporaneous changes in TOC and S2 from an adjacent sediment core suggests OM type and availability influenced As sequestration.

This research supports the hypothesis of Galloway et al. (2018) and others (*e.g.*, MacDonald et al., 2005) that the type and amount of organic carbon impacts As mobility in lake sediments over millennial to centennial timescales. Rock Eval pyrolysis data from Control Lake sediment cores (currently pending) will help develop these ideas further.

Following coarse-resolution examination of Control Lake sediments, we conducted spectral analyses on a proxy of sediment particle size (log(Zr/Ti)), a productivity proxy (log(Ca/Ti)), and a proxy for As preservation relative to sedimentary input into Control Lake (log(As/Ti)). All proxies exhibited quasi-periodic oscillations with ca. 8-15, 30-70, 90-130, and 180-280 yr periods. Several climate oscillations impact modern temperature and precipitation in the NT with similar periodicities They are: ENSO/AO/Schwabe cycles (ca. 8-15 yr), the Pacific Decadal Oscillation (ca. 30-70 yr), Gleissberg cycles (ca. 90-130 yr) and Suess cycles (ca. 180-280 yr). Throughout the sedimentary record, there were short intervals of co-occurrence of significant oscillations in sediment geochemistry with increasing period from 8–130 years. This co-occurrence suggests that only when several climate oscillations are in-phase is there a significant enough response of the climate in the NT to elicit a response in Control Lake sediment geochemistry. The significant periods corresponding to known solar cycles suggest variations in solar insolation play a significant part controlling regional climate in the NT. This was supported by cross-wavelet analysis of TSI and sediment geochemical proxies preserved in the sediment cores of Control Lake. Cross-wavelet analysis of log(As/Ti) to log(Zr/Ti) and log(Ca/Ti) showed convoluted phase-relationships. Phase relationships indicated that As preservation is generally in-phase with proxies for increased particle size and productivity during intervals of short-period oscillations (ca. 8–15 yr), which supports the hypothesis of productivity controlling As sequestration. However, deviations from this observed relationship occurred during intervals where longer periods were significant (ca. 60–300 yr), indicating that other mechanisms un-accounted for in this work contribute to variations in As preservation in sediment. To our knowledge, this represents the first attempt to quantify the response of As to short-term, quasi-periodic climate oscillations. Although it has been suggested previously that short-term As variations would not be preserved due to redox cycling obscuring past geochemical signals, the results presented herein suggest that lake archives do preserve an As signal, and that lake sediments can be used to

examine variations in As at high temporal resolution during the Holocene. Furthermore, the response of As concentrations to variations at multi-decadal to centennial climate phenomena suggests that changes in predominant state of multi-decadal oscillatory ocean-atmosphere phenomena should be considered when assessing possible future health of environmental systems.

Appendix 1: Supplementary Figures

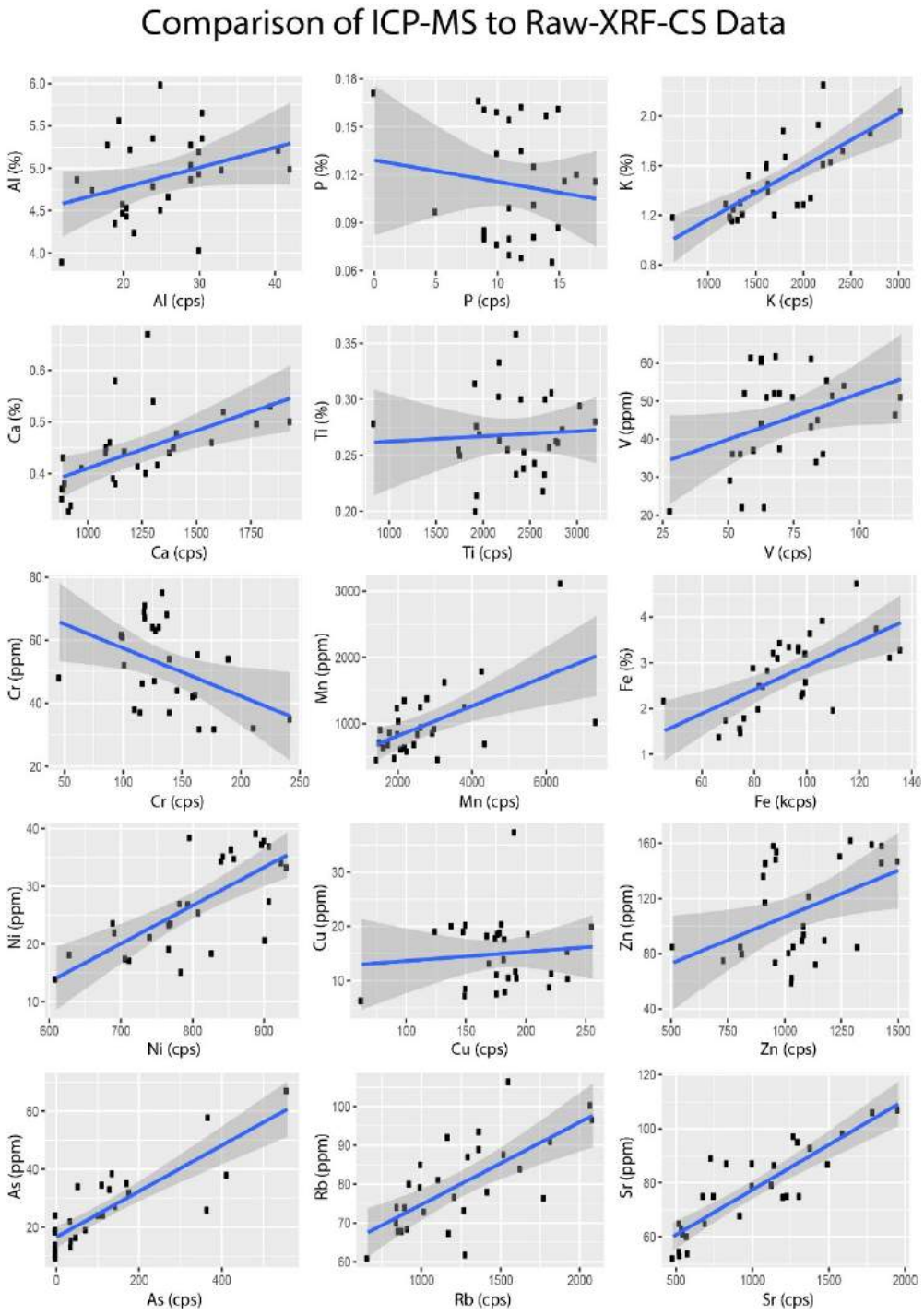

Figure A1.1: Comparison of Raw-XRF-CS to ICP-MS results. The blue line represents linear interpolation between raw XRF-CS and ICP-MS results. The dark grey shaded area represents the 95 % confidence interval for the linear regression.

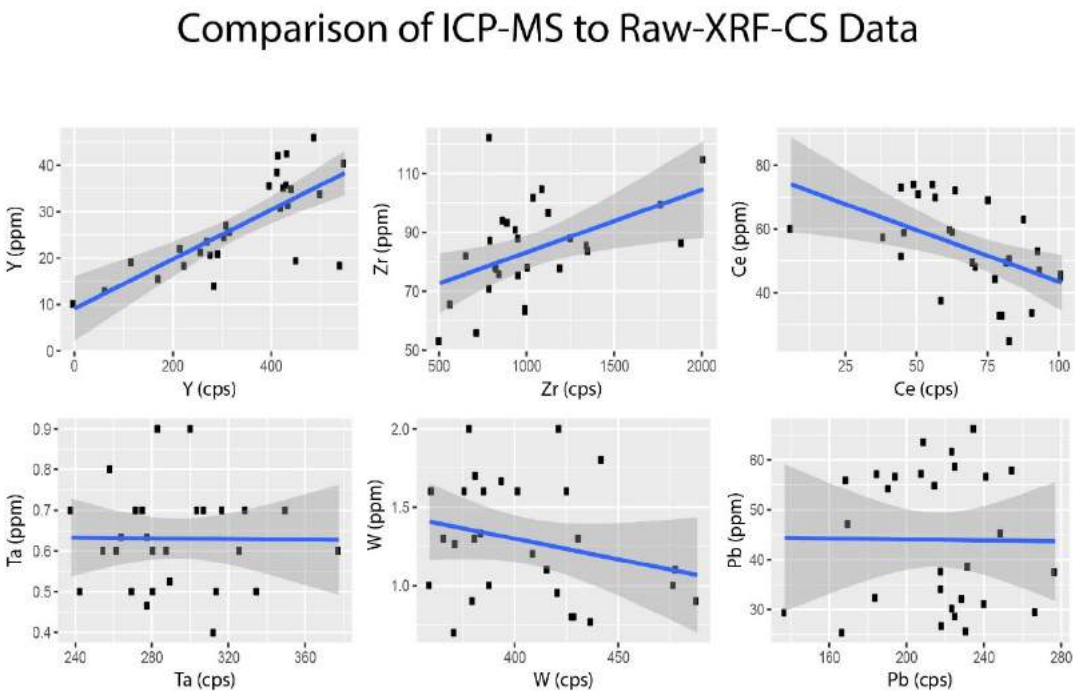

Figure A1.1 (cont'd): Comparison of Raw-XRF-CS to ICP-MS results. The blue line represents linear interpolation between raw XRF-CS and ICP-MS results. The dark grey shaded area represents the 95 % confidence interval for the linear regression

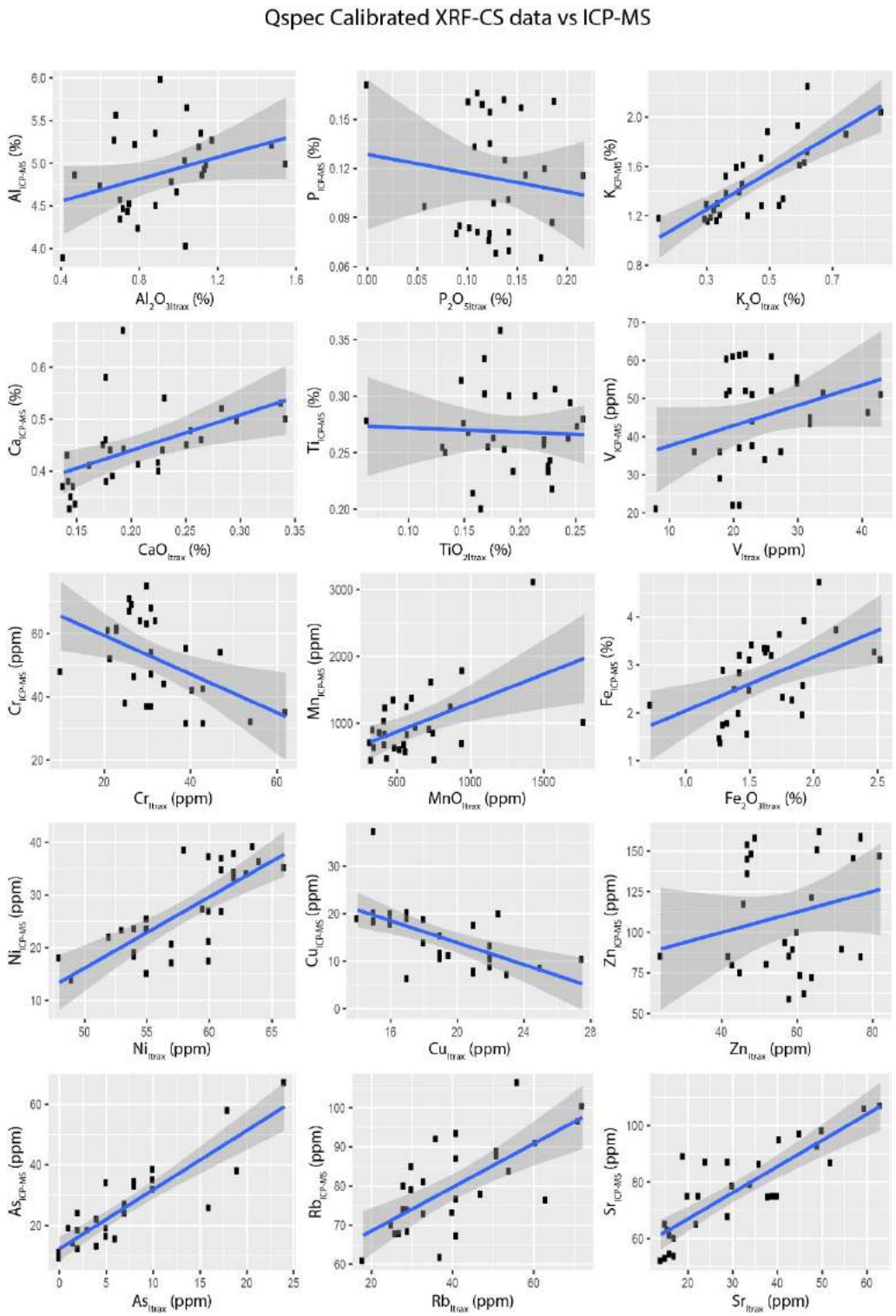

Figure A1.2: Comparison of Qspec-calibrated XRF-CS to ICP-MS results. The blue line represents linear interpolation between Qspec XRF-CS and ICP-MS results. The dark grey shaded area represents the 95 % confidence interval for the linear regression.

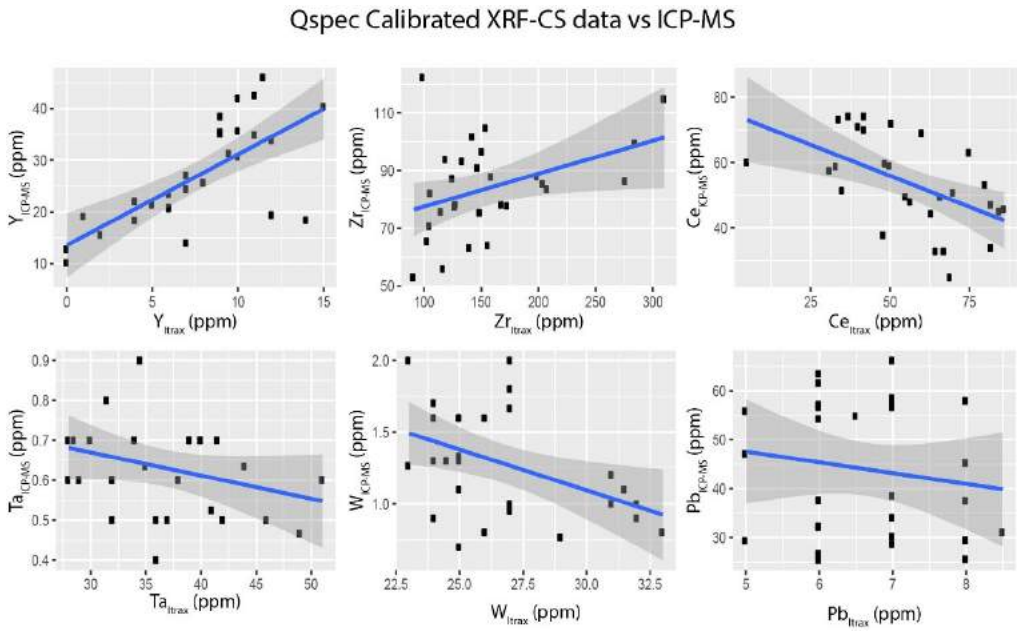

Figure A1.2 (cont'd): Comparison of Qspec-calibrated XRF-CS to ICP-MS results. The blue line represents linear interpolation between Qspec XRF-CS and ICP-MS results. The dark grey shaded area represents the 95 % confidence interval for the linear regression.

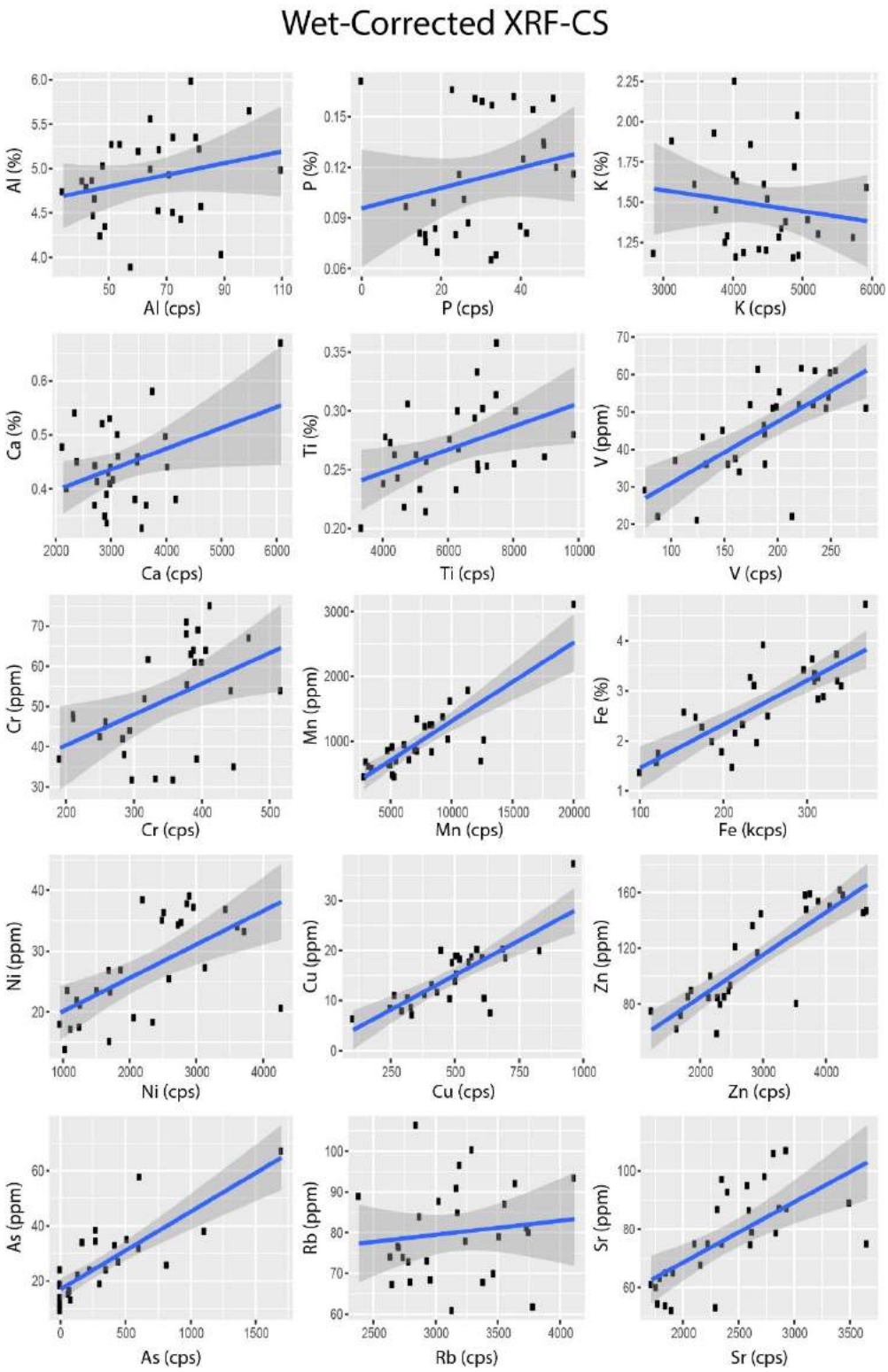

Figure A1.3: Comparison of Wet-corrected XRF-CS to ICP-MS results. The blue line represents linear interpolation between wet-corrected XRF-CS and ICP-MS results. The dark grey shaded area represents the 95 % confidence interval for the linear regression.

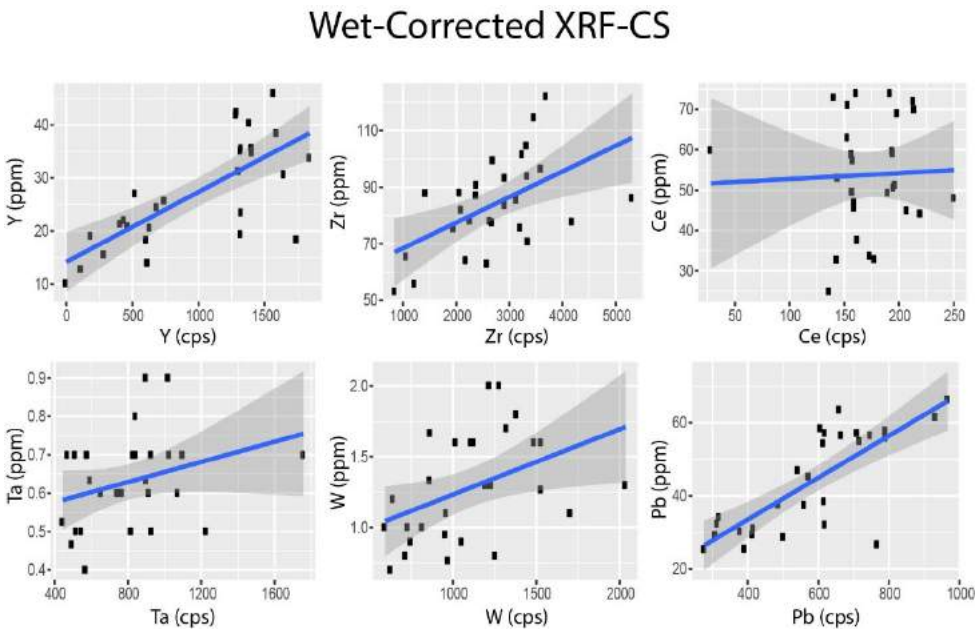

Figure A1.3 (cont'd): Comparison of Wet-corrected XRF-CS to ICP-MS results. The blue line represents linear interpolation between wet-corrected XRF-CS and ICP-MS results. The dark grey shaded area represents the 95 % confidence interval for the linear regression.

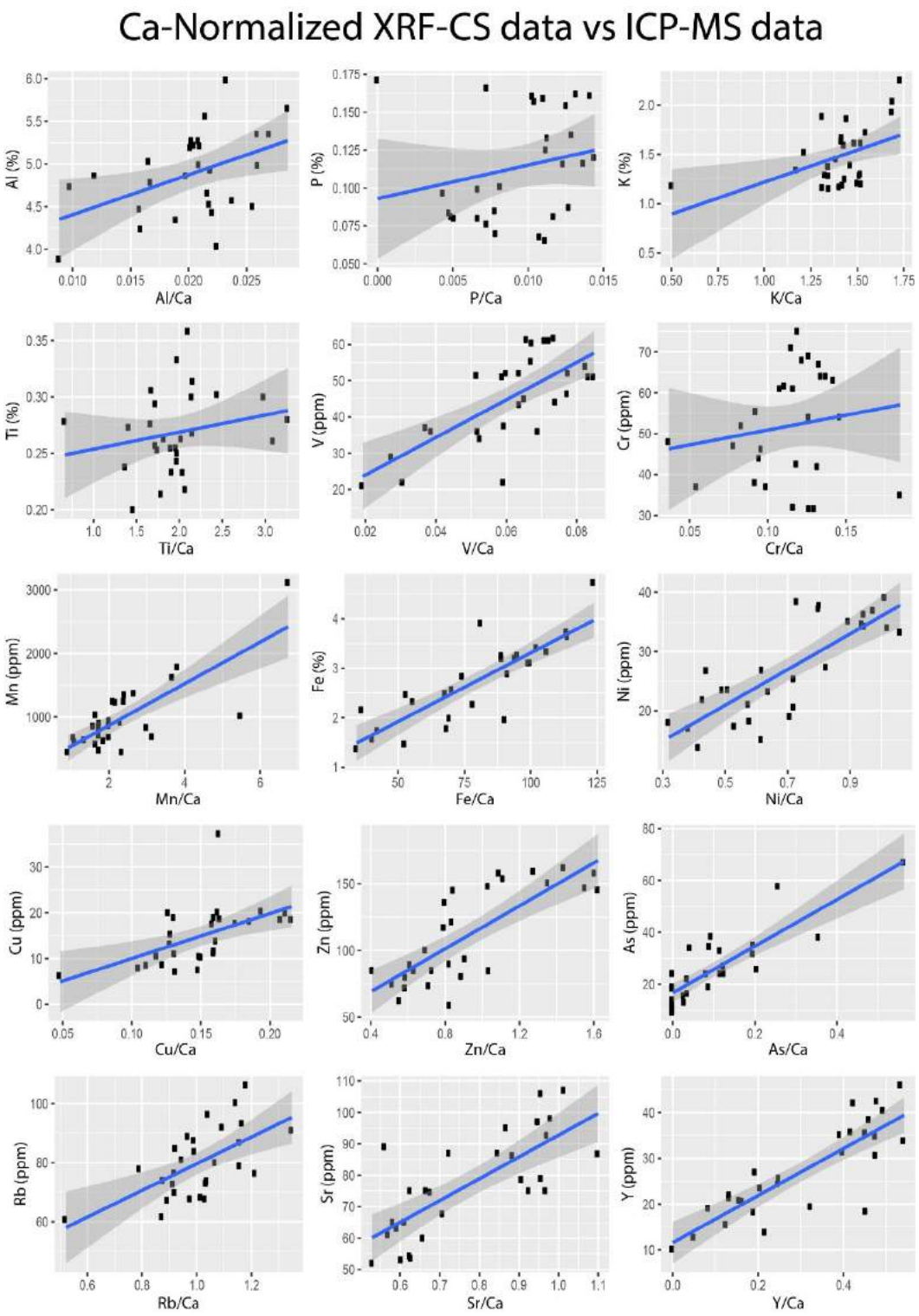

Figure A1.4: Comparison of Ca-normalized XRF-CS to ICP-MS results. The blue line represents linear interpolation between Ca-normalized XRF-CS and ICP-MS results. The dark grey shaded area represents the 95 % confidence interval for the linear regression.

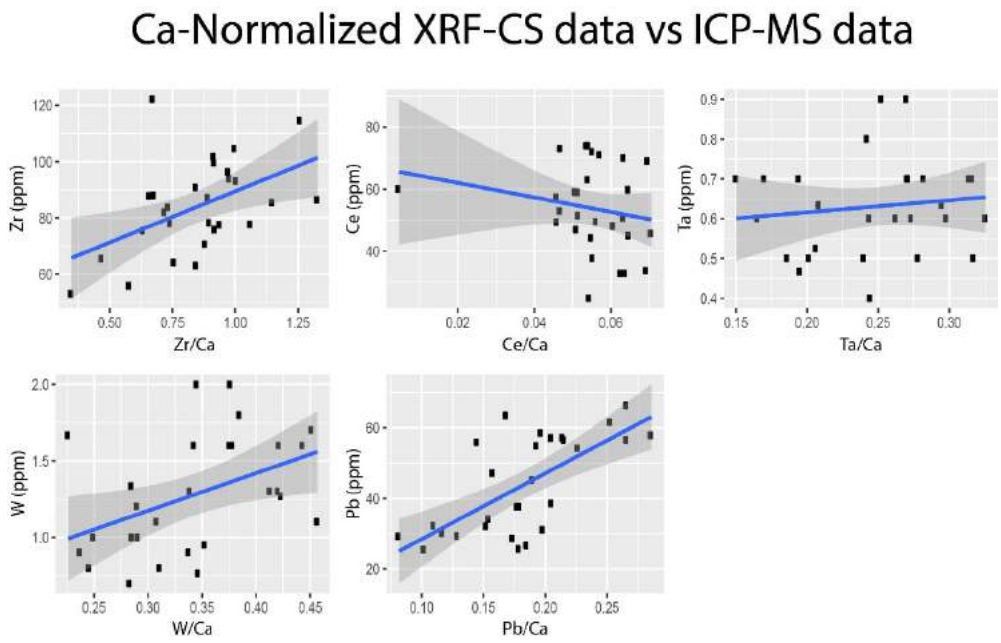

Figure A1.4 (cont'd): Comparison of Ca-normalized XRF-CS to ICP-MS results. The blue line represents linear interpolation between Ca-normalized XRF-CS and ICP-MS results. The dark grey shaded area represents the 95 % confidence interval for the linear regression.

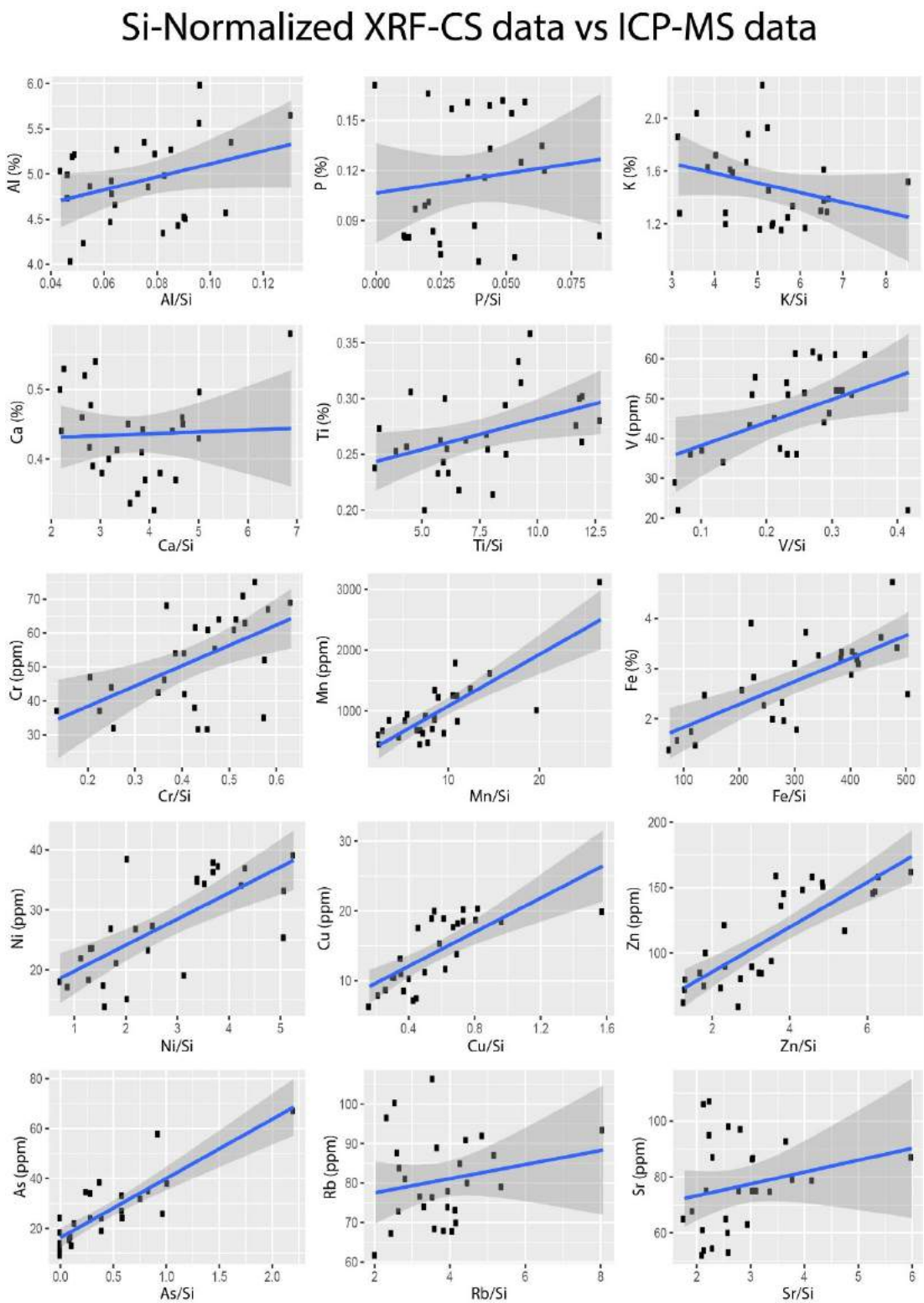

Figure A1.5: Comparison of Si-normalized XRF-CS to ICP-MS results. The blue line represents linear interpolation between Si-normalized XRF-CS and ICP-MS results. The dark grey shaded area represents the 95 % confidence interval for the linear regressions.

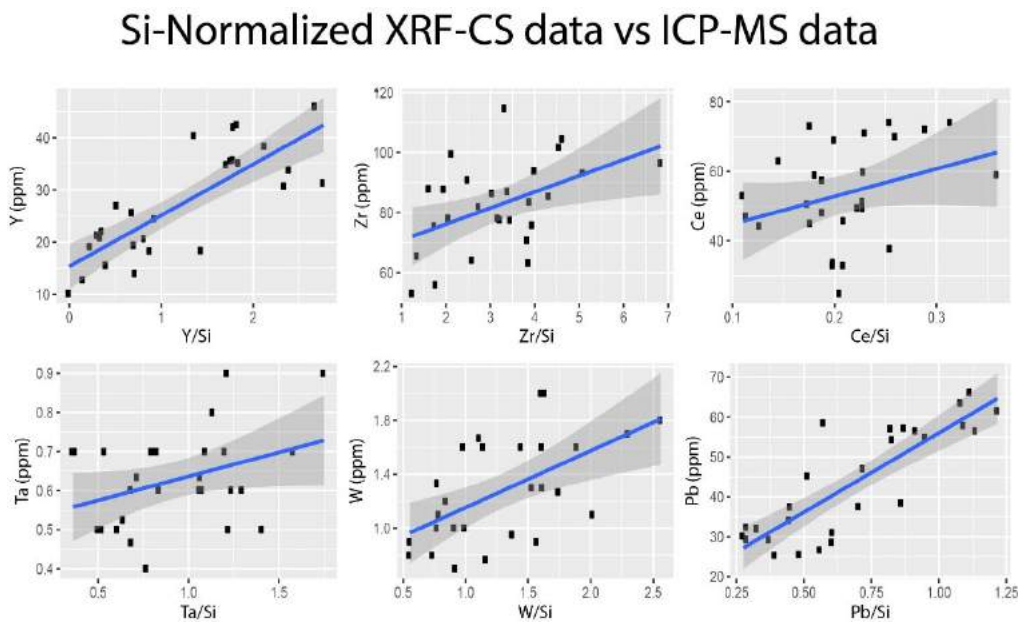

Figure A1.5 (cont'd): Comparison of Si-normalized XRF-CS to ICP-MS results. The blue line represents linear interpolation between Si-normalized XRF-CS and ICP-MS results. The dark grey shaded area represents the 95 % confidence interval for the linear regressions.

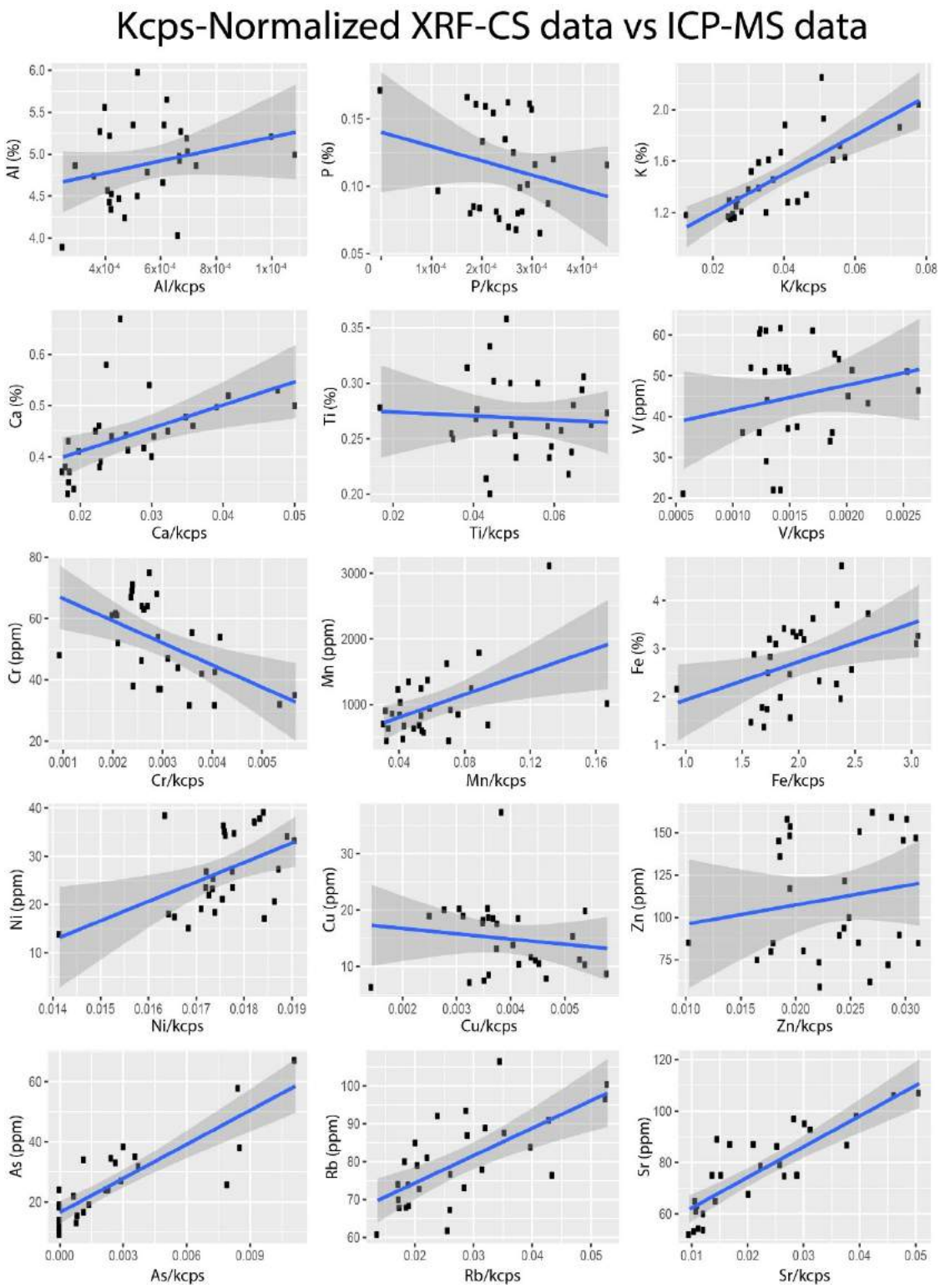

Figure A1.6: Comparison of kcps-normalized XRF-CS to ICP-MS results. The blue line represents linear interpolation between kcps-normalized XRF-CS and ICP-MS results. The dark grey shaded area represents the 95 % confidence interval for the regression.

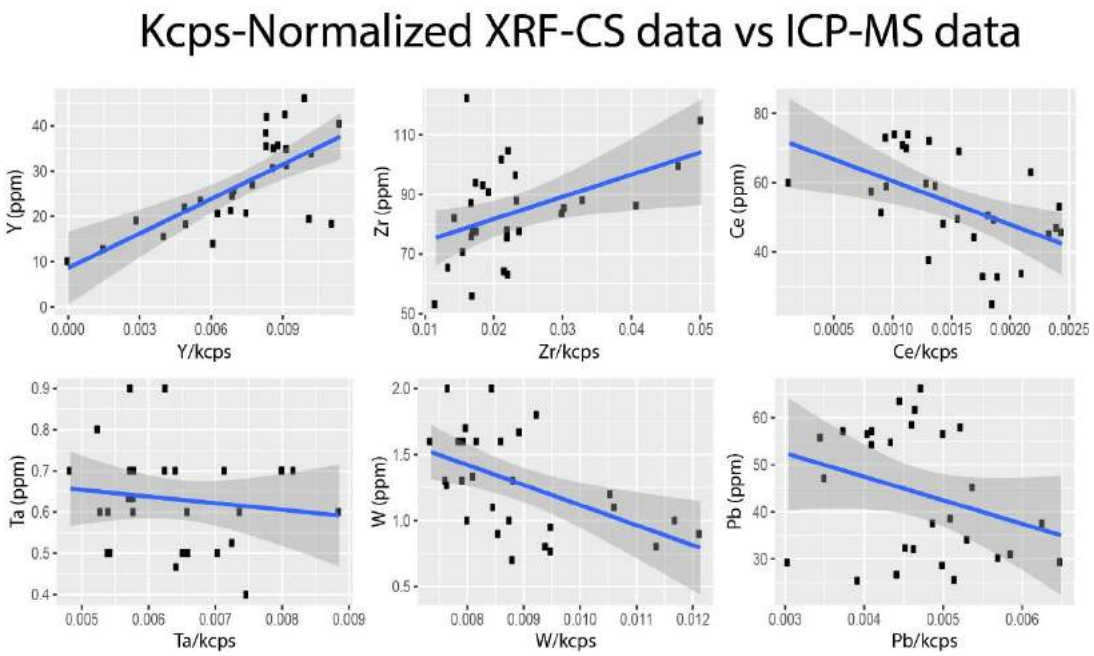

Figure A1.6 (cont'd): Comparison of kcps-normalized XRF-CS to ICP-MS results. The blue line represents linear interpolation between kcps-normalized XRF-CS and ICP-MS results. The dark grey shaded area represents the 95 % confidence interval for the regression.

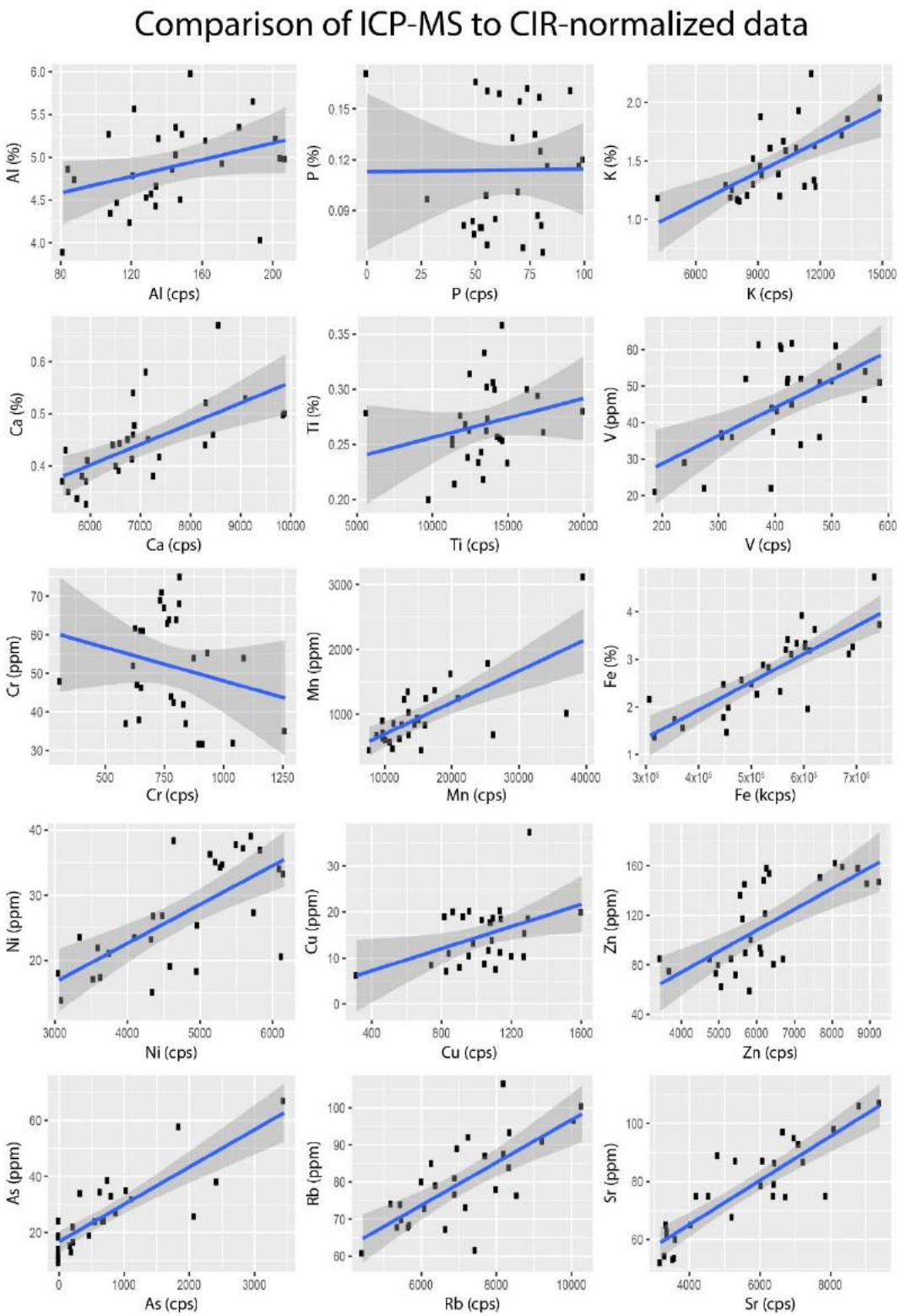

Figure A1.7: Comparison of CIR-normalized XRF-CS to ICP-MS results. The blue line represents linear interpolation between CIR-normalized XRF-CS and ICP-MS results. The dark grey shaded area represents the 95 % confidence interval for the linear regression.

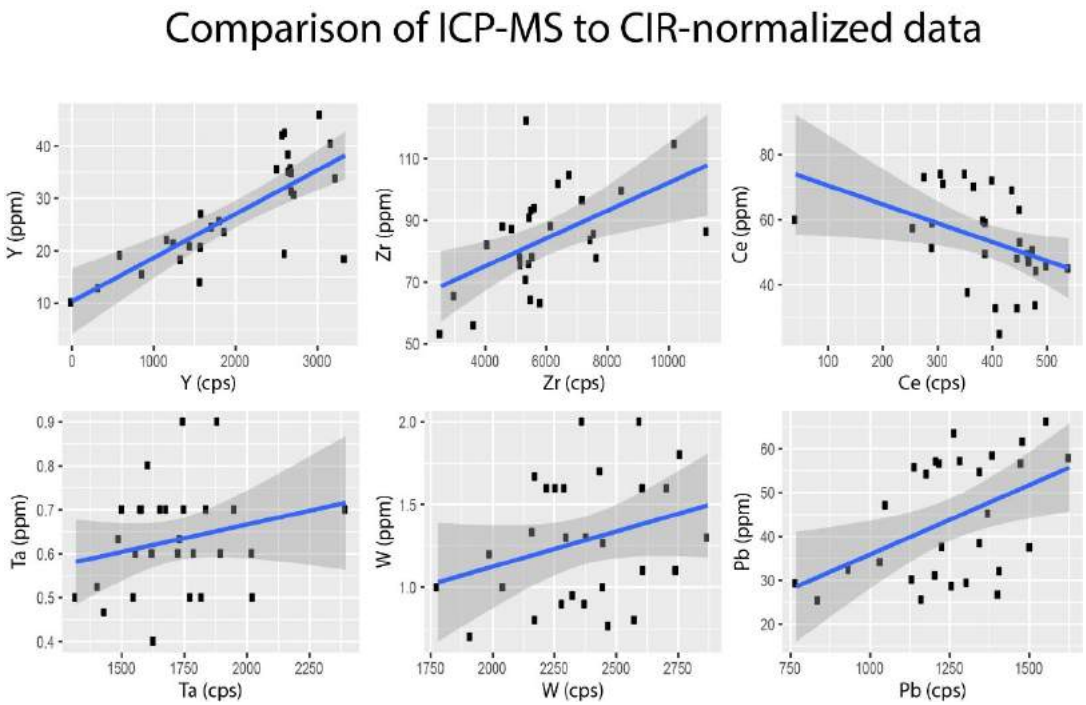

Figure A1.7 (cont'd): Comparison of CIR-normalized XRF-CS to ICP-MS results. The blue line represents linear interpolation between CIR-normalized XRF-CS and ICP-MS results. The dark grey shaded area represents the 95 % confidence interval for the linear regression.

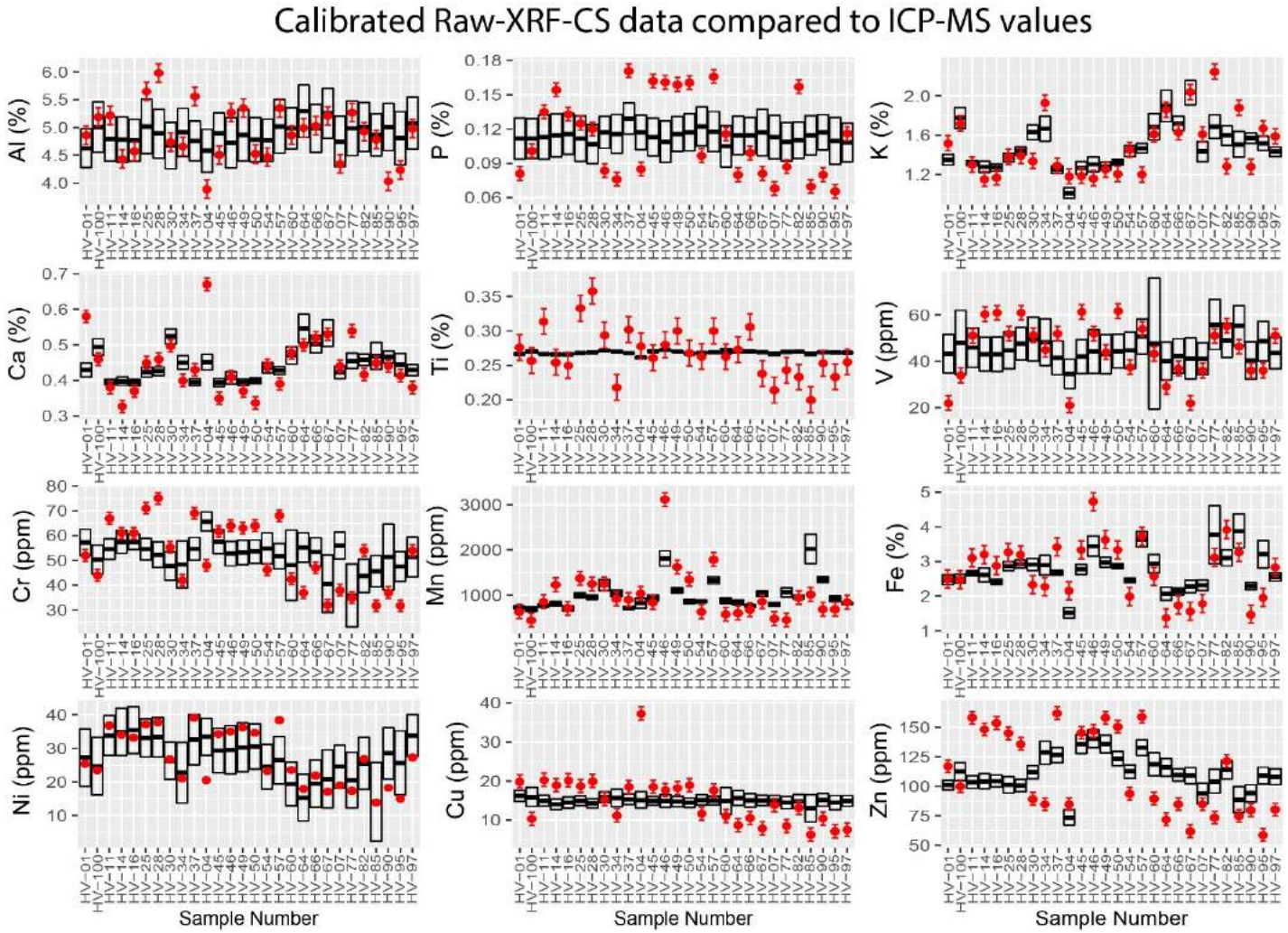

Figure A1.8: Comparison or predicted concentrations based on raw-XRF-CS data and ICP-MS results. The black boxes show median elemental concentrations predicted by calibrated XRF-CS data +/- the standard deviation of data. ICP-MS measurements are show with the red dots; the red crossbars show two relative standard deviations for elements calculated based on triplicate ICP-MS measurements.

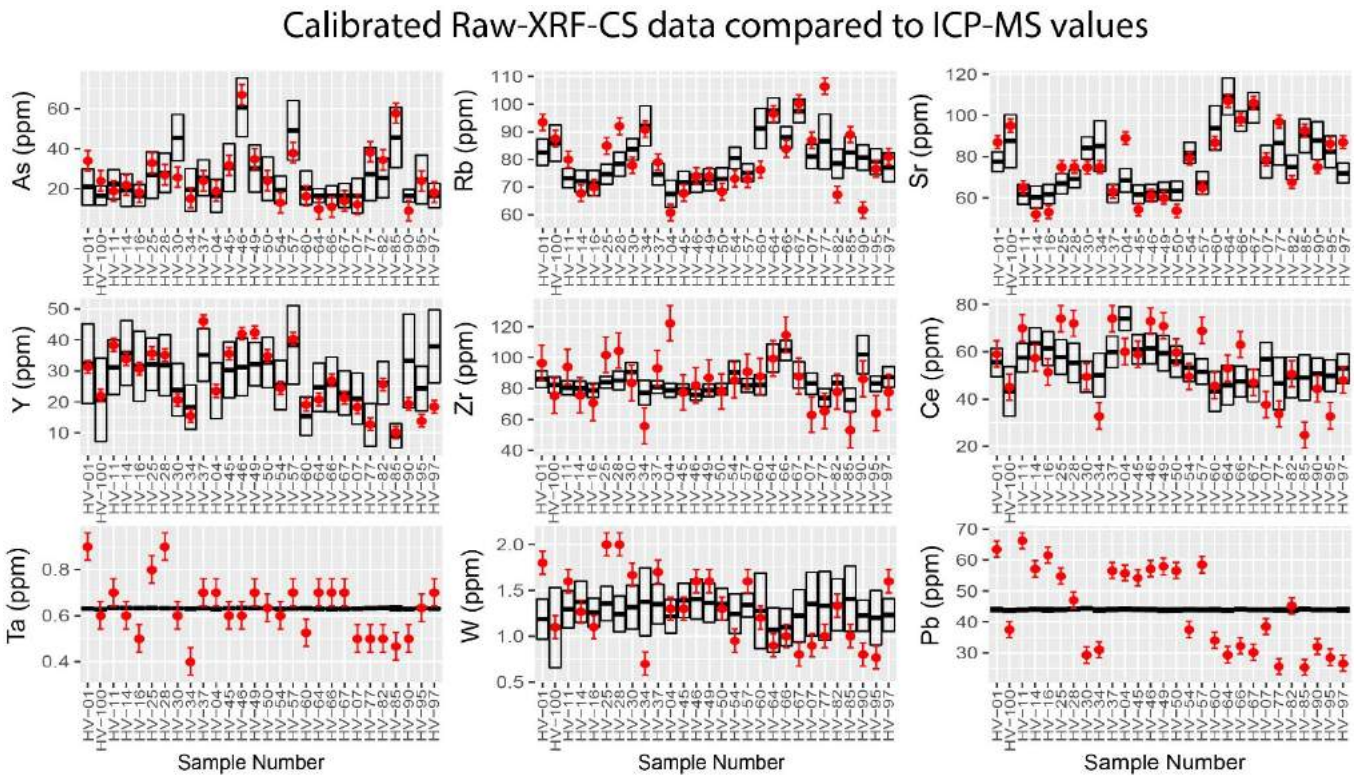

Figure A1.8 (cont'd): Comparison or predicted concentrations based on raw-XRF-CS data and ICP-MS results. The black boxes show median elemental concentrations predicted by calibrated XRF-CS data +/- the standard deviation of data. ICP-MS measurements are show with the red dots; the red crossbars show two relative standard deviations for elements calculated based on triplicate ICP-MS measurements.

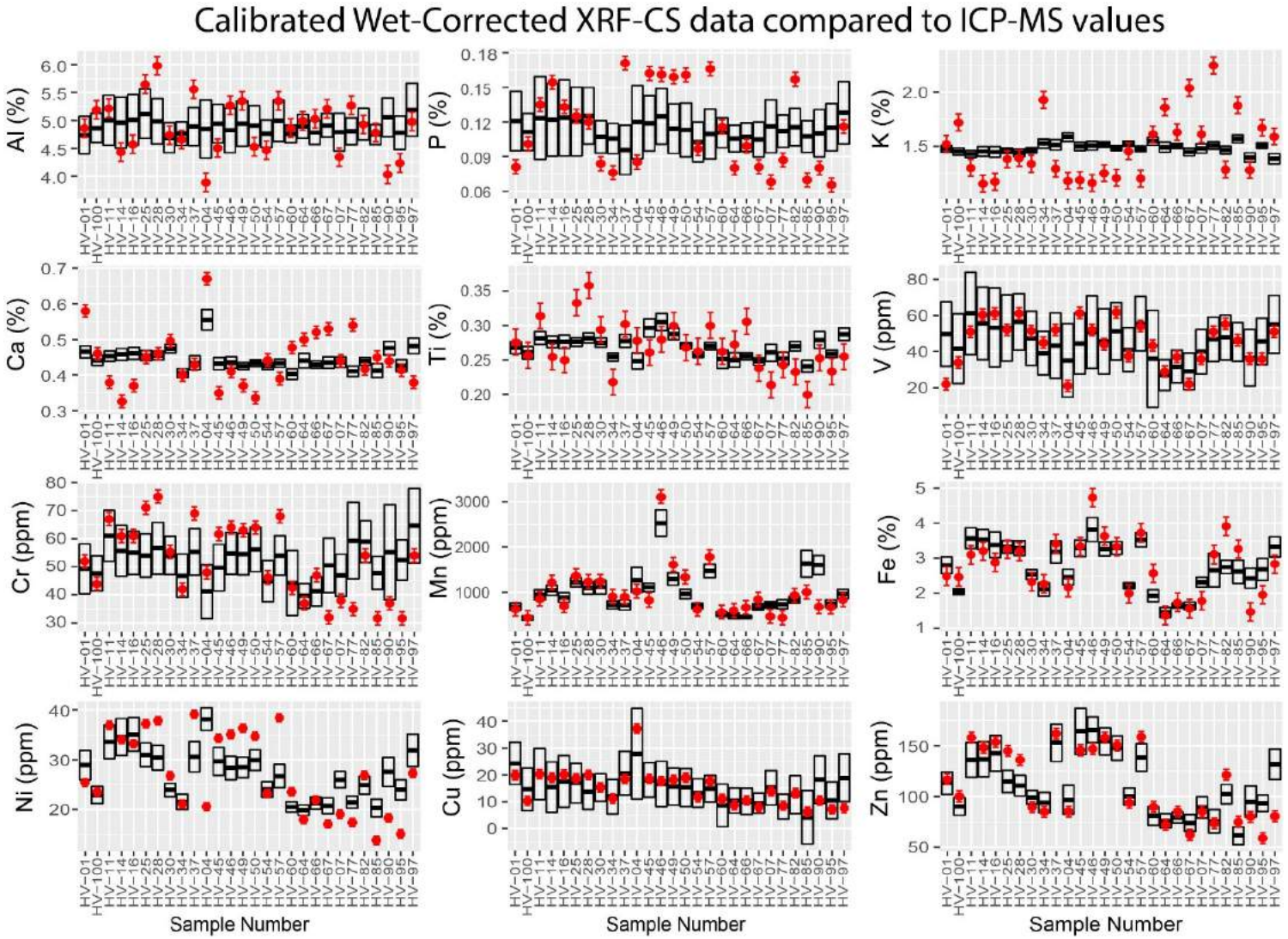

Figure A1.9: Comparison or predicted concentrations based on wet-corrected XRF-CS data and ICP-MS results. The black boxes show median elemental concentrations predicted by calibrated XRF-CS data +/- the standard deviation of data. ICP-MS measurements are show with the red dots; the red crossbars show two relative standard deviations for elements calculated based on triplicate ICP-MS measurements.

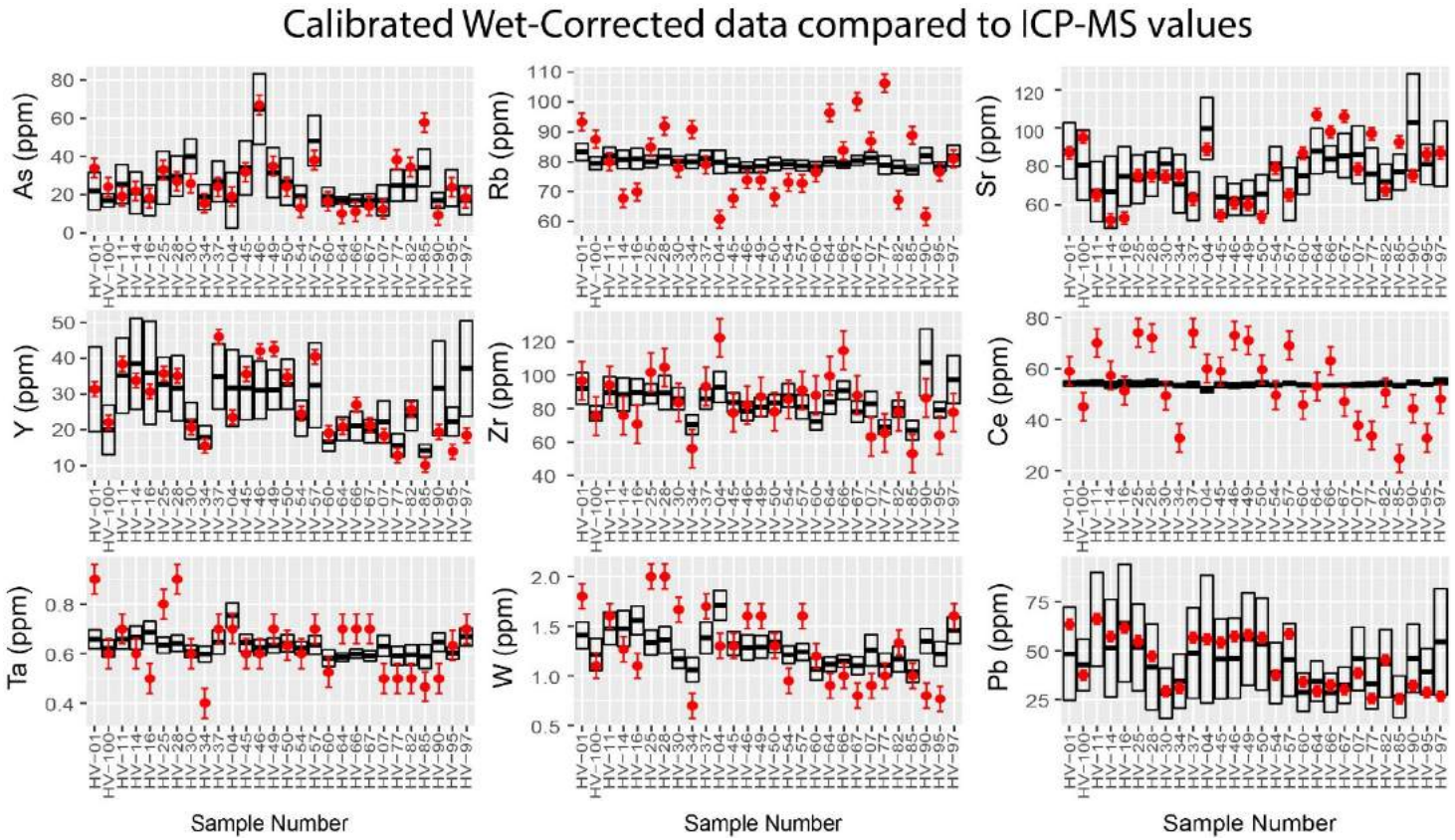

Figure A1.9 (cont'd): Comparison or predicted concentrations based on wet-corrected XRF-CS data and ICP-MS results. The black boxes show median elemental concentrations predicted by calibrated XRF-CS data +/- the standard deviation of data. ICP-MS measurements are show with the red dots; the red crossbars show two relative standard deviations for elements calculated based on triplicate ICP-MS measurements.

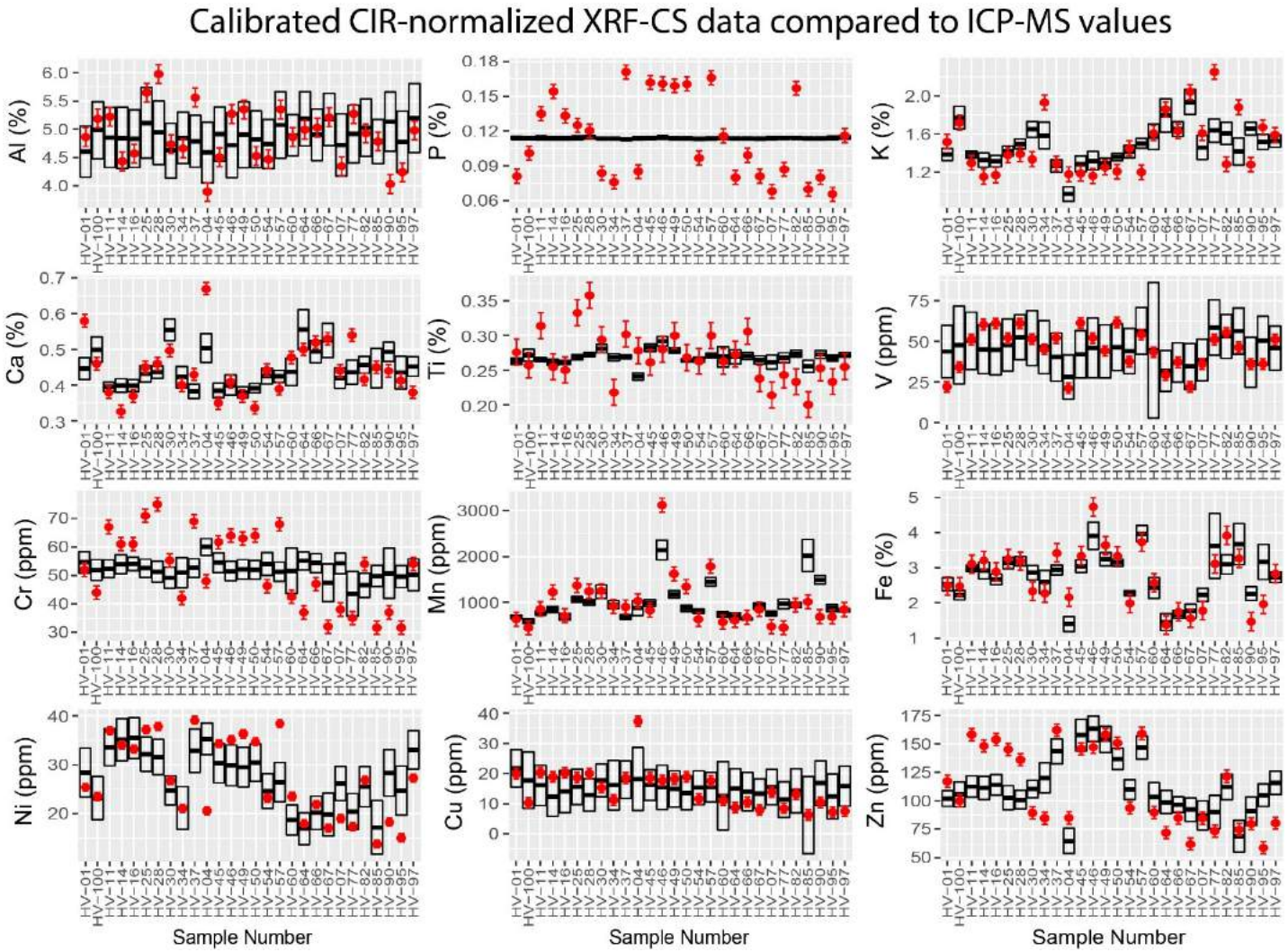

Figure A1.10: Comparison or predicted concentrations based on CIR-normalized XRF-CS data and ICP-MS results. The black boxes show median elemental concentrations predicted by calibrated XRF-CS data +/- the standard deviation of data. ICP-MS measurements are show with the red dots; the red crossbars show two relative standard deviations for elements calculated based on triplicate ICP-MS measurements.

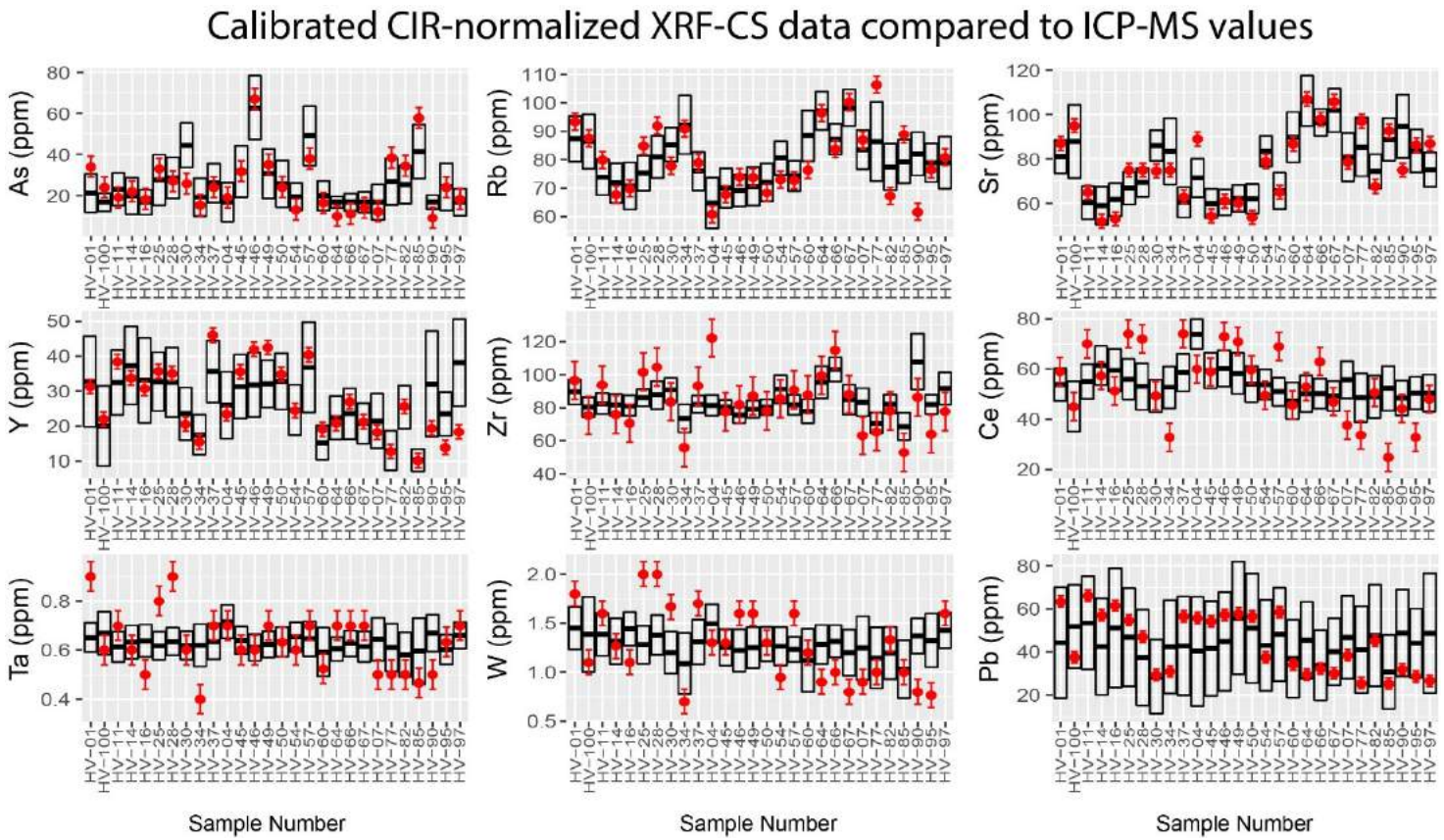

Figure A1.10 (cont'd): Comparison or predicted concentrations based on CIR-normalized XRF-CS data and ICP-MS results. The black boxes show median elemental concentrations predicted by calibrated XRF-CS data +/- the standard deviation of data. ICP-MS measurements are show with the red dots; the red crossbars show two relative standard deviations for elements calculated based on triplicate ICP-MS measurements.

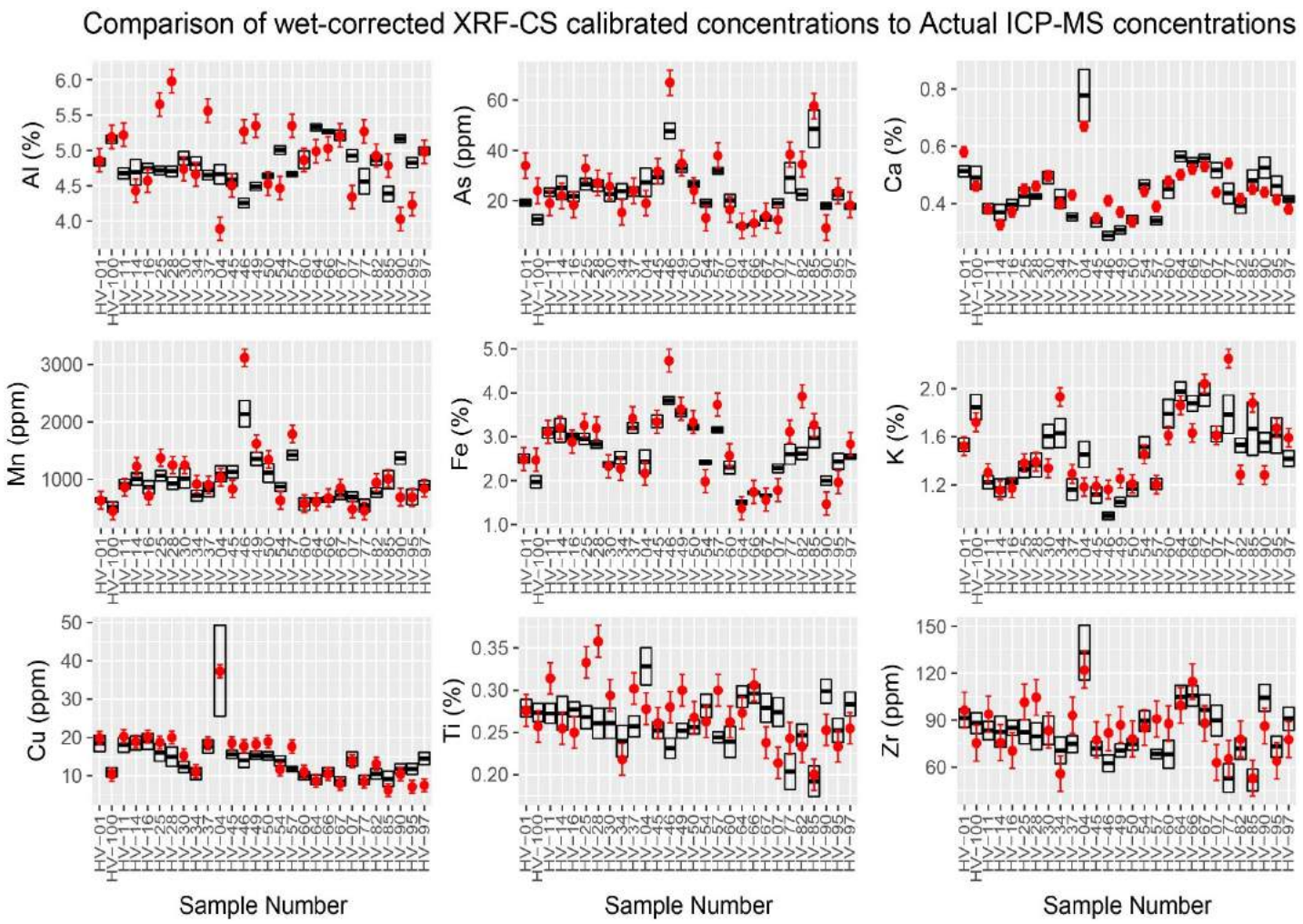

Figure A1.11: Comparison or predicted concentrations based on MLC-XRF-CS data and ICP-MS results. The black boxes show median elemental concentrations predicted by calibrated XRF-CS data +/- the standard deviation of data. ICP-MS measurements are show with the red dots; the red crossbars show two relative standard deviations for elements calculated based on triplicate ICP-MS measurement.

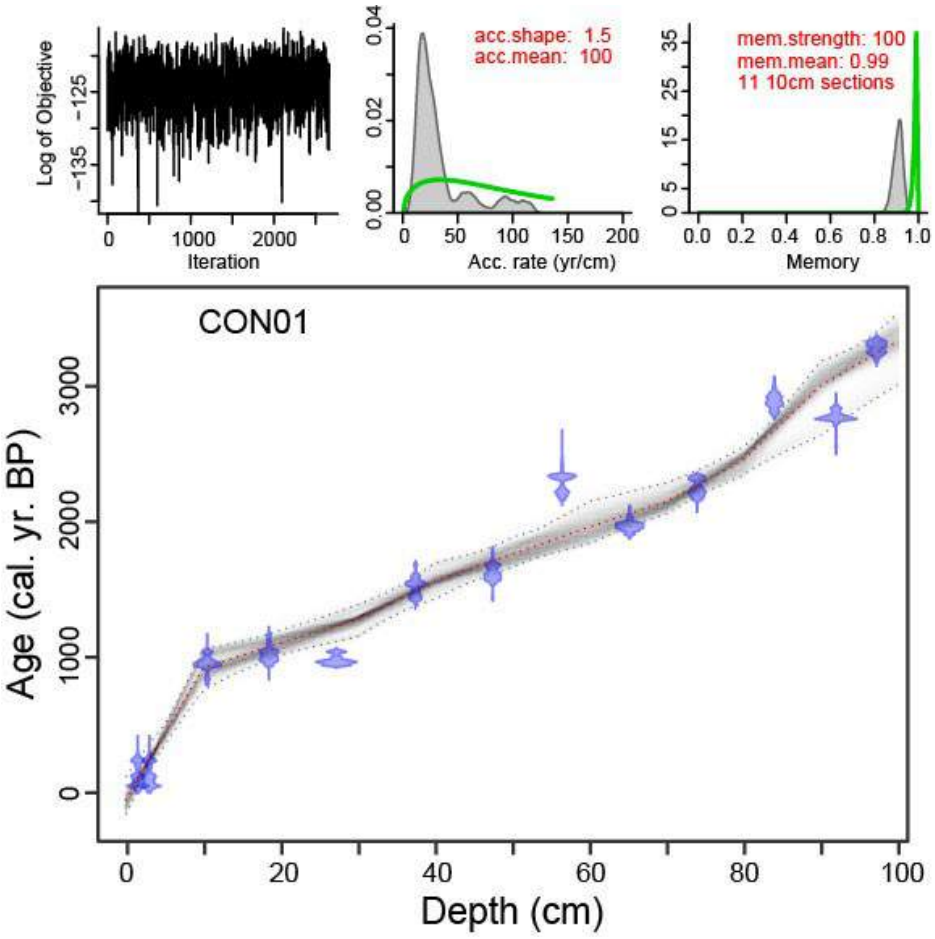

Figure A1.12: Age-depth model for Control Lake sediment core CON01 based on 13 radiocarbon dates created using BACON. Radiocarbon dates are shown in blue, and inferred age in grey – darker areas suggest greater likelihood of age at a given depth.

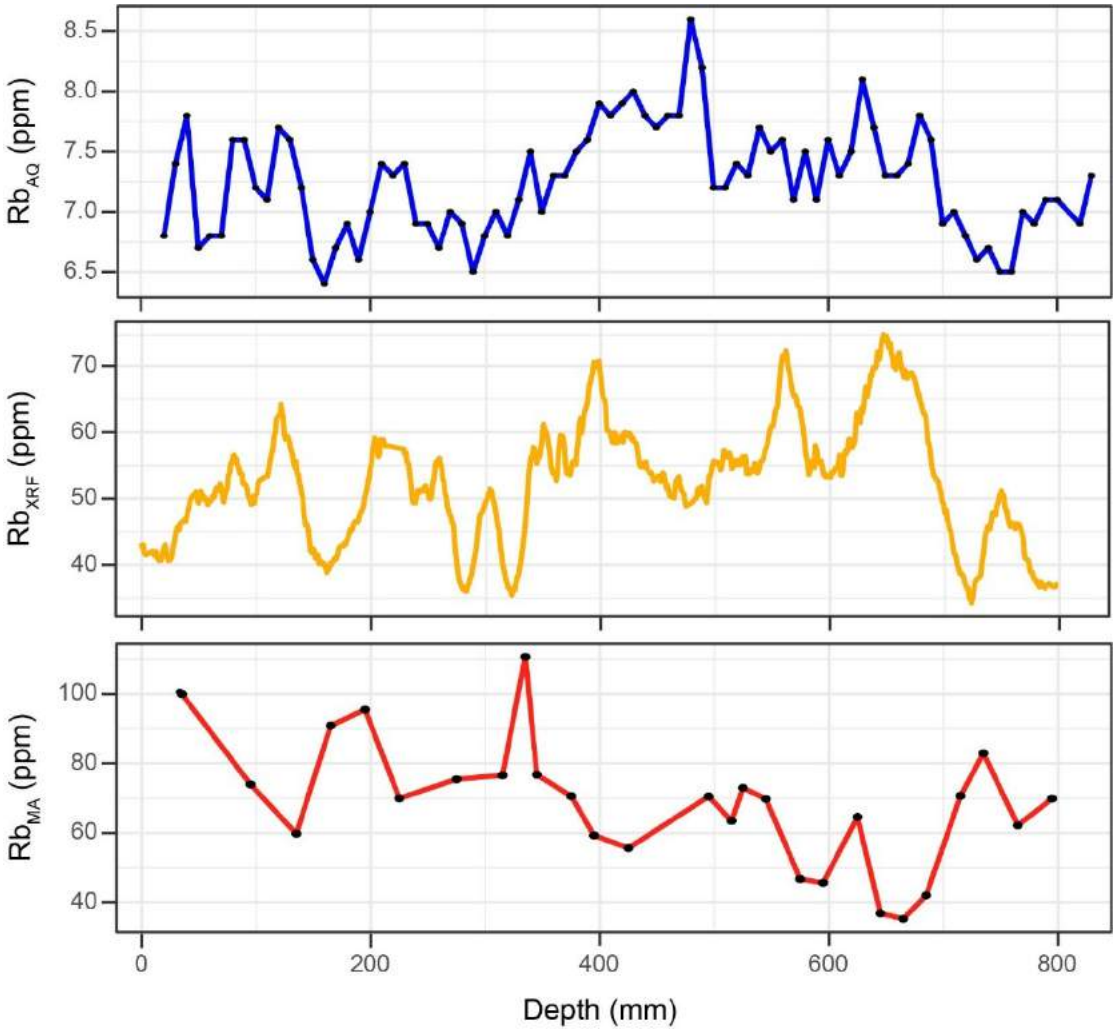

Figure A1.13: Comparison between Itrax-XRF results (Yellow) and ICP-MS results following multi-acid digestion (Red; MA-ICP-MS) from core CON01, and ICP-MS results following *aqua regia* digestion (Blue; AQ-ICP-MS) from core CON02 for the element Rb. Both cores are compared relative to depth (mm). Similar trend is apparent in both cores, although AQ-ICP-MS show lower concentration. This suggests that trends in RB are reliably captured by AQ digestion.

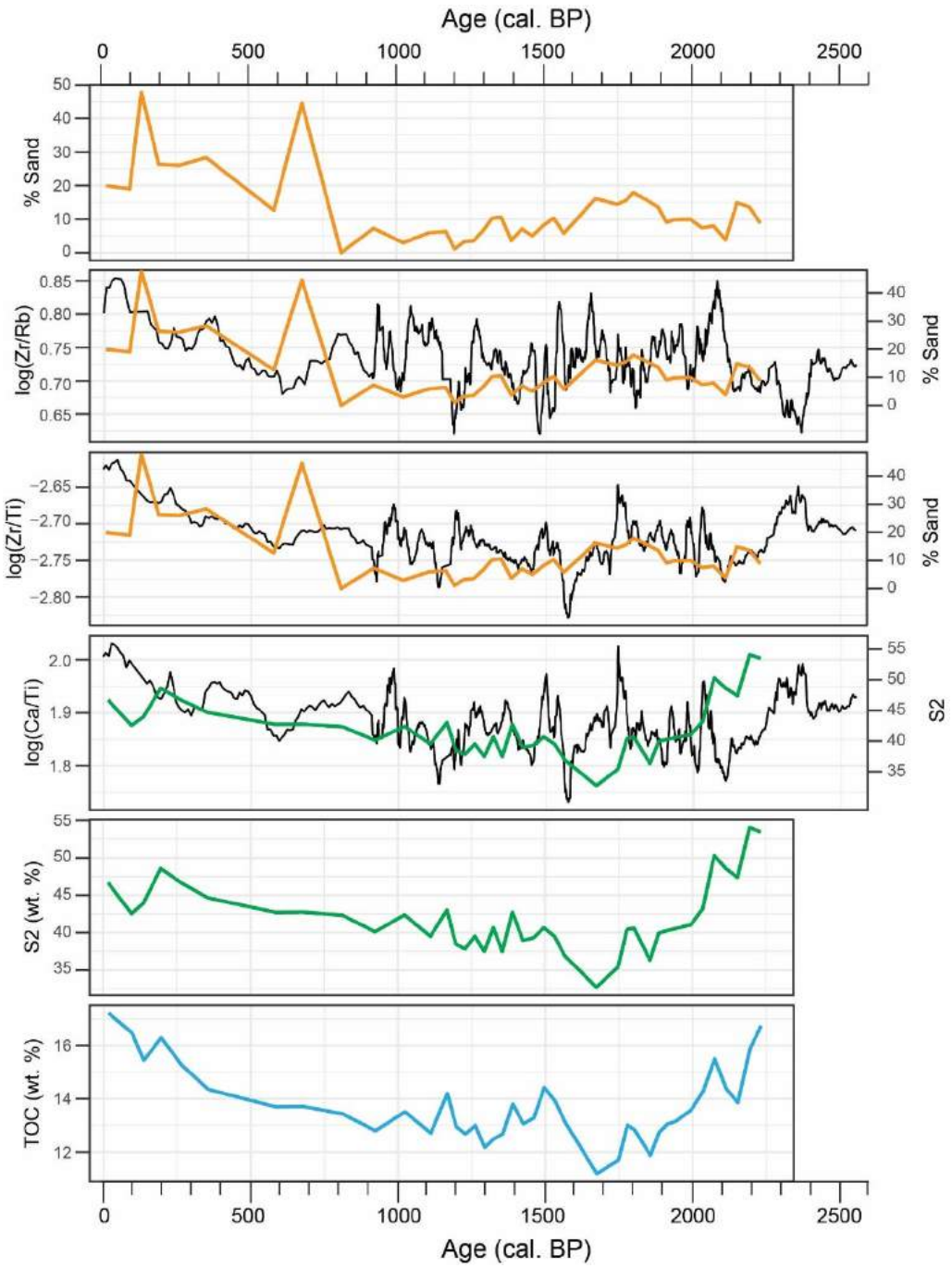

Figure A1. 14: Comparison of Itrax-XRF results from core CON01 to particle size and Rock Eval results from a 46-cm-long glew core from Control Lake studied by Miller et al. (in press). % Sand determine through laser-diffraction particle size analysis (Yellow) is compared to Itrax-XRF proxies for particle size (log(Zr/Rb) and log(Zr/Ti)) in black. Total organic carbon (TOC; blue) and S2 (labile organic matter; green) based on Rock Eval Pyrolysis results are compared to a proxy for in-lake productivity (log(Ca/Ti)).

Appendix 2: Supplementary Tables

Table A2.1: Radiocarbon results for analysis of bulk organic sediment from Control Lake core CON01 showing uncalibrated age (^{14}C yr BP) and the fraction of modern carbon (F^{14}C)

Lab ID	Core Depth (cm)	^{14}C yr BP	Error	F^{14}C	Error
UOC-3555	1 – 2	Modern	38	1.0386	0.0049
UOC-2107	2 – 4	Modern	21	1.0109	0.0026
UOC-3556	10 – 11	1276	38	0.8531	0.0040
UOC-3557	18 – 19	1336	38	0.8468	0.0040
UOC-2108	27 – 27.5	1304	21	0.8505	0.0022
UOC-3558	37 – 38	1868	38	0.7926	0.0038
UOC-3559	47 – 48	1942	38	0.7852	0.0037
UOC-3560	56 – 57	2529	38	0.7299	0.0034
UOC-2109	65 – 65.5	2252	22	0.7561	0.0020
UOC-3561	73.5 – 74.5	2489	38	0.7336	0.0035
UOC-3562	83.5 – 84.5	3020	38	0.6866	0.0032
UOC-3563	91.5 – 92.5	2879	38	0.6988	0.0033
UOC-2110	97 – 97.5	3297	21	0.6640	0.0017

Table A2.2: Fractional abundance of testate amoeba in samples identified to strain. Also included are total counts per samples and counts per cc.

Depth (cm)	Volume (cc)	*D. oblonga*	*P. compressa*	*D. protaeiformis* "acuminata"	*D. glans* "distenda"	*D. elegans*	*D. glans* "pulex"	*D. glans* "glans"	*D. minuta*	*D. globulosa*	*C. constricta* "constricta"	*C. constricta* "aerophila"
1.5	0.38	37.1	11.4	6.7	2.9	4.8	1.9	5.7	2.9	7.6	1.0	5.7
5.5	0.95	26.3	23.9	3.6	0.0	3.2	2.8	4.4	4.8	12.4	2.4	5.2
9.5	2.29	37.0	12.8	5.3	2.4	5.3	2.1	4.0	1.9	9.6	4.5	7.4
16.5	2.29	35.2	12.6	10.4	2.1	5.0	1.8	3.9	2.1	10.5	2.1	7.8
20.5	2.67	40.8	11.9	6.9	2.0	2.7	1.9	4.7	1.7	12.0	3.7	6.2
25.5	2.48	27.2	13.0	7.7	2.4	4.8	4.2	5.7	4.4	15.5	2.6	6.9
30.5	2.67	35.5	11.3	6.3	0.5	4.5	4.7	5.8	2.6	10.1	3.9	8.8
35.5	2.86	38.3	13.2	7.2	1.2	3.8	2.7	3.4	2.8	11.7	3.6	7.8
40.5	2.67	31.3	10.5	4.8	4.5	5.6	5.1	7.3	2.4	10.0	4.8	7.8
45.5	2.48	27.0	4.9	10.2	3.4	6.1	2.4	10.2	3.7	11.9	4.4	11.2
50.5	2.67	35.4	7.2	7.6	2.0	2.5	4.0	12.7	1.7	6.6	5.2	9.3
55.5	3.05	32.9	5.2	10.4	2.1	7.8	2.1	7.8	0.5	9.3	4.7	12.2
60.5	3.05	31.5	6.8	8.3	1.5	4.3	4.3	12.1	2.3	5.7	4.7	11.3
65.5	2.86	24.0	7.9	12.0	2.5	4.9	2.2	11.4	0.8	10.1	3.5	12.0
69.5	1.91	48.5	5.3	8.0	1.3	5.6	1.6	6.1	1.9	4.3	2.9	7.2
75.5	3.05	31.0	7.5	10.2	3.1	6.1	2.9	7.7	1.0	8.2	5.5	11.9
81.5	1.15	25.5	6.7	11.4	2.0	10.7	0.7	5.4	2.7	4.7	6.7	15.4
86.5	1.53	18.0	3.5	6.0	3.5	8.8	1.6	4.4	1.6	5.7	13.6	26.8
90.5	1.53	47.7	6.0	4.9	2.1	3.9	2.1	4.2	1.4	4.2	6.7	12.0
95.5	4.20	38.9	8.4	2.7	1.8	6.6	2.7	6.6	4.9	0.9	7.1	15.5
100.5	0.95	24.3	6.1	4.7	2.0	14.9	0.7	0.7	6.1	1.4	11.5	19.6
105.5	2.29	17.7	8.7	6.8	3.5	11.6	3.5	5.8	2.6	4.8	6.8	16.1
111.5	3.63	44.1	5.2	12.7	2.3	6.5	2.3	7.2	1.0	1.6	2.9	7.8
115.5	2.86	49.5	6.4	9.8	2.2	4.4	2.8	3.9	0.6	2.6	3.1	6.6
120.5	2.86	52.7	5.4	6.6	1.5	4.8	2.7	5.1	0.9	3.0	2.7	9.9
125.5	2.86	34.7	4.0	8.7	4.7	10.8	3.5	6.1	0.9	2.8	4.0	12.0
130.5	4.96	30.7	6.1	10.2	0.6	4.7	4.7	9.4	0.3	1.7	5.3	16.1

Table A2.2 (cont'd): Fractional abundance of testate amoeba in samples identified to strain. Also included are total counts per samples and counts per cc.

Depth	Volume	C. aculeata "discoides"	C. aculeata "aculeata"	C. constricta "spinosa"	Cucurbitella tricuspis	D. acutissima	Lesqueresia spiralis	Total	Total/cc
1.5	0.38	1.0	0.0	1.0	4.8	0.0	2.9	105	275
5.5	0.95	2.4	0.0	0.4	2.8	1.6	1.6	251	263
9.5	2.29	2.1	0.3	0.3	1.3	0.5	1.3	376	164
16.5	2.29	2.5	0.1	0.5	1.2	0.6	0.2	856	374
20.5	2.67	1.2	0.3	0.3	1.3	0.6	0.5	936	350
25.5	2.48	2.6	0.1	0.0	1.5	0.2	0.3	880	355
30.5	2.67	2.0	0.0	0.1	1.7	1.0	0.5	764	286
35.5	2.86	1.9	0.2	0.2	1.2	0.3	0.2	1453	508
40.5	2.67	1.4	0.3	0.6	1.9	0.5	0.5	627	235
45.5	2.48	1.7	0.2	0.2	1.2	0.2	0.0	589	237
50.5	2.67	2.8	0.4	0.5	0.9	0.3	0.0	754	282
55.5	3.05	2.3	0.5	0.0	1.0	0.0	0.3	386	126
60.5	3.05	3.2	0.1	0.0	1.1	1.3	0.1	750	246
65.5	2.86	1.9	1.4	0.0	2.2	0.3	0.8	367	128
69.5	1.91	0.0	4.5	0.0	1.1	0.8	0.0	375	196
75.5	3.05	2.0	0.2	0.0	0.7	1.2	0.0	587	192
81.5	1.15	0.7	2.7	0.0	0.7	0.0	0.7	149	130
86.5	1.53	2.2	0.9	0.0	1.9	1.3	0.3	317	208
90.5	1.53	3.5	0.0	0.0	0.4	0.4	0.0	283	185
95.5	4.20	1.8	0.9	0.0	0.4	0.0	0.4	226	54
100.5	0.95	3.4	0.0	0.0	0.0	0.0	0.7	148	155
105.5	2.29	2.6	1.6	0.3	1.6	1.6	1.9	310	135
111.5	3.63	1.0	0.3	0.0	1.0	0.7	1.3	306	84
115.5	2.86	2.6	0.9	0.0	0.9	1.7	0.9	543	190
120.5	2.86	0.9	0.0	0.0	2.1	0.3	0.3	334	117
125.5	2.86	1.4	1.2	0.2	1.4	1.2	0.9	426	149
130.5	4.96	3.6	1.9	0.0	1.7	1.4	1.1	361	73